UNIVERSITY OF SOUTHAMPTON

FACULTY OF ENGINEERING AND THE ENVIRONMENT

Aerodynamics and Flight Mechanics Research Group

Numerical simulation of vortex dipole formation and evolution in stably stratified fluid

by

Daniel Neil Mulvaney

Thesis for the degree of Doctor of Philosophy

June 2016

UNIVERSITY OF SOUTHAMPTON

ABSTRACT

FACULTY OF ENGINEERING AND THE ENVIRONMENT
Aerodynamics and Flight Mechanics Research Group

Doctor of Philosophy

NUMERICAL SIMULATION OF VORTEX DIPOLE FORMATION AND EVOLUTION IN STABLY STRATIFIED FLUID

by Daniel Neil Mulvaney

Direct numerical simulation has been used to study how axisymmetric vortical flow structures evolve whilst propagating horizontally in both homogeneous fluid and in fluid with a linear stable density stratification in the vertical direction. The structures studied were initially toroidal vortex rings and impulsive jets formed from a brief, horizontal injection of fluid into a quiescent domain. Previous experimental studies have demonstrated that when these initially axisymmetric structures are allowed to evolve under the influence of stable stratification, acceleration due to buoyancy acts to suppress vertical displacement of fluid particles, eventually reducing the flow to a pair of contra-rotating, planar vortices, commonly referred to as a vortex dipole.The numerical simulations documented in this thesis demonstrate the process by which the initially axisymmetric structures are transformed into late time dipoles in a stratified fluid, with the stages of this transformation categorised both through visual changes in the flow field as well as characteristic variations in kinetic energy and buoyancy variance histories that are inaccessible to the experimental work, thus allowing the energetics and vorticity fields of these flows to be directly correlated for the first time. Additionally, it has been demonstrated that while different means of imparting horizontal momentum to the fluid through an initial solution or different profiles of momentum injection may generate distinct vorticity fields at the early time, the energetics, scaling behaviours and agreement with theoretical models appear universal across the late time dipoles formed from these cases, which has not been addressed directly in previous literature.

Contents

List of Figures

List of Tables

Declaration of Authorship

I, Daniel Mulvaney, declare that the thesis entitled “Numerical simulation of vortex dipole formation and evolution in stably stratified fluid" and the work presented in the thesis are both my own, and have been generated by me as the result of my own original research. I confirm that:

- this work was done wholly or mainly while in candidature for a research degree at this University;
- where any part of this thesis has previously been submitted for a degree or any other qualification at this University or any other institution, this has been clearly stated;
- where I have consulted the published work of others, this is always clearly attributed;
- where I have quoted from the work of others, the source is always given. With the exception of such quotations, this thesis is entirely my own work;
- I have acknowledged all main sources of help;
- where the thesis is based on work done by myself jointly with others, I have made clear exactly what was done by others and what I have contributed myself.

Signed: _____

Date: _____

Acknowledgments

After finally concluding postgraduate studies and research, there are several people who are owed thanks for their support, advice and technical assistance. First thanks goes to my supervisors, Professors Gary Coleman, Glyn Thomas and latterly Neil Sandham, for allowing me to undertake this project and for their continued support and encouragement. Professor Sandham receives particular thanks for his continued patience and advice toward the completion of this work. Dr Roderick Johnstone and Dr John Redford are to be thanked for their advice whilst developing the functionality of the simulation code, and for help porting it between different computing clusters. Gratitude also goes out to Dr Bharath Ganapathisubramani for his insight into starting jet and vortex structures, and to fellow PhD students Shankar Balrishikan and Watchapon Rojanaratanangkule for their help familiarising me with the basics of the project.

This project is funded by the UK Engineering and Physical Sciences Research Council (EPSRC) (Grant EP/G05035X), as part of the UK Turbulence Consortium (EP/G069581/1). The simulations were run on the University of Southampton Iridis 3 cluster and HECToR, the UK's national high-performance computing service.

Final thanks goes to my colleagues at Mercedes AMG Petronas F1 Team, without whom I would not have developed the fortitude to finally write up this thesis, with many former University of Southampton students among their number.

Nomenclature

Subscript/superscript notation	
$\hat{B}$	Dimensional form of B
$\hat{B}_{\mathrm{Ref}}$	Constant reference value of $\hat{B}$
B_{Max}	Maximum value of B in a prescribed plane
B_{EM}	Edge mean values of B used in fringe method
B_{∞}	Volume mean value of B
B_0	Initial solution value of B
$\overline{B}$	Time average value of B
B_D	Property B of vortex dipole
B_F	Property B of virtual drag force region
B_J	Property B of jet/propulsive source
B_R	Property B of vortex ring
B_W	Property B of wake

N.B. All quantities are non-dimensional unless otherwise indicated.

Abbreviations	
DNS	Direct Numerical Simulation
LES	Large Eddy Simulation
RANS	Reynolds Averaged Navier-Stokes
PIV	Particle image velocimetry
Non-dimensional parameters	
Re	Reynolds number
Fr	Froude number
Ri	Richardson number
Pr	Prandtl number
St	Strouhal number

Upper case roman letters	
C	Courant number
C_R	Constant for determining vortex ring propagation velocity (Archer, 2008)
D	Diameter
F	Force
H	Vertical thickness
H_ω	Vorticity thickness
I	Impulse
I_i	Impulse vector
J_F	Kinematic momentum flux of drag source
J_J	Kinematic momentum flux of propulsive source
J_0, J_1	Bessel functions of zero and first order
K	Volume integrated kinetic energy
K	Volume integrated kinetic energy components K_u, K_v, K_w
K'_B	Volume integrated buoyancy flux
K'_f	Volume integrated kinetic energy flux from momentum source(s)
K'_ν	Volume integrated viscous dissipation of kinetic energy
K'_σ	Volume integrated kinetic energy flux from fringe region
K_B	Time integral of K'_B
K_f	Time integral of K'_f
K_ν	Time integral of K'_ν
K_σ	Time integral of K'_σ
L_i	Domain size (L_x, L_y, L_z)
M	Number of Fourier modes
N	Buoyancy frequency (stratification strength)
N_f	Number of grid points allocated to fringe method
P	Volume integrated buoyancy variance
P'_ν	Volume integrated viscous/thermal dissipation of buoyancy variance
P'_σ	Volume integrated buoyancy variance flux from fringe region
R	Radius
R^*	Radius with perturbation
T	Formation time
T_J	Jet duration in units of formation time
T_S	Vortex dipole starting time
T_Γ	Time of maximum leading ring circulation (formation time units)
U_B	Streamwise velocity of flow/structure B
U_T	Background reference frame velocity
V	Volume
X	Streamwise location

Lower case roman letters	
a	Lamb-Chaplygin model dipole radius
f_i	Acceleration vector from external body force(s)
g	Acceleration due to gravity
k	Lamb-Chaplygin model ratio = $a/3.8317$
k_n	Wavenumbers of Fourier transform
L_i	Domain size (L_x, L_y, L_z)
l_{fi}	Fringe region length scale (l_{fx}, l_{fz})
m	Mass
n_i	Computational grid size (n_x, n_y, n_z)
n_ϵ	Vortex ring perturbation wavenumber
p	Pressure
q	Velocity magnitude
r	Radial distance from origin
r_2	Radial distance from origin in a prescribed plane
r_F	Radius of drag source
r_J	Radius of propulsive source
t	Time
t_J	Duration of impulsive jet/momentum injection
t_w	Fringe region smoothness factor
t_X	Time offset for dipole streamwise position scaling law
t_D	Time offset for dipole diameter scaling law
t_ω	Time offset for dipole vorticity decay law
t_H	Time offset for dipole thickness scaling law
u_i	Velocity vector (u, v, w)
x_i	Position vector from origin (x, y, z)

Greek letters	
α_n	Fourier coefficient
α_X	Scaling coefficient for dipole streamwise position
α_D	Scaling coefficient for dipole diameter
$\alpha_X D$	Dipole entrainment coefficient
$\alpha_H D$	Dipole aspect ratio
α_ω	Scaling coefficient for dipole vorticity decay
δ_G	Gaussian function diameter
δ_H	Hyperbolic function diameter
δ_{ij}	Kronecker delta
δ_R	Vortex ring core radius
Γ	Circulation
Δv	Wake velocity deficit
Δx_i	Grid spacing
Δt	Time step
ϵ	Vortex ring perturbation magnitude
θ	Vertical acceleration due to buoyant displacement (buoyancy scalar)
κ	Scalar diffusivity
ν	Kinematic viscosity
Φ	Background density lapse rate
ρ	Density
ρ'	Density fluctuation
ρ_∞	Mean background density
σ	Fringe region strength at specific x, y, z location
σ_c	Maximum fringe region strength
Φ	Background lapse rate (density gradient) in stratified direction
ϕ	Internal wave angle
ϕ_i'	Angular velocity vector (ϕ_x, ϕ_y, ϕ_z)
ψ	Angular co-ordinate
Ω	Volume integrated enstrophy
ω_f	Angular frequency of oscillating force
ω_i	Vorticity vector $(\omega_x, \omega_y, \omega_z)$
$\lvert\omega\rvert$	Vorticity magnitude
ψ	Stream function
ψ_R	Angular coordinate around vortex ring circumference

Chapter 1

Introduction

1.1 Overview

The work conducted for this thesis is a numerical study looking to create a simulated analogy to the wide range of experimental and theoretical work documented in literature regarding the formation of vortex dipoles. Specifically, this work is concerned with dipoles that are formed when a horizontally propagating region of fluid, with an initially axisymmetric structure about its propagation axis, deforms due to the influence of the background density gradient in a stably stratified fluid. Such phenomena have been observed by Flór et al. (1995),Voropayev et al. (2008) and Praud and Fincham (2005) to name but a few, but by comparison numerical work in this field appears to be considerably lacking.

This thesis documents the generation of numerically simulated analogies to these experimental works, with the aim of not only verifying existing experimental observations and theoretical models, but also adding new insight to the formation process of late time dipoles through the energetics and buoyancy scalar field which are unavailable (or extremely difficult to determine) in experimental studies. The universality of the late time dipoles across a range of initial conditions, Reynolds numbers and stratification strengths is also demonstrated.

1.2 Literature review

1.2.1 The formation of a vortex ring and trailing jet from an impulsive momentum injection

The formation of coherent, vortical structures from impulsively acting momentum sources into fluid volumes is a widely observed phenomena in nature, has been studied extensively in both laboratory experiments and numerical simulations, and has a range of useful applied engineering applications. For the purposes of this project, we consider two such vortical structures, namely a toroidal vortex ring, and its two dimensional analogy, a vortex dipole.

In nature and the laboratory, a vortex ring can be formed when sufficient impulse is applied to a slug of fluid to accelerate it to a higher speed relative to fluid surrounding it. Often in laboratory experiments, a piston/cylinder arrangement is used to accelerate the fluid slug (Gharib et al., 1998; Dabiri and Gharib, 2004) though other novel methods involve the use of speakers connected to a waveform generator to create a short, controlled momentum addition to a fluid (Dawson et al., 2010) and the use of a cyclically closing/opening jet exhaust to break up an otherwise continuous fluid flow into shorter, impulsive intervals (Ruiz et al., 2010). Whichever method is used to create the impulsive injection, the physical mechanism that leads to the formation of a vortex ring is much the same.

A static, axisymmetric momentum source applied impulsively to an otherwise quiescent fluid of uniform density will first create a starting jet. As a consequence of viscous forces between the moving jet flow and the stationary fluid that surrounds it, a shear layer forms at the outer extreme of the jet's radius. At the leading edge of the jet, the outer part of this shear layer begins to decelerate and "roll up", with a radial component of motion introduced that eventually forms a vortex ring. A simple illustration of this is given in figure 1.1.

Gharib et al. (1998) studied the development of these jets in experiments using a round, piston driven jet nozzle with the jet velocity recorded at all times. Using a combination of flow visualisation and Particle Image Velocimetry (PIV), it was discovered that for an impulsive, constant velocity jet the circulation of the leading vortex ring initially increased linearly with time. If the jet was sustained long enough however, a point was reached where the vortex ring suddenly gains no further circulation and detaches from the shear layer that was feeding its development. This was described as vortex ring "pinch off". The authors proposed a non-dimensional time scale based on the

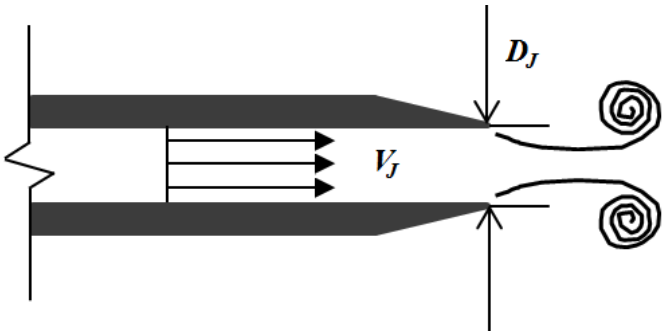

Figure 1.1: Schematic of vortex ring production from a jet nozzle with output velocity V_J and diameter D_J

jet velocity, U_J, and diameter of the jet orifice, D_J, to give

$$T = \frac{\overline{U_J} t}{D_J}. \tag{1.1}$$

The duration of the jet, and the time at which vortex pinch off is achieved can be given in terms of this non-dimensional time scale and are hereafter defined as T_J and T_Γ respectively. Both experimental studies (Akhmetov, 2001; Dawson et al., 2010) and numerical simulations (Boersma et al., 1998; Mohseni et al., 2001) have reported T_Γ to have a value of approximately 4. If $T_J < T_\Gamma$, all of the circulation input into the flow is entrained into the leading ring once the jet input has ceased. For $T_J > T_\Gamma$ the leading vortex ring is followed by a trailing jet that includes a series of smaller vortex ring structures. Boersma et al. (1998) observed that for a sustained jet, these secondary rings were formed through Kelvin-Helmholtz instability and were observed to break down to quasi-turbulent flow at a downstream point where $x/D \approx 8$, where x is the downstream distance from the fluid nozzle/outlet.

The concept of formation time and vortex ring pinch off has interesting applications when using impulsive jets or pulsed jets as a form of propulsion. Krueger and Gharib (2003) found that optimum propulsive efficiency (for a single momentum injection) is achieved when generating a vortex ring from a jet with $T_J = T_\Gamma$ i.e. by forming a vortex ring with maximum possible circulation and shutting off the momentum source at the exact time of pinch off. Such a phenomenon has been studied in nature with examples including marine creatures such as squid that utilise jet-like propulsion and cardiac flows in humans. Though not strictly relevant to the main aims of this project, a more comprehensive description of the formation time/propulsive efficiency relation for biological propulsion can be found in the review by Dabiri (2009) and the works cited therein.

The experimental study of Afanasyev (2006) attempted to extend the con-

cept of vortex ring pinch off and the non-dimensional time scale to a vortex dipole formed by a quasi two dimensional momentum injection into a shallow layer of fluid. The momentum injection was provided by a paddle partially submerged in the shallow layer between two bounding walls (analogous to the piston/cylinder arrangement for three-dimensional works), with the movement of the paddle through the channel creating a two dimensional starting jet. Instead of rolling up into a vortex ring, the shear layers at the outer edges of the starting jet roll up in opposite directions to create two contra-rotating vortex patches (the vortex dipole), which grow in size and circulation as they continue to receive mass and momentum from the source. Like the formation of a vortex ring, the circulation in the dipole initially grows linearly with time (assuming a constant rate of momentum addition), though instead of the circulation being maximised at some time, T_Γ, the circulation continues to rise linearly until a time T_S, after which linear increase continues but at a reduced rate. This time, T_S, was referred to as a vortex dipole "starting time".

For the purposes of this project, we are interested in the development of vortex dipoles, not from a two dimensional starting jet, but a three-dimensional vortex ring and trailing jet subjected to a constraint against motion in the vertical direction. Specifically, this project is concerned with how impulsive jet flows develop in a fluid volume with a linear, stable density stratification in the vertical direction.

1.2.2 Formation of a vortex dipole from a starting jet in a stratified fluid

When the momentum injection that creates an impulsive jet is shut off, the injected fluid propagates downstream as a quasi-axisymmetric starting jet, which may take the form of a single vortex ring (van Atta and Hopfinger, 1989), a sequence of laminar vortex rings (Gharib et al., 1998) or a turbulent cone (van Heijst and Flór, 1989) depending on the duration and Reynolds number of the source. In a sufficiently large domain of uniform density fluid, the propagating structure maintains a certain degree of axisymmetry with equal vertical and lateral length scales. However, a vertical constraint placed upon the flow either via the domain boundaries or buoyancy forces due to a non-uniform density will cause the axisymmetry to break down.

In the case of buoyancy forces affecting the development of the erstwhile axisymmetric structure, one of the most often considered scenarios is where the fluid has been given momentum in a horizontal plane in a domain with

a stable background density gradient in the vertical direction. In nature, a fluid layer with such a gradient can be found in the near-surface region of ocean bodies (the "pycnocline") which can typically feature a near linear, stable salinity-based density profile from depths of 100 to 1000 metres, depending on location, season and other factors.

The general effects of buoyant forces on fluid flow structures are documented extensively in Turner (1979). Within a stable density profile, motions induced by a three dimensional vortical structure will initiate mixing in the vertical direction, with the denser fluid from lower regions within the density gradient lifted upwards and lighter fluid carried downwards. Where denser fluid has been moved above lighter fluid, the density profile is no longer stable and buoyancy forces the displaced fluid particles back towards their equilibrium level. If we consider a single particle, if it is displaced from its equilibrium layer in an otherwise quiescent domain, the fluid particle will be subjected to a force, $m'g$, where m' is the difference in mass between the displaced particle and the fluid layer it currently lies within and g is the acceleration due to gravity. A negative value of m' (fluid particle less dense than surrounding layer) will result in an upward force and a positive value of m' (fluid particle more dense than surrounding layer) will result in a downward force. In the case of a slightly displaced fluid particle, these forces act to accelerate the particle back towards its equilibrium level. Each time it reaches the equilibrium level it will overshoot and now be subjected to buoyancy forces acting in the opposite direction, with the particle continuing to oscillate about the equilibrium level with an angular frequency,

$$N = \sqrt{-\frac{g}{\rho_{\mathrm{Ref}}}\frac{\partial \rho}{\partial z}}. \tag{1.2}$$

The quantity N is known as the buoyancy or Brunt-Väisälä frequency, and has a constant value throughout the domain provided the background density gradient, $\partial\rho/\partial z$ is uniform. The reference density, ρ_{Ref}, is taken as a representative density from within the domain. The Boussinesq approximation, as detailed by Turner (1979), allows for the use of a constant reference density provided that changes in density over the domain's vertical extent are sufficiently small. The amplitude of the particle oscillation about the equilibrium layer will decay over time due to viscous forces until they reach negligible levels.

In the case of a three-dimensional vortical flow, the mixing and subsequent particle displacement generates buoyancy forces which oppose the vertical motions within the flow, transferring some of the vertical component of kinetic

energy into internal energy of the buoyancy scalar field, referred to hereafter as buoyancy variance. If the magnitude of inertial forces within the flow is sufficiently high, compared to that of the buoyancy forces, then the development of the flow will be more or less equivalent to a neutrally stratified equivalent. In the case of a free shear flow where no additional kinetic energy is contributed to the flow, the magnitude of inertial forces will decay due to viscosity until the buoyancy forces become significant. Eventually, the buoyancy forces will become sufficiently dominant to completely suppress vertical motion within the flow, reducing the flow structures to a quasi-two-dimensional state, a process known as buoyant/gravitational collapse.

In the case of a decaying starting jet, the previously coherent vortical structures develop buoyant instabilities as they move downstream (van Atta and Hopfinger, 1989), with the individual structures collapsing to patches of two component, vertical vorticity. As observed by Voropayev et al. (1991), the most forward part of the starting jet (the leading vortex ring in an initially laminar case) is the first to undergo the process of buoyant suppression, forming a slow-moving front region once it has collapsed. As the trailing structures subsequently collapse, they advect forward to merge with the front region. All the while, the Reynolds number of the flow decays rapidly and the smaller structures, now that they have been reduced to an arrangement of planar eddies, begin to merge to form larger structures. This process has previously been described as an "inverse energy cascade" (Marino et al., 2013). Eventually, all the eddies merge to form two contra-rotating patches of vertical vorticity - the "vortex dipole".

The formation of vortex dipoles in a stratified fluid is a widely observed phenomena in large-scale flow systems in nature (Fedorov and Ginsburg, 1989). Past laboratory research to understand such structures has led to similar dipoles being created experimentally, with a commonly-used method utilising a horizontal momentum source acting impulsively into a fluid tank with stable density stratification (Voropayev et al., 1991; Flór et al., 1995). This stable stratification is achieved through layering saline solutions of different concentrations within the tank to create a linear density profile.

Whilst the collapse of a starting jet to a dipole under such conditions has been widely documented, available literature contains little quantitative data on the transformation from quasi-axisymmetric jet flow to a vortex dipole, with most focusing attention instead on the evolution of the late-time dipole once it has fully formed.

The most analogous literature that quantifies the buoyant collapse pro-

cess of a three-dimensional, vortical structure in some detail are experimental studies of a single, horizontally propagating vortex ring in a stably stratified fluid as studied by van Atta and Hopfinger (1989), Johari and Fang (1997) and Scase and Dalziel (2006). These studies generated isolated vortex rings using an impulsively acting momentum source in much the same way as was discussed in section 1.2.1, but with a sufficiently small injection duration such that only a single ring is formed that contains almost all of the flow circulation with no appreciable trailing jet (i.e. $T_J < T_\Gamma$). A vortex ring generated in such a way propagates horizontally with velocity, U_R, as

$$U_R = \frac{\Gamma}{4\pi R_R}\left(\ln\frac{8R_R}{\delta_R} + C_R\right), \tag{1.3}$$

where R_R is the ring radius, δ_R is the ring core radius and C_R is determined from the shape of the vorticity distribution within the core (see Archer et al. (2008)). The ring radius and volume gradually increases due to the entrainment of ambient fluid, which corresponds to a reduction in ring velocity and the rotational speed within the core. As with the more elaborate leading ring and trailing jet structures considered previously, an initially axisymmetric ring propagating horizontally through a stably stratified domain will maintain its axisymmetry provided the influence of buoyant forces is small compared to the rotational inertia within the ring core. The studies mentioned here quantify the ring in terms of two non-dimensional parameters, a ring Reynolds number, Re_R and a ring Froude number Fr_R. The exact definition of length and velocity scales used to determine each varies between studies, though a typical example is an adaption of that used by Scase and Dalziel (2006), viz.

$$Re_{Ry} = \frac{2U_R R_{Ry}}{\nu}, \tag{1.4}$$

$$Re_{Rz} = \frac{2U_R R_{Rz}}{\nu}, \tag{1.5}$$

$$Fr_R = \frac{U_R}{N R_{Rz}}. \tag{1.6}$$

The two Reynolds numbers given here are based on the lateral radius, R_{Ry}, and vertical radius, R_{Rz}, of the ring, which are initially identical for an axisymmetric ring but will differ as the ring is distorted under the influence of buoyancy. Provided the initial Froude number is high enough, the ring will initially maintain similar levels of circulation in both the vertical and lateral directions. As the ring speed decreases the Froude number rises, with baroclinic torque now acting to reduce the circulation in the lateral plane. As a consequence, the sections of the ring nearest the vertical midplane (predominantly consisting of vertical vorticity) will propagate faster than the higher and

lower sections, leading to a distortion of the formerly toroidal structure. van Atta and Hopfinger (1989) found that for rings with initial Froude numbers in the range 1.0-2.0, instability development and buoyant collapse occurred when the Froude number dropped to around half the initial value. The authors clarified that the relationship between initial and collapse Froude number could not be conclusively determined from the experiments due to the limited range of Froude numbers considered, as well as various experimental uncertainties. Johari and Fang (1997) proposed and experimentally verified that the collapse of the ring could be predicted in terms of either elapsed time or distance propagated, with the point of collapse increasingly linearly with a composite parameter $Re_{R0}Fr_{R0}^{2/3}$, where Re_{R0} and Fr_{R0} are respectively the initial Reynolds and Froude numbers of the ring.

In either case, while some effort has been made to quantify the point of buoyant collapse in terms of Froude number, the definition of when precisely collapse occurs remains somewhat vague, though the apparent Reynolds number and Froude number dependence discussed in these vortex ring studies provides a starting point from which to uncover such a definition. Scase and Dalziel (2006) noted that a collapsing vortex ring will go on to form a quasi-horizontal vortex dipole that bears a strong resemblance to those seen from the collapse of a more elaborate vortex ring and trailing jet structure.

1.2.3 Description of the late time stratified dipole

While the transformation of an axisymmetric vortex ring and trailing jet structure to a vortex dipole has not yet been quantified in significant detail, much more attention has been paid to the structure of the late time dipole itself, often involving comparison with a theoretical dipole model.

A vortex dipole, literally two contra-rotating vortices positioned sufficiently close to one another to significantly interact, is a widely recognised flow feature and source of considerable research interest in the field of fluid dynamics. As discussed by Voropayev et al. (1991), conceptually, the simplest example of a vortex dipole is two inviscid line vortices orthogonal to a two-dimensional plane, separated by distance, d, with equal magnitude but opposite signed circulation, $\pm\Gamma$, with no background velocity imposed (Llewellyn Smith and Nagem, 2013). In isolation, each vortex induces a circular velocity field around itself with the radial and tangential velocity components (u_r, u_θ) given by

$$u_r = 0, \tag{1.7}$$

$$u_\theta = \frac{\Gamma}{2\pi r}, \tag{1.8}$$

where $r = \sqrt{x^2 + y^2}$ and the cartesian coordinates system, (x, y), is centred at the vortex. The Cartesian velocity field, (u, v), around two such vortices centred at $(0, \pm d/2)$ is given in figure 1.2, and is determined by superposing two velocity fields calculated from equations 1.7-1.8. This vortex dipole arrangement will propagate along the x axis with a self-induced velocity,

$$U_D = \frac{\Gamma}{2\pi d}. \tag{1.9}$$

While this inviscid, point-vortex description is a valid example of a dipole flow, being a steady solution of the Euler equations, most recent literature concerning dipole development makes reference to more elaborate dipole models. The review paper of Meleshko (1994) discusses in depth a model referred to henceforth as the "Lamb-Chaplygin" dipole model. This model originates from the apparently unrelated works of British mathematician, Sir Horace Lamb, and Russian/Soviet mathematician, Sergey Chaplygin, who both presented very similar analyses of dipolar flow in the late nineteenth and early twentieth centuries. The model describes a circular region with radius, a, which contains two contra-rotating patches of vorticity, the stream function of which is given (in radial coordinates with origin at the dipole centre) as

$$\psi = -\frac{2U_D}{kJ_0(ka)} J_1(kr)\sin\theta, \text{ for } r \le a, \tag{1.10}$$

where U_D for this model is a prescribed dipole propagation velocity, J_0 and J_1 are respectively zeroth and first order Bessel functions of the first kind and k is given by

$$ka = 3.8317. \tag{1.11}$$

Outside of the region $r \le a$, the model gives the stream function

$$\psi = U_D\left(r - \frac{a^2}{r}\right)\sin\theta, \text{ for } r \ge a. \tag{1.12}$$

Equation 1.11 gives the first zero of Bessel function, J_1, and is required to give a smooth transition of ψ between the circular vortex and surrounding region. This model gives a stationary dipole with a background velocity U_D (as the coordinates system is centred at the dipole).

Flór et al. (1995) drew extensive comparisons between this dipole model and dipoles formed via a horizontal momentum injection into stably stratified fluid. In particular the authors make reference to the Lamb-Chaplygin model prescribing a linear relationship between stream function and vorticity within the two-dimensional plane i.e.

$$\omega_z(x, y) = k^2\psi(x, y). \tag{1.13}$$

This predicts that that streamlines within the vortex dipole are also lines of constant vorticity, and as such the vorticity level outside the bounding streamline of the dipole is taken to be zero, assuming a stationary or uniform background reference plane. An example of the vorticity distriubtion within a vortex dipole prescribed by this model is given in figure 1.2.

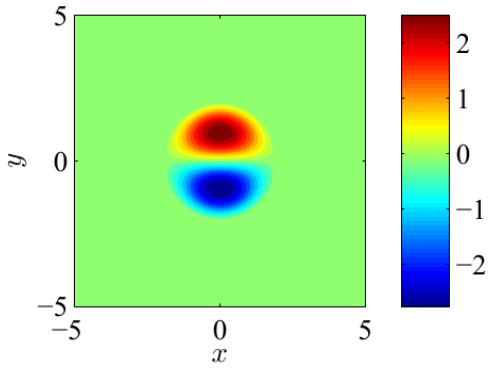

Figure 1.2: Contours of vorticity for a stationary Lamb-Chaplygin dipole, calculated from equations 1.10-1.12 with $U_D = 1$ and $a = 2$.

The work of Flór and van Heijst (1994) found that the relationship between vertical vorticity and stream function was linear for dipoles that evolved from a laminar starting jet prior to buoyant collapse, whereas a turbulent starting jet gave a relationship more akin to a hyperbolic sine function such as that seen demonstrated by the later work of Flór et al. (1995). Comparison of the experimentally generated dipole visualisations from Flór et al. (1995) and the vorticity contours in 1.2(b) indicates that this experimental dipole is indeed similar in shape to the circular Lamb-Chaplygin prediction, with the most obvious difference being the trailing part of the structure, which features two vortical extensions that appear to result from the dipole entraining additional fluid as it propagates downstream.

As is typical of many experimental studies of vortex dipoles forming in stratified fluid (Voropayev et al., 1991, 2008), the vertical vorticity data is taken from the same horizontal plane into which the momentum source injects fluid (often referred to as $z = 0$ or the "vertical midplane"). Limiting analysis of the dipole to this single plane provides for easy comparison between the experimental results and two-dimensional models such as Lamb-Chaplygin. However, while some agreement may be found between the model and the flow within this single plane, two important factors are excluded in such an analysis. First, even if a circular region exists at the front of the dipole that contains a vorticity field akin to that of a Lamb-Chaplygin model, behind this region exists a

vortical "tail" or wake. The nature of this tail and how significant it is with respect to the dipole front region appears to vary significantly between different studies, due to the wide range of case parameters and analysis/visualisation techniques utilised. Such a tail is not limited to the experimental, stratified domain cases. The two-dimensional simulations of Delbende and Rossi (2009) demonstrate the origin of a vortical tail from a combination of vorticity diffusing from the outer edges of the dipole front region, which is then left behind as the front region continues to advect forward at a higher velocity.

Secondly, the two-dimensional models do not consider how development of a vortex dipole's vertical structure can impact upon its evolution in the horizontal plane. In the case of Voropayev et al. (1991), the inherent assumption made is that the fully formed dipole has a sufficiently small vertical length scale compared to its size in the horizontal plane, that the dipole flow is two-dimensional to the first order, paving the way for a two-dimensional analysis. However, as discussed at length by Praud and Fincham (2005), vortex dipoles that evolve from impulsive injections into stratified fluid exhibit a distinct three dimensional structure that had been only fleetingly acknowledged in most relevant literature. They found that many of the key dipole statistics at any horizontal plane within the dipole (e.g. vertical vorticity and propagation speed) could be well predicted by Gaussian distributions in the vertical direction, using the value at the vertical midplane as a maximum and fitting a Gaussian profile to the data to determine measures of the dipole's vertical length scale, as had been previously explored by Flór et al. (1995) for a stratified vortex dipole and Beckers et al. (2001) for a stratified vortex monopole. Furthermore, whereas previous works had limited their comparison with the Lamb-Chaplygin model to the vertical midplane, it was found that an experimentally generated vortex dipole contained two "columns" of vertical vorticity, with the variation of vorticity in any horizontal plane lying within the columns well described by the model, with the value of U_D in the plane determined by an aforementioned Gaussian distribution. The columns were found to have a near-constant lateral separation throughout their vertical extent such that the local values of a, k in equations 1.10-1.12 can be considered to be constant.

Physically, the Gaussian variation of U_D in the vertical direction arises from similar Gaussian profiles of peak vorticity and circulation (which themselves arise from viscous diffusion, as will be discussed later). If we consider the vortex columns as two line vortices, then equation 1.9 can be used to show that for a constant horizontal separation between the vortices, the horizontal propagation speed of the dipole at any given height within the columns is

proportional to the circulation in the same horizontal plane (and thus both can be described by Gaussian distributions with identical vertical length scale). One of the interesting characteristics of such a vorticity distribution is that the horizontal dipole layers nearest the vertical midplane propagate more quickly than those above or below. This leads to a self-deformation of the vortex columns with the vertical extremities appearing to "bend back" as the dipole advects downstream. Such behaviour was observed by Praud and Fincham (2005) for both an experimentally created dipole and for a simulation which used an extended, three dimensional Lamb-Chaplygin model with a Gaussian distribution of U_D in the vertical direction. Even though this model does not consider the viscous effects that become increasingly dominant at the late time, reasonable correlation was found with experimental data.

1.2.4 Scaling of the late-time stratified dipole

However the structure of these late time dipoles is described, universally recognised traits are their slow propagation velocity and large lateral length scale when compared with the source of the momentum injection. van Heijst and Flór (1989) generated a dipole that propagated downstream at a velocity approximately 2000 times slower than the output velocity of the momentum source, but with a lateral length scale approximately 200 times larger than the source diameter. The velocity of these dipoles is observed to decrease and diameter increase over time due to the combined effects of viscous entrainment and diffusion.

Voropayev et al. (2008) details a number of scaling laws governing the late time dipole, with the downstream position and dipole diameter both scaling with the cube root of time, i.e.

$$X_D \propto D_D \propto t^{1/3}, \tag{1.14}$$

where X_D is the dipole's downstream position from the momentum source, D_D the dipole's diameter and t is time. As noted by Rojanaratanangkule et al. (2012), the power-law scaling behaviour will not commence at the start of the experiment ($t = 0$) as the dipole takes time to fully form via the process described previously. Instead, one expects to see a non zero time offset prior to the onset of the expected scaling behaviour, which can be accounted for in equation 1.14 to give

$$X_D = \alpha_X (t - t_X)^{1/3}, \tag{1.15}$$

$$D_D = \alpha_D (t - t_D)^{1/3}, \tag{1.16}$$

where α_X, α_D are constants of proportionality and t_X, t_D are the time offsets. These scaling laws were derived from momentum-balance and dimensional arguments based on the assumption that the fully formed dipole has a constant vertical thickness, as detailed in the prior work of Voropayev et al. (1991), but neglecting the influence of viscous diffusion on dipole growth. An entrainment coefficient,

$$\alpha_{XD} = \frac{\alpha_D}{\alpha_X}, \tag{1.17}$$

was defined in Voropayev et al. (1991) and found to have a mean value of approximately 0.46 for a range of experimental parameters. A value of 0.23 was reported instead in the subsequent work of Voropayev et al. (2008), which was attributed to the different measuring techniques for D_D used in the two studies. Similarly, the same authors proposed the maximum vertical vorticity within a single dipole core decays inversely proportional to elapsed time, i.e.

$$\omega_z|_{\text{Max}} = \alpha_\omega (t - t_\omega)^{-1}, \tag{1.18}$$

a relationship supported by experimental data with an approximate value of 17 found for α_ω. Comparison was drawn with the data of both Flór et al. (1995) and Praud and Fincham (2005), with the former giving reasonable agreement with equation 1.18, though the latter suggested a faster rate of decay (i.e. the exponent of equation 1.18 being a lower value than -1).

Perhaps the most significant disagreement between the experimental studies is how the vertical thickness of the dipole is considered. As mentioned previously, Voropayev et al. (1991) presents their dipole scaling laws working under the assumption that the late time dipole has a constant thickness once it has fully formed. This thickness, H_D, was proposed to be a function of the initial impulse imparted on the fluid by the momentum source and the strength of the stratification, such that

$$H_D = \gamma (I/N)^{1/4}. \tag{1.19}$$

The constant γ was found experimentally to be approximately 1.4. The same authors (Voropayev et al., 2008) later stated that whilst viscous diffusion may cause a slow vertical growth of the dipole structure at the late time, the constant thickness argument is a good first-order approximation. Both Flór et al. (1995) and Praud and Fincham (2005) demonstrated that at the late time the dipole's thickness scales with the square root of the multiple of elapsed time and fluid kinematic viscosity i.e.

$$H_D \propto (\nu t)^{1/2}. \tag{1.20}$$

As this is faster than the diameter scales with time, it suggests the vertical growth cannot be neglected when considering the dipole's three-dimensional structure. Flór et al. (1995) and Praud and Fincham (2005) went on to demonstrate that the planar velocity fields within the dipole are not uniform throughout its vertical extent and thus cannot be considered truly two-dimensional. At the vertical mid-plane, where the dipole has the greatest circulation, the propagation velocity and peak vorticity of the dipole are also the greatest. Towards the vertical extremes of the dipole the velocity and vertical vorticity reduce with a Gaussian profile, which had previously been observed by Beckers et al. (2001) for a shielded monopole in a stratified fluid, with

$$\langle\omega_z\rangle_{\mathrm{Max}}(z) = \omega_z|_{\mathrm{Max}} \exp\left(-\frac{z^2}{(H_\omega/2)^2}\right), \tag{1.21}$$

where $\langle\omega_z\rangle_{\mathrm{Max}}$ is the maximum vertical vorticity value for a fixed value of height, z, and H_ω is the "vorticity thickness" of the structure. Such a profile can be related to the diffusion model for vorticity proposed by Flór et al. (1995), which describes the vertical vorticity distribution within the dipole as it evolves from an initially two-dimensional Lamb-Chaplygin dipole. This model, like the later model of Praud and Fincham (2005), assumes a Lamb-Chaplygin vorticity distribution at any horizontal plane regardless of z, with the dipole initially occupying a two-dimensional plane at $t = 0$. The model coordinates system in the horizontal (x, y) plane has a varying origin in z, with (x', y') defining the horizontal position relative to the Lamb-Chaplygin centre within that plane. The model is thus given as

$$\omega_z(x', y', z, t) = \omega_z(x', y', t = 0)\frac{1}{\sqrt{t}} \exp\left(-t\nu k^2\right) \underbrace{\exp\left(-\frac{z^2}{4\nu t}\right)}_{\text{Vertical diffusion}}, \tag{1.22}$$

recalling that k is a Lamb-Chaplygin model constant. The final exponential term on the right hand side describes the vertical vorticity profile as it evolves in the z direction due to viscous diffusion, and is noted to be equivalent to the exponential term on the right-hand-side of equation 1.21. The denominators of the two can therefore be equated and rearranged to give

$$H_\omega = 2\sqrt{2}(\nu t)^{1/2} \approx 2.828(\nu t)^{1/2}. \tag{1.23}$$

Both Flór et al. and Praud and Fincham developed three-dimensional, time-dependent models for the vorticity distribution within the dipole, with the former showing a constant thickness model to be approximately valid for the early development of the dipole, but a vertical diffusion model being more appropriate at large times.

However, as these models are intended to predict the late-time growth of the dipole by a three-dimensional extension of a Lamb dipole model, they do not consider either the initial transformation from a three-dimensional structure to a vortex dipole and how this may affect the late-time development. Thus the exact relationship between the dipole's vertical growth and the governing parameters of impulse, buoyancy frequency, viscosity and elapsed time is still unclear.

Whilst the experimental studies mentioned here have well documented the evolution of the dipole from an impulsive momentum source in a stratified fluid, it appears from the literature examined that no comparable numerical study has been carried out to date. The numerical studies found to date appear to have focused on analytical models of the late-time dipole (Praud and Fincham, 2005) or two-dimensional simulations of dipole dynamics (Delbende and Rossi, 2009; Makarov and Kizner, 2011). A comparable numerical study is described in Rojanaratanangkule et al. (2012), though this concerned the generation of vortex dipoles through confining an impulsive jet-like flow between two non-deformable free surfaces, as opposed to stable density stratification. As discussed in Praud and Fincham (2005), shallow layer vortex dipoles may exhibit qualitative similarity to stratified vortex dipoles, though do not experience the same highly dissipative evolution at the late time.

1.3 Thesis objectives

Following the examination of the literature, it is possible to see areas in which this project can contribute to further understanding of how dipolar structures created by a horizontal momentum injection evolve in a stably stratified fluid. One obvious advantage of this work is the use of a DNS code to simulate the flow, which allows for precise control over the governing flow parameters and analysis of the flow field in much greater detail than would be possible for even a highly sophisticated experimental set up. At the time of writing, the author has not found any publicly documented study using DNS to study such flows to complement experimental work, and thus a window of opportunity exists to compare and contrast experimental work with analogous simulations for the first time. The rich data set that DNS provides allows for simple evaluation of the simulated flows to see how well they agreed with the experimental works from which they are derived, as well as providing additional data to help describe the mechanics of the flow in a much more quantitative fashion than is possible via experiment.

Broadly speaking, the questions to be answered by this project are as follows:

- How does a vortex dipole evolve in stably stratified fluid from an axisymmetric, horizontally directed, impulsive momentum injection?
- How does this flow vary from the equivalent case for a neutrally stratified fluid?
- Can such dipoles be considered as quasi-two-dimensional flow structures as described in Voropayev et al. (2008) etc., or do they exhibit a more distinct three-dimensional structure as described in Praud and Fincham (2005)?
- To what extent do the late-time dipoles simulated in this work corroborate the conflicting scaling laws and experimental observations of the experimental studies discussed previously.
- How are any of the above influenced by changes in the Reynolds number, stratification strength and total impulse imparted by the momentum source?
- Does the distribution of the momentum flux from the source (i.e. the "shape" of the momentum source) have any significant effect on the late-time dipole properties, particularly their adherence to scaling laws and theoretical models laid out in previous literature?

These questions could be answered by completing the studies described in subsequent chapters.

1.4 Thesis overview

The remainder of this thesis is summarised for each chapter as follows.

Chapter 2 documents the governing equations used by the numerical code employed for this project, which are the full Navier-Stokes equations subject to the Boussinesq approximation to allow for the influence of buoyant forces to be included. These equations are presented in their dimensional and non-dimensional forms, along with associated equations for energetics. A description of the Direct Numerical Simulation code used for this project is also provided, along with a description of the specific features relevant to the simulation of decaying vortical structures in stratified fluid.

Chapter 3 documents a series of small studies and analyses that test the functionality of the simulation code, and demonstrate good agreement with experimental works concerning the generation of vortex rings from impulsive momentum injections and internal waves generated from an oscillating body force in a stratified fluid. These studies, allied to the validation work conducted by previous users of the simulation code, help demonstrate the validity of its use for the research of this thesis.

The collapse of an isolated vortex ring has seemingly been studied in greater detail than a collapsing starting jet (Johari and Fang, 1997; Scase and Dalziel, 2006), providing a rich set of quantitative data with which to compare numerical simulation. As discussed previously, the quantitative data available from experimental work for describing the collapse process and transformation of an axisymmetric jet to a vortex dipole is relatively sparse by comparison. One way to verify that simulations conducted for this project are a good representation of experiment is to evaluate how well the simulation code predicts the collapse of a horizontally propagating vortex ring, both with and without the influence of stratification. Chapter 4 documents such simulations, with the following outcomes:

- A demonstration of the process by which an initially axisymmetric vortex ring is deformed by, and eventually collapses under the influence of stable stratification (and how this compares to a ring in neutrally stratified fluid), with particular attention paid to the energy levels in the flow that are not available from experimental literature.

- How this varies with initial ring Reynolds and Froude numbers, showing a weak relation between the energetics and Reynolds number, but a much stronger dependence on stratification level during the collapse process.

- That initially perturbing the ring as previous numerical studies have done in order to accelerate turbulent breakdown has negligible effect on the development of the ring due to buoyant forces.

The most significant body of work to be undertaken for this research is to create a simulated analogy to many of the experimental studies of vortex dipole formation in a stratified fluid. Specifically, this involved simulating a horizontal momentum injection into an otherwise quiescent domain with a linear, stable density profile. The key results are given in chapter 5 and summarised as follows:

- A demonstration of the time evolution of kinetic energy components, the rate of transfer of kinetic energy to buoyancy scalar variance through

buoyancy flux and how these can be used to quantify the point of gravitational collapse for stably stratified case. As with the study of collapsing vortex rings, the energy levels documented in these simulations are not presented in experimental literature, thus this numerical work adds a further layer of understanding to the collapse process.

- The three-dimensional shape of the fully formed vortex dipole structure at different times using vorticity-based visualisations similar to those of Praud and Fincham (2005) and Voropayev et al. (2008), and how these structures correspond to the changing energy levels.

- Scaling laws for the dipole's streamwise position, diameter, vertical thickness and maximum vertical vorticity from experimental precedents are verified.

- Discussion of how the above results are linked to the governing flow parameters of Reynolds number, stratification strength and impulse.

- Demonstration of the variation in the buoyancy scalar field due to the motion induced by the dipole and identifying internal wave generation (particularly at times during the process of gravitational collapse), which is another aspect of the flow that experiment struggles to capture.

As discussed in more detail in chapter 5, the momentum source utilised in the simulations of that chapter uses a smooth, Gaussian forcing profile that, while preferable for numerical reasons, may not resemble an initial starting jet seen in experiments of, for example Gharib et al. (1998). As the primary goal of the simulation work of that chapter was to investigate the effect of key parameters (Reynolds number etc.) on the late-time dipole, this apparent discrepancy is not of great concern so long as the structure of the dipole for a Gaussian forcing profile is not significantly different to that produced by a more representative forcing profile. This will be verified by investigating how sensitive the late-time dipole is to the initial forcing conditions with similar simulations but with differently distributed forcing profiles. The results of these final simulations are given in chapter 6 and demonstrate:

- That while the shape of the initial momentum injection profile is decisive in shaping the vortical field in neutrally stratified cases or at early times in stably stratified cases, the late dipoles formed in stably stratified cases are structurally very similar and obey the same scaling laws verified in chapter 4, indicating that the agreement with these scaling laws may well be universal for all dipoles formed in stably, linearly stratified fluid.

- That the dipoles give excellent agreement with each other and with the Lamb-Chaplygin dipole model at the late time in terms of vorticity profile across the dipole, further indicating the universal similarity of such dipoles.

A summary of the key results achieved during the research for this thesis, and how future studies might lead on from this, is given in chapter 7.

Chapter 2

Numerical methods

2.1 Governing equations

2.1.1 Formulation

In order to derive the non-dimensional governing equations used by the simulation code for this project, we first consider the dimensional Navier-Stokes equations for an incompressible flow with the continuity equation

$$\frac{\partial \hat{u}_i}{\partial \hat{x}_i} = 0, \tag{2.1}$$

and the momentum equation for a flow subject to a gravitational field acting in the vertical direction,

$$\frac{\partial \hat{u}_i}{\partial \hat{t}} + \hat{u}_j \frac{\partial \hat{u}_i}{\partial \hat{x}_j} = -\frac{1}{\hat{\rho}_\infty}\frac{\partial \hat{p}}{\partial \hat{x}_i} + \hat{\nu}\frac{\partial^2 \hat{u}_i}{\partial \hat{x}_j \partial \hat{x}_j} - \hat{g}\frac{\hat{\rho}}{\hat{\rho}_\infty}\delta_{3i} + \hat{f}_i. \tag{2.2}$$

The final two terms in equation 2.2 are respectively the accelerations due to gravitational force and applied body forces. If density variations in the vertical direction are to be considered, but small enough for the Boussinesq approximation to be valid (Turner, 1979), then the vertical acceleration due to gravity can be given as $-\hat{g}\hat{\rho}/\hat{\rho}_\infty$, with density in the pressure gradient term assumed to be $\hat{\rho}_\infty$ at all points. An assumption of constant density also allows the continuity equation (2.1) to be used in the incompressible form without the need to consider the effect of density variation on mass conservation. With $\hat{g}$ and $\hat{\rho}_\infty = \hat{\rho}_{\mathrm{Ref}}$ taken to be constants, the evolution of the gravitational term throughout the flow field can determined by the transport equation for density,

$$\frac{\partial \hat{\rho}}{\partial \hat{t}} + \frac{\partial \hat{\rho}\hat{u}_i}{\partial \hat{x}_i} = \hat{\kappa}\frac{\partial^2 \hat{\rho}}{\partial \hat{x}_i \partial \hat{x}_i}, \tag{2.3}$$

where κ is the scalar diffusivity of the fluid and represents the rate at which a scalar such as temperature conducts through a fluid beyond the transport provided by convection. The density itself can be broken down into a constant mean component, $\hat{\rho}_{\text{Ref}}$, the background lapse rate multiplied by vertical position, $\hat{\Phi}\hat{z}$ (which together give the initial vertical density profile), and some fluctuation from this initial profile due to motion within the fluid, $\hat{\rho}'$, such that

$$\hat{\rho} = \hat{\rho}_{\text{Ref}} + \hat{\Phi}\hat{z} + \hat{\rho}'.$$

Substituting this into equation 2.3, the time derivative of all but the fluctuation is zero, and eliminating terms through substitution of equation 2.1 leaves

$$\frac{\partial \hat{\rho}'}{\partial \hat{t}} + \frac{\partial \hat{\rho}' \hat{u}_i}{\partial \hat{x}_i} + \hat{u}_i \frac{\partial (\hat{\Phi}\hat{z})}{\partial \hat{x}_i} = \hat{\kappa} \left(\frac{\partial^2 (\hat{\Phi}\hat{z})}{\partial \hat{x}_i \partial \hat{x}_i} + \frac{\partial^2 \hat{\rho}'}{\partial \hat{x}_i \partial \hat{x}_i} \right).$$

Next, if we assume an initially linear density profile in the vertical direction, this gives $\hat{\Phi}$ as a constant, and with $\hat{\Phi}\hat{z}$ only varying in the vertical direction this eliminates all second spatial derivatives of $\hat{\Phi}\hat{z}$ and leaves just the first spatial derivative in the vertical direction,

$$\frac{\partial \hat{\rho}'}{\partial \hat{t}} + \frac{\partial \hat{\rho}' \hat{u}_i}{\partial \hat{x}_i} + \hat{u}_3 \hat{\Phi} = \hat{\kappa} \frac{\partial^2 \hat{\rho}'}{\partial \hat{x}_i \partial \hat{x}_i}. \tag{2.4}$$

We can define a scalar quantity, $\hat{\theta}$, that gives the magnitude of the gravity induced acceleration in the vertical direction as

$$\hat{\theta} = \hat{g} \frac{\hat{\rho}'}{\hat{\rho}_{\text{Ref}}},$$

which now gives us the momentum equation as

$$\frac{\partial \hat{u}_i}{\partial \hat{t}} + \hat{u}_j \frac{\partial \hat{u}_i}{\partial \hat{x}_j} = -\frac{1}{\hat{\rho}_\infty} \frac{\partial \hat{p}}{\partial \hat{x}_i} + \hat{\nu} \frac{\partial^2 \hat{u}_i}{\partial \hat{x}_j \partial \hat{x}_j} - \hat{\theta} \delta_{3i} + \hat{f}_i. \tag{2.5}$$

If we multiply equation 2.4 by $\hat{g}/\hat{\rho}_{\text{Ref}}$, the evolution of $\hat{\theta}$ with time can be solved as a scalar transport equation given by

$$\frac{\partial \hat{\theta}}{\partial \hat{t}} + \frac{\partial \hat{\theta} \hat{u}_i}{\partial \hat{x}_i} = \hat{N}^2 \delta_{3i} \hat{u}_3 + \hat{\kappa} \frac{\partial^2 \hat{\theta}}{\partial \hat{x}_i \partial \hat{x}_i}, \tag{2.6}$$

where $\hat{N}^2$, the square of the buoyancy frequency, is given by

$$\hat{N}^2 = -\frac{\hat{g}}{\hat{\rho}_{\text{Ref}}} \hat{\Phi}. \tag{2.7}$$

Combined with the continuity and momentum equations, this gives the three governing equations of the stratified flow using the Boussinesq approximation.

2.1.2 Non-dimensionalisation

If we define a reference length and velocity value, $\hat{L}_{\text{Ref}}$ and $\hat{U}_{\text{Ref}}$, these can be used to return a series of non-dimensional quantities i.e.

$$u_i = \frac{\hat{u}_i}{\hat{U}_{\text{Ref}}},$$

$$x_i = \frac{\hat{x}_i}{\hat{L}_{\text{Ref}}},$$

$$t = \hat{t}\frac{\hat{U}_{\text{Ref}}}{\hat{L}_{\text{Ref}}}.$$

We assume that the density changes in the fluid are sufficiently small such that the viscosity is approximately constant and is itself a reference quantity. Combining this with reference length and velocity allows for defining a non-dimensional viscosity in terms of a reference Reynolds number as

$$\nu = \frac{\hat{\nu}}{\hat{U}_{\text{Ref}}\hat{L}_{\text{Ref}}} = \frac{1}{Re_{\text{Ref}}}.$$

Considering another reference quantity, the mean density of the flow field, $\hat{\rho}_\infty = \hat{\rho}_{\text{Ref}}$, the non-dimensional pressure is given by

$$p = \frac{\hat{p}}{\hat{\rho}_{\text{Ref}}\hat{U}^2_{\text{Ref}}}.$$

The non-dimensional form of equation 2.1 is achieved simply by dividing through by the reference velocity scale and multiplying by the reference length scale. Given that the form of equation 2.2 used here is a balance of accelerations, we can consider a reference acceleration to be

$$\left(\frac{\partial \hat{u}}{\partial \hat{t}}\right)_{\text{Ref}} = \frac{\hat{U}^2_{\text{Ref}}}{\hat{L}_{\text{Ref}}}.$$

The dimensional momentum equation can be divided across by this reference acceleration value.

Recalling the scalar transport equation (2.6), we consider the square of the buoyancy frequency, $\hat{N}^2$, as an input flow parameter. This in turn can be considered as a non-dimensional flow parameter, by multiplying by the square of the reference time scale ($L_{\text{Ref}}/U_{\text{Ref}}$) to give

$$N^2_{\text{Ref}} = \left(\frac{\hat{N}\hat{L}_{\text{Ref}}}{\hat{U}_{\text{Ref}}}\right)^2.$$

This can also be used to define a reference Richardson number, $Ri_{\text{Ref}} = N^2_{\text{Ref}}$ or the analogous Froude number, $Fr_{\text{Ref}} = 1/N_{\text{Ref}}$. Taking the scalar diffusivity, $\hat{\kappa}$

to be $\hat{\kappa} = \hat{\nu}/Pr$ and dividing equation 2.6 by $\hat{U}^3_{\text{Ref}}/\hat{L}^2_{\text{Ref}}$ to non-dimensionalise leaves us with the final non-dimensional governing equations to be solved by the DNS code as

$$\frac{\partial u_i}{\partial x_i} = 0, \tag{2.8}$$

$$\frac{\partial u_i}{\partial t} + u_j \frac{\partial u_i}{\partial x_j} = -\frac{\partial p}{\partial x_i} + \frac{1}{Re_{\text{Ref}}} \frac{\partial^2 u_i}{\partial x_j \partial x_j} - \theta \delta_{3i} + f_i, \tag{2.9}$$

$$\frac{\partial \theta}{\partial t} + \frac{\partial \theta u_i}{\partial x_i} = N^2_{\text{Ref}} u_3 \delta_{3i} + \frac{1}{Pr Re_{\text{Ref}}} \frac{\partial^2 \theta}{\partial x_i \partial x_i}, \tag{2.10}$$

where Re_{Ref}, Pr and N^2_{Ref} are governing flow parameters. If the characteristic length and velocity scales in the flow are taken to be the non-dimensional unit length and unit velocity from the simulation code, we can replace Re_{Ref} and N^2_{Ref} with Re and N^2 respectively.

Pr, the Prandtl number, is given here as the ratio of viscous diffusivity to scalar diffusivity of the fluid. Strictly speaking, the Prandtl number is the ratio of momentum/viscous diffusivity to thermal diffusivity of a fluid and relates how quickly momentum and temperature of a fluid is dispersed via viscous diffusion and thermal conduction respectively. Similarly, the Schmidt number is the ratio of momentum/viscous diffusivity to molecular diffusivity. The Prandtl number is thus more suited to describing buoyant flows where the effects of buoyancy are realised through thermal stratification of the fluid, with Schmidt number more appropriate where buoyancy effects arise from density stratification. In the case of numerical simulation where a more generic active scalar field is defined, Prandtl number has been given as the governing flow parameter by Redford et al. (2015) and de Stadler et al. (2010), with the former using an earlier iteration of the simulation code for the research documented in this thesis. In the case of the latter, the authors conducted a numerical study to determine the effect of varying Prandtl number on a temporally evolving wake of a towed bluff body. The need for such a study arose from an inherent difficulty in simulating flows of high Prandtl or Schmidt number (with a typical Schmidt number of 700 reported for saline stratified water, and a Prandtl number of 7 for air). As the Prandtl/Schmidt number increases above unity, the Batchelor length scales formed in the scalar field will be smaller than the Kolmogorov length scales within the velocity field, with the relative Batchelor length scale reducing by half with each fourfold increase in Prandtl/Schmidt

number. Thus a higher computational resolution is required in order to properly resolve the scalar field for these higher Prandtl/Schmidt numbers, with the velocity field "over"-resolved. In the case of numerical simulations of the towed bluff body, the velocity field of the turbulent wake this produced was found to be relatively insensitive to choice of Prandtl number, though the scalar field did show some weaker structures at lower Prandtl number. Nonetheless, the work of those authors demonstrated a Prandtl number of unity was not an unreasonable assumption for simulating stratified wake structures and also avoids the computational cost that would be required to fully resolve a scalar field for a Prandtl number more representative of analogous experiments. The numerical simulations of this thesis take this as a precedent and the Prandtl number is set to unity for all stably stratified cases.

2.1.3 Energetics

When studying the flows considered in this project, the kinetic energy and buoyancy variance levels (and the transfer between them) are to be determined both as an analytic tool and a means of verifying the accuracy of the DNS code. The integral non-dimensional kinetic energy of the domain can be given as a volume integral of the square of velocity magnitude i.e.

$$K = \frac{1}{2}\int_V |u|^2 \mathrm{d}V, \tag{2.11}$$

where $|u|^2 = u^2 + v^2 + w^2$. Similarly, the integral non-dimensional buoyancy variance within the domain (per unit mass) can be found through integrating

$$P = \frac{1}{2N^2}\int_V \theta^2 \mathrm{d}V. \tag{2.12}$$

Physically, this buoyancy variance represents a form of internal energy within the domain that arises from the displacement of buoyant fluid particles from an equilibrium layer. This can be thought of as a form of potential energy within the domain, though rather than being gravitational potential energy, the buoyancy variance represents the potential of the scalar field to perform work on the velocity field, with energy transferred back and forth between the two forms. In the context of this thesis, the buoyancy variance can be considered a proxy to gravitational potential energy, with which it is dimensionally consistent.

Multiplying equations 2.9 and 2.10 by u_i and θ/N^2 respectively and rearranging using the rules of product differentiation yields transport equations for kinetic energy components and buoyancy variance with

$$\frac{1}{2}\left(\frac{\partial(u_i^2)}{\partial t} + u_j\frac{\partial(u_i^2)}{\partial x_j}\right) = -u_3\theta\delta_{3i} + K'_\nu + u_i f_i, \tag{2.13}$$

$$\frac{1}{2N^2}\left(\frac{\partial(\theta^2)}{\partial t} + u_i\frac{\partial(\theta^2)}{\partial x_i}\right) = u_3\theta\delta_{3i} + P'_\nu, \tag{2.14}$$

with

$$K'_\nu = \frac{1}{Re}\left(\frac{1}{2}\frac{\partial^2(u_i^2)}{\partial x_j^2} - \frac{\partial u_i}{\partial x_j}\frac{\partial u_i}{\partial x_j}\right),$$

$$P'_\nu = \frac{1}{PrReN^2}\left(\frac{1}{2}\frac{\partial^2(\theta^2)}{\partial x_i^2} - \frac{\partial\theta}{\partial x_i}\frac{\partial\theta}{\partial x_i}\right).$$

The first terms on the right hand side of equations 2.13 and 2.14 are equal in magnitude but opposite in sign. This is the buoyancy flux term, and gives the rate at which energy is transferred between kinetic and buoyant forms. The terms K'_ν and P'_ν represent the viscous/thermal transport and dissipation of the kinetic energy and buoyancy variance in the domain. The buoyancy variance transport equation can also be considered analogous in this context to the transport equation of gravitational potential energy, though the latter would omit the scalar dissipation terms included within P'_ν. Through use of the buoyancy variance as a proxy to potential energy, a similar proxy for total energy can be given as

$$E_{total} = K + P.$$

For sake of conciseness, this proxy in referred to as "total energy" in the remainder of this thesis, though strictly is a summation of kinetic energy and buoyancy variance.

2.2 Spectral DNS

Direct numerical simulation (DNS) within computational fluid dynamics refers to explicitly solving the governing equations of the fluid motion (i.e. Navier-Stokes equations) at all scales of motion, from the largest eddies to the smallest turbulent scales. This allows the effect of turbulent fluctuations on the bulk, mean flow to be accurately depicted. This contrasts with Reynolds averaged Navier-Stokes (RANS) or Large eddy simulation (LES) methods, which use a turbulence model to approximate the effect that either some or all of the turbulent scales of the flow (those smaller than the resolution of the computational domain) have on the explicitly resolved scales.

Provided that grid resolution is sufficient to include the smallest scales of the flow, DNS offers superior accuracy to the methods that utilise turbulence models. However, the high number of grid points required for a sufficient resolution means that DNS is extremely expensive in terms of computational resources, and for complex 3D flows of moderate Reynolds number will usually require a large parallel computing resource to complete in practical time periods. The relative benefits and drawbacks of DNS compared to other computational methods are discussed further in Coleman and Sandberg (2010).

The flow solving components of the code used in this project are implemented using spectral numerical methods, as opposed to the finite differencing used by many DNS codes. In contrast to finite differencing methods, the spectral methods do not evaluate velocity gradients in Cartesian space but instead uses Fourier transformations to represent the velocity field as the sum of a series of basis functions. For codes using periodic boundaries, this often takes the form of a Fourier series of complex exponentials. For a velocity component, u_M, varying with spatial position, x, and time, t. Coleman and Sandberg (2010) represent the Fourier basis functions as

$$u_M(x,t) = \sum_{n=-M/2}^{+M/2} \alpha_n(t) e^{ik_n x} = \sum_{n=-M/2}^{+M/2} \alpha_n(t)(\cos(k_n x) + i\sin(k_n x)), \qquad (2.15)$$

where k_n is the wavenumber of the mode, n, from the total number of modes, M. $\alpha_n(t)$ is the expansion coefficient for a given mode, n, at time, t. This is essentially a truncated Fourier series, with the number of Fourier modes/wavenumbers being equal to the number of grid points in the relevant spatial direction of the domain.[1] Gottlieb and Orszag (1977) refer to this as a "Galerkin approximation". The key benefit of the approximation is that these basis functions have exact derivatives for all wavenumbers. This allows the spatial gradients to be calculated precisely as shown by Hussaini and Zang (1987) i.e.

$$\frac{d}{dx} u_M(x,t) = \frac{d}{dx} \sum_{n=-M/2}^{+M/2} \alpha_n(t) e^{ik_n x} = \sum_{n=-M/2}^{+M/2} ik_n \alpha_n(t) e^{ik_n x}. \qquad (2.16)$$

The larger the value of M, the larger the number of modes that can be resolved (or in Cartesian space, more spatial scales are evaluated). As such, if the sum of the basis functions gives a good approximation of $u_M(x,t)$ across the domain,

[1] It should be noted that the series given here is not a general method for all spectral DNS, but is applicable to computational domains such as that used for this project, which feature periodic boundaries and a uniform grid spacing. Non-uniform spacing, wall boundaries etc. would potentially make use of polynomial basis functions and/or weighting functions for each mode.

as M increases, the expansion coefficients for the higher wavenumbers will tend towards zero i.e.

$$M \to \infty, |\alpha_n| \to 0$$

The expansion coefficients therefore can give a measure of how well resolved the computational domain is at a given time. If the higher mode coefficients are still large, it suggests that the smaller scales in the simulation are not completely resolved and a finer grid spacing/higher number of modes is required. This is particularly relevant for DNS of turbulent flows, as insufficient resolution will lead to the smaller, dissipative scales of the flow being under-resolved, reducing the accuracy of the simulation at the larger scales as well.

Provided that the Galerkin approximation to the flow field is suitably accurate, the computational error reduces significantly with increasing M. For a finite difference method of order P, the error will be proportional to $(1/M)^P$. By contrast, error with spectral methods decreases exponentially with increasing M, an effect known as "infinite order accuracy". As such, spectral methods can yield solutions that converge very quickly, and yield more accurate results, even with a coarser grid than an equivalent finite difference simulation.

Incompressible, viscous flow cases and the spatial derivatives within them are usually smooth, making a Fourier series approximation a good fit for the solution. The use of Fourier series also requires that the computational domain make use of periodic boundaries (i.e. inflow conditions are equal to outflow conditions), in order for periodic basis functions to be applicable. Spalart et al. (1991) made use of a code to simulate boundary layer flow that used polynomial basis functions in the direction normal to the physical boundary (where periodic boundary conditions would not be suitable for meeting the no-slip condition at the boundary) and Fourier basis functions in the other two directions where periodic boundaries were utilised.

2.3 Specific code features

2.3.1 Domain and discretisation

The code used in this project uses Fourier based spectral methods, applied over a triply periodic domain. Equations 2.9-2.10 are discretised through the use of Fast Fourier Transforms (FFTs) and are evolved in time using a third order Runge-Kutta technique, with the non-linear terms evaluated in Cartesian space and the viscous terms evaluated using an exact, integration factor method. The domain size is chosen to allow sufficient space for the large scale structures

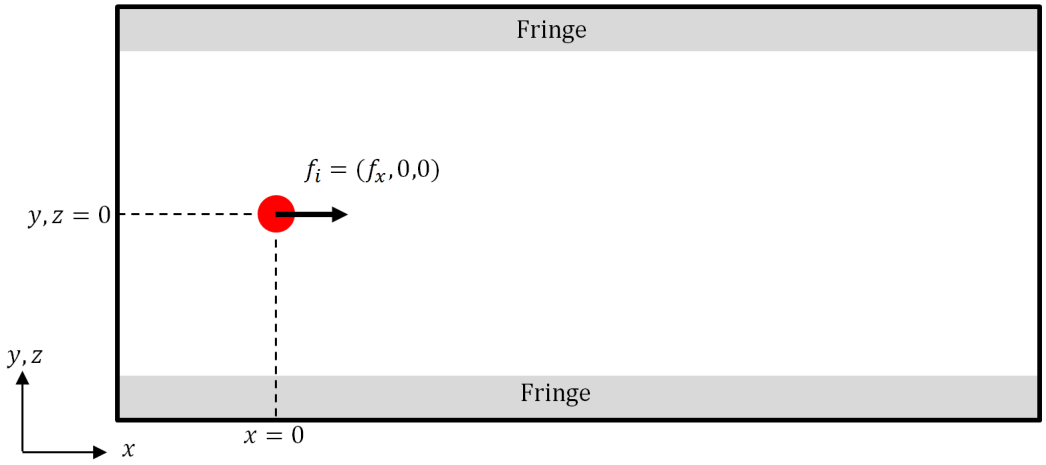

Figure 2.1: Schematic indicating the computational domain, with an origin at the centre of the momentum source.

expected at the later times to evolve without excessive interaction with any of the periodic boundaries or the fringe regions discussed in section 2.3.4.

The lateral (y) and vertical (z) domain sizes are the same with identical, uniform grid spacing, with the streamwise (x) direction somewhat longer. As one of the main considerations of this work is to evaluate how vertical density stratification affects initially axisymmetric flows, the equal domain sizing and grid spacing helps eliminate one potential cause for axisymmetry to break down. The domain origin is located at the centre of the momentum source for impulsive source simulations, or the radial centre of the vortex ring at $t = 0$ for vortex ring initialised simulations, with the origin placed just downstream of a streamwise boundary and equidistant between the lateral and vertical boundaries as indicated in figure 2.1.

The time step used in the Runge-Kutta method is either prescribed manually as an input parameter, or the code determines a suitable value based on the selected maximum Courant number of the code. The Courant number in each direction at a given point in the domain is defined as

$$C = \frac{u_i \Delta t}{\Delta x_i}. \tag{2.17}$$

For the spectral DNS code used here, the maximum value permitted value for the Courant number anywhere in the domain is 1.6. When prescribing its own time step, the code uses the maximum value of Δt that ensures $C \leq 1.58$ at all points, in order to ensure a stable time integration. In practical terms, this means that for a decaying flow where the maximum velocity values are decreasing with time, the time step can become progressively larger whilst maintaining numerical stability.

2.3.2 Evaluating convective terms, applying momentum sources and moving reference frame

One stumbling block with using spectral methods for fluid dynamics is the need to evaluate the convective, non-linear terms of the momentum equation (2.9), which is not easily achieved in Fourier space. Instead, the code used here uses inverse Fourier transforms to return Cartesian velocity and vorticity fields, calculates the non-linear terms in Cartesian space, then Fourier transforms the result for use in Fourier space.

This does allow additional forcing terms defined in Cartesian space to be added to the non-linear terms prior to converting back to Fourier space. This feature is utilised extensively in the simulation code to modify the momentum equations to create momentum sources to represent the effect of a propulsive or drag force of a manoeuvring body, apply the acceleration due to buoyancy effects, and also to apply the fringe method discussed in section 2.3.4.

Aside from adding momentum sources to the domain, manipulating the convective terms allows us to simulate the effect of freestream velocity on the flow field by adding an additional velocity component into the convective term for the streamwise direction i.e.

$$u\frac{\partial u_i}{\partial x_j}$$

is replaced by

$$(u + U_T)\frac{\partial u_i}{\partial x_j},$$

where U_T is the desired freestream velocity and can be prescribed directly. This essentially places the flow field within a moving reference frame.

2.3.3 Zero mode treatment and moving reference frame

Another potential issue with using this particular code for evaluating spatially evolving flow fields is the treatment of the zero (mean) modes in Fourier space for the velocity and scalar fields. The code discretises each velocity and buoyancy scalar component into Fourier modes in each of the x, y, z directions. The numerical algorithm used in the code is such however, that the "zero" mode is decoupled from the rest of the Fourier mode calculations and is thus unchanged throughout the simulation. The Fourier coefficient associated with this zero mode determines the mean velocity or scalar component in a given spatial direction. The code is written such that the "zero" modes for all velocity and scalar components in all directions have Fourier coefficients of zero at all times

e.g.

$$\overline{u}(t) = \alpha_n(t)e^{i0x} = \alpha_n(t) = 0, \tag{2.18}$$

or alternatively,

$$\int_V u(t)\mathrm{d}V = 0. \tag{2.19}$$

For the momentumless wake flows previously simulated using this spectral CFD code, this zero mode treatment is acceptable as equation 2.19 is valid at all times. This is not true however, for the cases studied in this project where some net momentum is added to the domain via an impulsively acting momentum source.

The practical effect of the zero mode treatment is that when streamwise momentum is added to the flow from the source, the value of u within and immediately adjacent to the source increases, while a background velocity is imposed on the whole domain in the opposite direction such that the spatial mean of u remains zero. The more momentum is added into the domain, the greater this background velocity becomes, remaining constant once the momentum injection has ceased. At the early times in the simulations conducted for this work, the important flow structures are relatively small compared to the domain volume and are moving at a velocity with a magnitude far greater than this background velocity. The influence of the zero mode treatment is therefore barely apparent at the early times. However, at the late times, the structures of interest grow in volume and slow considerably, such that the background velocity can no longer be neglected as key statistics such as the propagation velocity of fluid structures through the domain and volume integrated kinetic energy will be unduly influenced by the zero mode.

It should be noted that this effect has no influence on the fluid mechanics at work within the flow field, nor does it change the vorticity field (which, as calculated from the spatial derivatives of the velocity field, is independent of any background velocity). Thus the structures observed in the domain will not appear different in any significant way other than their position and relative velocity being shifted by the background velocity.

In order to combat this issue, a new zero mode treatment is implemented. As the acceleration due to the momentum source is prescribed directly in the code as f_i (see equation 2.9), we can determine the kinematic impulse, I_i, added to the domain at any point in the simulation by the time and volume integral of $f_i(x, y, z, t)$ i.e.

$$I_i(t) = \int_0^t \int_V f_i \mathrm{d}V \mathrm{d}t. \tag{2.20}$$

As this gives a precise measure of the momentum added to the domain in the streamwise direction, and with no other momentum sources or sinks acting on the fluid, we see that the expected mean value for the velocity components in the domain is given by

$$\overline{u_i}(t) = \frac{I_i(t)}{V} = \frac{I_i(t)}{L_x L_y L_z}. \tag{2.21}$$

The precise value of I_i implemented within the simulation can be determined in the code by performing simple addition of $f_i \Delta x \Delta y \Delta z$ throughout the domain to determine the total kinematic momentum flux, multiplying this by the time step used and adding to the value of I_i at iteration. This value is then divided by the domain volume to determine the exact mean velocity required. The Fourier coefficient of the zero mode for the relevant discretised velocity component is then set to this value i.e.

$$\alpha_n(t) = \frac{I_i(t)}{L_x L_y L_z}. \tag{2.22}$$

This removes the background velocity that would otherwise be enforced by the zero mode treatment. It would also be possible to correct for this background velocity by manipulating the convective term directly as discussed in section 2.3.2, which is a more transparent and easily implemented way of applying a moving reference frame to the domain. However, as the code performs all kinetic energy calculations within Fourier space, it is more convenient to modify the Fourier modes directly, as changes made to the velocity field by manipulating the convective terms are not accounted for when transforming the non-linear, convective terms back into Fourier space. Though the velocity fields may differ, the vorticity field produced by either of these two approaches should be identical, and is something to be verified during code testing.

2.3.4 Fringe method

As mentioned previously, one consequence of utilising periodic boundary conditions in the simulation code is that internal waves, generated by buoyancy effects, propagate to the edge of the domain, re-enter on the opposite side and subsequently interact with other flow structures until they are dissipated by viscous diffusion. This of course would not be the case for the infinite domain case that the code approximates, as the waves would propagate away from their source with increasingly negligible effect. As such, the code needs to be modified to either remove or severely diminish the strength of internal waves in the flow when they reach the domain boundaries.

One method previously employed in a variant of the simulation code used for this project was implemented by Redford et al. (2015), and is reused again here. The method's basic function is to create an additional forcing term in the momentum equation (2.9) and scalar transport equation (2.10) near the vertical and lateral boundaries of the domain. The magnitude of the forcing term, S, is given by $S = \sigma(s - s_0)$ where s is the appropriate component of velocity or the buoyancy scalar and s_0 is a target value. σ is a scaling function calculated in two dimensions by

$$\sigma = \sigma_c(\sigma_y + \sigma_z - \sigma_y\sigma_z), \tag{2.23}$$

where σ_c is the maximum strength of the forcing term and

$$\sigma_y = -\frac{1}{2}\left(\tanh\left(t_w\left[\frac{y}{l_{fy}} - 1\right]\right) + \tanh\left(t_w\left[\frac{l_y - y}{l_{fy}} - 1\right]\right) + 1\right), \tag{2.24}$$

$$\sigma_z = -\frac{1}{2}\left(\tanh\left(t_w\left[\frac{z}{l_{fz}} - 1\right]\right) + \tanh\left(t_w\left[\frac{l_z - z}{l_{fz}} - 1\right]\right) + 1\right), \tag{2.25}$$

where $l_{fy} = l_y N_f y/2n_y$, l_y is the lateral domain size, n_y is the lateral grid sizing and $N_f y$ is the number of grid points utilised at the edges of the domain to implement the forcing. t_w sets a smoothing length over which the value of The region where the forcing is implemented is known as the domain "fringe" and the application of forcing as the "fringe method".

The target value, s_0, is prescribed as the lateral/vertical boundary mean value of the velocity or scalar component, which was used previously to determine the zero mode background velocity correction as discussed in section 2.3.3. When this moving reference frame is taken into account, the fringe essentially enforces a weak no-slip like condition at the lateral and vertical domain boundaries in order to dissipate the internal waves. Obviously, the presence of the fringe can have an adverse effect on flow structures other than the internal waves when they increase in size at the late time, as the fringe forcing will act against the motion in the outer edges of the structure. Therefore the size and strength of the fringe region needs to be chosen to be sufficiently "aggressive" to dissipate the internal waves to negligible levels, without occupying so much of the domain as to make the late time simulation unrepresentative of the infinite domain approximation.

2.3.5 Regridding

One characteristic of the flows simulated in this work, particularly those subject to a linear density stratification, is that at the late time the length scales of

the main flow structures increase significantly and the corresponding velocity scales reduce significantly. As a consequence, the high level of spatial resolution (or large number of Fourier modes) required for sufficient fidelity at the early times are somewhat excessive at the late time, meaning an unnecessarily large number of computations requiring high levels of compute time, processor cores and memory. The fine grid resolution also severely limits the maximum time step in order to ensure sufficiently small Courant number (see equation 2.17).

In order to combat this problem, it is favourable to regrid the simulation onto a coarser domain, achieved by removing the higher wavenumber modes from the domain in Fourier space. This greatly reduces computational cost and allows for a larger time step, allowing the late time flow development to be assessed over large time intervals. Typically, n_x, n_y, n_z can be reduced by as much as 50% at the late time without compromising simulation accuracy.

2.3.6 Post-processing

The code writes data files containing certain flow statistics at every time step throughout the simulation, examples being the volume integrated kinetic energy and buoyancy variance levels. Aside from this, large data files containing the entire computational domain in Fourier space are dumped at regular intervals, which can be used for flow visualisation and more complex analysis of the flow structures. The vast majority of the post-processing is conducted using a variety of bespoke scripts written for Matlab.

Chapter 3

Validation of numerical methods

Before conducting simulations of the wake structures of interest to this project, it is useful to conduct some validation tests within some "warm up" simulations. This ensures the code correctly evaluates the governing equations it is presented with, so that results from later, production quality runs can be considered trustworthy.

Variants of the project's code have been used to evaluate cases from an initial velocity field of domains containing a vortex ring (see Archer et al. (2008)), axisymmetric wakes (Rind (2010)) and stratified wakes (Redford et al. (2015)). For this work, the code's evaluation of the Navier-Stokes equations has been tested extensively, with simpler governing equations such as a one dimensional wave and heat equation solved correctly as well.

Unlike those examples of previous work, this code makes use of two additions to facilitate simulation of impulsively generated wake flow. These are the application of freestream effects through modifying the convective term of the Navier-Stokes equations, and the addition of a momentum source that is to generate propulsive flow and emulate the drag forces on a manoeuvring body. These features were tested, along with an additional test to evaluate the application of both buoyancy effects and the fringe method implemented in the code, and checks to examine the effects of domain regridding and domain size on flow field evolution.

3.1 Impulsive starting jet

3.1.1 Background and simulation set up

In order to test the code's ability to simulate propulsive structures in the flow domain, a subroutine was implemented to accelerate fluid in a selected

region of the domain. For purposes of validation, this momentum source was implemented as a thin axisymmetric actuator disc with a hyperbolic forcing profile in the radial and streamwise directions i.e.

$$f_y(x,y,z) = \frac{f_0}{4}(\tanh(20(0.5-r))+1)(\tanh(20(0.1-|y|))+1), \tag{3.1}$$

where $r = \sqrt{x^2+z^2}$. [1] This profile produces an actuator disc like momentum source with a diameter of 1 and a thickness of 0.2, centred about $(x,y,z) = 0$. The factor of 20 in the hyperbolic tangent functions defines the smoothness of the edge of forcing region, with this value giving a well defined disc, whilst smoothing the transition from maximum f_y to zero over enough grid points in the domain to reduce the likelihood of Gibbs phenomena associated with discontinuities in the flow field.

This actuator disc is intended to generate a laminar starting jet, with a well defined vortex ring followed by a trailing jet structure of smaller rings. As discussed in Section 1.2.1, previous experimental studies demonstrated that the evolution of the jet can be considered in terms of non-dimensional formation time, T with

$$T = \frac{\overline{V_J}t}{D_J},$$

where

$$\overline{V_J} = \frac{1}{t_f}\int_0^{t_J} V_J(t)\mathrm{d}t.$$

The strength of the actuator disc, f_0, is adjusted using proportional control to create a jet at the desired velocity, V_j i.e.

$$f_0 = f_g(V_j - V_J),$$

where f_g is the controller gain. V_J is not measured directly in the flow, but taken to be twice the velocity at the centre of the actuator disc. This is explained further in Ruijgrok (1996), where an actuator disc (used to model propeller flow) adds a velocity component to a cylindrical region of fluid. Half the fluid acceleration is achieved upstream of the disc and half downstream, with the velocity at the centre of the disc denoted at V_0. As the freestream velocity in the case simulated here is zero, this gives $V_J = 2V_0$. Additionally, treating the accelerated cylinder of fluid as a stream tube, the doubling of velocity from the centre of the disc to the resulting jet means that the stream-tube must constrict to half the area of the disc in order to conserve mass flow,

[1] This set of validation simulations was performed on an early iteration of the code, where the y direction was defined as streamwise, and the x direction defined as the lateral direction, with z the vertical direction. The axes were reorganised for the main research simulations documented in later chapters, but were not retroactively altered for these validation tests.

giving an effective streamtube diameter of $1/\sqrt{2}$ of the actuator disc diameter, D_0 where $v = V_J$.

This controller was given sufficient gain to increase V_0 quickly enough to consider the jet flow from the disc akin to an impulsive starting jet. Using the downstream velocity induced by the actuator disc and the diameter of the constricted streamtube as the velocity and length scales this gives the formation time of the jet flow as

$$T = \frac{\overline{2V_0}t}{D_0/\sqrt{2}} \tag{3.2}$$

The actuator disc set up was implemented in a computational domain with $(nx, ny, nz) = (192, 384, 192)$ and $(Lx, Ly, Lz) = (1.5\pi, 3.0\pi, 1.5\pi)$, with a time step equal to approximately 1/60th of a formation time unit. The actuator disc was operated continuously throughout the simulation, providing a constant rate of momentum addition once the desired jet velocity was achieved. The Reynolds number of the flow based on V_J and $D_J = D_0/\sqrt{2}$ was approximately 8000.

3.1.2 Results and analysis

Visualisations of the impulsively started jet and the resulting vortex ring pattern are given in figure 3.1 and figure 3.2. The characteristic leading vortex ring and its trailing jet of smaller rings are clearly seen in the vorticity contours, with these smaller rings produced at regular intervals of just over 3 formation time units. Within this pattern, if we assign the leading ring a title of "ring 1", the first trailing ring as "ring 2" and so on, then it is observed that every even numbered ring is eventually entrained by the preceding odd numbered ring. Such entrainment was observed in Gharib et al. (1998) and noted to result in a temporary increase in the circulation of the entraining ring.

As found in experimental studies of vortex ring formation, measuring the circulation in the leading ring is somewhat problematic, as it requires distinction between which parts of the flow domain are within the leading ring and which are part of the trailing jet. This also poses issues when determining both the ring radius and downstream position.

To overcome this, we consider a two dimensional slice of the vortex ring at $z = 0$ (given the axisymmetric nature of the problem, this should be representative of the ring as a whole). Next, an initial guess as to the location of the centre of the leading ring vortex cores is made by tracking the location of the points of both maximum and minimum azimuthal vorticity, ω_z. Once

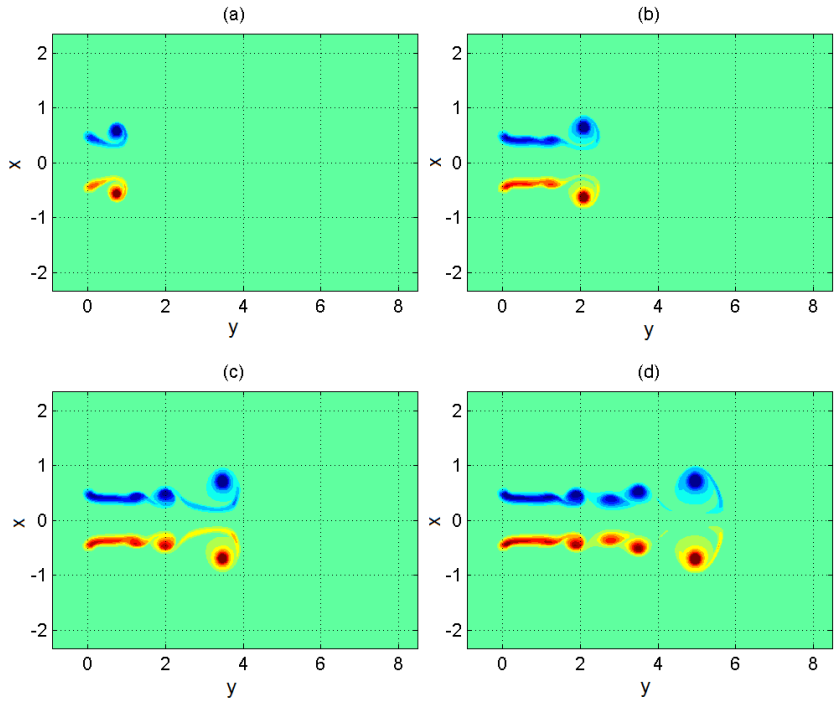

Figure 3.1: Contours of azimuthal vorticity, ω_z, for starting jet and resulting vortex ring formation at (a) T = 4.8 (b) T = 9.5 (c) T = 14.3 (d) T = 19.0 - red indicates positive ("clockwise") vorticity, with blue indicating negative vorticity

located, all vorticity in the field that lies beyond one actuator disc radius (0.5) from these points is excluded, isolating the vorticity within the leading ring. A threshold value of 5% maximum vorticity magnitude is applied, with all vorticity that has a magnitude below this threshold excluded as well. This is intended to create a tangible disconnect between the leading ring and the shear layer feeding in from the trailing jet. Once these conditions have been applied, the ring circulation, radius and downstream position are determined using similar analysis to the vortex ring tracking in Archer et al. (2008).

As seen in figure 3.3, the non-dimensional circulation, $\Gamma_z/(V_J D_J)$, in the leading ring does increase linearly with formation time. It continues to do so until $T \approx 4$, after which the circulation does continue to rise, albeit at a rate, $d\Gamma_z/dT$, approximately 1/6th the rate prior to T = 4. This is somewhat contrary to the constant circulation state noted by Gharib et al. (1998) and Rosenfeld and Gharib (1998). Closer examination of results from these previous works showed that for impulsively generated starting jet flows, small circulation gains in the late time can be inferred (see figure 8,10 in Gharib et al. (1998)). The Reynolds number of the flow in the leading ring, based on the non-dimensional circulation, is found to be approximately Re_Γ = 1500. At

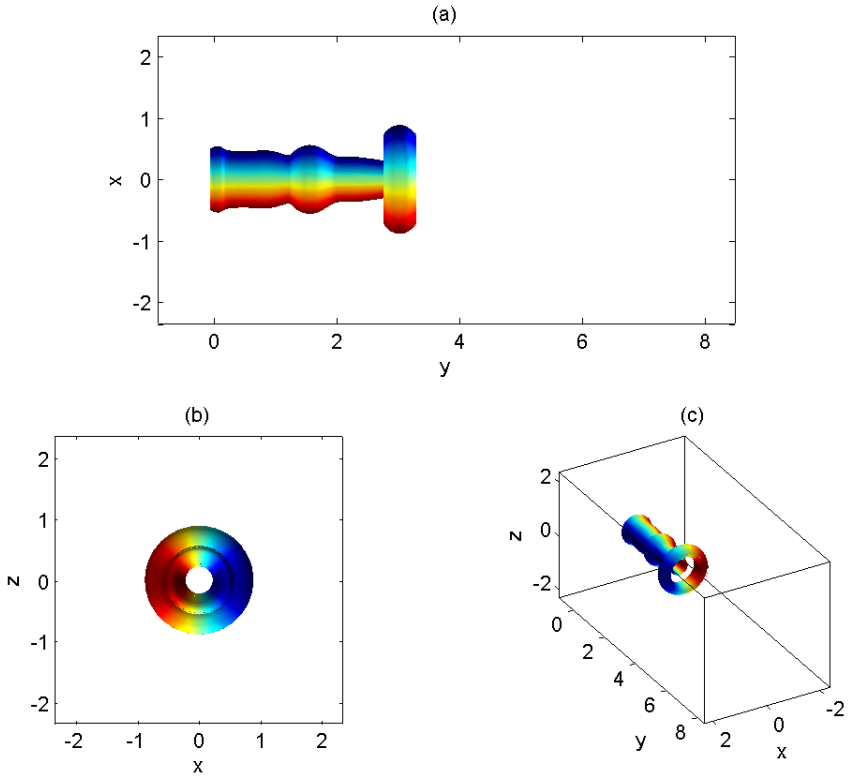

Figure 3.2: Isosurfaces of 15% maximum vorticity magnitude ($\sqrt{\omega_x^2 + \omega_y^2 + \omega_z^2}$) for T = 12.7, coloured by value of ω_z (a) Top down view (b) Frontal view (c) Isometric view

around T = 13, the second ring is entrained into the leading ring. This temporarily increases the rate of circulation input into the leading ring, though the rate returns to its previous level by around T = 15, suggesting that some of the excess vorticity the entrainment provides is shed into the trailing jet structure. In order to determine how representative these results are compared to experimental works, the time history of ring circulation is normalised by the value at T = 4, and contrasted with analogous data from Gharib et al. (1998) as shown in figure 3.4. The same linear increase of total circulation up to $T \approx 4$ is observed, along with a much more gradual rise in ring circulation thereafter, once it has pinched off from the starting jet.

Next we examine the ring's streamwise velocity and radius, given in figure 3.5. The velocity appears to rise in a roughly linear manner until $T \approx 4.2$, then remains constant thereafter. There are some poorly correlated data points in these results, which have likely arisen from the particular tracking method used for the vortex ring. Somewhat more consistent are the measurements of the ring radius, which retains a near constant value throughout the initial vortex ring formation of $r_R \approx D_0/2$. At the same value of T where the circulation increase slows, the radius of the ring begins to increase.

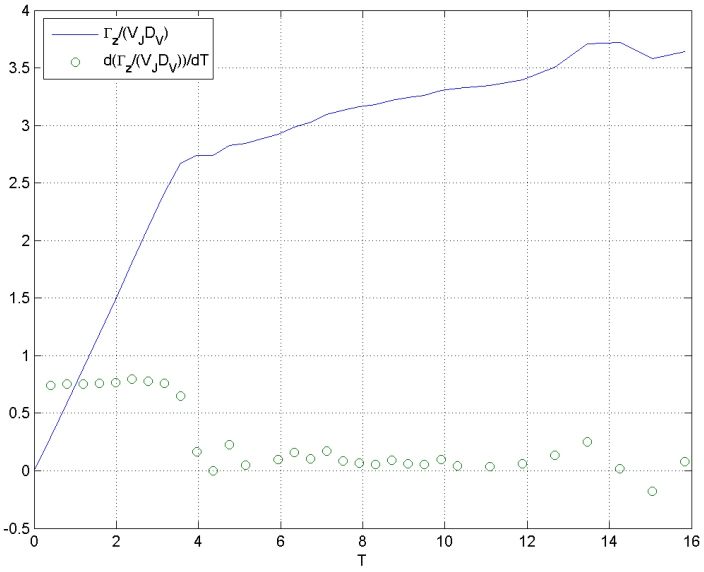

Figure 3.3: Evolution of leading vortex ring circulation, $\Gamma_z/(V_J D_J)$, and rate of change, $d(\Gamma_z/(V_J D_J))/dT$ with formation time

This increase in ring radius may explain the continued circulation rise for $T > 4$. As the ring radius increases, the maximum circulation it can entrain will increase accordingly. If we now non-dimensionalise circulation in the ring by its r_R rather than D_J (figure 3.6 we can see that the ring circulation per unit radius remains approximately constant for $T > 4$, suggesting that for a given radius, the ring circulation has indeed been maximised. Coincidentally, the value of this ring normalised circulation is roughly equal with formation time until $T \approx 3.8$. In the literature that was consulted, little reference was made to the evolution of ring radius and how or if this related to observed circulation, so the validity of this result is somewhat unclear.

Nonetheless, the flow structures formed by an impulsive jet noted in relevant literature have been reproduced with reasonable accuracy, validating the code's ability to simulate the generation of impulsive jets and subsequent vortical structures.

3.2 Cross-pattern internal waves in stratified fluid

3.2.1 Background and simulation set up

As discussed previously, the code implements the effects of density stratification on a flow through use of the Boussinesq approximation in the Navier-Stokes equations, assuming a constant initial lapse rate, Φ (and hence constant buoyancy frequency, N). It is prudent to try and replicate simple test cases

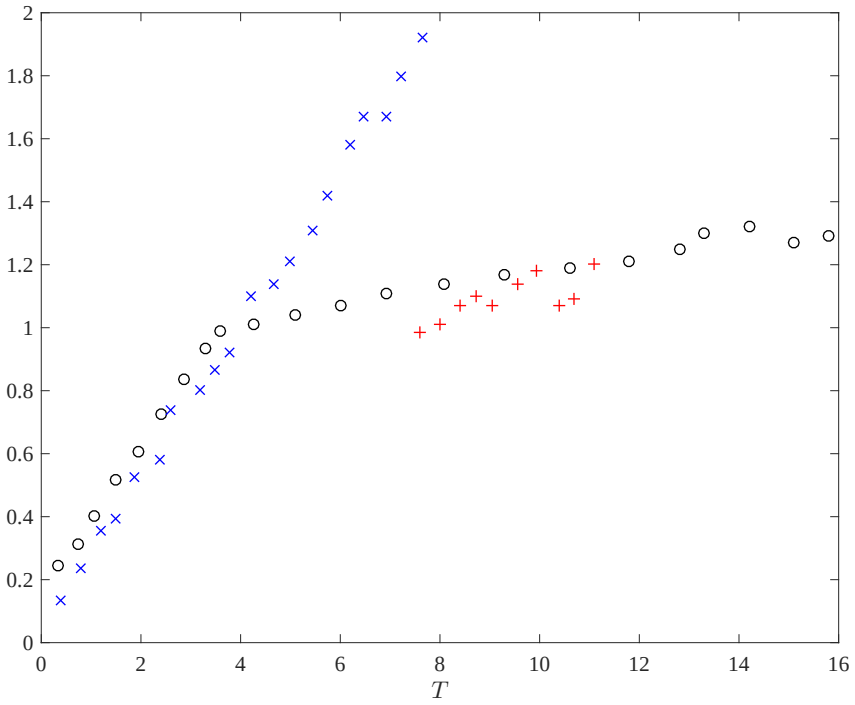

Figure 3.4: (○) Circulation of leading vortex ring, normalised by total circulation in domain at $T = 4$ for simulation conducted for this chapter, (×) Total domain circulation, normalised by total circulation in domain at $T = 4$ as presented in figure 10 from Gharib et al. (1998), (+) Leading ring circulation, normalised by total circulation in domain at $T = 4$ as presented in figure 10 from the same publication.

from previous experimental work with stratified fluids under these conditions to check that the code implementation of stratification is valid.

3.2.2 Background and simulation set up: Cross pattern internal waves

An often cited case in relevant literature is work published by Mowbray and Rarity (1967), concerning work where a small circular cylinder was suspended in a tank of liquid with uniform buoyancy frequency. The cylinder was then oscillated horizontally at a particular angular frequency, ω_f, generating an internal wave pattern in the tank that was visualised using Schlieren imagery. As shown in the experiments, and discussed further by Lighthill (1978), when the magnitude of the radial frequency of the cylinder was less than the buoyancy frequency of the liquid, the Schlieren images revealed an "x" shaped pattern of density variation (often referred to as a "Southern Cross" or "St. Andrews Cross").

The experiments found where the ratio between the radial frequency of the

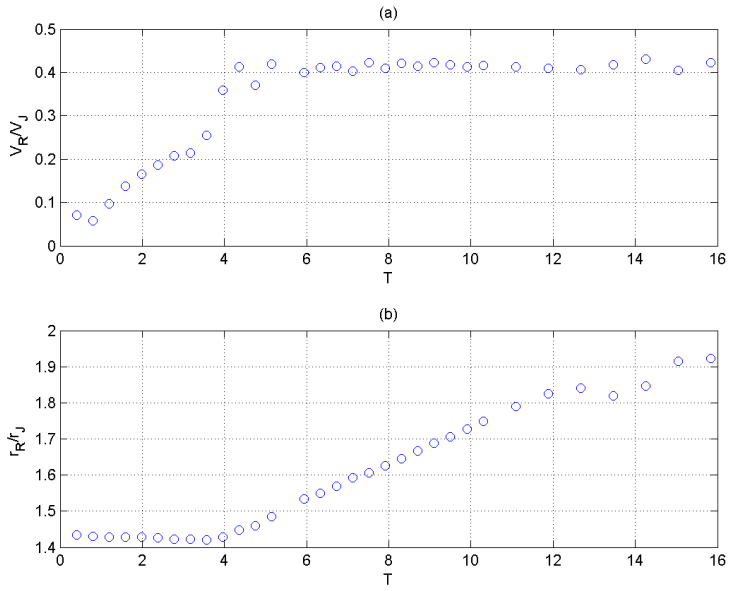

Figure 3.5: Evolution of (a) leading vortex ring translational velocity, $V_R = dY_R/dT$ (b) leading vortex ring radius, r_R, with formation time

oscillation and the buoyancy frequency (ω_f/N) was varied over the interval of 0 to 1, the angle of the cross pattern's "spokes" (the internal waves) from vertical was found to vary. This angle, ϕ, is given as

$$\phi = \cos^{-1}(\omega_f/N).$$

Hence, when ω_f/N is near a value of 1, the spokes appear near vertical as ϕ approaches zero, with near horizontal results for ω_f/N close to zero.

A similar effect to this can be observed by setting up a case using the DNS code, involving a two dimensional, square domain with stratification applied in the vertical (z) direction to give a known, constant vale of N. At the centre of the domain, an unsteady momentum source is applied in the lateral (x) direction varying in x, z at t as

$$f_1 = \sin(2\pi f t)\frac{J_J e^{-(r_2/r_J)^2}}{(\pi {r_J}^2)^{3/2}},$$

where $r_2 = \sqrt{x^2 + z^2}$. This momentum source is intended to emulate the body force exerted on the fluid by the solid, oscillating cylinder in the experimental cases.

The test cases were run on a 256 by 256 square grid with domain size $-\pi \leq x, z \leq \pi$ with a fixed time step of approximately 0.36 of the buoyancy period ($1/N$). The momentum source was centred at $(x, z) = (-0.5, -1)$. The radius of the source, r_J, was set as 0.125, peak momentum flux, J_J, was set to 0.01 and reference Reynolds number, Re_{Ref} was set artificially high to try

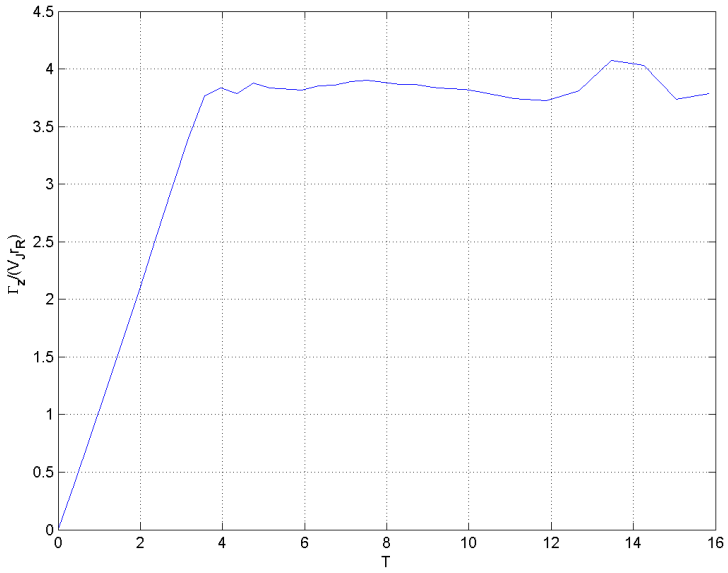

Figure 3.6: Evolution of leading vortex ring circulation (normalised by ring radius), $\Gamma_z/(V_J r_R)$

and limit the influence of viscous dissipation on internal wave propagation. ω_f/N was varied for five different cases to emulate the experimental work, starting with an initially quiescent domain each time. As density is not stored in the code (with buoyancy determined by the Boussinesq approximation and a known value of N), the Schlieren plots from experimental work cannot be reproduced directly. Instead, we plot contours of θ, the magnitude of vertical acceleration due to buoyancy effects as given in equation 2.9.

3.2.3 Results and analysis

First, we look at a single case where $\omega_f/N = 0.426$, which would be expected to give the wave angle, ϕ, as approximately 64.8° from vertical. The evolution of θ over time is demonstrated in figure 3.7. The plots show the initial evolution of the internal waves (high magnitude areas of θ), propagating outwards from the momentum source to form the expected cross shape pattern. Once formed, the angle of the waves is invariant in time. The value of ϕ was observed to be approximately 65°, giving very good agreement with the relationship suggested by the experimental work.

One effect observed here, unlike the experimental work, is the presence of additional, weaker wave formation above and below the expected cross pattern region. These are a consequence of utilising periodic boundary conditions for the computational domain, with the waves leaving one side of the domain and re-entering at the other. The presence of these additional waves appears to have little or no effect on ϕ however, and can be potentially eliminated through

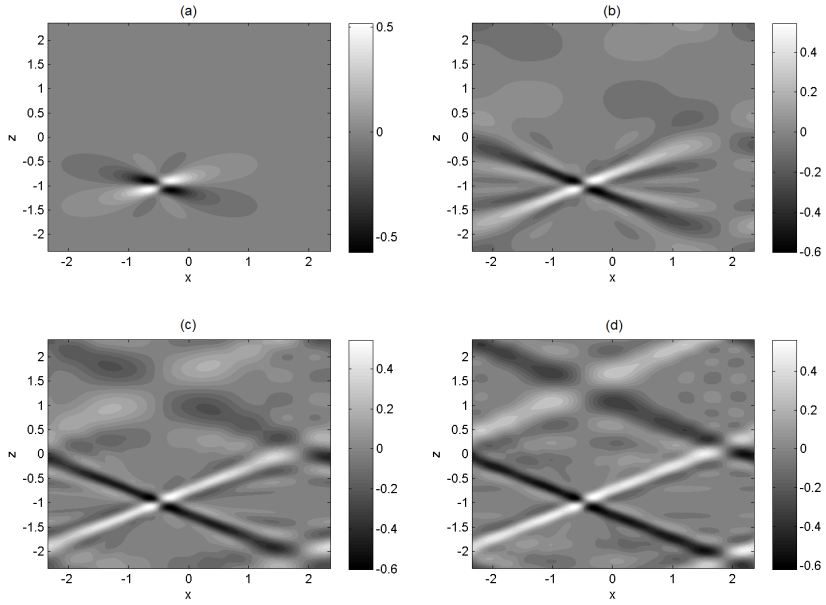

Figure 3.7: Contours of θ for ω_f/N = 0.426 at (a) Nt=7.2 (b) Nt=21.6 (c) Nt=36 (d) Nt=50.4

the use of the fringe method (discussed in section 3.3).

Next, the frequency of the oscillation was varied in order to observe whether ϕ would change accordingly. Four additional runs were performed with frequencies both higher and lower than the first test. The wave patterns generated at these different frequencies is given in figure 3.8.

The values of $\cos\phi$ for the five runs are plotted in figure 3.9, along with a line showing the theoretical relationship. It can be seen that for all frequency ratios, ω_f/N, that were tested, the resultant angle of the wave pattern was in close agreement with theory. In this respect, the buoyancy forcing implemented in the code via the Boussinesq approximation can be considered valid.

3.3 Suppressing internal waves using fringe method

3.3.1 Background and simulation set up

As observed in figure 3.7 and figure 3.8, the internal waves generated by the momentum source in the domain transmit across the periodic boundaries, with their energy continuing to contribute to the total energy in the domain, rather than propagating away to infinity. The fringe method discussed in section 2.3.4 can be applied to dissipate these waves at the periodic boundaries, and is tested here. Aside from the activation of forcing in fringe regions and adjusting the fringe parameters, these test cases use the exact same parameters as the

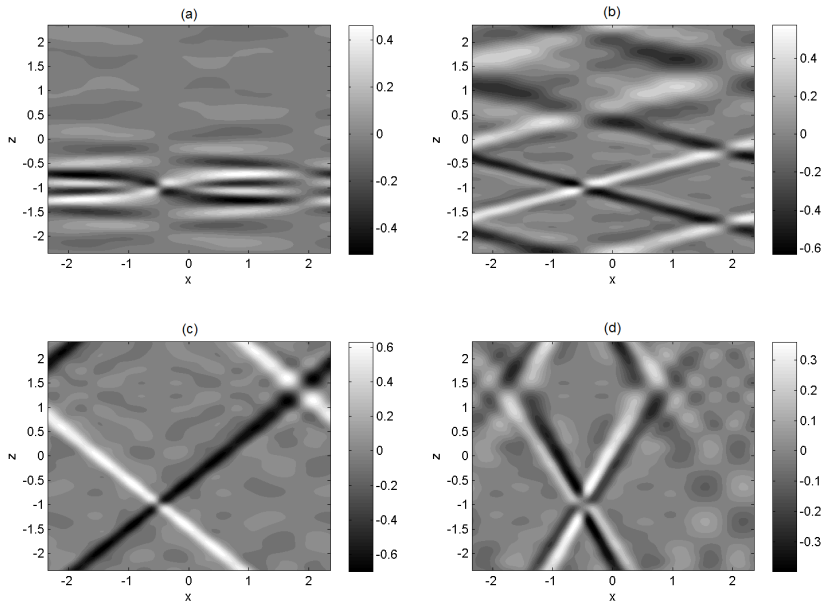

Figure 3.8: Contours of θ at $Nt = 72$ for (a) $\omega_f/N = 0.1$, (b) $\omega_f/N = 0.3$, (c) $\omega_f/N = 0.7$, (d) $\omega_f/N = 0.9$

first cross pattern wave test (figure 3.7, $\omega_f/N = 0.426$).

The original implementation of the fringe method in the DNS code was retooled slightly from the version used by Redford et al. (2015). Recalling equation 2.23-2.25, the terms are relabeled to apply a fringe region at the x and z periodic boundaries in this validation work:

$$\sigma = \sigma_c(\sigma_x + \sigma_z - \sigma_x\sigma_z),$$

$$\sigma_x = -\frac{1}{2}\left(\tanh\left(t_w\left[\frac{x}{l_{fx}} - 1\right]\right) + \tanh\left(t_w\left[\frac{l_x - x}{l_{fx}} - 1\right]\right)\right) + 1,$$

$$\sigma_z = -\frac{1}{2}\left(\tanh\left(t_w\left[\frac{z}{l_{fz}} - 1\right]\right) + \tanh\left(t_w\left[\frac{l_z - z}{l_{fz}} - 1\right]\right)\right) + 1.$$

.

Firstly a range of test cases were run to evaluate the effect of varying σ_c, l_{fx}, l_{fz} and t_w on how effective the fringe would be on dissipating the cross pattern waves generated by the oscillating force. The length scales l_{fx} and l_{fz} were both set as the same percentage of the domain width and height, $l_{f\%}$. Some of the cases are presented here to demonstrate both the geometry of the fringe and the resulting effect on the scalar field. The case names and fringe parameters are given in table 3.1. The geometry of the fringe is illustrated in figure 3.10, with the resultant scalar fields illustrated in figure 3.11.

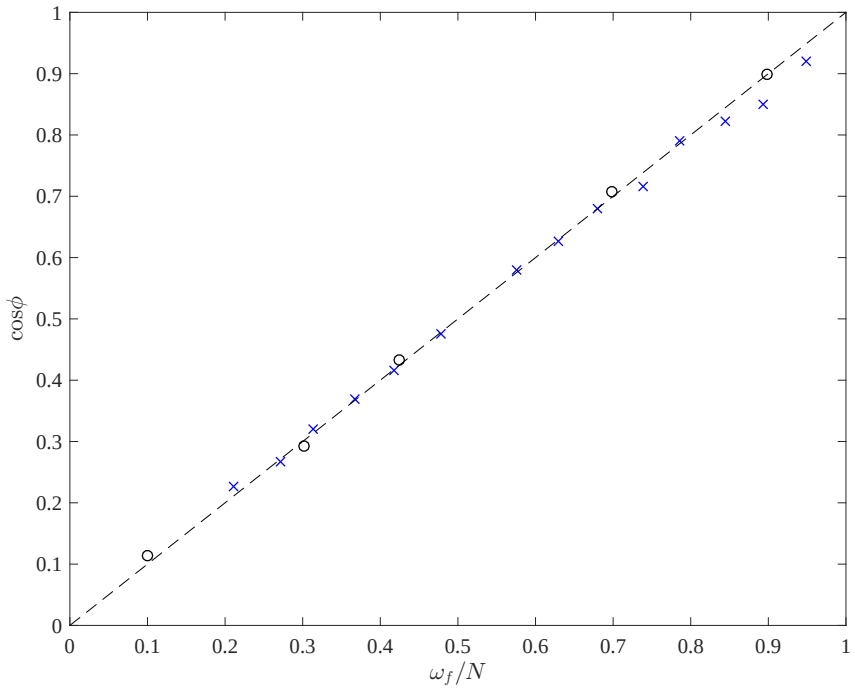

Figure 3.9: (○) $\cos\phi$ for varying ω_f/N across numerical simulations documented in figure 3.7, (×) analogous experimental data taken from figure 6 in Mowbray and Rarity (1967). The dashed line represents $\cos\phi = \omega_f/N$ prediction)

3.3.2 Results and analysis

Scalar field

It is easily observed from figure 3.11 that the extent and strength of the fringe regions has a marked effect on the extent that the wave pattern is allowed to transmit through the periodic boundaries and pervade throughout the rest of the domain. Lengthening the fringe region to include more of the domain and reducing t_w to smooth the transition from the non-fringe region both appear to be effective methods of dissipating the internal waves at the boundaries. However, this is at the expense of giving over a large proportion of the domain to the fringe region (e.g. NF23, NF27). By comparison, increasing σ_c also appears to weaken the waves as they pass through the boundaries, but for high values (e.g. NF25) close observation demonstrates that the internal waves are no longer just passing through the fringe region but are partially reflected by it. This is no more desirable than waves transmitting through the boundaries, as the reflected wave pattern also pervades throughout the domain (albeit with a different geometry to the transmitted wave pattern).

After examining the test cases presented here (and a number of others with different combinations of fringe parameters), the impression given is that for

Table 3.1: Fringe method test simulation parameters

Case	$l_{f\%}$	σ_c	t_w
NF20	No fringe		
NF21	5%	4.0	2.5
NF22	10%	4.0	2.5
NF23	25%	4.0	2.5
NF24	10%	0.4	2.5
NF25	10%	40.0	2.5
NF27	10%	4.0	0.5
NF28	10%	4.0	1.5
NF29	10%	4.0	3.5

the oscillating force case the ideal fringe region should:

- be relatively small to reduce computational cost ($l_{f\%}$ = 5%)
- have a smooth transition region (t_w=1.0)
- have the peak forcing strength "tuned" to eliminate transition whilst not inducing reflection

It should be noted that even with a relatively thin fringe region, the effects of the resulting σ field are felt throughout most of the domain, with slightly over 63% of the domain having a σ value more than 5% of σ_c. The value of σ_c required to meet the last of these criteria is not obvious and requires a certain degree of trial and error to determine a suitable value, with a closer examination of the values of θ near the boundaries.

After a further round of simulations, a value of σ_c = 16 was chosen as the optimum peak fringe strength. Contours of fringe σ and resulting contours of θ are given in figure 3.12. It can be seen that the fringe significantly dissipates the internal waves at the boundary. Some of the wave does still transmit through and continue throughout the domain, but it was found that whilst increasing σ_c reduced the transmitted waves, it strengthened the wave reflection, nullifying the gains.

To better understand the effect of the fringe on the scalar field, we examine the vertical variation of θ with z at both x = −1.5 and x = 1.5 (see figure 3.13). In the lateral extent of the fringe, this represents two lines where $\sigma_x \approx 5\%$. The scalar contours are given again, labeled with equivalent points on the line

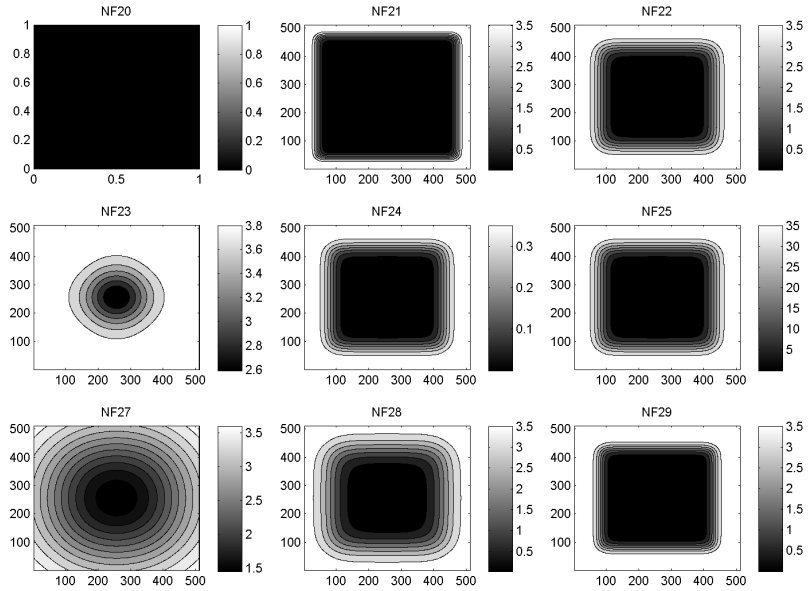

Figure 3.10: Contours of σ for selected fringe method test cases

plots to better identify the relevant scalar values. The reduction in scalar value between the original wave and reflected/transmitted values at these points are also given in table 3.2.

Table 3.2: "Optimum" fringe scalar values at selected points

Wave Points	**Original θ**	**Trans./refl. θ**	**Reduction %**
A, A_R	–0.390	–0.055	86%
B, B_R	0.390	0.095	76%
C, C_T	0.345	0.065	81%
D, D_T	–0.350	–0.060	83%

Reductions in wave strength (based on the peak θ values presented here) were in the region of 80% across the fringe region. Some wave transmission was still observed, as were some wave reflections from within the fringe. No value of θ was found that gave a near 100% reduction with the fringe geometry chosen. Two possible reasons present themselves for why this may be so. First, the fringe geometry chosen is designed to maintain a region of the domain outside of the influence of the fringe (such that the observed wave pattern is considered credible). This limits the size of the fringe, thus it may be insufficient to dissipate the waves entirely. Second, the flow studied here is driven by a combination of buoyant forcing and the oscillating momentum source. The

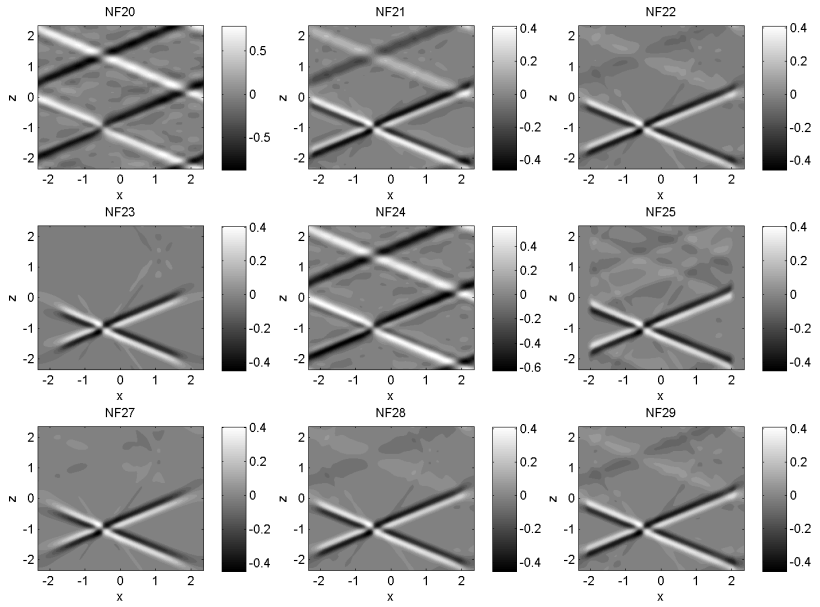

Figure 3.11: Contours of θ at $Nt = 144$ for selected fringe method test cases

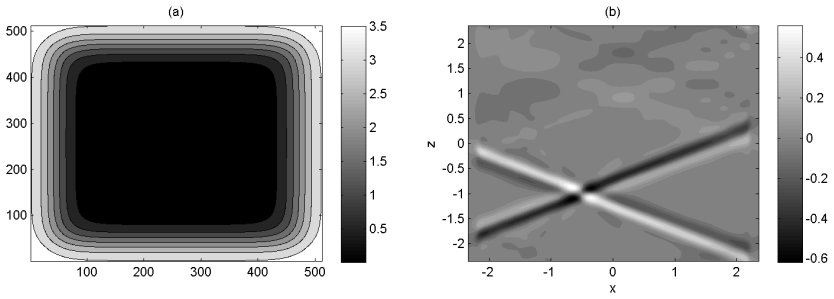

Figure 3.12: (a) Contours of σ for "optimum" fringe (b) Contours of θ at $Nt = 72$ for "optimum" fringe

momentum source maintains a regular energy input into the domain, meaning that if the waves it generates are not fully dissipated by their first passage through the fringe region, then another will be generated behind it which also will not be fully dissipated and so on, with the energy of each wave partially retained.

The decaying stratified wake simulations of Redford et al. (2015) featured internal waves that were not driven by a continuous momentum source but by an initial velocity field with non-zero momentum, that was allowed to decay over time. If the waves were not dissipated on the first pass through the fringe they would be after subsequent passes. Additionally, the initial strength of the waves generated by the flow would reduce with time as the Reynolds and Froude numbers of the wake decay.

This would suggest that the fringe method employed here is not fully suited to fully dissipating the internal waves as desired. Nonetheless, a significant

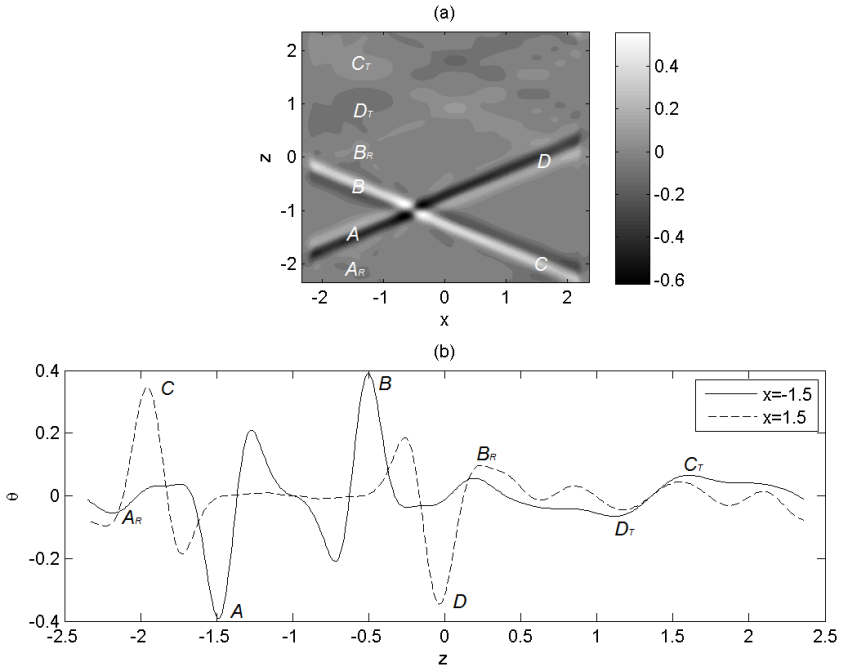

Figure 3.13: (a) Annotated contours of θ at $Nt = 72$ for "optimum" fringe (b) Annotated plot of θ with varying z for fixed x locations for "optimum" fringe

reduction in strength is achieved, with the resulting wave pattern resembling the original work of Mowbray and Rarity (1967) much more closely than the cases with no fringe employed.

Energy balance

We can further examine the effects of the fringe method by considering both the domain integrated kinetic energy and buoyancy variance of the flow induced by the oscillating force. Recalling equations 2.13-2.14,

$$\frac{1}{2}\left(\frac{\partial(u_i^2)}{\partial t} + u_j\frac{\partial(u_i^2)}{\partial x_j}\right) = -u_3\theta\delta_{3i} + K'_\nu + u_i f_i,$$

$$\frac{1}{2N^2}\left(\frac{\partial(\theta^2)}{\partial t} + u_i\frac{\partial(\theta^2)}{\partial x_i}\right) = u_3\theta\delta_{3i} + P'_\nu,$$

we can now distinguish the meaning of each term on the left and right hand side of these energy transport equations as well as adding in an additional term to account for the energy extracted from the domain in the fringe region to give

$$\frac{dK}{dt} = -K'_B + K'_\nu + K'_f + K'_\sigma,$$

$$\frac{dP}{dt} = K'_B + P'_\nu + P'_\sigma,$$

where K'_σ and P'_σ are respectively the rates of change of kinetic energy and buoyancy variance due to the presence of the fringe.

The code records each of the components on the right hand side of the equations based on the instantaneous velocity and scalar fields, as well as the instantaneous integration of the kinetic energy and buoyancy variance over the whole domain. A simple central differencing in time is used to obtain the time derivative of these total energies, and thus allows a check of whether the left and right hand sides of the equations add up. The oscillatory nature of the momentum input is reflected in the energy flux terms with a sinusoidal variation in time noted for all. The period of these oscillating energy flux readings was found to be one half the period of the oscillating momentum source, which is to be expected as the momentum source will produce two "peak" energy inputs when imparting maximum acceleration on the fluid in either direction during a cycle.

As can be seen in figure 3.14, the kinetic energy input from the momentum source is positive throughout, with the buoyancy flux component negative at all times, with the maximum rate of kinetic energy lost due to buoyancy concurrent with the maximum rate of kinetic energy gain from the momentum source. As expected, the viscous dissipation in the domain is near zero at all times, as was intended through the use of artificially high Reynolds number. Of more interest is the kinetic energy lost to the fringe . Initially zero, the energy removed from the domain by the fringe increases until it reaches a quasi-steady state with small oscillations thereafter. These oscillations have the same frequency though a slight phase shift from the momentum source input, suggesting a lag between the energy input into an internal wave from the source and the energy lost at the fringe (i.e. the time taken for the wave to propagate from the source to the fringe). As this fringe energy flux reaches a quasi-steady state, the total rate of change of kinetic energy for the domain begins oscillating about zero with a constant frequency and amplitude. This shows that the domain has reached a state of maximum kinetic energy (albeit with periodic oscillations).

In addition to analysing these terms individually, the flux terms were added together and the result compared with the calculated rate of change of kinetic energy. The sum of the flux terms was found to equal the rate of change of kinetic energy, showing that there are no terms in the governing energy equation unaccounted for, and that the energetics are correctly resolved in the DNS code.

Similar patterns are observed in the flux terms for the buoyancy variance (figure 3.15). The buoyancy flux term is simply the positive equivalent of that shown for kinetic energy, and the viscous term is again near zero. Like the

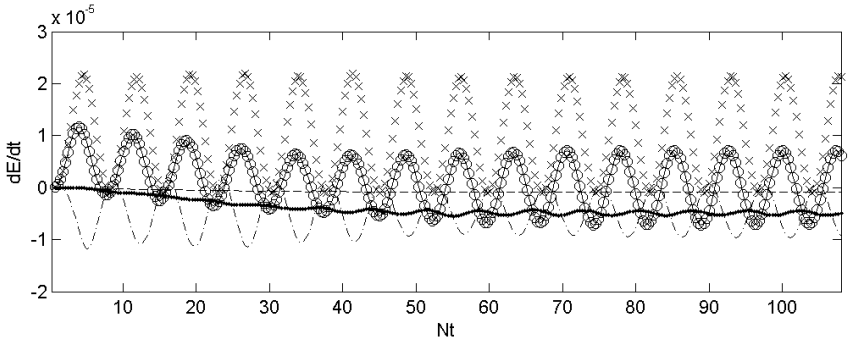

Figure 3.14: Domain integrated kinetic energy fluxes for "optimum" fringe case with dK/dt (—), K'_B ($-\cdot-$), K'_ν (- -), K'_σ ($\bullet$), K'_f ($\times$), $-K'_B + K'_\nu + K'_\sigma + K'_f$ ($\circ$)

domain integrated kinetic energy, the buoyancy variance reaches a maximum level with a time derivative oscillating about zero at the same time the buoyancy variance removed by the fringe also reaches a quasi steady state. Again, the sum of the flux terms and the time derivative of buoyancy variance overlay near perfectly, further adding trust to the code's ability to resolve the flow field.

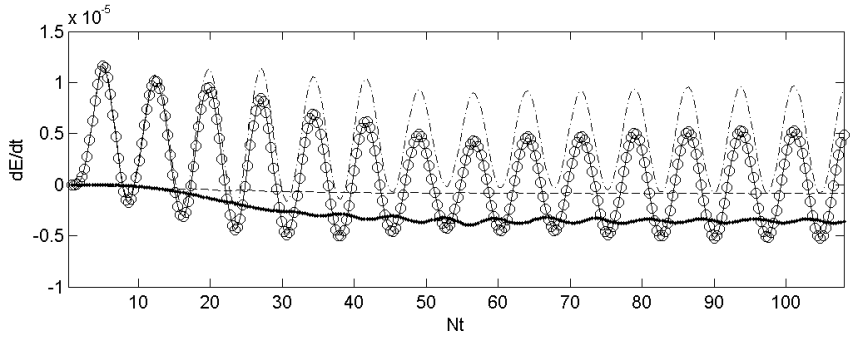

Figure 3.15: Domain integrated buoyancy variance fluxes for "optimum" fringe case with dP/dt (—), K'_B ($-\cdot-$), P'_ν (- -), P'_σ ($\bullet$), $K'_B + P'_\nu + P'_\sigma$ ($\circ$)

Domain enlargement

Although the fringe method used here showed promising results when adjusted to the "optimum case" discussed previously. It was decided to conduct one final series of simulations to determine whether expanding the domain itself could be used to facilitate a more effective fringe for dissipating internal waves. A new set of test cases were run with the domain size enlarged by 50% in both directions. By adjusting the fringe parameters accordingly, all of this additional domain was given over to extend the maximum strength fringe region, whilst maintaining the same length of the transition region and hence the same size

of the region outside of the fringe influence.

Scalar contours for two of these cases are given in figure 3.16. The additional fringe length was observed to significantly reduce the transmission of waves across the boundaries to negligible levels, with a large reduction in the reflected wave pattern observed also. By reducing the fringe strength slightly from $\sigma_c = 16$ to $\sigma_c = 12$, the reflections were weakened further, such that almost no additional wave pattern is visible in the domain. This confirms that additional fringe length can help dissipate internal waves more effectively than the tuned but size-limited fringes used previously, although here the area of the domain (and hence the number of grid points) was increased by over 50%, sacrificing a certain degree of computational efficiency.

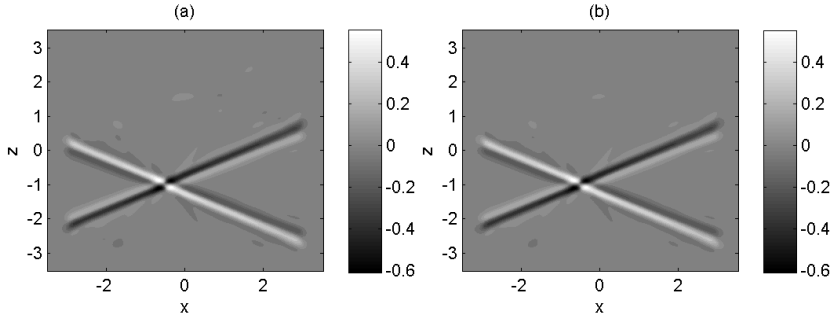

Figure 3.16: Contours of θ at $Nt = 72$ for domain enlarged "optimum" fringe with (a) $\sigma_c = 16$ and (b) $\sigma_c = 12$

Oddly, the most significant unexpected pattern in the domain were a quartet of additional waves propagating from the origin (with those on the right side of the origin more visible with a slightly jagged appearance). These waves are short lived within the domain and appear to not propagate all the way to the fringe region. Measurement of these waves showed that where the original waves were generated by a force oscillating with $\omega_f/N = 0.426$, the additional waves have a value of ϕ more characteristic of $\omega_f/N \approx 0.8$, around double the original waves and hence just under the frequency of the first harmonic.

A similar effect is observed in the Mowbray and Rarity (1967) for $\omega_f/N = 0.366$, with weaker waves at a more vertical inclination than the "original" wave pattern. Such waves are also faintly visible in previous test cases presented here (NF27-NF29 being notable examples). The authors of the paper attributed such additional waves to first harmonic induced motion and also demonstrated that for higher forcing frequencies with $\omega_f/N > 0.5$, the first harmonic is above the frequency where cross pattern waves are observed, so the additional pattern will not appear.

As these harmonic waves arise through mode coupling within the non linear,

convective terms of the Navier-Stokes equations, the velocity scales within the waves will rise approximately proportional to the square of the scales in the original wave. As such, it was found that reducing the forcing strength in the simulation by a factor of 10, and thus reducing the velocity of the original waves, reduced the harmonic wave pattern strength to a point where the density fluctuations they induced were below the visible contours of θ.

3.4 Evaluating domain sizing and re-gridding

3.4.1 The influence of regridding on energy levels

As discussed in section 2.3.5, it is possible to regrid the simulations to a lower resolution at the late time to save on computational cost per iteration and also allow for an increased Δt. This regridding is applied extensively for the simulations of chapter 5, where vortical structures are formed via a horizontal momentum injection into an initially quiescent domain with either neutral of stable background stratification. At early times, these simulations feature fields of small eddies formed through turbulent breakdown, buoyant instability or a combination of the two. At the late time, these structures tend to relaminarise to the point where grid resolution is more than sufficient to fully resolve the length scales in the flow field. The full details of these simulations are given in chapter 5, but two examples here are cases JSD1 and JSD2, which have neutrally and stably stratified initial domains respectively.

Figures 5.2-5.6 demonstrate that at the late time, the length scales of the smallest eddies in both cases have increased, with the drop in kinetic energy levels implying that the flow velocity within these eddies has decreased significantly, with both cases after 2250 iterations to take advantage of this. In order to check whether this was a suitable stage to regrid, the simulations were allowed to run for an additional 50 iterations at both the new, coarser resolution and the original fine resolution to determine whether the change in resolution had any significant impact on the simulation results. It would be expected that if significant kinetic energy and buoyancy variance is contained within small scale structures (the higher wavenumber modes in Fourier space), reducing the resolution by removing some of the higher modes would remove this energy from the domain. Even though the flow appears to have lost most of its fine scale structure for both cases (particularly for the stably stratified case) by 2250 iterations, the regrid removed just the highest 25% of the wavenumbers from each direction, reducing the total grid count to around 42% of the initial

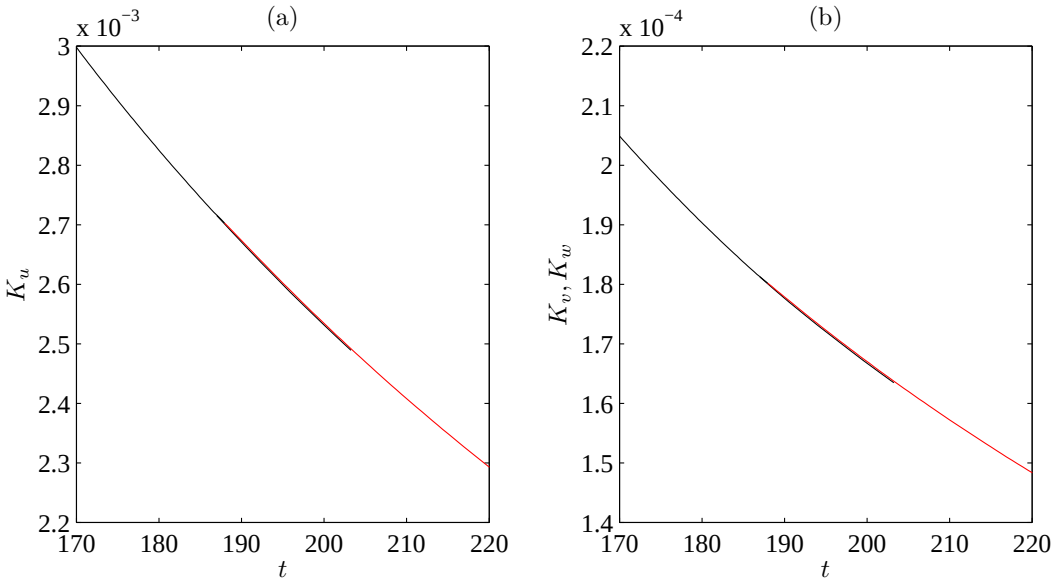

Figure 3.17: Time evolution of K_u (—), K_v, K_w (—) for case JSD1 from shortly before to shortly after regridding takes place at 2250 iterations. The × markers indicate the equivalent values from 2250 to 2300 iterations if the simulation continues at its original resolution.

value. Figure 3.17 demonstrates that for the case JSD1, the initial resolution used and the new resolution both gave equal streamwise and lateral/vertical kinetic energy levels after 2250 iterations. It can be inferred from this that the energy contained within the higher Fourier modes that were removed from the simulation during regridding was negligible.

3.4.2 The influence of domain sizing on late time structures

Also detailed in chapter 5 are the two domain sizes used for simulating impulsive momentum injection into a stably stratified fluid. Two domain sizes were used for these simulations with the JSD type simulations used to evaluate the early time flow features in a high level of detail without the extra computational cost associated with a large domain, while JLD type simulations feature a larger domain to provide sufficient room for the larger structures to develop without being unduly affected by domain boundary proximity. The initial grid spacing for these simulations is identical in all directions, and remains so until any regridding is applied. As an example, case JLD1 is essentially a direct repeat of case JSD2, but with the domain 67% larger in each direction.

The evolution of volume integrated kinetic energy and buoyancy variance components for the two cases are given in figure 3.18. It can be seen that

Case	Re	N	t_J	$Nt_J/2\pi$	L_x, L_y, L_z	n_x, n_y, n_z
JSD2	1400	0.2	5	0.16	$24\pi, 8\pi, 8\pi$	$768, 384, 384$
JLD1	1400	0.2	5	0.16	$40\pi, 13.3\pi, 13.3\pi$	$1280, 640, 640$

Table 3.3: Cases and flow parameters for selected simulations of chapter 5

there is no significant change in the flow behaviour between the two cases, an assertion further corroborated by visualising the vorticity field over time, showing the same injection, quasi-axisymmetry, collapse and planar dipole stages for both JSD2 and JLD1. However, in spite of the similarity, it can be seen that during the collapse phase shortly after $t \approx 50$, the larger domain case gives higher kinetic energy in the lateral and vertical directions, along with higher buoyancy variance. Given that the only change in parameters between the two cases is the domain size (and by extension, the size of the fringe regions), and the timing of the change in energy behaviour, it is reasonable to assume that the energy discrepancies arise as a result of differences between the internal wave characteristics of the two cases and the handling of the waves within the fringe regions.

As the fringe region is inherently an artificial condition when compared to the experimental studies of previous literature, differences between the energy levels in the fringes between the two cases are not as relevant as the energy levels within the evolving dipole structure itself. The volume integration of kinetic energy and buoyancy variance levels conducted by the code at every time step includes the whole domain including the fringe region and is calculated during a stage where the velocity field is stored in Fourier space. By extracting the velocity field in cartesian space at regular time steps, it is possible to isolate a volume within the domain for each case that does not include the fringe but does include the collapsing jet structure. Figure 3.19 shows the kinetic energy levels for both cases, evaluated at regular time intervals during the collapse phase, but limiting the integration to a volume defined as

$$-2.4\pi \leq x \leq +21.6\pi,$$

$$-3.6\pi \leq y \leq +3.6\pi,$$

$$-3.6\pi \leq z \leq +3.6\pi.$$

As in figure 3.18, there was no significant difference in the streamwise kinetic energy between cases with the fringe region removed from consideration. The lateral kinetic energy was also approximately equal throughout, suggesting the

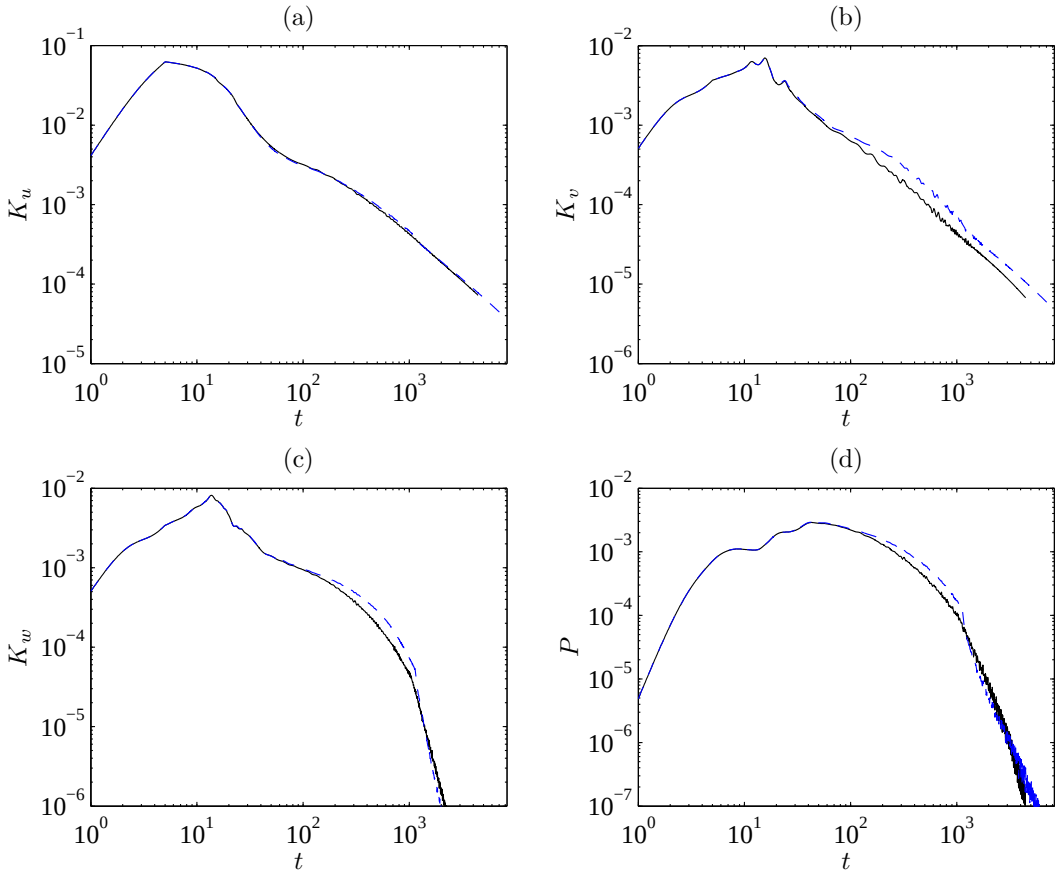

Figure 3.18: Time evolution of kinetic energy and buoyancy variance levels for smaller domain case, JSD2 (—) and larger domain equivalent, JLD1 (– –).

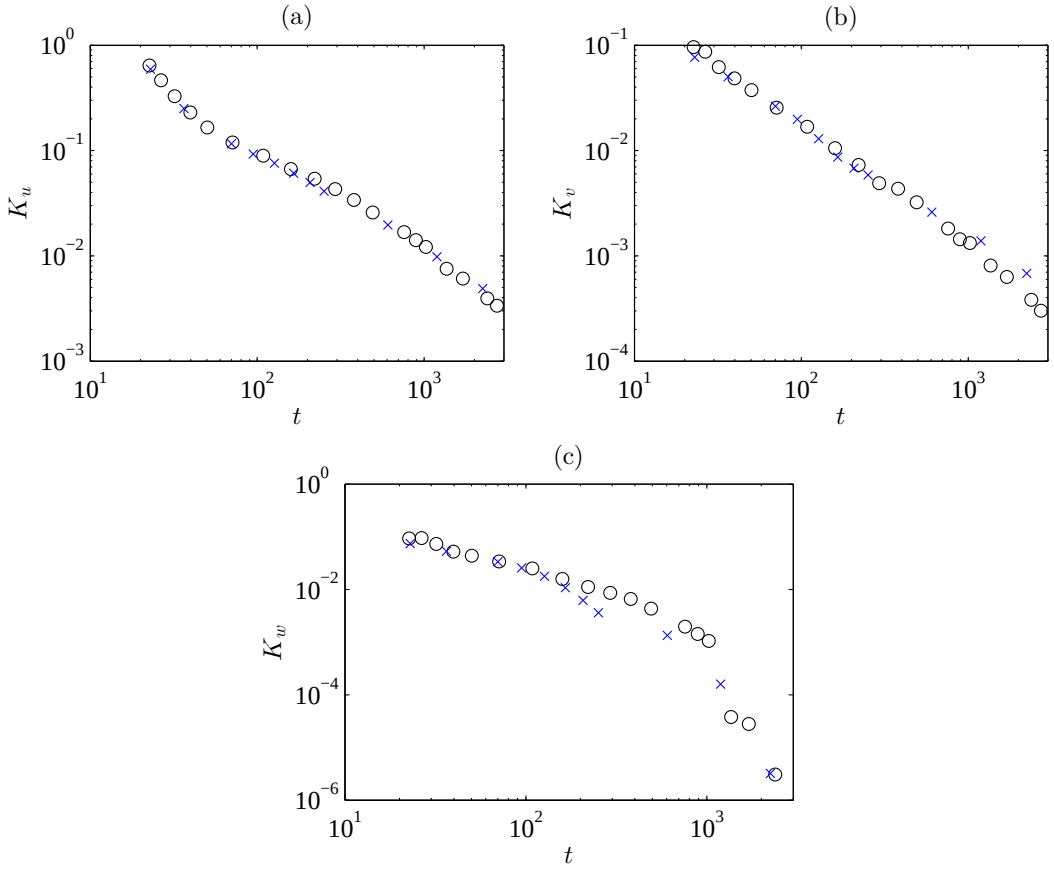

Figure 3.19: Time evolution of kinetic energy levels for inner domain volume for smaller domain case, JSD2 (○) and larger domain equivalent, JLD1 (×).

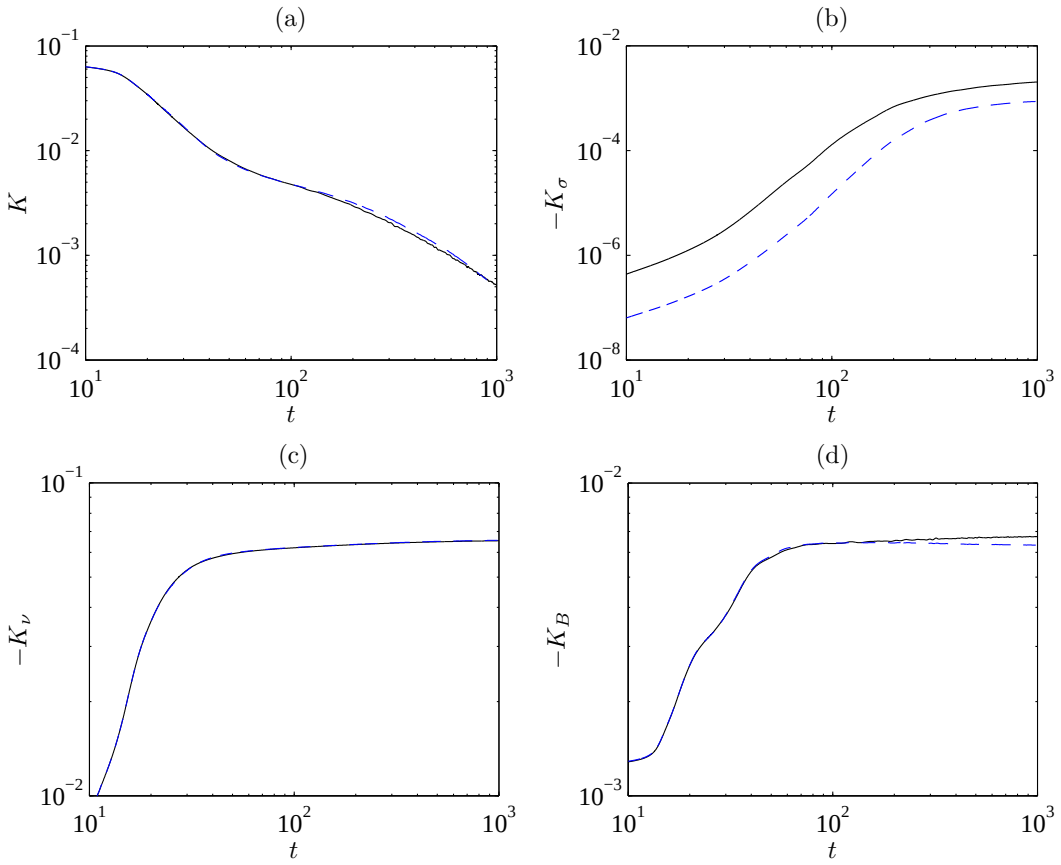

Figure 3.20: Time evolution of (a) total kinetic energy level along with the energy level lost/transferred due to (b) fringe region dissipation, (c) viscous dissipation and (d) buoyancy flux for smaller domain case, JSD2 (—) and larger domain equivalent, JLD1 (– –).

additional energy seen in 3.18(b) was contained either in internal waves propagating away from the inner domain or within the fringe region. Interestingly, the vertical kinetic energy for the larger domain case was is within the inner domain during the collapse phase than for the full domain volume integration. In order to better understand why this is so, the three mechanisms for kinetic energy flux in the domain are considered individually, namely: viscous dissipation, transfer to the scalar field through buoyancy flux and artificial dissipation in the fringe. The time history of kinetic energy lost to these mechanisms is given in figure 3.20, with

$$K_\nu = \int_0^t K'_\nu \mathrm{d}t, \tag{3.3}$$

$$K_B = \int_0^t K'_B \mathrm{d}t, \tag{3.4}$$

$$K_\sigma = \int_0^t K'_\sigma \mathrm{d}t. \tag{3.5}$$

The first significant difference observed from these energy histories is that the energy extracted by the fringe is somewhat higher for the smaller domain

case. However, the difference appears most pronounced prior to the collapse phase, becoming smaller as the two simulations progress. Prior to the collapse phase, the extra energy extracted by the fringe in the smaller domain case is almost certainly due to the closer proximity of the fringe to the quasi-axisymmetric jet structure. The increased rate of energy lost to the fringe for the larger domain case during the collapse phase can be attributed to the proportionately larger fringe region. As was demonstrated in section 3.3.2, even a modest increase in fringe size can markedly increase the amount of energy extracted from internal waves at the domain boundaries, and similar behaviour would explain the fringe energy extraction for the cases considered here. It should be noted that after the conclusion of the collapse phase, the vertical kinetic energy for the two cases converges to similar levels, as both have now almost completely dissipated the internal waves and removed their energy from the domain.

Further evidence of the fringe proving more effective for the larger domain cases can be garnered from the history of kinetic energy transferred to the scalar field. After the start of the collapse phase at around $t \approx 50$, the rate at which energy is transferred to the buoyancy field sharply reduces. For the larger domain case, the flow of energy plateaus, but for the smaller domain case the level continues to rise slowly. This is consistent with the higher value of K_w seen in figure 3.19(c), suggesting that internal waves are able to pass through the fringe regions, re-enter the domain and interact with the collapsing jet structure, allowing vertical motion within the structure to persist. This is corroborated again by the vorticity contours given in figure 3.21. The contours for the smaller domain case demonstrate vorticity patches surrounding the collapsing jet structure that appear to be a result of lingering internal wave motion, particularly those far ahead of the jet. Even at a significantly earlier time in the larger domain case, such patches are not evident, with only a few waves emanating from the collapsing structure visible. This data seems to suggest that the fringe used in the larger domain case is well suited to eliminating the influence of internal waves on the late time flow.

With the early time and collapse phase differences between the two cases having been considered, the final comparison carried out was to evaluate what effect the relative proximity of the domain boundaries has on the evolution of the vortex dipole at the late time. Neglecting the effect of the fringe for the moment, the use of periodic boundaries in all directions essentially means that instead of a single vortical structure propagating through the domain, the simulation gives us an infinite, periodic three dimensional array of structures

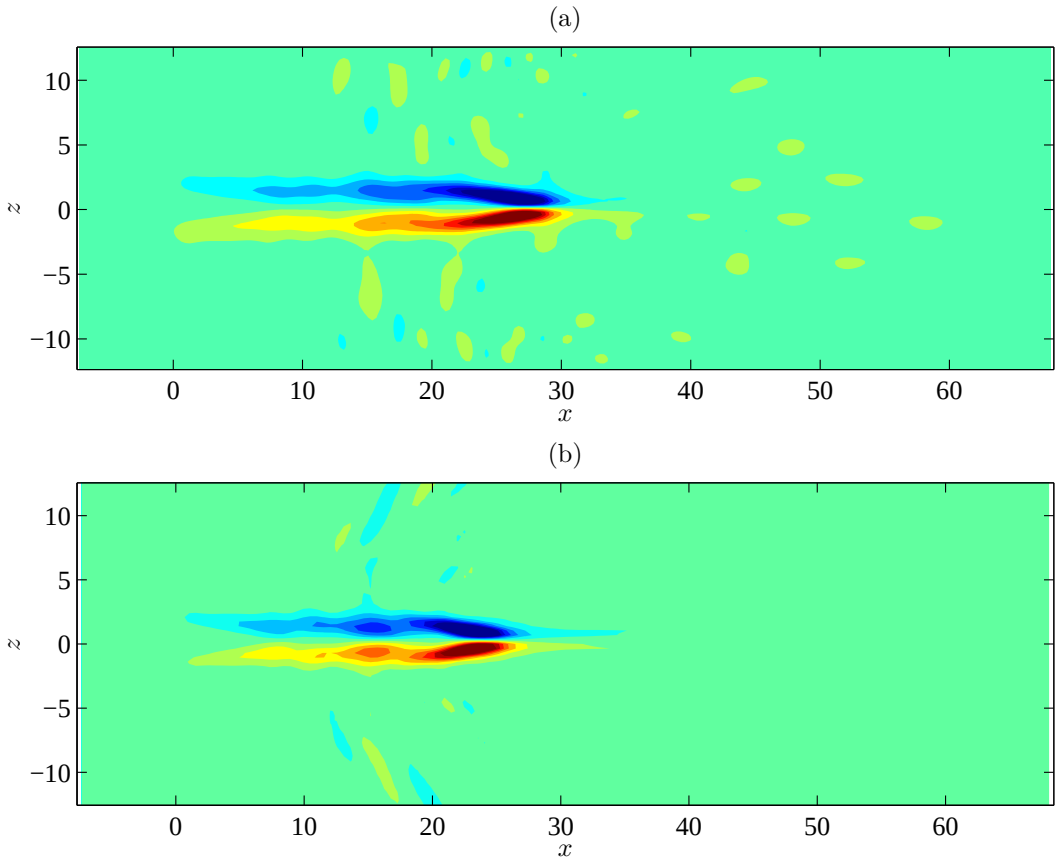

Figure 3.21: Contours of ω_y at $y = 0$ for (a) case JSD2 at $t = 380$ and (b) case JLD1 at $t = 251$. The contour levels at each time range between $\pm 0.6|\omega_y|_{\text{Max}}$, where $|\omega_y|_{\text{Max}}$ is the instantaneous, absolute maximum of lateral vorticity at $y = 0$. Note the additional vorticity patches in (a) suggesting lingering internal waves not seen in (b) even at the later time.

("image dipoles") each physically identical to the original dipole, with their geometric centres each separated by L_x, L_y, L_z in the respective directions. The induced velocity from the image dipoles acts to slow the original dipole as it propagates in the streamwise direction, an effect that becomes markedly more pronounced as the dipole expands laterally and vertically at the late time.

Archer et al. (2008) considered such a problem for the simulation of a propagating vortex ring within a periodic domain and was able to quantify the induced streamwise velocity deficit based on the ring radius and circulation as well as the periodic separation distance between the ring and its images. Such an evaluation is more difficult here, partly due to the more irregular shape of the stratified vortex dipole compared to a toroidal vortex ring, but more due to presence of the unphysical influence of the fringe region. Like the presence of neighbouring image dipoles, the fringe will act to slow the propogation speed of the original dipole, the exact impact of which is difficult to quantify analytically.

In order to estimate at what point in a simulation the boundary effects begin to significantly impact the development of the late time dipole, we track both the dipole's propagation in the streamwise direction and its lateral growth over time for both cases. The precise criteria for determining the values of the dipole's streawmise centre, X_D and diameter, D_D are not always well defined or necessarily consistent in relevant literature, so here we evaluate the two using a similar enstrophy weighted method to the numerical study of Rojanaratanangkule et al. (2012) i.e.

$$X_D = \frac{1}{\Omega}\int_V x|\omega|^2 \mathrm{d}V, \tag{3.6}$$

$$D_D = \frac{2}{\Omega}\int_V |y||\omega|^2 \mathrm{d}V, \tag{3.7}$$

$$\Omega = \int_V |\omega|^2 \mathrm{d}V. \tag{3.8}$$

Equation 3.7 can still be applied due to the apparent symmetry of the dipole about the lateral midplane. For dipoles that deviate from this symmetry, $|y|$ can be replaced with $|y - Y_D|$, where Y_D is the lateral coordinate of the dipole centre.

The time history of dipole position and diameter for both JSD2 and JLD1 are given in figure 3.22. The two cases give approximately equal values of X_D and D_D until $t \approx 6000$ implying that, up until this point, the boundary effects in both cases on propagation speed and lateral growth can be neglected. After this, while the lateral growth rate apparently remained consistent, the dipole

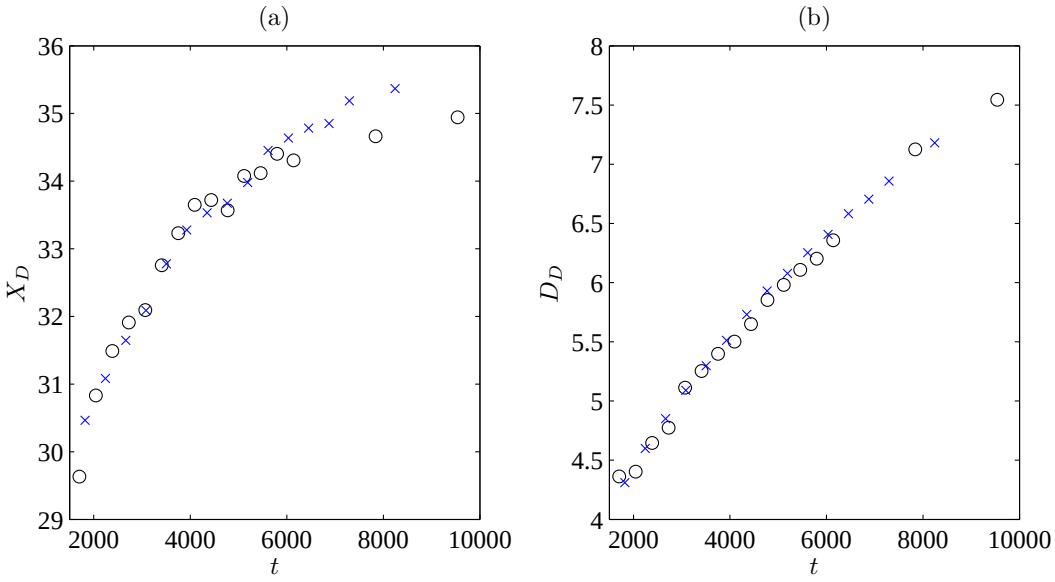

Figure 3.22: Time history of (a) dipole streamwise centre, X_D and (b) diameter, D_D. Circle markers (○) indicate the smaller domain case, JSD2, with cross markers (×) indicating the larger domain case, JLD1.

in JSD2 begins to slow more rapidly than that in JLD1, indicating that the closer boundaries and fringe region had now impacted significantly on the late time dipole. At this time, the two dipoles each have a diameter of around 6.5, approximately 26% of the domain width, L_y. Given that the larger domain cases are two thirds larger in each direction than the smaller domain cases, we can infer that when the dipole diameter in the larger cases reaches the same percentage, the results thereafter may be regarded with suspicion, but are reliable until then. Thus the results for the larger domain cases exclude boundary effects from consideration until $D_D \approx 10.8$.

3.5 Chapter summary

This chapter has documented the validation and testing of the simulation code used for the research described in this thesis. The code is able to generate starting jet structures akin to those reported by Gharib et al. (1998) for a momentum injection into a quiescent domain, and also replicate the internal wave patterns observed by Lighthill (1978) for an oscillating body within a stably stratified fluid. The combination of these two validation studies, allied to the validation work conducted for the earlier iteration of this code by Redford et al. (2015) demonstrate that the Naiver-Stokes equations, including the terms for buoyancy required by the Boussinesq approximation, are applied correctly in this code and provide a good representation of experimentally generated

flows.

Additionally, the fringe method used to dissipate internal waves in buoyancy driven flows at the domain boundaries has been tested and optimised, and the effects of domain boundary proximity and grid resolution have also been accounted for. All of this gives confidence to the results of simulations presented in the following chapters.

Chapter 4

Evolution of a horizontally propagating vortex ring in neutrally/stably stratified fluid

4.1 Simulation set up and study parameters

The first main body of numerical work for this research involves the simulation of a horizontally propagating vortex ring in stably stratified fluid with a linear density profile in the vertical direction. The primary objective of this set of simulations was to gain a more quantitative measure of how parameters such as Reynolds number and stratification strength affect the collapse process, as well as gaining more insight into the physical mechanisms of the collapse process itself. There exists a significant literature base of comparable experimental work looking into the buoyant collapse of an isolated ring (Johari and Fang, 1997; Scase and Dalziel, 2006), but there appears to be little or no analogous literature detailing any numerical studies. In the experimental works, the vortex rings are generated via a horizontal fluid injection into a stably stratified domain through a round orifice, with the duration of the injection kept sufficiently small such that all circulation added to the domain is entrained into the forming ring once the injection has ceased (i.e. $T_J < T_\Gamma$) as noted by Gharib et al. (1998). The benefit of this numerical approach is to allow access to the energetics and buoyancy scalar fields within the vortex ring as it evolves in a stratified domain, with such information extremely difficult to attain experimentally. As a result, no comparison between the energy levels observed in the simulations of this chapter and previous experimental literature is made here.

For this numerical study, the vortex rings were not created through the

use of a momentum injection but were instead created by imposing a suitable vorticity field on the domain as an initial condition and allowing it to evolve over time. The initial vorticity field defines a ring with initial core circulation, Γ_{R0}, and a Gaussian distribution of azimuthal vorticity, ω_θ, within the core, with mean ring radius, R_{R0}, and core radius, δ_{R0}. This is much the same definition used to generate a vortex ring in the numerical work of Archer et al. (2008) with

$$\omega_\theta = \frac{\Gamma_{R0}}{\pi {\delta_{R0}}^2} \exp(-s^2/{\delta_{R0}}^2). \tag{4.1}$$

The distance from the centre of the vortex ring core, s, is calculated by

$$s = \sqrt{x^2 + (r - R^*_{R0})^2}, \tag{4.2}$$

where $r = \sqrt{y^2 + z^2}$ and R^*_{R0} is the initial ring radius subject to an applied perturbation. A perturbation to the otherwise uniform ring radius is introduced here in order to help accelerate the turbulent transition of the ring at sufficiently high Reynolds number. The perturbation is sinusoidal in nature and thus R^*_{R0} can be defined as

$$R^*_{R0} = R_{R0} + \epsilon \sin(n_\epsilon \psi_R), \tag{4.3}$$

where ϵ is the magnitude of the perturbation, n_ϵ is the wavenumber of the perturbation and $\psi_R = \tan^{-1}(z/y)$. The azimuthal vorticity, ω_θ can be converted to Cartesian equivalents by

$$\omega_y = \omega_\theta \sin(\psi_R); \tag{4.4}$$

$$\omega_z = -\omega_\theta \cos(\psi_R). \tag{4.5}$$

All of this provides for a ring which should initially propagate directly along the x-axis in the positive direction (assuming Γ_{R0} is positive). For the purposes of these simulations, Γ_{R0} is set to 1 such that the circulation based Reynolds number, Re_Γ, is simply equal to Re. The mean ring radius is set to 0.5 to give a unit diameter, with a core radius of 0.2 to give $\delta_{R0}/R_{R0} = 0.4$, a similar value to simulations A1 and A2 from Archer et al. (2008).

For the perturbation about the ring circumference, the magnitude, ϵ, was chosen to be $R_{R0}/50$ and n_ϵ was chosen to be 7. This choice of perturbation wavenumber gives the ring a very slight heptagonal appearance, and was decided upon based on the work of Dazin et al. (2005, 2006). In those experimental studies of vortex ring transition from a laminar to turbulent state, it was found the transition took place in two phases. In the first phase, naturally occurring deformation of the vortex rings occurred as linear instabilities,

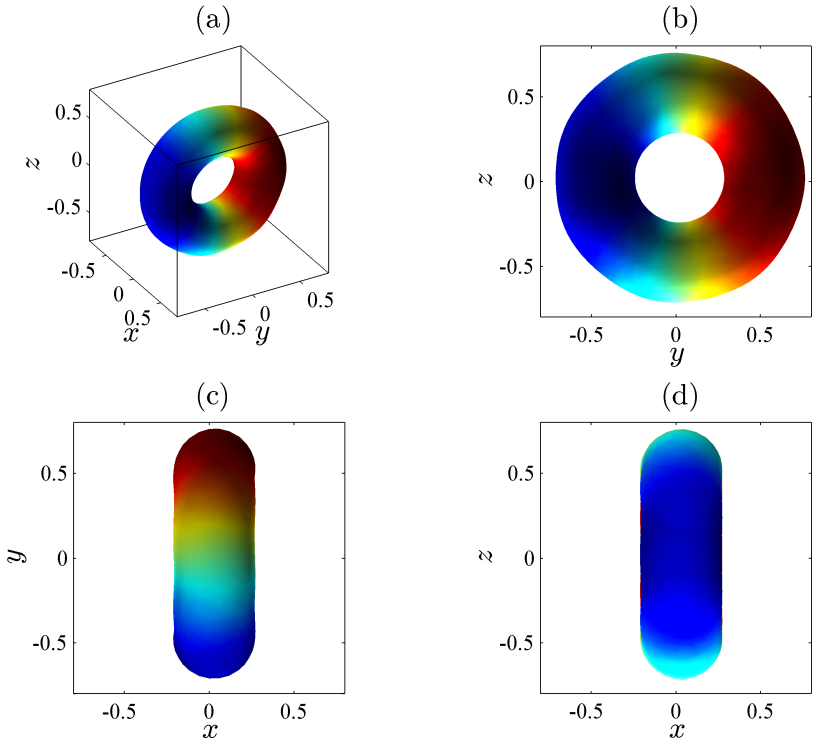

Figure 4.1: Isosurfaces of constant vorticity magnitude, $|\omega|$, for perturbed vortex ring cases at $t = 0$ with views looking from (a) positive x, negative y, positive z to negative x, positive y, negative z, (b) positive x to negative x, (c) positive z to negative z (d) negative y to positive y. Colour contouring ranges between $\pm 0.6|\omega_z|_{\text{Max}}$, with isosurface threshold set at $0.25|\omega|_{\text{Max}}$.

developing as a waveform about the ring circumference. It was found that the most pronounced instabilities occurred within a band of unstable modes with wavenumbers from 7 to 10. It follows from this that the turbulent transition of a vortex ring initially defined in a laminar state can be accelerated by perturbing its radius to create such a waveform. The initial vortex ring for these cases is presented through isosurface visualisations in figure 4.1.

To determine the influence of initial Reynolds and Froude numbers on the collapse process, a baseline case with high Reynolds and low Froude number (with values comparable to those tested in the experimental literature) was simulated (case RSD2), along with further cases with a range of inital Reynolds and Froude numbers as documented in table 4.1. Additionally a single case with the same non-dimensional parameters as the baseline stably stratified case, but without a radial perturbation applied to the ring, allowing the effects of the perturbation on the collapse process to be better understood (case RSD3). As mentioned previously, the initial Reynolds number of the

Case	Re	Fr	Notes
RSD1	5000	∞	Neutrally stratified baseline
RSD2	5000	1.0	Stably stratified baseline
RSD3	5000	1.0	As RSD2 but no perturbation
RSD4	3000	1.0	Testing initial Re sensitivity
RSD5	1000	1.0	Testing initial Re sensitivity
RSD6	5000	5.0	Testing initial Fr sensitivity
RSD7	5000	10.0	Testing initial Fr sensitivity
RSD8	5000	2.0	Testing initial Fr sensitivity
RSD9	5000	0.5	Testing initial Fr sensitivity
RSD10	5000	0.2	Testing initial Fr sensitivity

Table 4.1: Cases and flow parameters

cases based on the unit ring circulation can be given as

$$Re_\Gamma = \frac{\Gamma}{\nu} = \frac{1}{\nu} = Re, \tag{4.6}$$

and the initial Froude number based on unit ring circulation and unit diameter is given by

$$Fr = \frac{\Gamma}{2NR_{R0}} = \frac{1}{N}. \tag{4.7}$$

All cases were run on a computation grid with $(L_x, L_y, L_z) = (4.5\pi, 3\pi, 3\pi)$ and $(n_x, n_y, n_z) = (512, 512, 512)$. This grid was confirmed through energy budget analysis to suitably resolve the flow field at the highest Reynolds number used. Grid resolution was kept constant throughout the duration of each simulation, as the simulations run here were not run long enough to yield significant savings in computational cost by reducing resolution at the late time.

4.2 Results and analysis

4.2.1 Vortex ring evolution in neutrally stratified domain

The first simulation conducted for this study, case RSD1, initially places a vortex ring in a neutrally stratified domain ($N = 0, Fr = \infty$). As time elapses, the ring propagates along the x axis, undergoing a readjustment phase in the early time steps as the ring detrains some of its circulation in the negative x direction, with the apparent core radius becoming smaller and the ring profile no longer Gaussian as was initially defined by equation 4.1. This readjustment had been previously documented by Archer et al. (2008) and other works cited

therein. Figure 4.2 gives isosurfaces representing the ring as it propagates and changes in appearance over time. At the early times, the ring maintains a smooth, toroidal appearance before adopting a more heptagonal shape beyond $t \approx 5$. Such an appearance is to be expected given the perturbation wavenumber of 7 chosen for these simulations, with this change in shape to a stationary waveform leading to the development of an azimuthal instability. This instability results in the manifestation of smaller scale structure within the core itself, as well as the generation of "halo vorticity", looping structures that surround the inner vortex core (visible at $t = 21.51$ in figure 4.2). After a period of continued breakdown to smaller scale, turbulent structure, the ring begins to relaminarise as the smaller scale structures diffuse under the influence of viscosity, with the ring eventually returning to a smooth appearance (though notably deformed from its initial toroidal state).

These stages of vortex ring evolution can also be illustrated via the time history of the volume integrated kinetic energy components as detailed in figure 4.3, with the energy levels calculated by

$$\begin{aligned} K &= K_u + K_v + K_w, \\ K_u &= \frac{1}{2}\int_V u^2 \mathrm{d}V \end{aligned} \tag{4.8}$$

etc.

The initial ring adjustment phase occurs approximately during the period up to $t \approx 3$, with kinetic energy quickly transferred from the lateral and vertical directions to the streamwise direction and back again as vorticity is redistributed within the vortex ring core. Thereafter, during the laminar phase ($t < 15$), the kinetic energy in each direction appears to reduce steadily due to viscous diffusion. As the ring begins to breakdown to small scale structure, the rate of energy loss due to diffusion increases, with the smaller scale, low energy containing structures more susceptible to the influence of the viscous term in the Navier-Stokes equations than the larger, high energy structures seen up to the point of breakdown. The start of the relaminarisation appears to be characterised by another back and forth exchange of kinetic energy from the streamwise to lateral and vertical directions ($t \approx 30$), followed by a subsequent resumption in energy decay for all directions, though the rate of decay is slower than noted during the turbulent phase as the energy within the ring is now once again primarily contained in larger scale structures. Although the initial ring is not perfectly axisymmetric about the x axis, the lateral and vertical kinetic energy levels remain largely similar throughout and are nearly identical at the early time, suggesting the perturbation applied was not so excessive

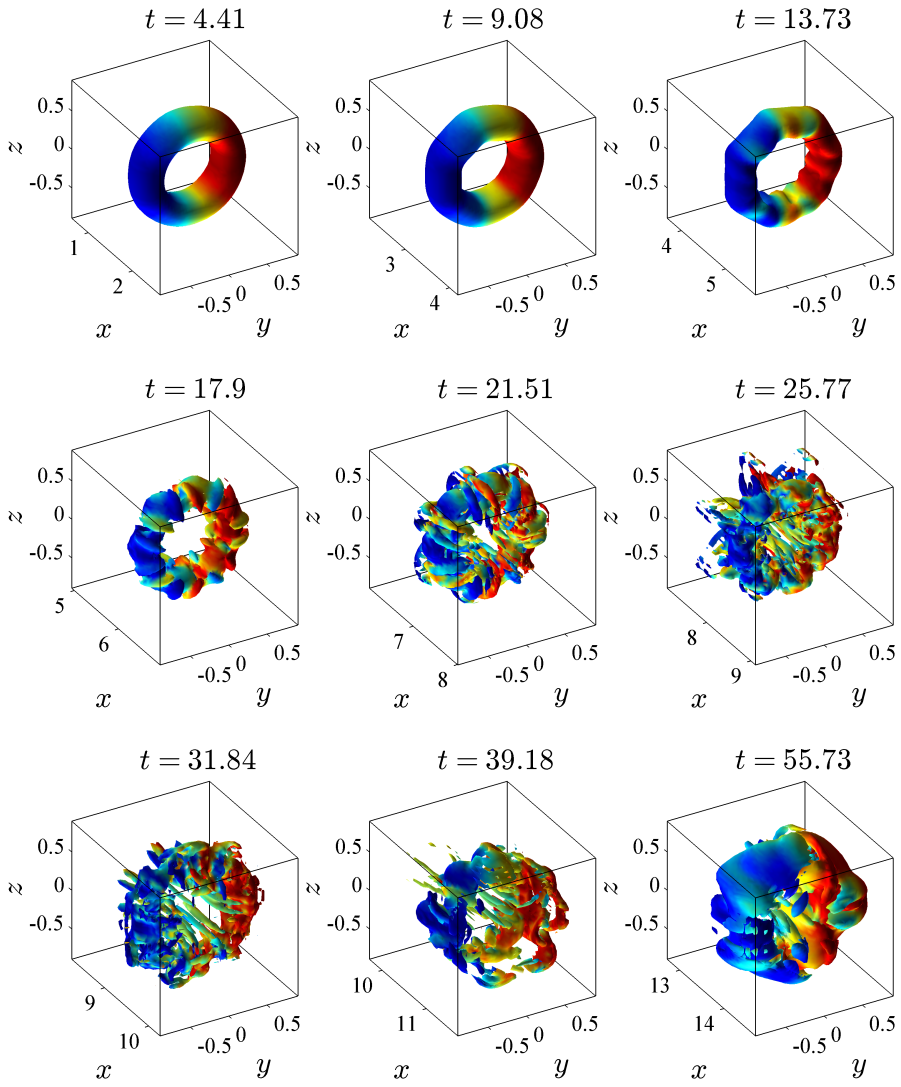

Figure 4.2: Isosurfaces of constant vorticity magnitude, $|\omega|$ for case RSD1 (Re = 5000, Fr = ∞) at various times from the early laminar stage, through turbulent breakdown and finally relaminarisation. Viewing angle is identical to figure 4.1(a). Colour contouring ranges between $\pm 0.6|\omega_z|_{\mathrm{Max}}$, with isosurface threshold set at $0.25|\omega|_{\mathrm{Max}}$.

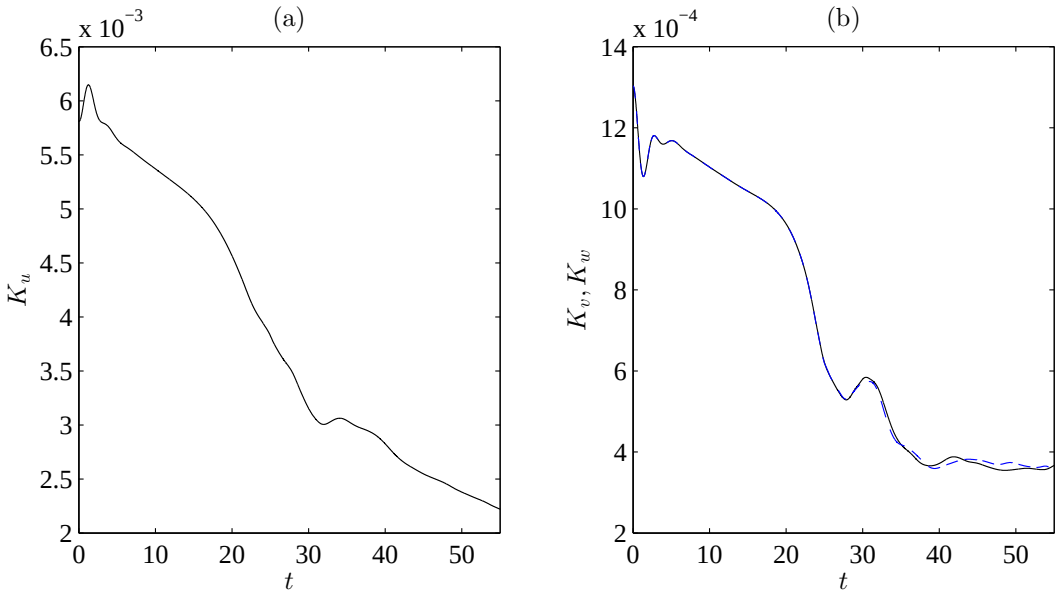

Figure 4.3: Time history of volume integrated kinetic energy levels for case RSD1 ($Re = 5000$, $Fr = \infty$) with (a) streamwise kinetic energy, K_u, (b) lateral kinetic energy, K_v (—), vertical kinetic energy, K_w (– –).

that the initial condition was unrepresentative of a toroidal vortex ring.

4.2.2 Vortex ring evolution in stably stratified domain

The evolution of a propagating vortex ring in neutrally stratified fluid has previously been studied extensively in both experiment and numerical simulation by previous authors and so is not examined in great detail here. Of more relevance to this study is identifying how the same vortex ring evolves in a stably stratified fluid and identifying the differences in the flow that said stratification creates. Case RSD2 defines an identical initial ring to case RSD1, but now with unit initial Froude number. Figures 4.4 and 4.5 illustrate the early time evolution of the ring through a series of vorticity contours, showing both the lateral vorticity at the lateral midplane ($y = 0$) and the vertical vorticity at the vertical midplane ($z = 0$). All the contours are given on identically scaled and positioned axes for clarity. Like the neutrally stratified case, the ring undergoes an initial adjustment from the initial Gaussian core distribution of vorticity.

Whereas the neutrally stratified case showed the vortex ring to maintain approximate axisymmetry (initial perturbation aside) up until $t \approx 10$, the stably stratified case shows the vortex ring to deviate from the axisymmetric state much more quickly. Indeed, comparing the lateral and vertical vorticity contours demonstrates axisymmetry has been clearly lost by $t \approx 4$. Thereafter, fig-

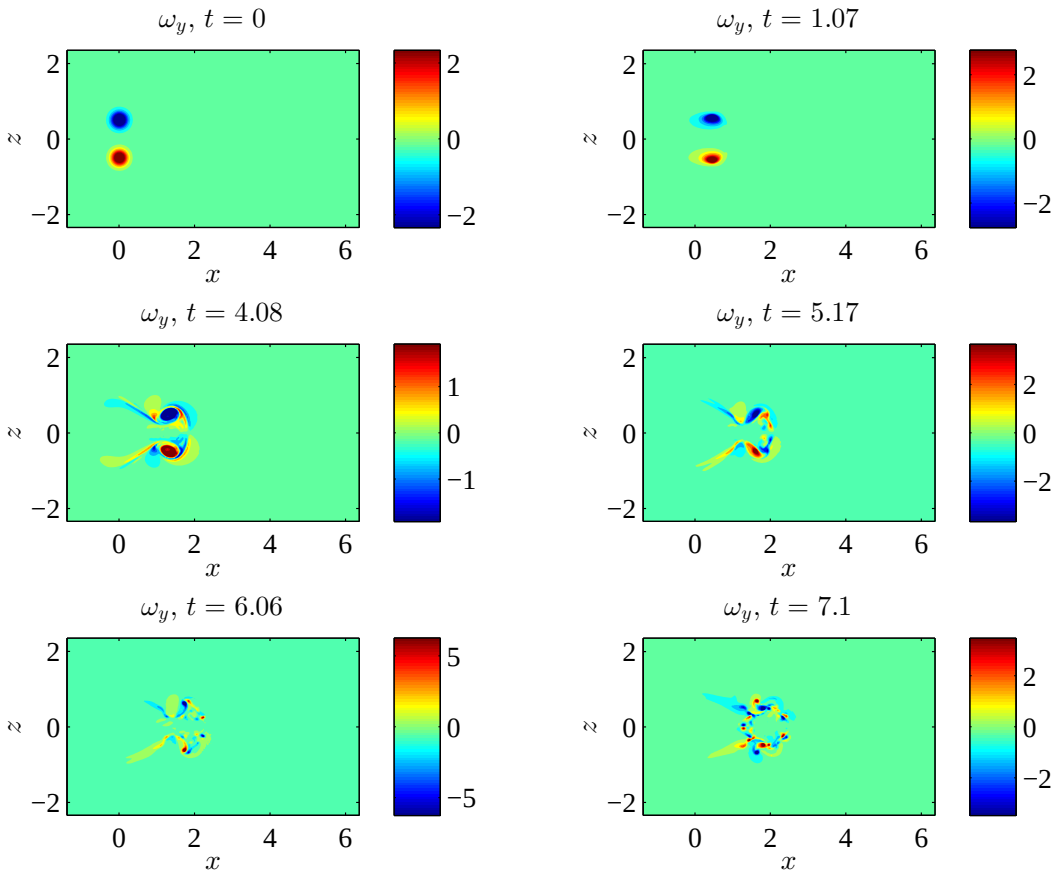

Figure 4.4: Contours of lateral vorticity, ω_y at $y = 0$ for case RSD2 ($Re = 5000$, $Fr = 1$) for various times from initial condition to early stages of buoyant collapse. Colour contouring ranges between $\pm 0.6|\omega_y|_{\text{Max}}$.

ure 4.4 shows the rapid change from the coherent vorticity minima/maxima in the ring's lateral cross section to a front of smaller eddies, while also appearing to detrain some vorticity behind this front, forming a v-shaped tail extending in the vertical direction. The coherence of the vorticity minima/maxima appears to persist longer in the vertical direction as shown in figure 4.5, though vorticity within the cores is still detained, in this instance forming a tail consisting of two adjacent stripes of counter-rotating vorticity, indicating a streamwise acceleration of fluid in the direction of travel of the initial vortex ring. By $t \approx 7$, the vertical vorticity contours also show production of smaller eddies in a similar manner to the lateral vorticity contours.

Figure 4.6 shows the evolution of the vorticity profile across the ring in the lateral and vertical direction at the very early time, prior to the ring losing its apparent axisymmetry. The initially Gaussian distribution of vorticity in the ring as prescribed by the initial solution appears to persist until ≈ 1, though after this the peak lateral vorticity, ω_y, appears to increase, reaching up to 150% its original value. This result is somewhat unexpected as it was

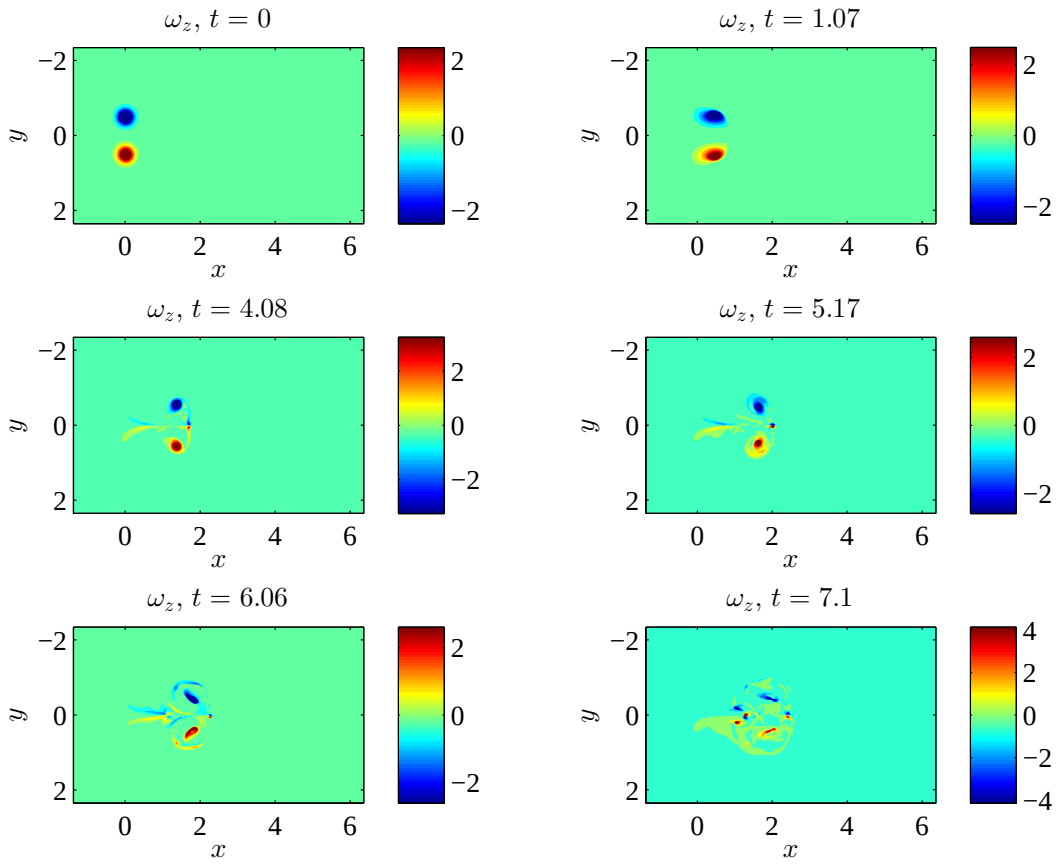

Figure 4.5: Contours of vertical vorticity, ω_z at $z = 0$ for case RSD2 ($Re = 5000$, $Fr = 1$) for various times from initial condition to early stages of buoyant collapse. Colour contouring ranges between $\pm 0.6|\omega_z|_{\text{Max}}$.

anticipated that Baroclinic torque would act to slow the rotation of the vortex ring in the lateral direction. As an example, the lateral views of the ring in figure 4.4 show an upper core of negative sign vorticity (flow rotating anti-clockwise relative to the lateral view). Fluid forward in x of the core centre has a positive z component of velocity, with the fluid behind the core centre having a negative component of vorticity. Recalling the governing equations 2.9 and 2.10,

$$\frac{\partial u_i}{\partial t} + u_j \frac{\partial u_i}{\partial x_j} = -\frac{\partial p}{\partial x_i} + \frac{1}{Re_{\mathrm{Ref}}} \frac{\partial^2 u_i}{\partial x_j \partial x_j} - \theta \delta_{3i} + f_i,$$

$$\frac{\partial \theta}{\partial t} + \frac{\partial \theta u_i}{\partial x_i} = N^2_{\mathrm{Ref}} u_3 \delta_{3i} + \frac{1}{PrRe_{\mathrm{Ref}}} \frac{\partial^2 \theta}{\partial x_i \partial x_i},$$

it may be expected that the initial vertical velocity of the fluid would result in a locally non-zero value of θ, with a positive vertical velocity locally inducing a positive θ, which in turn contributes a negative accelerative term to the momentum equation, acting to suppress the positive velocity, and a locally negative velocity inducing the same effects in the reverse direction. In the case of the upper core in the lateral views of 4.4, this would imply a positive value of θ ahead of the core and a negative value behind, creating a clockwise torque to suppress the anti-clockwise rotation. The evolution of the ω_z profile across the ring appears more intuitive, with a slight reduction of the initial peak vorticity magnitude in the positive and negatively signed cores. Also visible for $t > 2$ are two smaller peaks between the main cores, which may well be an early signature of the tail between the cores seen in figure 4.5, formed from the detrainment of vorticity from the main cores.

Returning to the question of why the peak lateral vorticity in the ring increases after the initial solution, the value of θ at the lateral midplane is given in figure 4.7. Between $t \approx 1$ and $t \approx 2$, it can be seen that the value of θ is not exclusively positive ahead of the upper core nor exclusively negative behind it. The transport of the buoyancy scalar due to the prevailing circulation appears to convect fluid with positive θ above the core in z initially, and then behind it in x resulting in a positive value of θ immediately adjacent to and behind the core centre, and similarly a negative value of θ ahead of the core centre. As a physical analogy, one may imagine that ahead of the core, denser fluid particles are displaced upward and rearward initially by the vortex, but are then pulled down behind it sufficiently quickly that before buoyant forces are sufficient to dominate the flow, the particles initially ahead of the ring now sit behind the ring in x, but still above their equilibrium plane in z. These

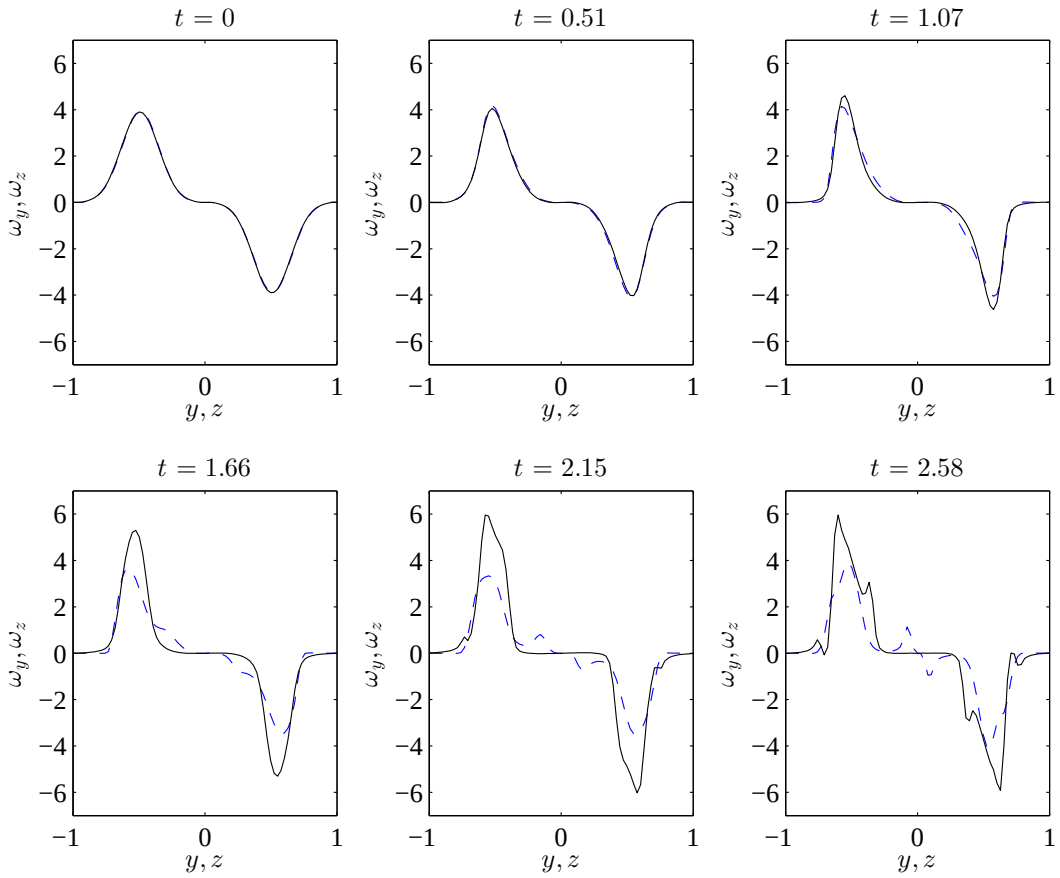

Figure 4.6: Vorticity profiles across the vortex ring of case RSD2 ($Re = 5000$, $Fr = 1$) at various times prior to the onset of buoyant collapse. The solid black lines (—) show the variation of lateral vorticity, ω_y, with varying z, where the x, y coordinates are those of the point where $\omega_y = \omega_y|_{\text{Max}}$. The dashed blue lines (– –) show the variation of vertical vorticity, ω_z, with varying y, where the x, z coordinates are those of the point where $\omega_z = \omega_z|_{\text{Max}}$.

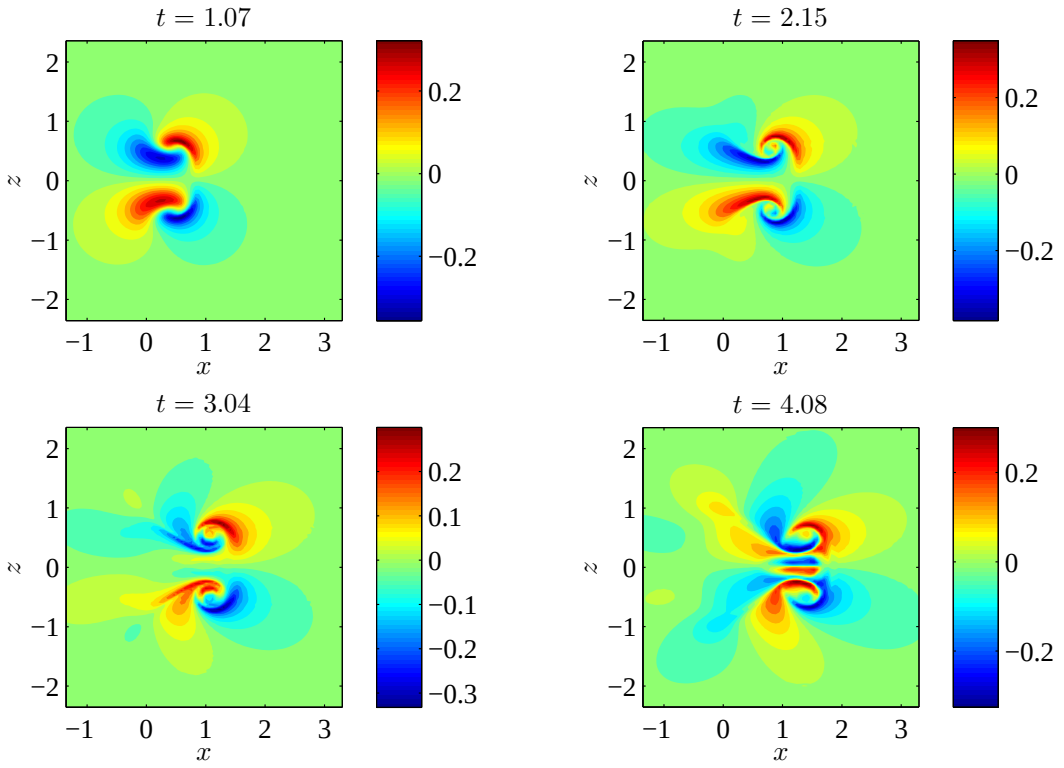

Figure 4.7: Contours of buoyancy scalar, θ, at $y = 0$ for case case RSD2 ($Re = 5000$, $Fr = 1$) at various times during and just after completion of a single buoyancy cycle.

particles, represented in 4.7 as areas of positive θ above the centre of the upper core in z and behind the core centre in x, will be subject to a downward acceleration. The reverse effect is seen for the the areas of negative θ below the upper core centre. The consequence of this is a local anti-clockwise torque which temporarily serves to increase the peak lateral vorticity in the core as seen in figure 4.6. Between $t \approx 2$ and $t \approx 4$, the extent to which the buoyancy scalar field is positive behind the upper core, and negative ahead of it, begins to reduce, which may explain why the peak lateral vorticity in the core does not rise beyond $t \approx 2.2$.

The effect of the background density gradient on the structure of the vortex ring is further represented in the isosurfaces of figure 4.8, showing (at the six consecutive time intervals shown here): 1. Initial solution; 2. The axisymmetric ring after initial core readjustment; 3. Vertical distortion of the ring with the increase in lateral vorticity seemingly manifesting as a thicker upper and lower core; 4.-6. detrainment of vorticity from the core into the surrounding fluid. The evolution of the ring from its initially axisymmetric state to the more complex structures seen in these isosurfaces is further described by the integrated kinetic energy and buoyancy variance levels within the ring pre-

sented in figure 4.9. The time measure used here is chosen not to be the raw solution time, t, but the number of buoyant cycles that have elapsed since the initial solution, with this buoyant time measure given as $Nt/2\pi$. As would be expected, the initial streamwise kinetic energy gradually reduces, with time, though the rate of decrease suddenly levels out somewhat at the conclusion of one buoyant cycle ($Nt/2\pi = 1$, $t \approx 6.28$). Immediately after this, the rate of energy decrease is notably more gradual. Buoyancy variance levels also rise initially, which can be inferred also from the spread of non-zero areas of θ across the domain as indicated by figure 4.7. Interestingly, the rise in buoyancy variance commences between zero and one-quarter buoyant cycles, plateaus for the next quarter of a buoyant cycle, then continues to rise before reaching a maximum at one buoyant cycle, coincident with the change in streamwise kinetic energy behaviour indicated previously. Thereafter, the buoyancy variance level beings to reduce, but as shown in figure 4.9, the proportion of the total energy in the domain provided by buoyancy variance plateaus, and until nearly 100 buoyant cycles into the simulation the internal energy from buoyancy variance makes up approximately 30% of the total energy in the domain i.e.

$$\frac{P}{K+P} = 0.3, \tag{4.9}$$

with no clear indication from either governing equations or experimental literature as to why this would be so. The lateral and vertical components of kinetic energy also show a surprising result, maintaining a similar order of magnitude until approximately 100 buoyant cycles, at which stage the vertical kinetic energy and buoyancy variance levels decrease rapidly. As buoyant forces were expected to suppress the vertical motion within the fluid and not (directly) suppress the streamwise or lateral velocity components, it is curious why the vertical kinetic energy persists for so long.

Once again considering the early time evolution of kinetic energy and buoyancy variance levels, it is useful to examine what proportion of energy is being lost to viscous dissipation, and what proportion is simply transferred between the velocity and scalar fields. Recalling the energy transport equations 2.13 and 2.14,

$$\frac{1}{2}\left(\frac{\partial(u_i^2)}{\partial t} + u_j\frac{\partial(u_i^2)}{\partial x_j}\right) = -u_3\theta\delta_{3i} + K'_\nu + u_i f_i,$$

$$\frac{1}{2N^2}\left(\frac{\partial(\theta^2)}{\partial t} + u_i\frac{\partial(\theta^2)}{\partial x_i}\right) = u_3\theta\delta_{3i} + P'_\nu,$$

the left hand sides of these equations give the absolute time derivative of kinetic energy, dK/dt and buoyancy variance, dP/dt. For kinetic energy, the

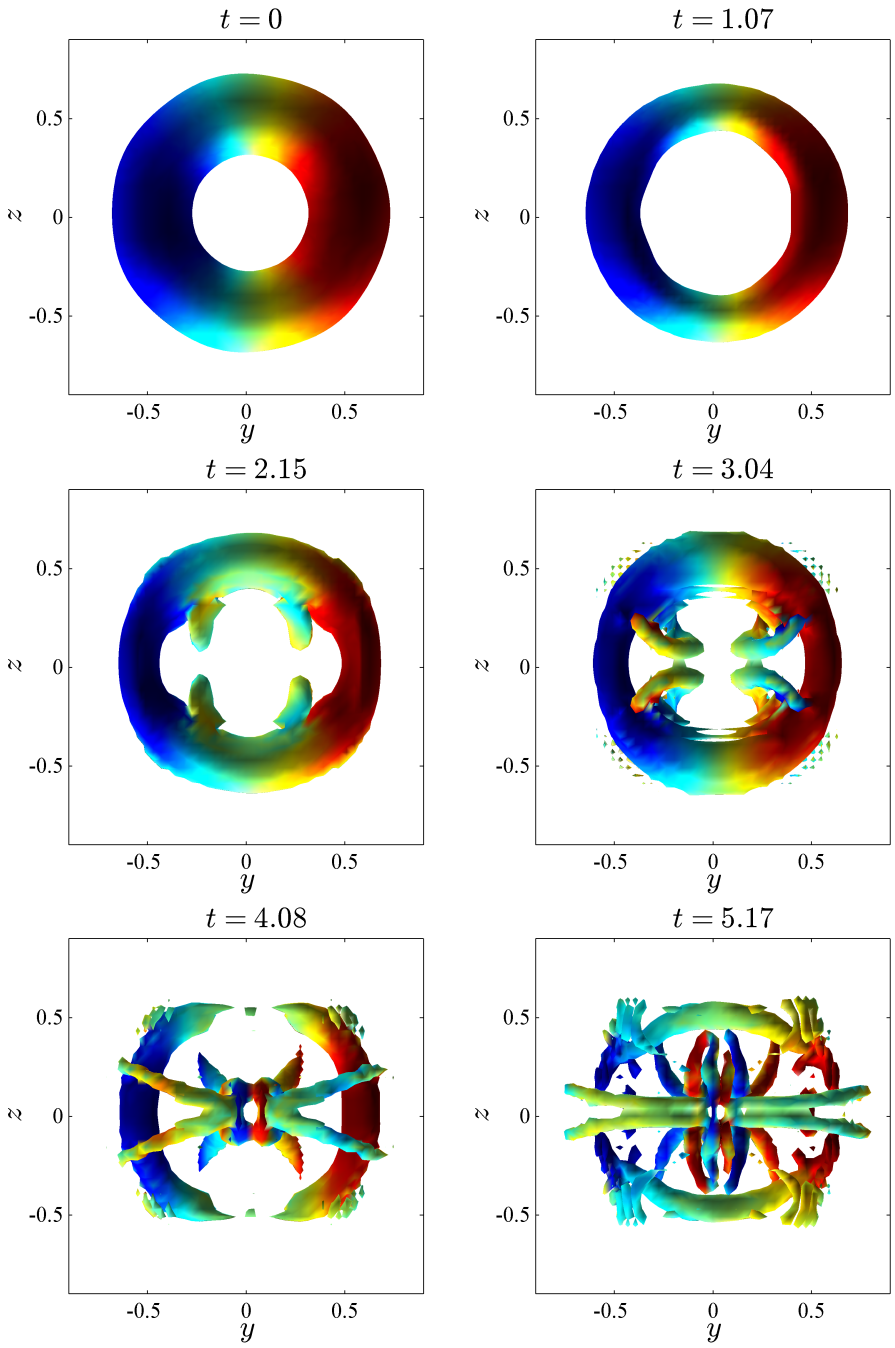

Figure 4.8: Isosurfaces of constant vorticity magnitude, $|\omega|$, for case RSD2 ($Re = 5000$, $Fr = 1$) at various times from the early laminar stage to the early stages of buoyant collapse. Viewing angle is from positive x to negative x. Colour contouring ranges between $\pm 0.6|\omega_z|_{\text{Max}}$, with isosurface threshold set at $0.25|\omega|_{\text{Max}}$.

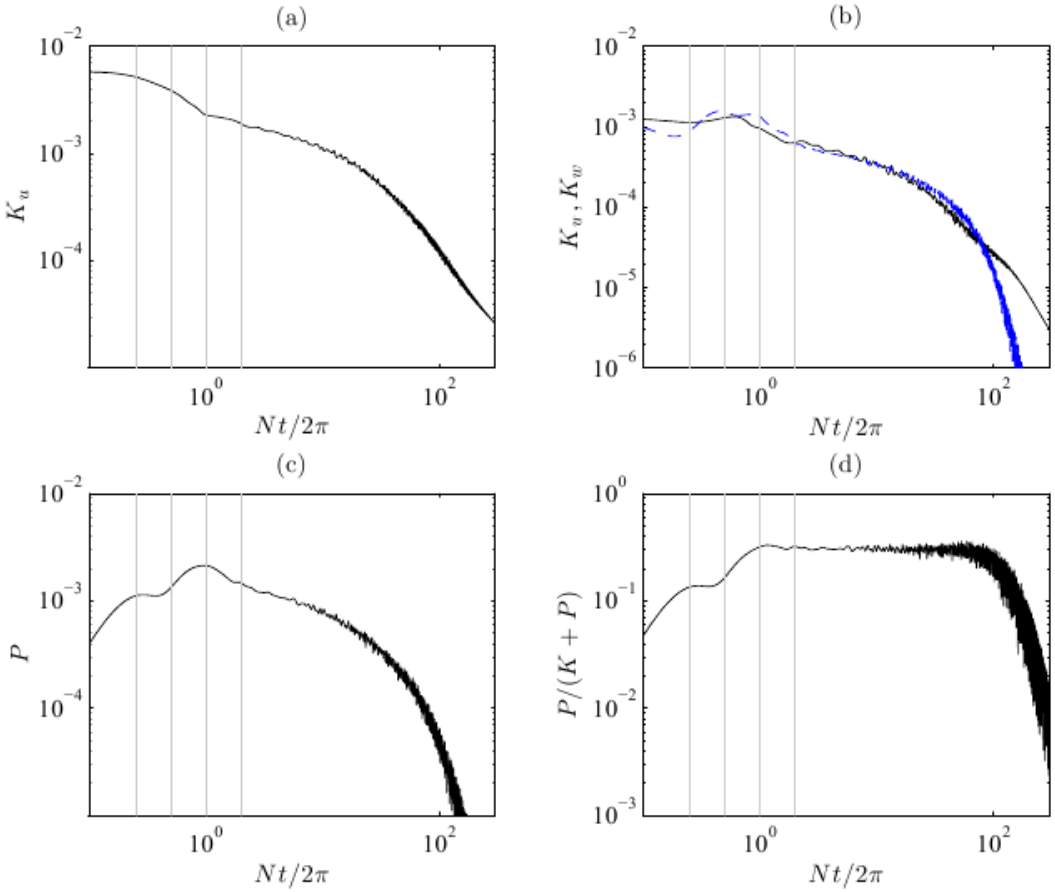

Figure 4.9: Time history of volume integrated kinetic energy and buoyancy variance levels for case RSD2 ($Re = 5000$, $Fr = 1$) with (a) streamwise kinetic energy, K_u, (b) lateral kinetic energy, K_v (—), vertical kinetic energy, K_w (−−), (c) buoyancy variance, P and (d) buoyancy variance expressed as a fraction of the total energy in the domain. The vertical lines (from left to right) indicate $Nt/2\pi = 0.25$, $Nt/2\pi = 0.5$, $Nt/2\pi = 1$, $Nt/2\pi = 2$.

external forcing term, $u_i f_i$ is zero for the simulations of this chapter as no impulse is added to the fluid after the initial solution. This leaves just the first term on the right hand side as the rate of transfer of kinetic energy to the scalar field, and the second term being viscous dissipation. Similarly, the rate of change of buoyancy variance is given by the summation of the kinetic to internal transfer term, and its own viscous/thermal dissipation term. The balance of these terms can be seen in figure 4.10. For the first two buoyant cycles, the rate of change of kinetic energy and buoyancy variance are almost equal in magnitude though opposite in sign, as the only significant change in energy is the transfer between the two states, with viscosity making a minimal contribution by comparison over this time period. Indeed, the rate of change of kinetic energy due to buoyancy flux peaks at around ten times the loss of energy due to viscosity, with a similar trend seen for buoyancy variance. From this we can infer that virtually all of the structural change in the stably stratified case at this early time, as demonstrated by the figures 4.4, 4.5, 4.8 etc. are driven by the effects of buoyancy, rather than the viscous effects that shape the ring in the neutrally stratified case. After reaching a near zero buoyancy flux at $Nt/2\pi = 2$, the transfer rate increases again, though more gradually and to a lower peak value than within the first two buoyant cycles, before the flux term gradually reduces. Beyond approximately ten buoyant cycles, the magnitude of the buoyancy flux and viscous dissipation terms are well within the same order of magnitude, indicating that subsequent evolution of the structures in the flow is driven more equally by buoyancy and viscosity. This also indicates that the rates of kinetic energy and buoyancy variance redduction beyond this time are very similar, which would go some way to explaining the constant ratio of internal to total energy described previously.

The isosurfaces in 4.11 depict the evolution of the vortex ring beyond the completion of the first buoyant cycle. From the deformed ring and tail structure seen previously as $t \approx 6$, at $t \approx 8.4$ the ring is now only discernible from two slender columns of counter-rotating vertical vorticity, surrounded by several smaller eddies, giving an appearance bearing some similarity to the turbulent vortex ring in the neutrally stratified case, though the time from initial solution to the appearance of smaller eddies is significantly shorter (similar eddies were not seen in the neutrally stratified case until $t \approx 20$). As quickly as they appear however, the smaller eddies begin to merge into larger eddies to give an increasingly laminar appearance, culminating in the formation of a laminar, flat, disc shaped structure colloquially known in literature as a “pancake” vortex. Two patches of counter-rotating vorticity are clearly visible, main-

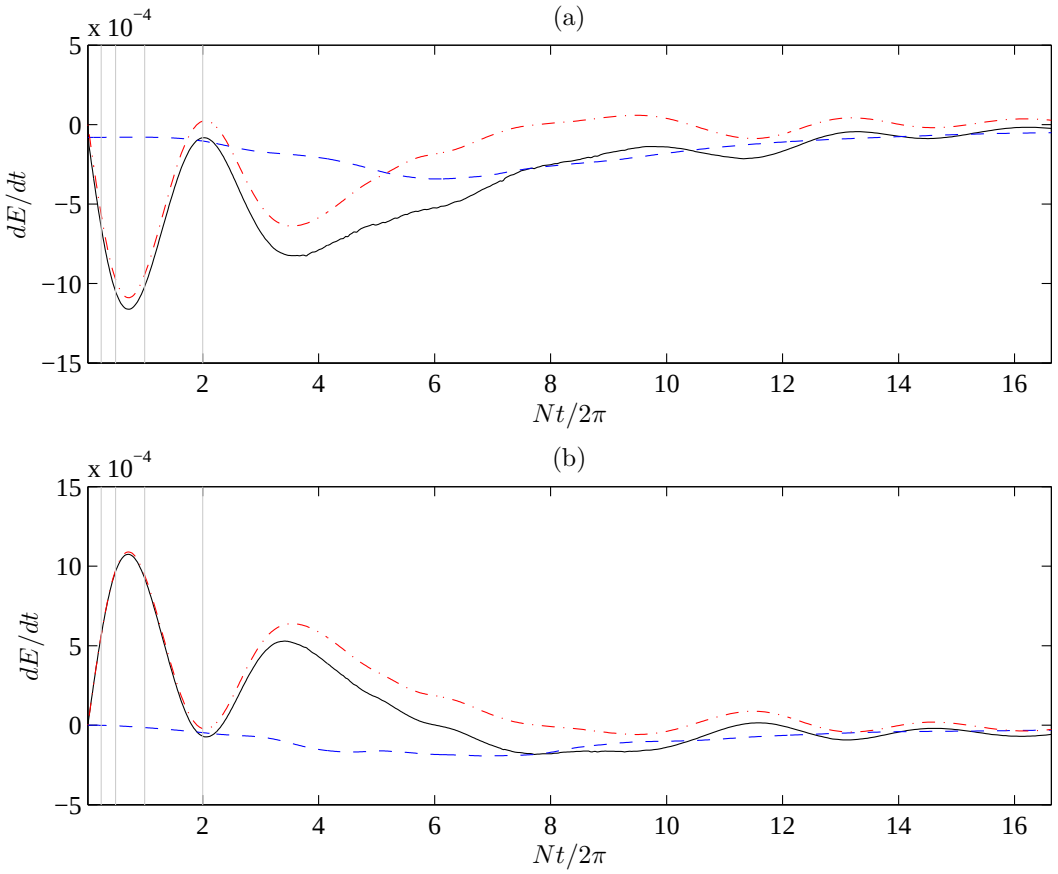

Figure 4.10: Time history of volume integrated kinetic energy and buoyancy variance fluxes for case RSD2 (Re = 5000, Fr = 1) with (a) rate of change of kinetic energy, dK/dt (—), rate of kinetic energy lost to viscous dissipation, K'_ν (– –), reverse buoyancy flux $-K'_B$ (– · –), (b) rate of change of buoyancy variance, dP/dt (—), rate of buoyancy variance lost to viscous dissipation, P'_ν (– –), buoyancy flux K'_B (– · –). The vertical lines (from left to right) indicate $Nt/2\pi = 0.25$, $Nt/2\pi = 0.5$, $Nt/2\pi = 1$, $Nt/2\pi = 2$.

taining the same sense of rotation of the two sides of the initial vortex ring core at the vertical midplane. The ring at this stage can be considered to have undergone buoyant collapse, a process apparently complete at the late time when both buoyancy variance and vertical kinetic energy levels reduce sharply as seen in figure 4.9. The three-dimensional structure at the late time is depicted in figure 4.12. Qualitatively, this structure appears similar to the three-dimensional vortex dipole as described by Praud and Fincham (2005) in both an experimental and analytically modelled context. The two columns of contra-rotating vorticity are clearly visible in front view, bounded by a thick shear layer above and below. Vorticity contours presented in figure 4.13 show the structure at the lateral and vertical midplanes, with the dipolar cores of vertical vorticity and the "v" shaped form taken by the shear layers above and below the vertical midplane. Subsequent analysis in chapter 5 demonstrates that this shape arises from pure shear, and the value of vorticity shown in the lateral midplane contours arises from this shear alone, rather than rotation of fluid in the horizontal plane.

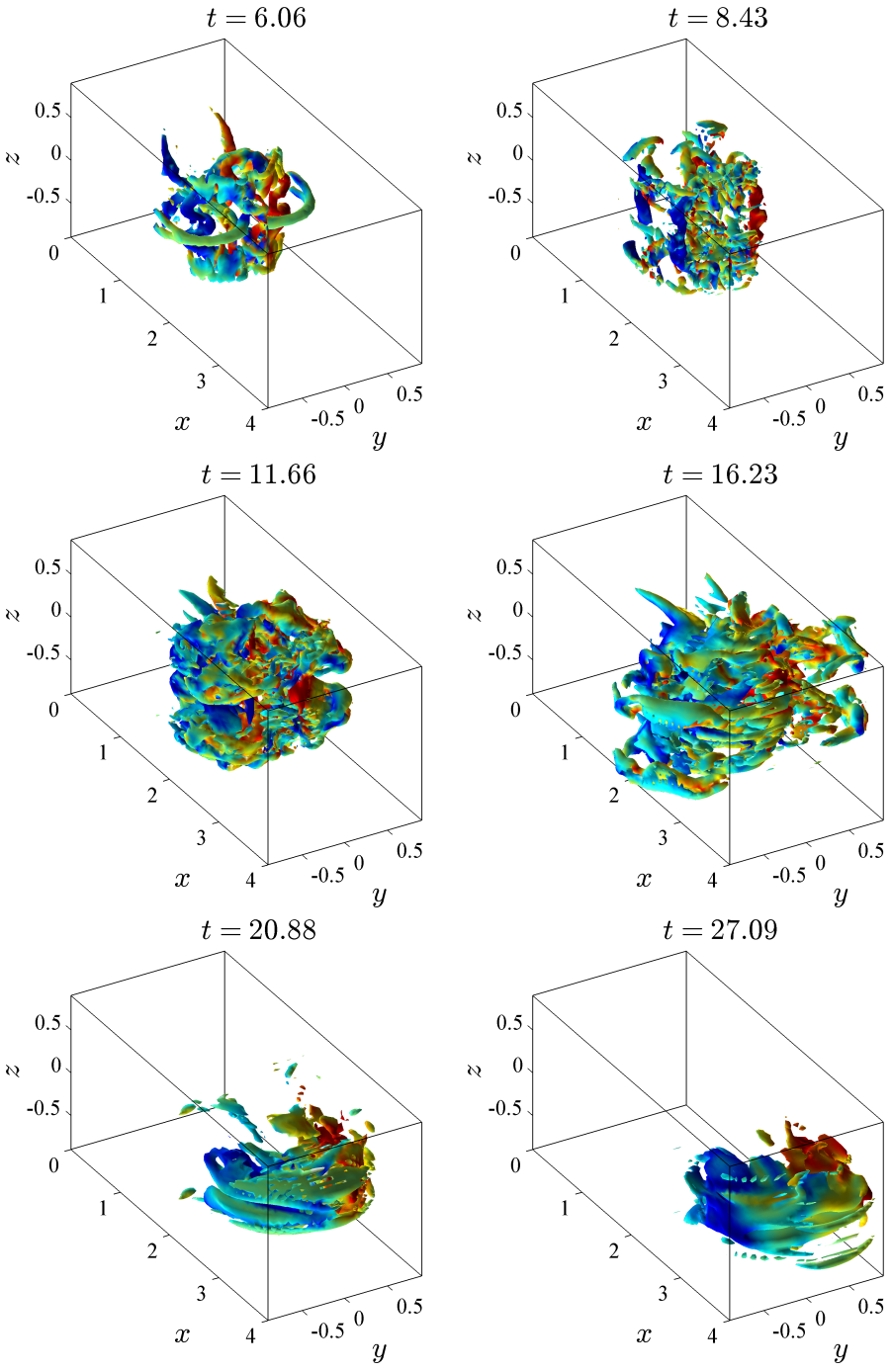

Figure 4.11: Isosurfaces of constant vorticity magnitude, $|\omega|$, for case RSD2 ($Re = 5000$, $Fr = 1$) at various times from the early stages of buoyant collapse through to the emergence of a late time laminar dipole. Viewing angle is from positive x, negative y, positive z to negative x, positive y, negative z. Colour contouring ranges between $\pm 0.6|\omega_z|_{\text{Max}}$, with isosurface threshold set at $0.25|\omega|_{\text{Max}}$.

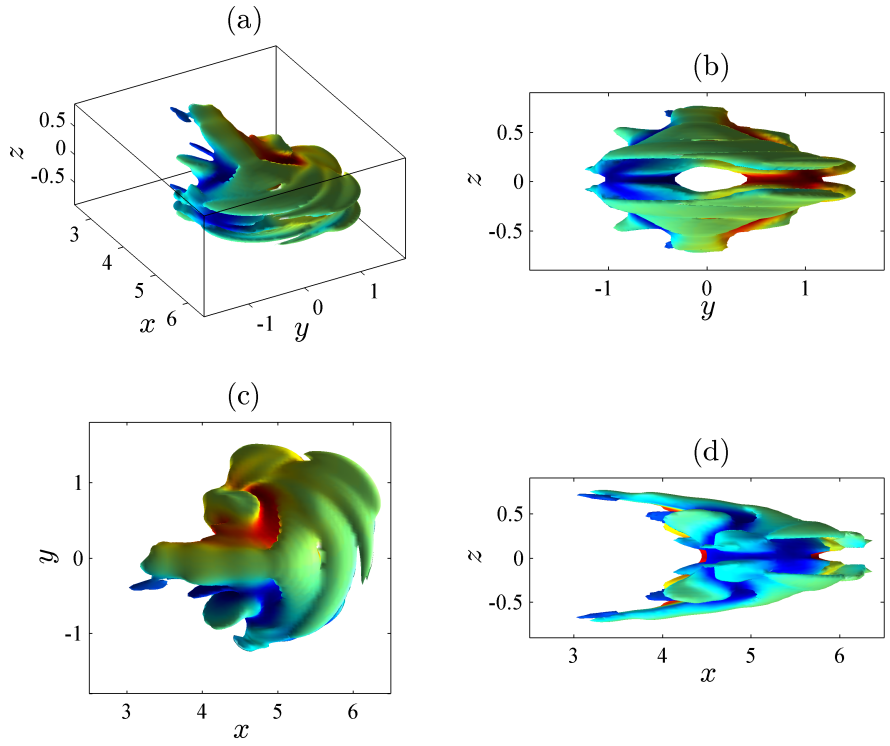

Figure 4.12: Isosurfaces of constant vorticity magnitude, $|\omega|$, for case RSD2 (Re = 5000, Fr = 1) at t = 50.9 demonstrating the structure of the late time dipole, with views looking from (a) positive x, negative y, positive z to negative x, positive y, negative z, (b) positive x to negative x, (c) positive z to negative z (d) negative y to positive y. Colour contouring ranges between $\pm 0.6|\omega_z|_{\text{Max}}$, with isosurface threshold set at $0.25|\omega|_{\text{Max}}$.

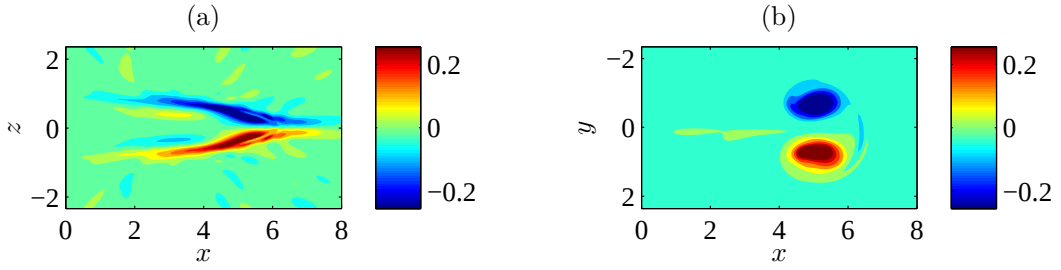

Figure 4.13: Contours of vorticity for case RSD2 (Re = 5000, Fr = 1) at t = 50.9 with (a) lateral vorticity, ω_y at $y = 0$, (b) vertical vorticity, ω_z at $z = 0$. Colour contouring ranges between $\pm 0.6|\omega_y|_{\text{Max}}$ and $\pm 0.6|\omega_z|_{\text{Max}}$ respectively.

Returning to the comparison between the neutrally stratified and stably stratified cases, the vertical and horizontal length scales of the vortex ring at the early time can be given by

$$D_{Ry} = \frac{2}{\Omega}\int_V |y||\omega|^2 \mathrm{d}V, \tag{4.10}$$

$$D_{Rz} = \frac{2}{\Omega}\int_V |z||\omega|^2 \mathrm{d}V, \tag{4.11}$$

and its streamwise centre position given by

$$X_R = \frac{1}{\Omega}\int_V x|\omega|^2 \mathrm{d}V, \tag{4.12}$$

where,

$$\Omega = \int_V |\omega|^2 \mathrm{d}V.$$

The early time history of these values for the neutrally stratified case RSD1 and the stably stratified case RSD2 are given in figure 4.14. Also presented are the values for case RSD3, which has an identical initial solution to RSD2 with the exception that the radial perturbation to the initial vortex ring is not applied, such that it is truly axisymmetric as opposed to the near-axisymmetry of the initial solution of all other cases presented in this chapter. In the neutrally stratified case, after the initial readjustment of the ring between $t = 0$ and $t = 1$, the vertical and horizontal length scales of the ring appear equal and are near-constant for the time interval considered here. The evolution of the ring's x location also appears to rise near linearly i.e. ring propagation velocity is near constant. Recall that vortex ring velocity was defined in Archer et al. (2008) as

$$U_R = \frac{\Gamma}{4\pi R_R}\left[\ln\frac{8R_R}{a} + c\right], \tag{4.13}$$

where R_R, a is a measure of core radius and c is a constant determined by the vorticity profile within the ring core, and for a Gaussian defined core such as those used here has a value of approximately -0.558 (Saffman, 1970). The definition of vortex radius used for calculating velocity in this instance is chosen not based on equations 4.10-4.11, but instead determined as half the distance between the vorticity minima and maxima across a radial slice though the ring. In the case of simulation RSD1, the approximate ring radius using this definition is 0.57 immediately after initial readjustment, with an estimated average core radius of 0.27. Using the value of c given by Saffman (1970) and the unit value of circulation defined previously, this gives a predicted velocity of 0.313. The mean measured velocity of the ring, dX_R/dt, between $t = 6$ and $t = 20$ was found to be 0.316. Though some discrepancy is to be expected in the

method used to determine core radius (given that after readjustment, the ring profile is no longer truly Gaussian), this nonetheless suggests this simulation gives excellent agreement with the predicted velocity from literature and helps verify that the numerical methods in use here are valid.

In the stably stratified cases, immediate differences are apparent in terms of ring length scales, which initially appear to increase in the vertical direction and decrease in the lateral direction over the first quarter buoyant cycle. For the remainder of the first buoyant cycle, the ring's vertical length scale reduces as can be seen in the isosurfaces of figure 4.8. Over the next buoyant cycle, the ring length scale increases in the lateral direction to beyond its original value and the vertical length scale again decreases. One may imagine that the detrainment of vorticity into structures surrounding the ring core and ejected from it may now be skewing the measurements given that the structure no longer resembles a toroidal vortex ring. The velocity of the structure as a whole is perhaps a more relevant quantity, with the propagation speed of the structure notably slowing beyond one buoyant period.

Also of note is that the cases RSD2 and RSD3, despite the lack of initial perturbation in the latter, give near identical results for length scale and x positioning. Further to this, examining the isosurfaces in figure 4.15 demonstrates qualitatively similar evolution of the vortical structures in the fluid for case RSD3 to those in case RSD2, with the initially unperturbed case giving more exact symmetry about the lateral and vertical midplanes but no new feautres beyond that. Finally, the time evolution of the kinetic energy and buoyancy variance components in the fluid for both cases are plotted in figure 4.16. The energy levels are almost exactly equal for each component throughout. The conclusion to draw from this would appear to be that, while an initial perturbation may be useful to accelerate the breakdown of a laminar vortex ring to a turbulent state in a neutrally stratified environment, the buoyant forces within the stably stratified cases are sufficient to break such structures into smaller eddies. As has already been demonstrated, the influence of buoyancy on the stably stratified case presented here would appear to far outweigh the effects of viscosity anyway.

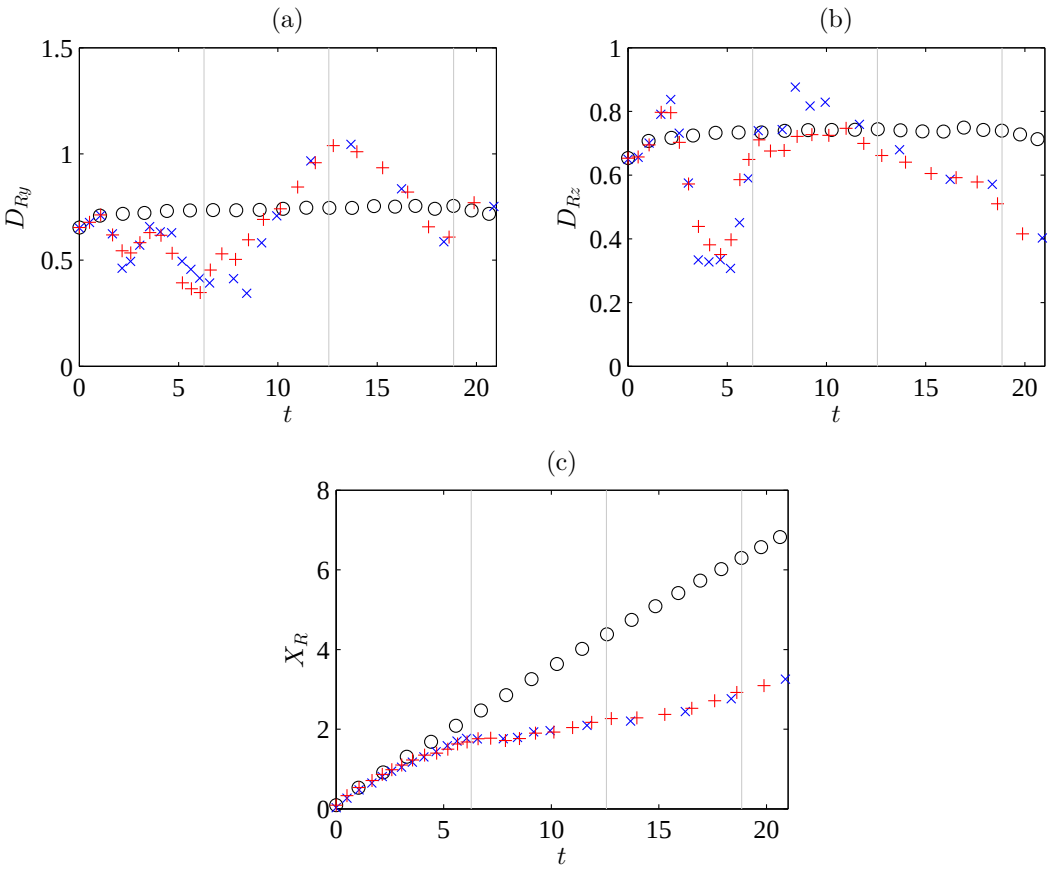

Figure 4.14: Time history of (a) vortex ring horizontal length scale, D_{Ry}, (b) vortex ring vertical length scale, D_{Rz}, (c) vortex ring streamwise location, X_R, for cases RSD1 (○), RSD2 (×) and RSD3 (+). The vertical lines are spaced at intervals of 2π to indicate the completion of each buoyant cycle for cases RSD2 and RSD3.

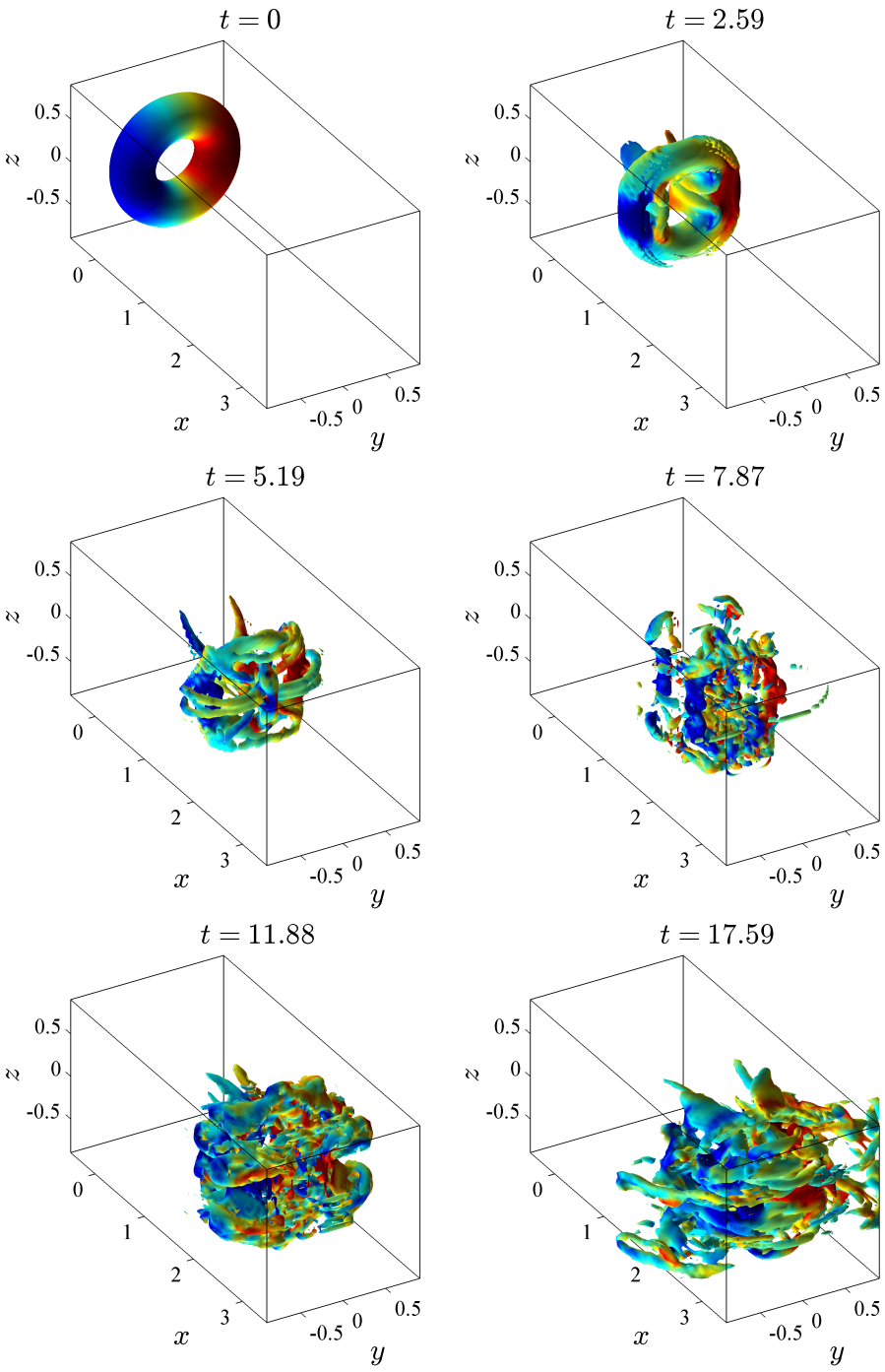

Figure 4.15: Isosurfaces of constant vorticity magnitude, $|\omega|$, for case RSD3 (Re = 5000, Fr = 1, unpeturbed initial ring) at various times from the early stages of buoyant collapse through to the emergence of a late time laminar dipole. Viewing angle is from positive x, negative y, positive z to negative x, positive y, negative z. Colour contouring ranges between $\pm 0.6|\omega_z|_{\text{Max}}$, with isosurface threshold set at $0.25|\omega|_{\text{Max}}$.

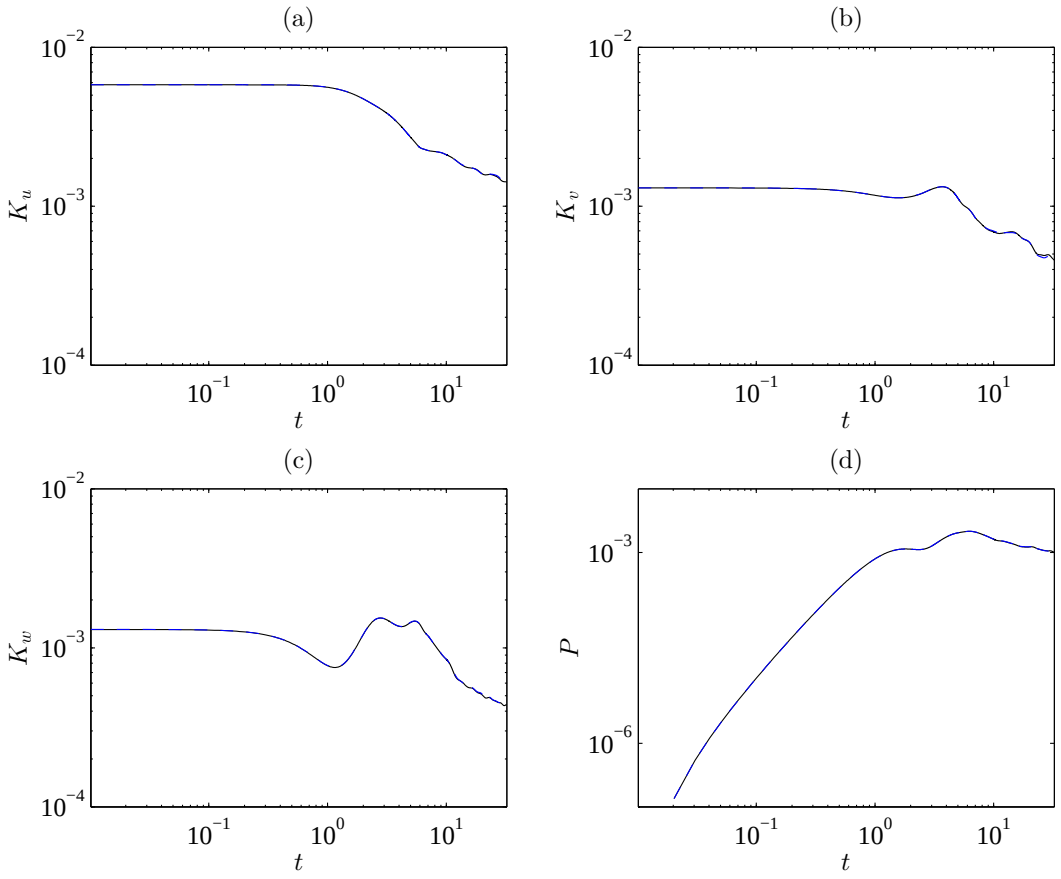

Figure 4.16: Time history of volume integrated kinetic and buoyancy variance levels for cases RSD2 (—) and RSD3 (– –). Levels shown are (a) streamwise kinetic energy, K_u, (b) lateral kinetic energy, K_v (c) vertical kinetic energy and (d) buoyancy variance, P.

4.2.3 The influence of initial Reynolds and Froude numbers on buoyant collapse

In order to gain further understanding of how viscous and buoyant forces determine the fate of the initial vortex ring in stably stratified cases, further cases were run as listed in table 4.1 that varied both the initial Reynolds and Froude numbers of the ring. Figure 4.17 plots the time evolution of the kinetic energy and buoyancy variance levels for three cases with initial Reynolds numbers of 1000, 3000 and 5000. The time history of each energy component is markedly similar between the three cases, with the key points at which energy levels vary as described previously occur at the same time for each of the three cases. As an example, buoyancy variance levels between the three cases appear near identical until just before peak buoyancy variance level is reached. Thereafter, the lower Reynolds number cases show a slightly more rapid decay of buoyancy variance, with similar trends seen for the three kinetic energy components. The more rapid drop in energy can be attributed both to increased viscous dissipation extracting energy from the domain, with the smaller value of Re giving a more dominant viscous contribution to the momentum equation.

The greater influence of viscosity can also be seen in the streamwise location of the vortex ring as it evolves from its initial axisymmetric state to the late time dipole. All three cases give a near identical initial structure propagation velocity over the first buoyant cycle, but thereafter the lower Reynolds cases show a more rapid deceleration. This is attributable both to increased dissipation extracting kinetic energy directly from the flow as mentioned previously, as well as increased diffusion spreading the momentum of the fluid over a larger volume, giving a slower propagation velocity. Overall though, the variation of Reynolds number alone does not appear to raise any particularly unexpected behaviours or offer any further detailed insight into the initial evolution and buoyant collapse of the vortex ring in a stably stratified background. These simulations were not run on long enough to consider how the structure evolves at the latest times under the influence of viscosity after the collapse process is complete, this instead being a focus of the next chapter.

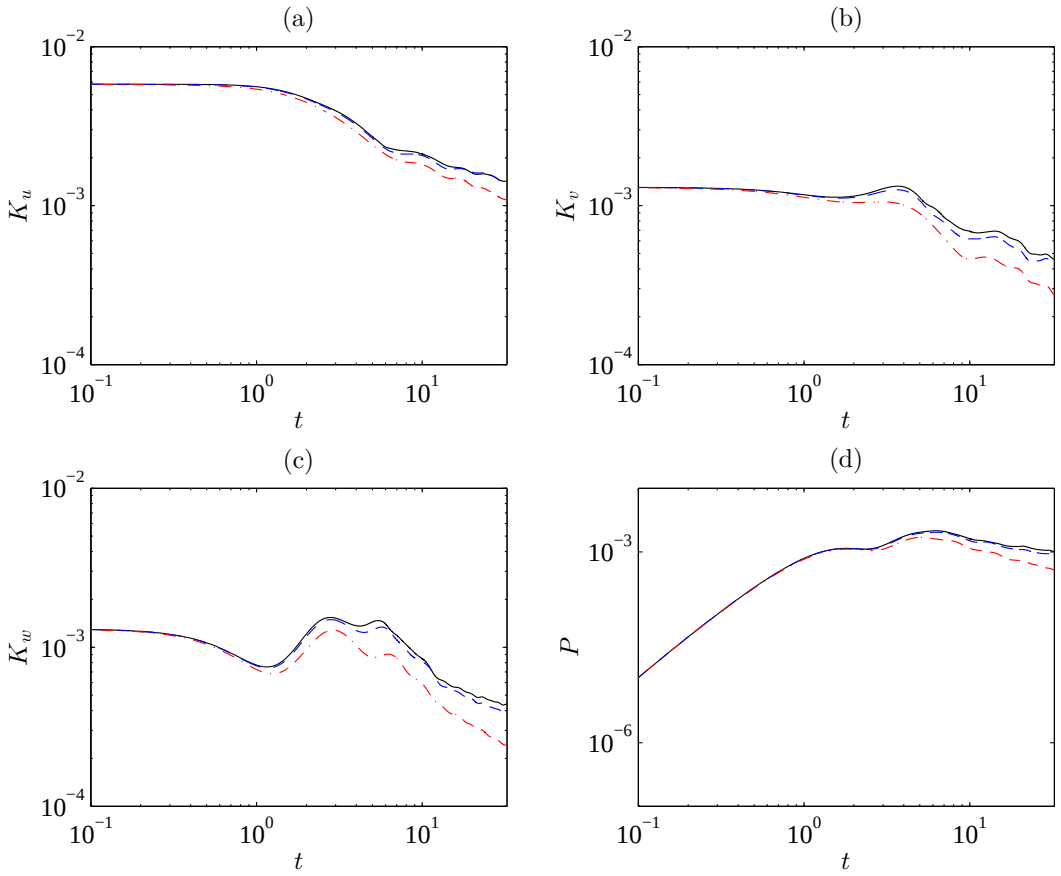

Figure 4.17: Time history of volume integrated kinetic energy and buoyancy variance levels for cases RSD2 (Re = 5000) (—), RSD4 (Re = 3000) (−−) and RSD5 (Re = 1000) (−·−) . Levels shown are (a) streamwise kinetic energy, K_u, (b) lateral kinetic energy, K_v (c) vertical kinetic energy and (d) buoyancy variance, P.

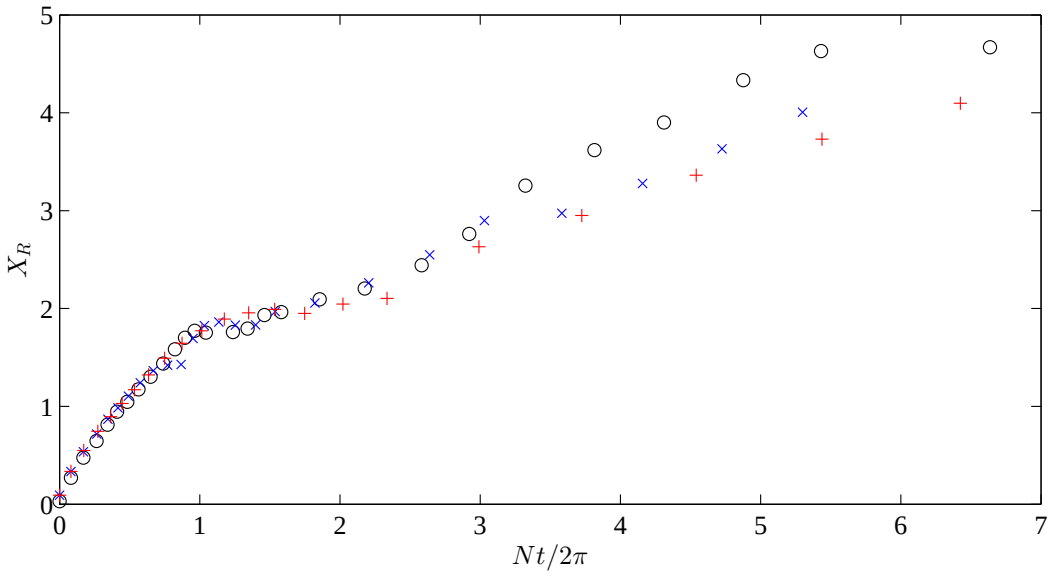

Figure 4.18: Time history of vortex ring streamwise location, X_R, for cases RSD2 (Re = 5000) (○), RSD4 (Re = 3000) (×) and RSD5 (Re = 1000) (+).

Of greater influence on the ring energy at the early time is the strength of the background density gradient. Figure 4.19 gives the time evolution of kinetic energy and buoyancy variance levels for three stably stratified cases with differing initial Froude number, as well as the kinetic energy levels for neutrally stratified case ($Fr = \infty$) documented previously. Immediately apparent is that the stably stratified case and the higher Froude number stably stratified case give very similar kinetic energy histories for the early stages of the solution. Examining the buoyancy variance level in the solution, the higher Froude number results in much lower buoyancy variance than the lower Froude number cases. This results from a much reduced rate of kinetic energy to buoyancy variance transfer, with the work required to displace a fluid particle by a unit vertical distance from its equilibrium plane reduced in a more weakly stratified background. The other two stably stratified cases give a higher level of buoyancy variance at the early time, and show bigger deviation from the neutrally stratified case in terms of kinetic energy as a result. Interestingly, all three stably stratified cases show very similar buoyancy variance trends with time (albeit with differing maximum values), with the time at which the key features identified in figure 4.9 occurring at a later solution time for the higher Froude number cases. Figure 4.20 shows the variation of the ratio of internal to total domain energy for four stably stratified cases at different initial Froude number, but plotted against the number of elapsed buoyant cycles. In each case this ratio increases rapidly initially before briefly plateauing or at least slowing notably between one quarter and one half buoyant cycles, before rising again thereafter. As mentioned before, the $Fr = 1$ case plateaus at a internal to total energy ratio of around 0.3 at almost exactly one buoyant cycle. The ratio for two intermediate Froude number cases plateau between two and three buoyant cycles into the simulation with the highest Froude number case not run sufficiently long to reach the point of this ratio plateauing. The intermediate Froude number cases appear to reach a ratio of nearer 0.5, as opposed to the 0.3 observed previously. Returning to figure 4.19, we see that while the initial value of buoyancy variance for the $Fr = 1$ case is higher than for the other stably stratified cases, beyond $t = 10$ it has a lower buoyancy variance level than the $Fr = 2$ case and beyond $t = 100$ has a lower buoyancy variance than the $Fr = 5$ case, despite this being within the time period where the internal to total energy ratio has plateaued. The streamwise kinetic energy level in the higher Froude number cases also appears to drop to a lower level at later times than the lower Froude number cases. In order to better understand these kinetic energy levels, the streamwise position of the vortex ring

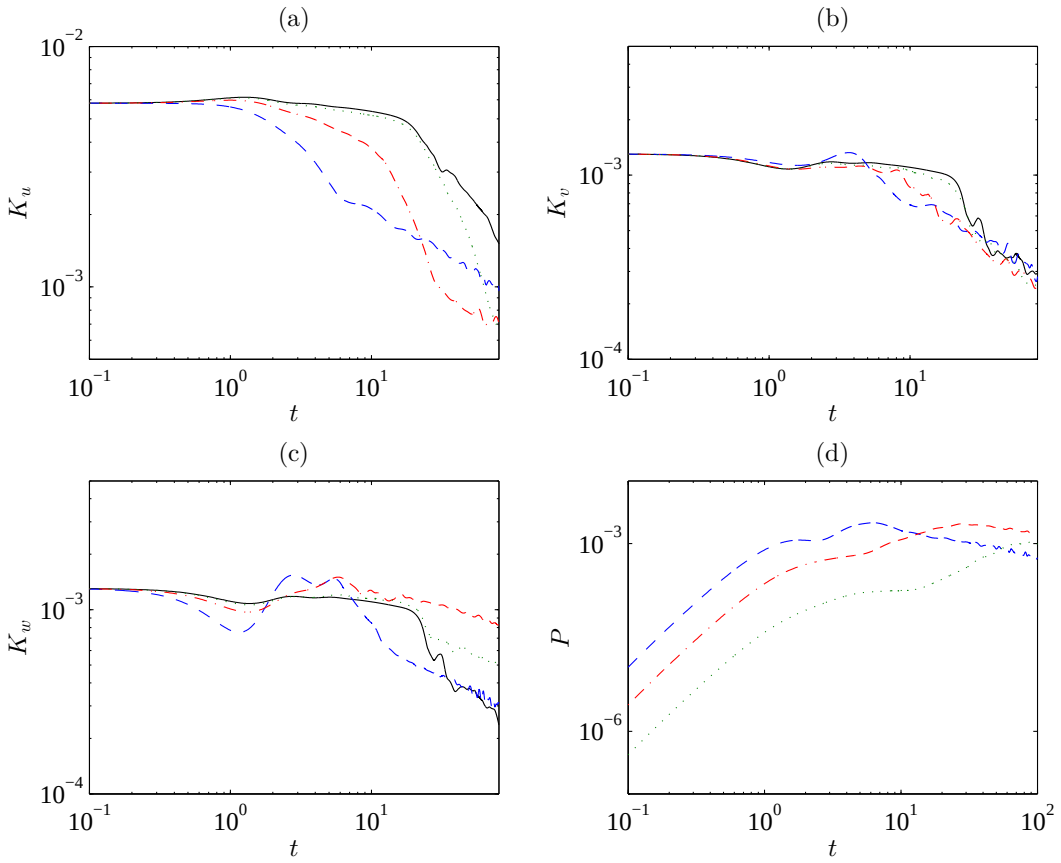

Figure 4.19: Time history of volume integrated kinetic energy and buoyancy variance levels for cases RSD1 (Fr = ∞) (—), RSD2 (Fr = 1.0) (−−), RSD8 (Fr = 2.0) (−·−) and RSD6 (Fr = 5.0) (···) . Levels shown are (a) streamwise kinetic energy, K_u, (b) lateral kinetic energy, K_v (c) vertical kinetic energy and (d) buoyancy variance, P.

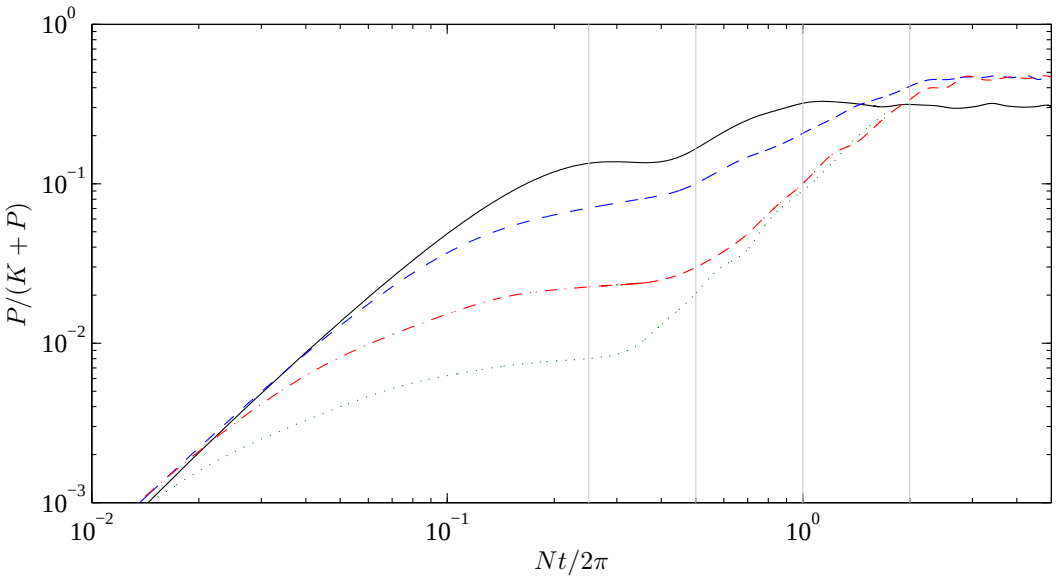

Figure 4.20: Time history of volume integrated buoyancy variance levels, expressed a fraction of total domain energy, for cases RSD2 (Fr = 1.0) (—), RSD8 (Fr = 2.0) (– –), RSD6 (Fr = 5.0) (– · –) and RSD7 (Fr = 10.0) (· · ·) .

is considered with the position history over elapsed buoyant cycles plotted in figure 4.21. Taking cases RSD2 and RSD8 as a comparison, these two cases appear to give a similar rate of change of position per buoyant cycle at later times, though given each buoyant cycle is longer for the latter case as a result of higher Froude number, this means the absolute propagation velocity of the ring is lower, which would explain the reduced streamwise kinetic energy at the later times. The lateral and vertical extent of the ring, also given in figure 4.21 is seen to oscillate in an irregular manner for all three cases with no clear pattern other than the peak of the oscillations being slightly more extreme for reduced Froude number. From the isosurfaces given in figure 4.22, it is apparent that the structure of the ring after a given number of buoyant cycles is highly dependent on the initial Froude number, particularly at the later times. After two buoyant cycles, an initial Froude number of 1 has given the expanding structure of smaller eddies discussed previously. By contrast, an initial Froude number of 5 has given a structure that is qualitatively more reminiscent of the neutrally stratified case, with the ring appearing to have undergone the same breakdown to smaller eddies and return to laminar state shown in 4.2 and discussed in the previous section. This difference in structure highlights that while the changes in buoyancy variance level showed similar trends after similar buoyant cycles had elapsed for different cases, the use of buoyant cycles as a non-dimensional time measure does not result in agreement for the kinetics of the vortex ring for the cases where initial Froude

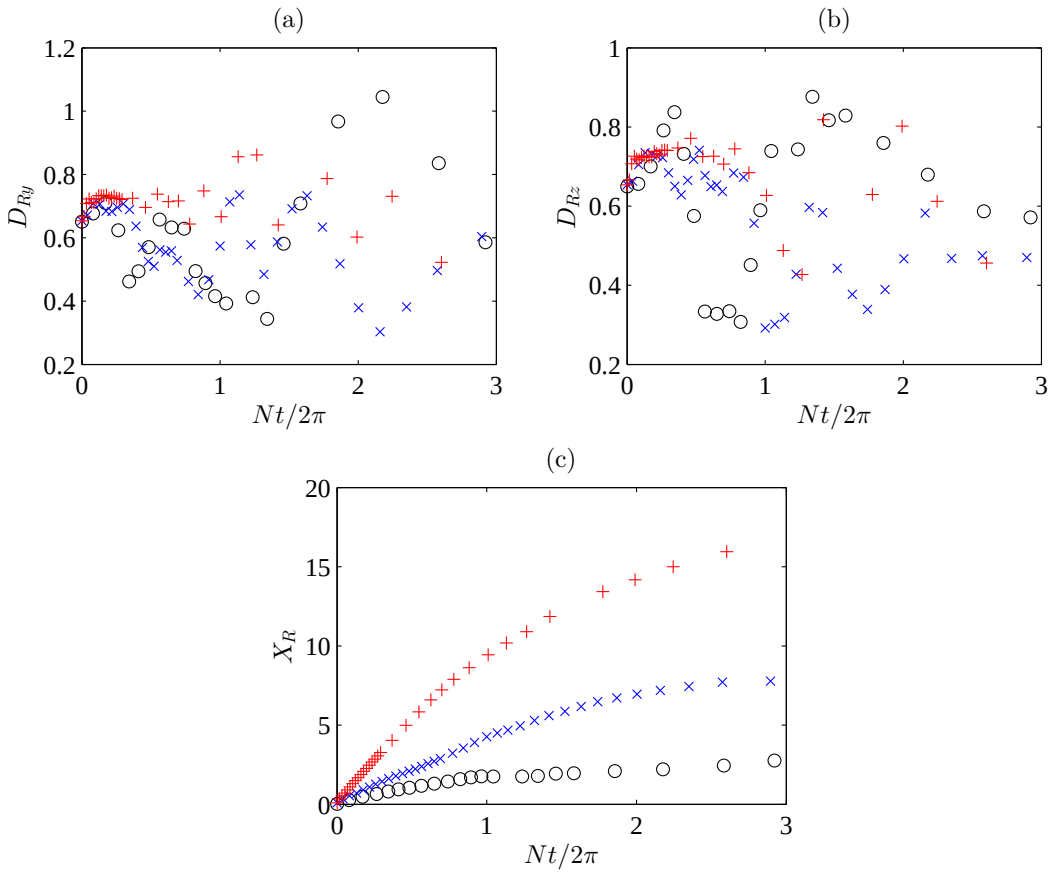

Figure 4.21: Time history of (a) vortex ring horizontal length scale, D_{Ry}, (b) vortex ring vertical length scale, D_{Rz}, (c) vortex ring streamwise location, X_R, for cases RSD2 (Fr = 1.0) (○), RSD8 (Fr = 2.0) (×) and RSD6 (Fr = 5.0) (+).

number was varied.

4.3 Chapter summary

This chapter has documented Direct Numerical solution of the evolution of a horizontally propagating vortex ring, both in neutrally and stably stratified fluids. While both cases show the initially laminar ring to break down into many smaller eddies soon after the simulation is commenced, the breakdown is accelerated in the stably stratified case due to the influence of the buoyant term in the momentum equation. Regardless of stratification, the eddies eventually merge to form a laminar structure once more at later times, with the stably stratified cases forming a pancake like dipolar vortex structure very similar to those documented in literature. Varying both the Reynolds and Froude numbers of the simulations has further demonstrated that the initial breakdown process in the stably stratified cases has little sensitivity to viscosity, instead being dominated by the strength of the background density gradient, with the vortical structure and energetics of the vortex ring deviating significantly from a neutrally stratified case at lower Froude number. Emphasis has been placed on relating the changes in the vorticity field to the trends shown for both kinetic energy and buoyancy variance levels within the flow, with no experimental analogy found in literature, and thus offering insight into this relationship for the first time.

The late time evolution of late-time dipolar structures is not considered in detail in this chapter, but is the primary focus of the following chapter. The following chapters will also consider how a vortex ring-like structure forms from an impulsively acting momentum source, and how this formation is also affected by the presence of a stable background density gradient.

Though not exhaustively considered here, a comparison of cases where the initial vortex ring has or has not been radially perturbed to accelerate the breakdown process showed that such perturbation had minimal quantitative effect on the breakdown in a stably stratified background. As a consequence, radial perturbation was not employed for the impulsive momentum injection cases of the following chapters.

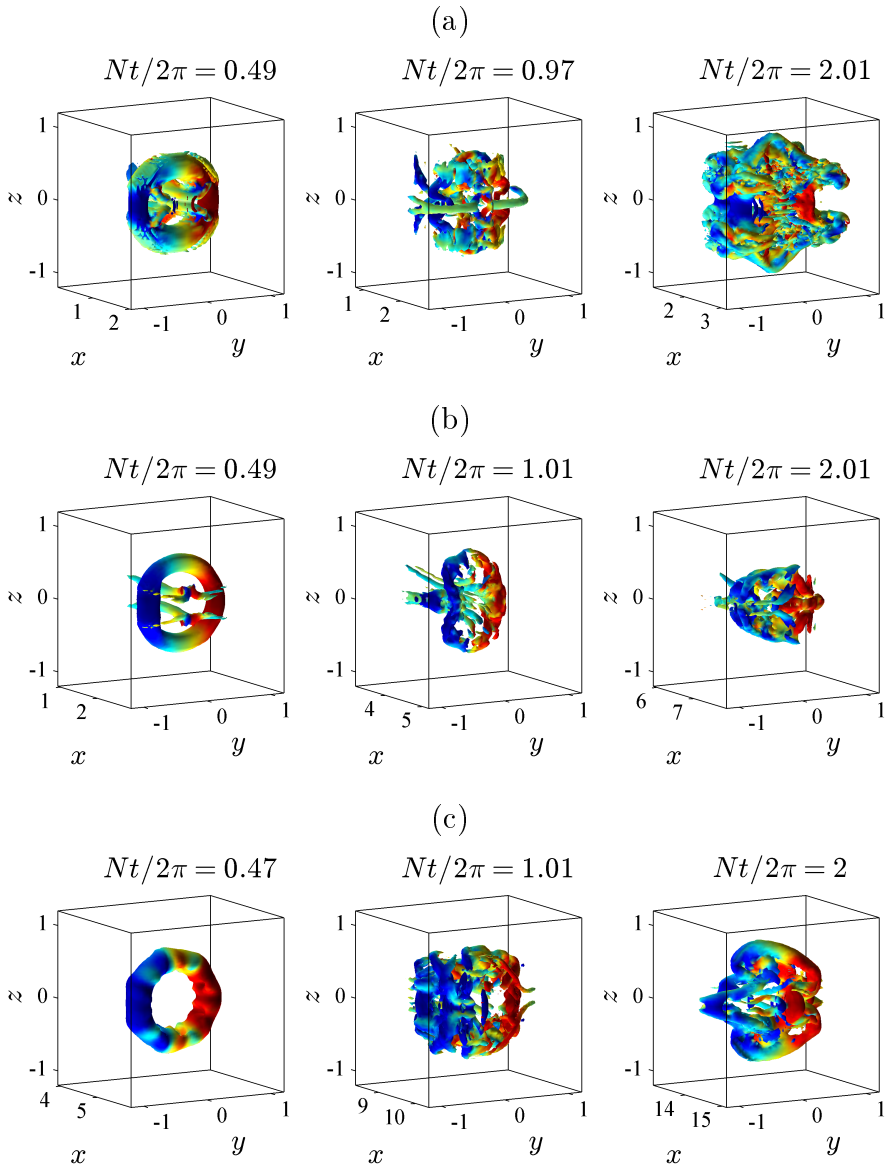

Figure 4.22: Isosurfaces of constant vorticity magnitude, $|\omega|$, after approximately one half, one and two buoyant cycles have elapsed for (a) case RSD2 ($Fr = 1.0$), (b) case RSD8 ($Fr = 2.0$) and (c) case RSD6 ($Fr = 5.0$). Viewing angle is from positive x, negative y, positive z to negative x, positive y, negative z. Colour contouring ranges between $\pm 0.6|\omega_z|_{\text{Max}}$, with isosurface threshold set at $0.25|\omega|_{\text{Max}}$.

Chapter 5

Vortex dipole formation in a stratified fluid

5.1 Simulation set up and selecting study parameters

The next stage of this research involves simulating an axisymmetric momentum injection into an initially quiescent, stably stratified domain in order to create a numerical analogy to many of the experimental works discussed in sections 1.2.2 and 1.2.3. The injection is generated by a mometum source region centred at the origin of the computational domain, which delivers a total kinematic momentum flux, J. The momentum flux is distributed across the computational grid by the same 3D Gaussian function utilised in the work of Rojanaratanangkule et al. (2012), where impulsive momentum injections were simulated and then allowed to form a dipole under the vertical constraint of free surfaces placed above and below the injected fluid. The forcing term, f_i, in equation 2.9 is defined as

$$f_i = (f_x, 0, 0),$$
$$f_x = \frac{J}{((\delta_G/2)^2\pi)^{3/2}} \exp\left(-\frac{x^2+y^2+z^2}{(\delta_G/2)^2}\right), \tag{5.1}$$

where δ_G is the Gaussian diameter of the forcing region. The denominator, $((\delta_G/2)^2\pi)^{3/2}$, scales the acceleration applied to the fluid at any one grid point such that

$$\int_V f_x \mathrm{d}V = J,$$

regardless of the value of δ_G. The momentum injection is switched on at $t = 0$ and turned off at $t = t_J$, with no further momentum injection thereafter. A Gaussian forcing profile is favoured here over a smoothed top hat

such as those used for the impulsive jet simulations of Mohseni et al. (2001) and Rojanaratanangkule et al. (2014), as it is less likely to produce sharp velocity gradients that the spectral numerical method of the simulation code will struggle to capture without a very high level of resolution. Both these latter studies used a finite differencing method to discretise the computational domain, so were less susceptible to such issues.

The values of input flow parameters for the simulation are chosen based on equivalents noted from previous literature. The three parameters to be varied between simulations are the Reynolds number, Re, the non-dimensional buoyancy frequency, N and the duration of the fluid injection, which for stably stratified cases can be given in terms of the number of buoyant periods that elapse during the injection, $Nt_J/2\pi$.

The Reynolds number selected here is applied in terms of the kinematic momentum flux of the injection source i.e.

$$Re = Re_J = \frac{\hat{J}_J^{1/2}}{\hat{\nu}} = J^{1/2} Re_{Ref}. \tag{5.2}$$

This is the definition used in Voropayev et al. (2008) and differs from some other literature that makes use of the injection velocity and inlet diameter to give a Reynolds number as

$$Re_S = \frac{\hat{U}_J \hat{D}_J}{\hat{\nu}}.$$

The range of Reynolds numbers used in a selection of previous studies is presented in the table 5.1, with some given by the Re_J definition and some by Re_S. For the latter, an estimate of Re_J is calculated from the injection velocity and diameter (with $\hat{J}_J = \hat{U_J}^2 \pi \hat{D}_J/4$) and given in brackets for comparative purposes. As can be seen from the table, the Reynolds number based on momentum flux is estimated to be around 10% lower than the velocity/length scale counterpart.

Some of these sources also present the uniform buoyancy frequency applied throughout the fluid and the duration of the injection, with dimensional values given in table 5.2. Also presented are typical non-dimensional equivalents, found with a reference time scale, $\hat{t}_{\text{Ref}}$ determined from the injection diameter, D, and the kinematic momentum flux of the source, J, i.e.

$$\hat{t}_{\text{Ref}} = \frac{\pi \hat{D}/4}{\hat{J}^{1/2}}. \tag{5.3}$$

The non-dimensional injection times and stratification strengths from experiment are long enough and weak enough that it would take lengthy simulations and a very large domain to capture the full evolution of an axisymmetric jet

Source	Re_S	Re_J
van Heijst and Flór (1989)	2000	(1800)
Flór et al. (1995)	360-11500	(320-10200)
Praud and Fincham (2005)	10000	(8900)
Voropayev et al. (2008)	N/A	650-1400
Rojanaratanangkule et al. (2012)	N/A	625-2000

Table 5.1: Injection source Reynolds numbers (Re_J, Re_S) from relevant literature

flow to the late time vortex dipole we expect if using similar non-dimensional parameters. However, we can create simulations that closely match the values of $Nt_J/2\pi$ seen in experiment i.e. the number of buoyant cycles over which the momentum injection is sustained. This gives an alternative means of normalising elapsed time in the simulations and can be used to compare with the time evolution of the flow properties seen in experimental work.

Source	$\hat{N}$ (rad s^{-1})	$N/10^{-3}$	$\hat{t}_J$ (s)	t_J	$Nt_J/2\pi$
van Heijst and Flór (1989)	1.68	0.74	1.0	2256.8	0.27
Flór et al. (1995)	1.2-3.0	1.26	0.2-0.7	752.8	0.15
Praud and Fincham (2005)	0.3	7.68	1.0-8.0	175.7	0.21
Voropayev et al. (2008)	0.8-1.2	2.75	3.0-5.0	1452.5	0.72

Table 5.2: Stably stratified domain buoyancy frequency and from relevant literature

A total of eight simulations were conducted for this part of the study, with the governing flow parameters and details of the computational grid detailed in table 5.3. The first two simulations, JSD1 and JSD2, were conducted to compare the early time differences that develop between a momentum source injection into both a neutrally and stably stratified domain. The remaining simulations, JLD1-6, are all stably stratified cases with a larger domain, intended for studying the effect of the governing flow parameters on the late time dipole development. It should be noted that while the values of N and t_J are somewhat higher than their experimental counterparts, the values of $Nt_J/2\pi$ are representative of previous work as detailed in table 5.2. A uniform lateral and vertical domain size is used to eliminate the proximity of

Case	Re	N	t_J	$Nt_J/2\pi$	L_x, L_y, L_z	n_x, n_y, n_z
JSD1	1400	0.0	5	-	$24\pi, 8\pi, 8\pi$	$768, 384, 384$
JSD2	1400	0.2	5	0.16	$24\pi, 8\pi, 8\pi$	$768, 384, 384$
JLD1	1400	0.2	5	0.16	$40\pi, 13.3\pi, 13.3\pi$	$1280, 640, 640$
JLD2	800	0.2	5	0.16	$40\pi, 13.3\pi, 13.3\pi$	$1280, 640, 640$
JLD3	2000	0.2	5	0.16	$40\pi, 13.3\pi, 13.3\pi$	$1280, 640, 640$
JLD4	1400	1.0	5	0.80	$40\pi, 13.3\pi, 13.3\pi$	$1280, 640, 640$
JLD5	1400	0.2	15	0.48	$40\pi, 13.3\pi, 13.3\pi$	$1280, 640, 640$
JLD6	1400	1.0	15	2.39	$40\pi, 13.3\pi, 13.3\pi$	$1280, 640, 640$

Table 5.3: Cases and flow parameters

boundary conditions as a potential cause for the breaking of axisymmetry seen in the stably stratified cases. The grid spacing used for each direction is identical for both JSD and JLD cases so that the effects of changing domain size can be fairly evaluated. The initial grid resolution for all cases was verified to be suitable through a combination of grid convergence testing and energy budget analysis. The fringe region parameters were chosen based on the work conducted in section 3.3, and are universal across all the cases with $(\sigma_c, \sigma_a, \sigma_b, t_w, l_{fy}, l_{fz}) = (0.04, 0.5, 0.5, 2.5, L_y/40, L_z/40)$. These parameters were found to be sufficient to dissipate internal waves generated during the evolution of the stratified cases without significantly impacting on the development of flow structures until the very latest times in the simulation for the larger domain cases. The combined effect of domain size and fringe proximity is discussed in more detail later in this chapter.

During the momentum injection phase ($t \leq t_J$), the time step was held fixed at $\Delta t = 0.02$ in order to maintain a stable time integration. This also has the advantage of being able to precisely implement the t_J cut-off within the code. After t_J, the code was free to prescribe its own time step based on the Courant number of 1.58 as discussed in section 2.3.1.

5.2 Results and analysis

5.2.1 Initial development of momentum injection in neutrally/stably stratified domains

The first two simulations conducted, JSD1 and JSD2, involve a momentum injection at $Re = 1400$ with $t_J = 5$ into both a neutrally and stably stratified

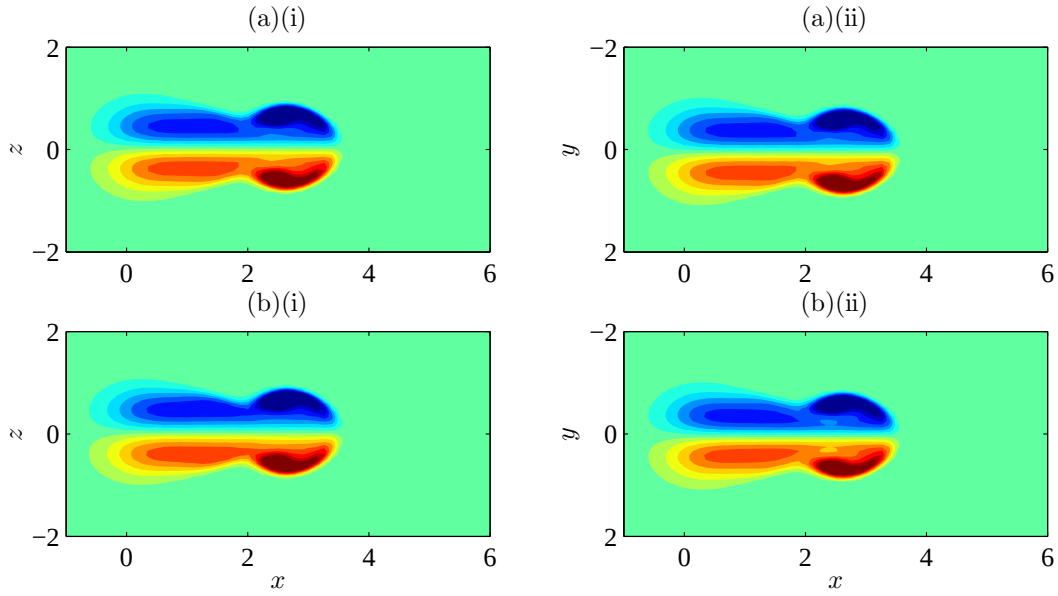

Figure 5.1: Comparison of midplane vorticity contours at $t = t_J = 5$ for (a) neutral stratification, $N = 0$ (b) stable stratification, $N = 0.2$; (i) ω_y at $y = 0$ (ii) ω_z at $z = 0$. All contour levels range from −2 (blue) to +2 (red) and are viewed looking from negative to positive along the normal axis.

domain, where the stably stratified case uses $N = 0.20$.

The momentum source produces a starting jet originating from the domain origin, creating an axisymmetric shear layer protruding in the x direction. At the leading edge of the jet, the shear layer rolls up into a vortex ring in a process well documented in previous experimental studies (see Gharib et al. (1998) etc.), with the shear layer forming a trailing jet behind the ring. The ring observed here is somewhat more spherical than that observed in experimental studies of starting jets, ostensibly due to the use of a Gaussian forcing profile, though qualitatively the behaviour is consistent with experimental observations.

Figure 5.1 shows vorticity contours, taken at the lateral and vertical midplanes of the domain at the end of the momentum injection for both cases. The axisymmetry of the starting jet and vortex ring is clearly observed for the neutrally stratified case, with the stably stratified case showing little difference at this early stage.

Once the injection has ceased, the ring and trailing jet propagate downstream. Figure 5.2 illustrates that the neutrally stratified case maintains axisymmetry throughout, with the leading vortex ring propagating faster than the trailing jet, becoming detached and moving away, with a secondary ring forming at the leading edge of the separated trailing jet. Until $t \approx 15$ (around

1 complete buoyant period into the simulation), the quasi-axisymmetry of the stably stratified case (figure 5.3(a)) is maintained and appears qualitatively similar to the neutrally stratified case as seen in figure 5.2(a).

Beyond a full buoyancy period, the quasi-axisymmetry breaks down. At this point, instabilities develop in both the leading and secondary vortex, forming a quasi-turbulent arrangement of much smaller vortical eddies. These structures form two distinct patterns in the midplane vorticity contours, both of which are symmetric about the x axis and visible in figure 5.3(b).

Approximately, three buoyant periods after this stage, the propagation velocity of the total fluid structure reduces rapidly, with some of the smaller eddies moving laterally away from the x axis, such that the width of the structure undergoes a significant increase. By contrast, the eddies do not significantly expand in the vertical direction, instead remaining confined in a layer of fluid comparable in height to the quasi-axisymmetric stage (figure 5.3(c)).

Over a period of an additional 2-15 buoyancy periods, the small eddies within the structure begin to merge together and advect forward into the frontal region of the structure. The merging eddies, when viewed along the z axis, form a series of dipolar vortices that each advect into the front region in turn. During this stage of small eddies merging, significant generation of internal waves can be implied by examining the lateral midplane vorticity field as seen in figure 5.3(c)(i). These waves are generated along the length of the structure and propagate away forwards and either up or down from the evolving dipolar structure. The fringe region at the vertical and lateral domain boundaries dissipates the waves before they can re-enter the domain.

At the late time (t>300), the dipolar eddies have merged together to form two large contra-rotating vortex columns, bounded by two relatively thin shear layers above and below the columns, with a "tail" of trailing fluid extending behind as seen in figure 5.3(d). At this stage, vertical motion in the structure has been almost entirely suppressed, reducing the previously three dimensional flow to a vertical arrangement of planar flow layers. The contours of ω_y observed in figure 5.3(d)(i) result from the shear between these layers, with the layers nearest $z = 0$ moving faster than those above and below.

The vertical vorticity contours at the late time exhibit a similar appearance to the two dimensional dipoles considered in the analytical and numerical work of Delbende and Rossi (2009), which also demonstrated the presence of a weak, vortical tail extending behind the leading dipole structure. The isosurfaces given in figure 5.4 further illustrate this three dimensional structure, with the

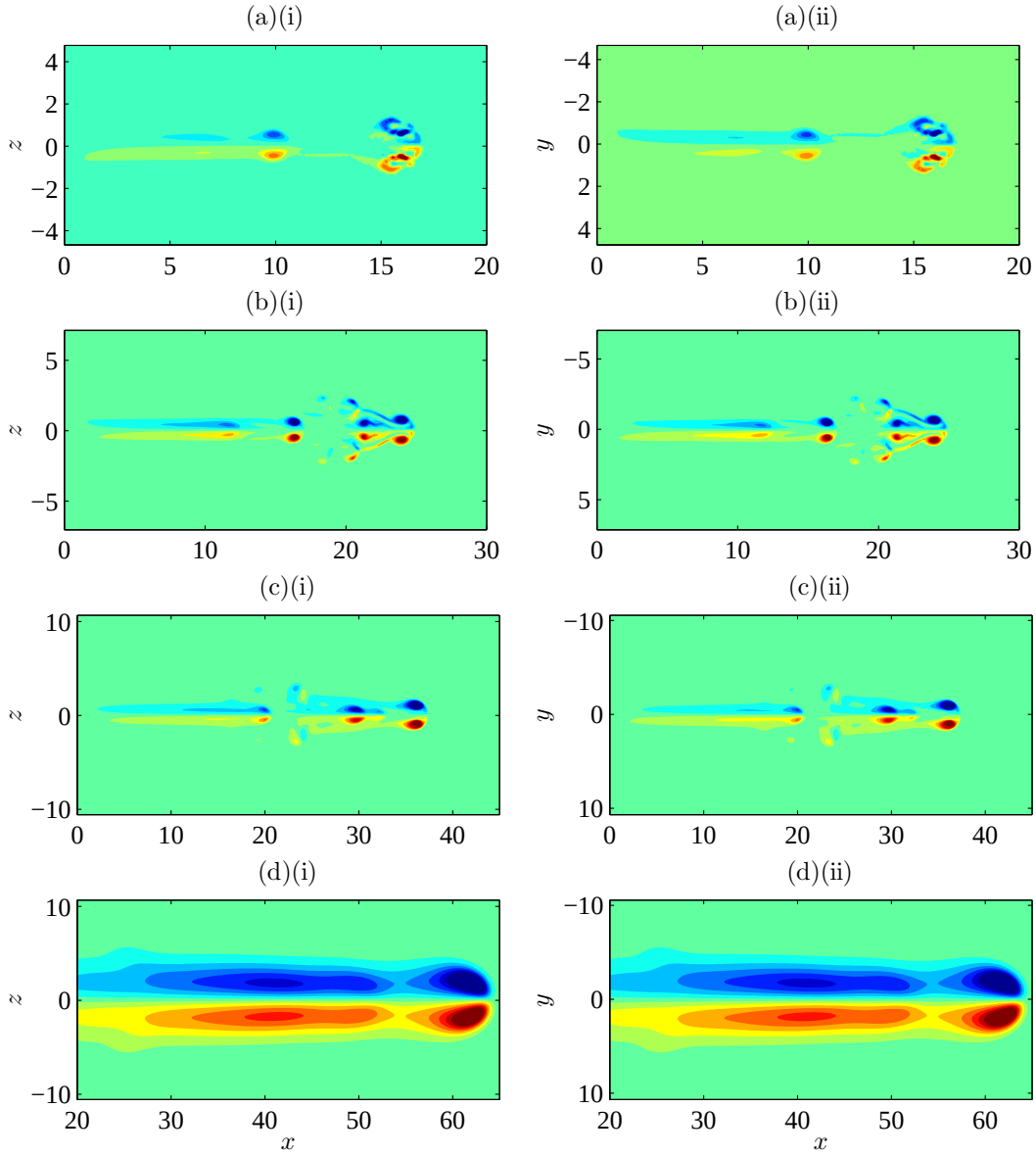

Figure 5.2: Comparison of midplane vorticity contours for case JSD1 ($N = 0.0$) at (a) $t = 25.6$ (b) $t = 52.3$ (c) $t = 170.2$ (d) $t = 2073.9$. As in figure 5.1, displayed contours are (i) ω_y at $y = 0$, (ii) ω_z at $z = 0$. The contour levels at each time range between $\pm 0.6|\omega_z|_{\text{Max}}$, where $|\omega_z|_{\text{Max}}$ is the instantaneous, absolute maximum of vertical vorticity at $z = 0$.

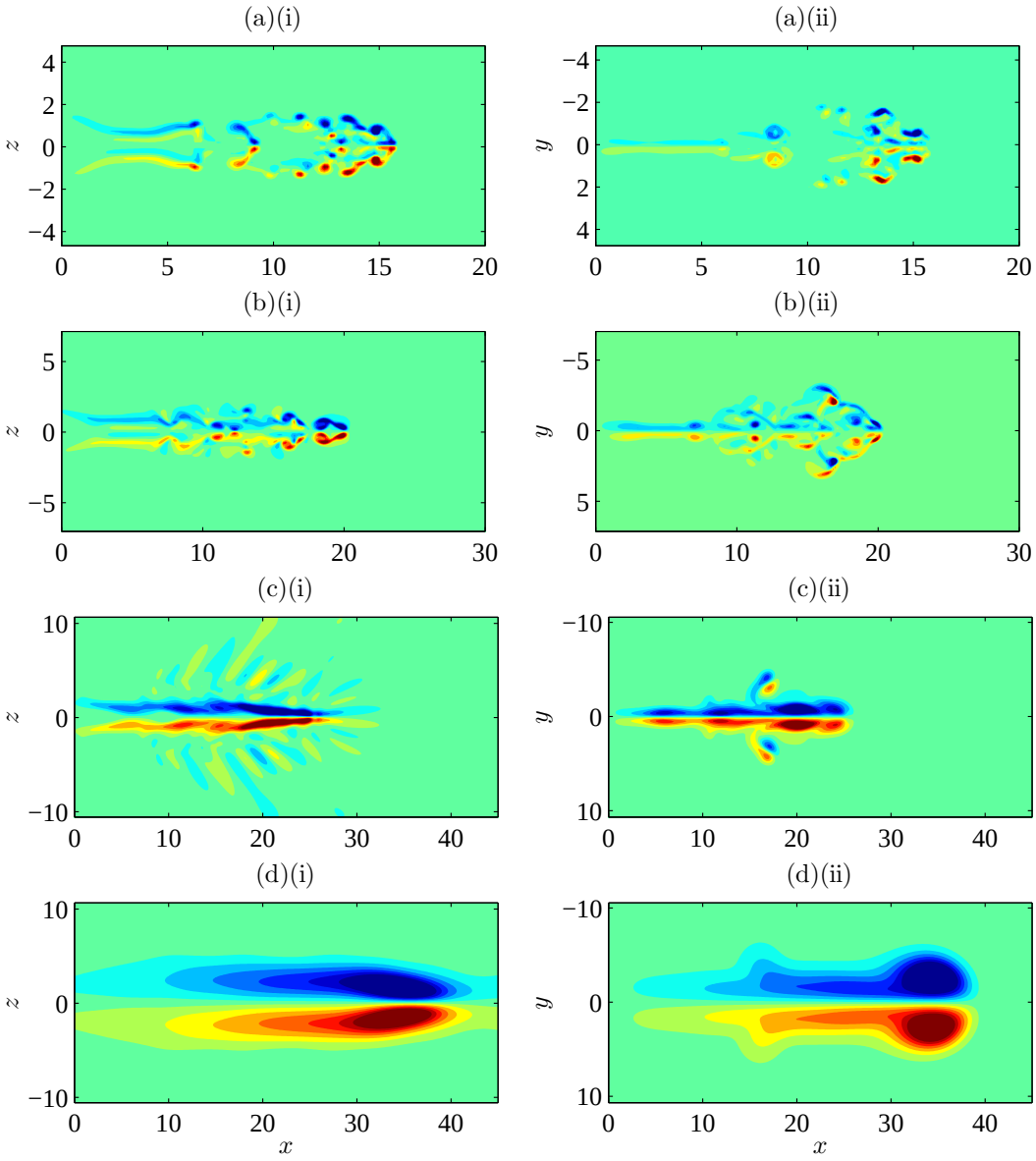

Figure 5.3: As figure 5.2 but for case JSD2 ($N = 0.2$) at (a) $t = 26.5$ (b) $t = 50.2$ (c) $t = 159.2$ (d) $t = 2045.8$.

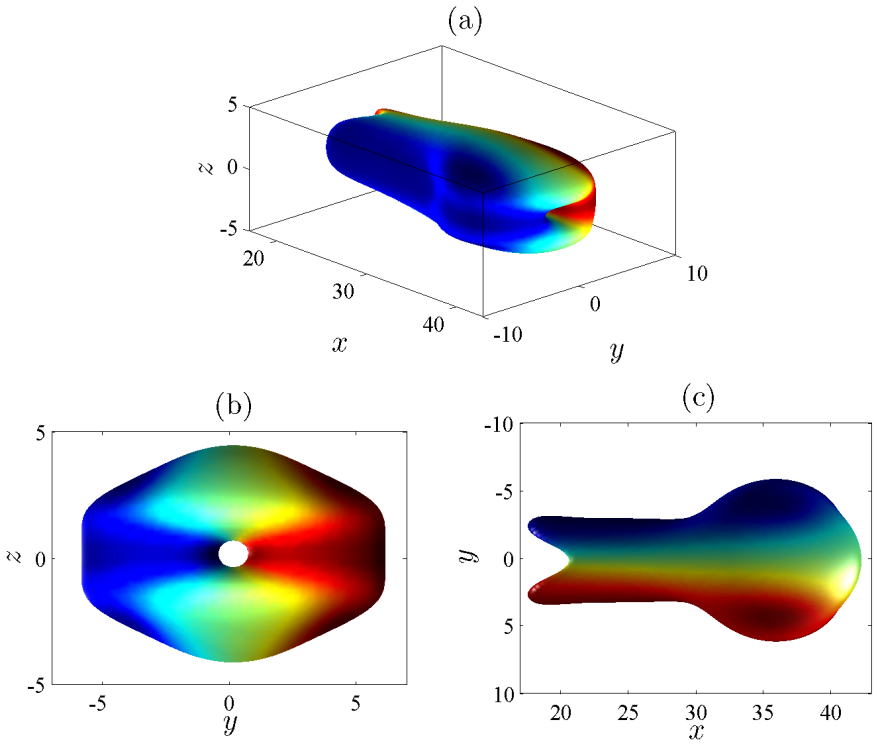

Figure 5.4: Isosurfaces of constant vorticity magnitude, $|\omega| = (\omega_x + \omega_y + \omega_z)^{1/2}$ for $N = 0.2$ at $t = 3410$, with colour contours to the same scale as figure 5.3(d). Isosurface threshold set at $0.3|\omega|_{\text{Max}}$, looking from (a) maximum x, y, z to minimum x, y, z (b) positive x to negative x (c) negative z to positive z.

columns, shear layers and tail region clearly visible, giving good qualitative agreement with the features observed in previous experimental work (see figure 12 in Praud and Fincham (2005)). Referring to this complete structure as a dipole is something of a misnomer, as it exhibits a distinct non-uniformity throughout its vertical extent and cannot be considered truly two dimensional, though for lack of a simpler title it will be continued to be referred to as a dipole hereafter.

The visualizations of the dipole are useful for illustrating the dipole features and corroborating that the flow observed in these simulations is representative of the experimental equivalents, but they yield little quantitative information on the mechanisms behind the change from a quasi-axisymmetric jet to a vortex dipole. In order to better understand these mechanism we consider key statistics of the flow as they evolve in time, and relate them to the visual changes in the flow structures noted previously. As indicated by the visualisations given previously, there are four distinct stages of flow evolution for the stably stratified case, which can also be identified by considering the volume-

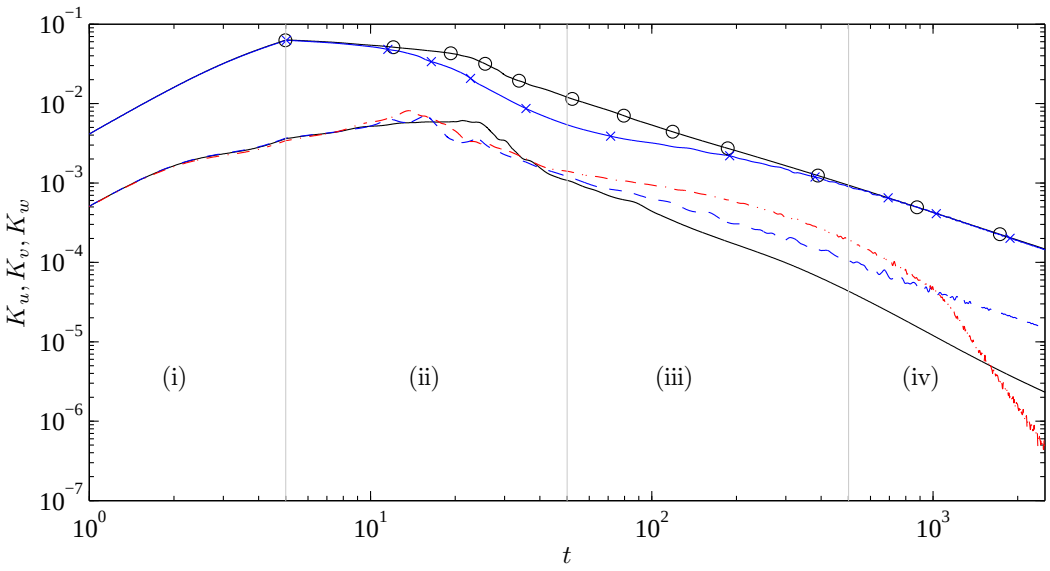

Figure 5.5: Time evolution of K_u for $N = 0.0$ (-o-) K_v, K_w for $N = 0.0$ (—), K_u for $N = 0.2$ (-x-), K_v for $N = 0.2$ (– –), K_w for $N = 0.2$ (– · –). The plot regions (i)-(iv) indicate the subsequent phases of evolution for $N = 0.2$ i.e. (i) $t \leq t_J$ (ii) instability development (iii) buoyant collapse (iv) planar flow.

integrated kinetic energy and buoyancy variance in the domain. The time evolution of some of these integrated energy components is given in figures 5.5 and 5.6, with the transition point between the four stages indicated. During the momentum injection (stage (i) in figure5.5), K_u rises as fluid velocity is increased in the x direction. Viscous roll up at the leading edge of the starting jet transfers some of this energy to the y and z directions, forming the leading vortex ring seen in figure 5.1. For the neutrally stratified case, the simulation maintains perfect axisymmetry about the streamwise axis such that $K_v = K_w$ throughout, and are therefore represented by a single line. For the stably stratified case, the vertical motions induced during this roll up displace fluid particles from their equilibrium layer in the z direction, leading to a concurrent production of buoyancy variance. At this early stage, P is at least one order of magnitude less than either K_v or K_w, suggesting that the potential of the buoyancy scalar field to influence the velocity field is minimal. As such, K_v and K_w are almost identical, to each other and to their equivalents for the neutrally stratified case, and quasi-axisymmetry is maintained.

Shortly after the momentum injection is ceased at $t = t_J$ (stage (ii) in figure5.5), K_u begins to reduce, partly as a result of viscous drag slowing the propagating structure's advance in the x direction and partly due to continued transport of energy into the other directions as the trailing jet rolls up into further ring-like structures (note the secondary ring visible in figure 5.2(a).

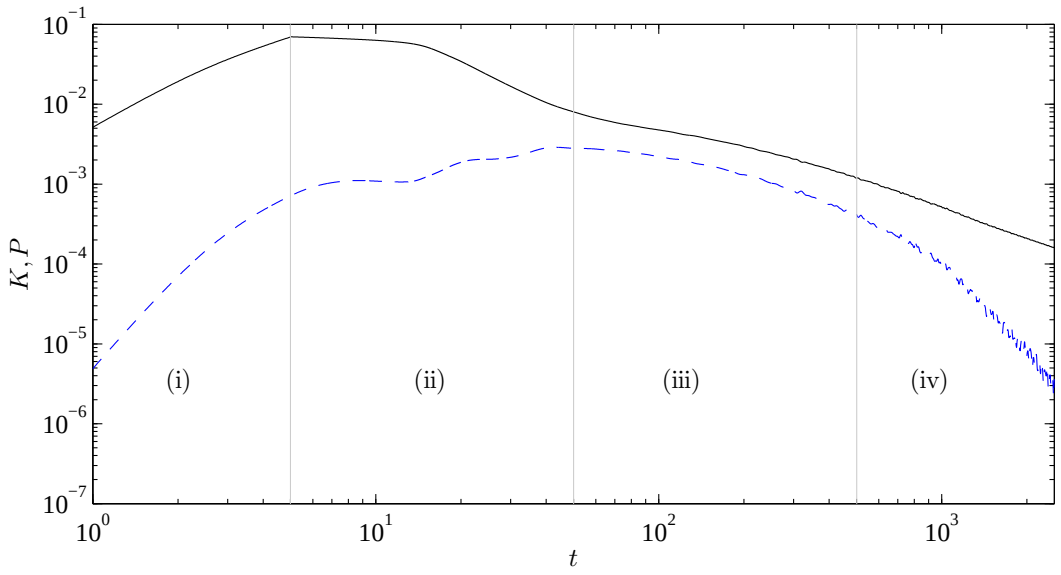

Figure 5.6: Time evolution of K (—) and P (– –) for $N = 0.2$. Plot regions (i)-(iv) indicate the same time periods as figure 5.5

.

During this additional roll up in the stably stratified case, P appears to temporarily reach a plateau, not unlike the vortex ring cases of chapter 4. Beyond $t \approx 50$, a small disparity begins to develop between K_v and K_w as instabilities develop in the leading ring and trailing jet structures, visible in 5.3(a).

As indicated in figure 5.7, the start of instability development within the leading ring is approximately coincident in time with the peak angular velocity within the ring reducing to a level below the buoyancy frequency. The angular velocity of each rotating fluid particle about its own centre of mass, ϕ', can be given as half the vorticity at that point and can be separated into individual components with

$$\begin{aligned} \phi'_x &= \omega_x/2, \\ \phi'_y &= \omega_y/2, \\ \phi'_z &= \omega_z/2. \end{aligned} \tag{5.4}$$

The instabilities appear to manifest when $|\phi'_y|_{\mathrm{Max}}, |\phi'_z|_{\mathrm{Max}} < N$. Physically speaking, this is the point at which the changes in the velocity of fluid particles due to the buoyant force term in the momentum equation ($-\theta\delta_{3i}$ in equation 2.9) occur at a faster rate than changes due to the overturning of the vortex ring core. As previously noted in the experimental work of Scase and Dalziel (2006), the trailing vortical structures behind the leading ring also develop instabilities in a similar manner, such that the whole flow structure appears to become turbulent. Initially, this newly turbulent flow regime creates further

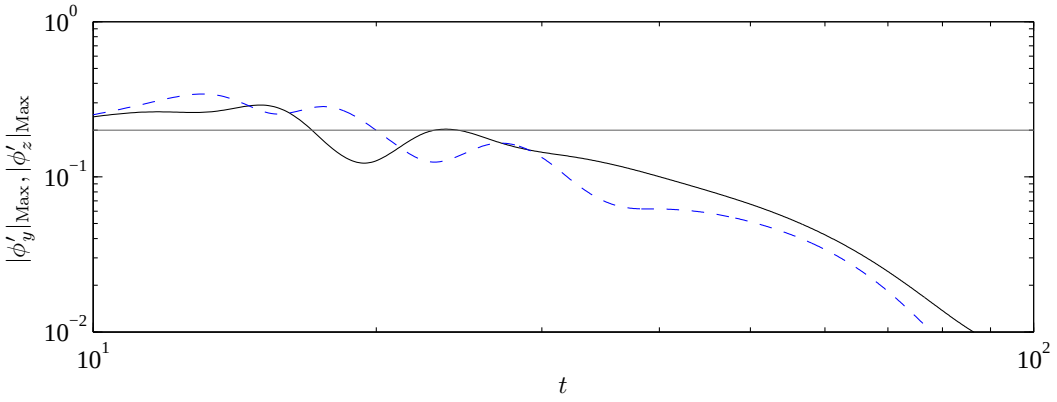

Figure 5.7: Time evolution of peak angular velocities within the leading vortex ring core. Horizontal line indicates $\phi' = N$.

buoyant displacement thanks to the increased mixing in the z direction that the smaller eddies provide. Thus between $t \approx 20$ and $t \approx 50$, K_v and K_w reduce quickly, partly due to the increased viscous dissipation associated with the small scale structures now present, and the increased transfer of energy to the buoyancy scalar field that in turn explains the rise in P.

Beyond this time, the integrated buoyancy variance within the scalar field is somewhat greater than the vertical and lateral kinetic energy components, suggesting that the inertial forces within the unstable vortex ring will become overwhelmed by the greater forces generated due to buoyant displacement. The buoyancy variance level in the domain begins to reduce as the energy is transferred back to kinetic energy field (primarily to K_w), with the vertically displaced fluid particles returning to their equilibrium layers (stage (iii) in figure5.6).

The kinetic energy is carried through the domain in the form of the buoyancy waves first observed in figure 5.3(c)(i). These waves appear to carry most of their kinetic energy and buoyancy variance away from the streamwise axis in the z direction, explaining why $K_w > K_v$ at this stage, with the majority of this energy dissipated by the fringe region at the vertical and lateral boundaries. The individual waves propagate with a straight trajectory and form a pattern that appears symmetric about both the horizontal and lateral midplanes as seen in figure 5.8. This pattern is qualitatively very similar to that observed to form around the decaying monopole of Beckers et al. (2001), with the waves initially containing a high level of kinetic energy and buoyancy variance at the onset of the collapse phase, though rapidly becoming weaker as K_w and P decay. At $t \approx 500$, the vertical kinetic energy and buoyancy variance fields quickly become depleted as the energy carried by the waves is dissipated

within the fringe region, and vertical motion within the remaining structure is almost completely suppressed. Both K_w and P quickly reduce by several orders of magnitude compared to K_u and K_v, reducing the structure to the planar flow regime described previously (stage (iv) in figure5.6). Such is the rapid reduction of w and θ throughout the flow field at the late time, we can infer that once the dipole has fully formed the buoyant field has no further influence on the future development of the structures within the domain.

5.2.2 Evolution of the vortex dipole at the late time

With the transformation from an axisymmetric flow to the vortex dipole now documented, our attention turns to how the fully formed dipole evolves at the late time and how well this relates to the dipoles created in the experimental studies mentioned previously. Figure 5.9 shows the time evolution of the two contra-rotating vortex patches characteristic of the dipole and shows that once the dipole is fully formed, it continues to grow laterally at the late time as well as propagating forward in the x direction. Although the lateral vorticity contours seen previously (figure 5.3 etc.) suggest that rotational motion persists at the late time, all motion in the domain is now quasi-horizontal. The magnitude of ω_y at any given point in the domain is dominated entirely by shear in the vertical direction i.e.

$$\omega_y = \partial w/\partial x - \partial u/\partial z \approx -\partial u/\partial z \tag{5.5}$$

as $|\partial u/\partial z| \gg |\partial w/\partial x|$, as illustrated by figure 5.10.

Using the horizontal location of the vertical vorticity maximum as a rough estimate for the centre of one of the dipole cores, a vertical profile for the buoyancy scalar through the core can be obtained at various times as shown in figure 5.11. These profiles show us that within the dipole core's vertical extent there remains fluid displaced from buoyant equilibrium, with the dense fluid above the vertical midplane giving a negative value of θ, with the lighter fluid below the midplane giving a positive value. Hence, even at the late time, there are still weak buoyant forces driving fluid towards the vertical midplane, though the magnitude of θ decays so rapidly that the forces become negligible at the late time (particularly when considered against the influence of viscous diffusion on the dipole's vertical structure). These profiles are qualitatively similar to those seen experimentally for both a stratified monopole (Beckers et al., 2001) and a stratified vortex dipole (Voropayev et al., 1991), though in those cases the profiles provided are of fluid density, rather than the profile of θ such density would yield.

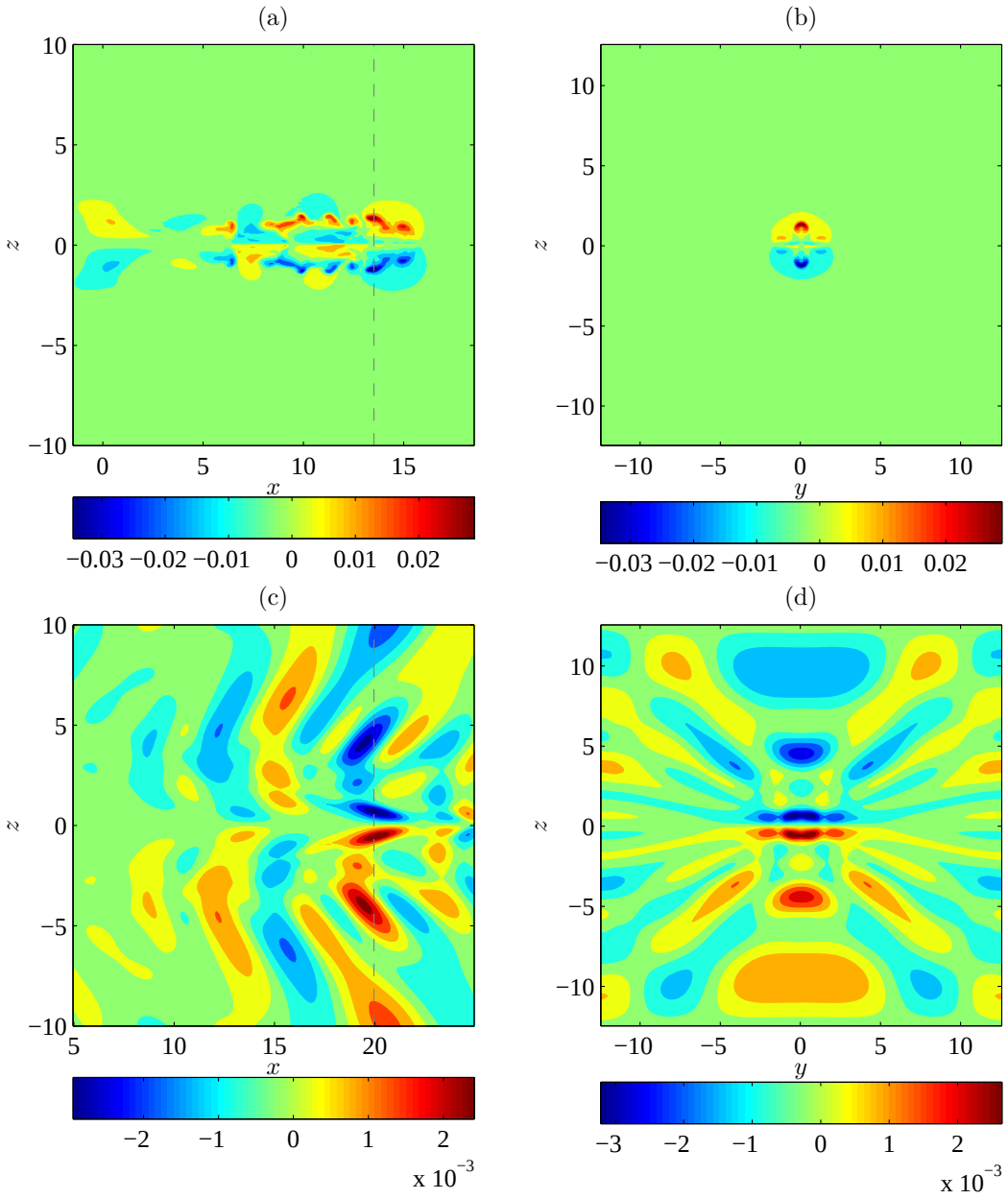

Figure 5.8: Contours of buoyancy scalar, θ at (a) $t = 26.5$, $y = 0$ (b) $t = 26.5$, $x = 13.5$ (c) $t = 159.2$, $y = 0$ (d) $t = 159.2$, $x = 19.9$. Contour levels range from the instantaneous value of $\theta|_{\text{Min}}$ (blue) to $\theta|_{\text{Max}}$ (red)). The dashed lines in (a) and (c) indicate the x coordinate of the planes presented in (b) and (d) respectively.

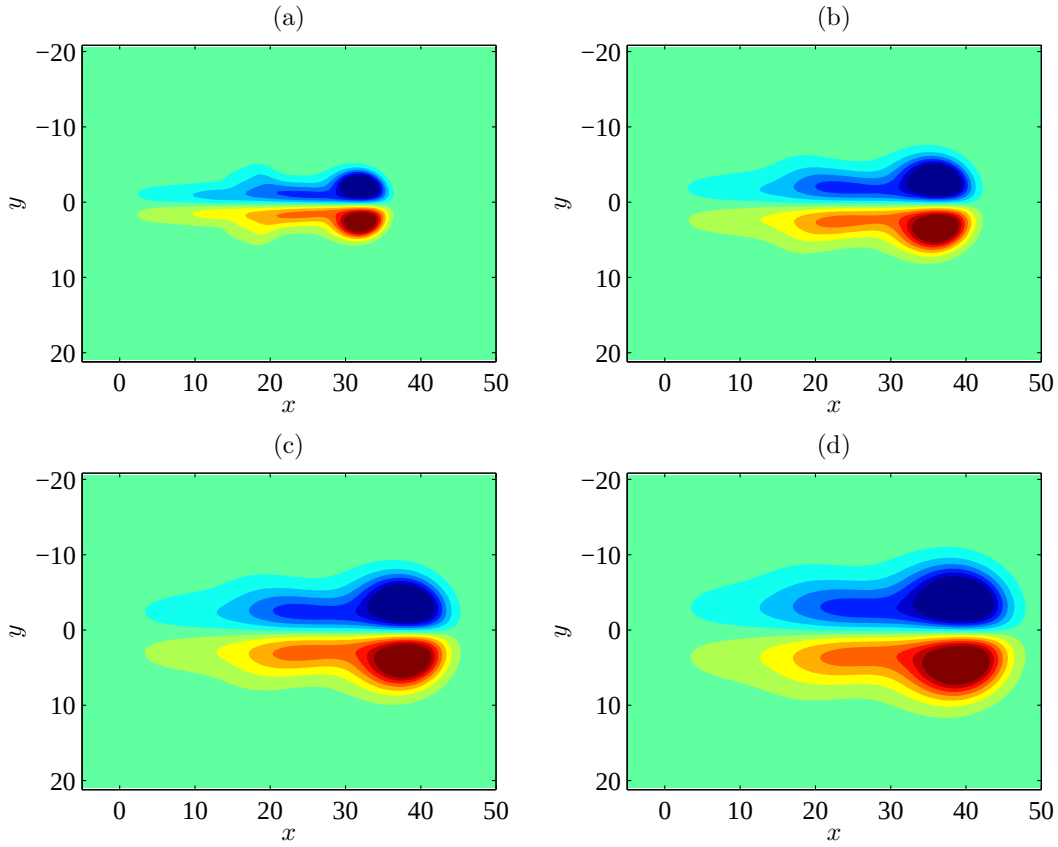

Figure 5.9: Contours of vertical vorticity, ω_z at $z = 0$ for case JLD1 at (a) $t = 1400$ (b) $t = 3506$ (c) $t = 5612$ (d) $t = 8245$. The contour levels at each time range between $\pm 0.6|\omega_z|_{\text{Max}}$.

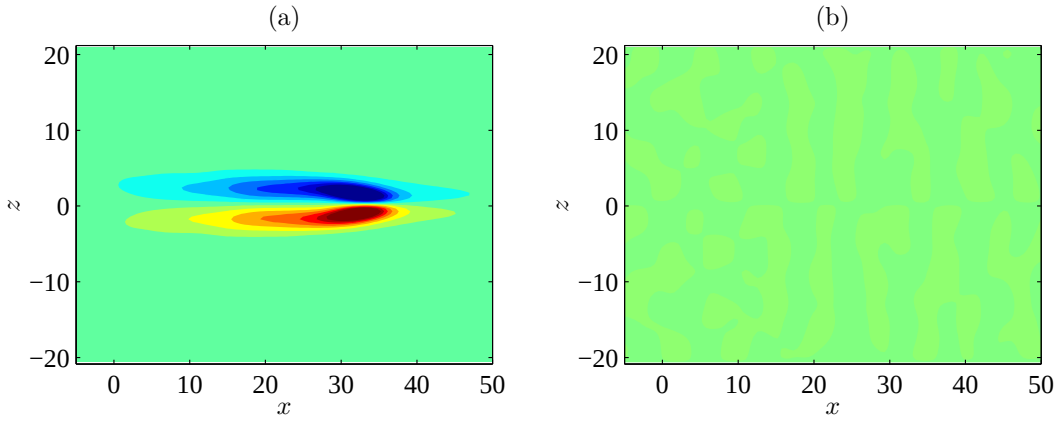

Figure 5.10: Contours of velocity gradients for case JLD1 with (a) $-\partial u/\partial z$ (b) $\partial w/\partial x$, both at $y = 0, t = 1400$. The contour levels at each time range between $\pm 0.6|\partial u/\partial z|_{\text{Max}}$. Note that $|\partial u/\partial z| \gg |\partial w/\partial x|$ at this late time such that $\omega_y = \partial w/\partial x - \partial u/\partial z \approx -\partial u/\partial z$.

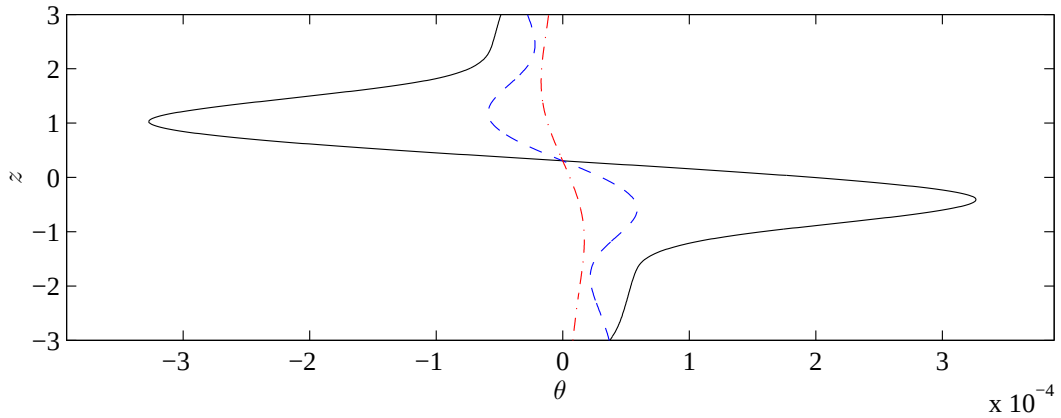

Figure 5.11: Vertical profile of buoyancy scalar, θ, passing through point where $\omega_z = \omega_z|_{\text{Max}}$ at $t = 604$ (—), $t = 1191$ (– –), $t = 2242$ (– · –).

With the basic structure of this late time dipole appearing to be comparing favourably with those seen in experiment, our attention now turns to the late time scaling behaviours of the expanding dipole to see how well it agrees with those documented in experimental works. First, we examine the dipole's streamwise centre, X_D and diameter, D_D, calculated using equations 3.6 and 3.7. To this end we can recall equations 1.15-1.16 derived from the work of Voropayev et al. (2008) i.e.

$$X_D = \alpha_X (t - t_X)^{1/3},$$

$$D_D = \alpha_D (t - t_D)^{1/3},$$

where t_X, t_D are the time offsets and α_X, α_D are the proportionality constants.

Figure 5.12 shows the time history of X_D and D_D, both raised to the third power. The plots suggest there is indeed a proportional relationship between D_D^3 and elapsed time at the late time, hence $D_D = \alpha_D (t - t_D)^{1/3}$ appears to be valid. This scaling behaviour appears to apply for $t > 2000$, with this information and examination of vorticity contours suggesting the dipole is fully formed at this point. This is approximately consistent with the sharp reduction in vertical kinetic energy and buoyancy variance between $t = 1000$ and $t = 2000$, implying that almost all vertical motion has been suppressed by this point and the structure has entered the planar flow regime. However, whilst the experimental scaling law for D_D appears to be strongly supported by this data, the same cannot be said for X_D. There appears to be reasonable agreement with the scaling law for $2000 < t < 4000$, but beyond this time the dipole propagation rate is somewhat lower than predicted, suggesting that both the assertion $X_D \propto t^{1/3}$ and subsequently $X_D \propto D_D$ are invalid at the late time.

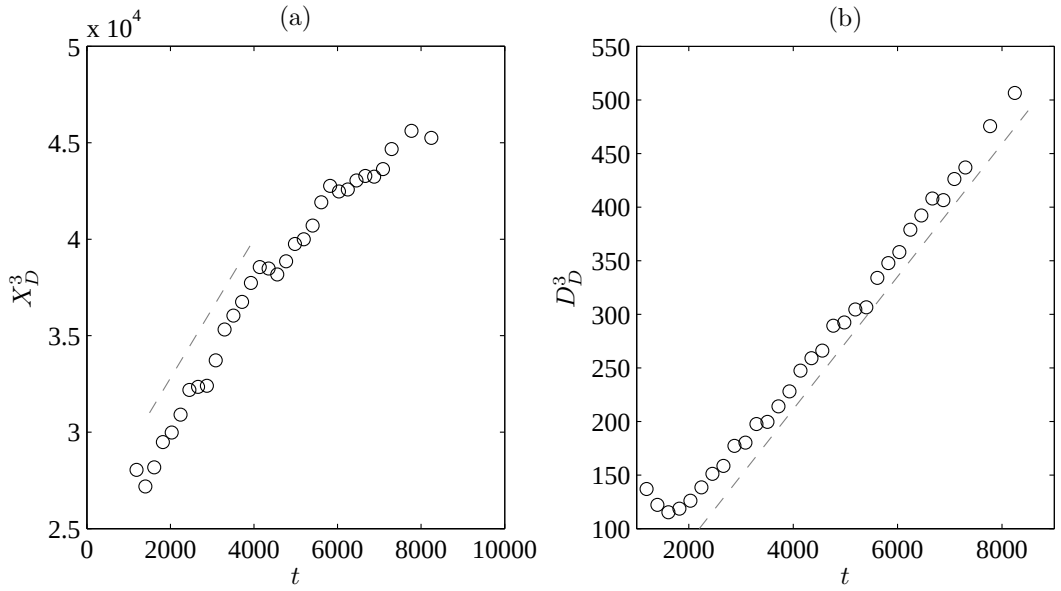

Figure 5.12: Time history of dipole streamwise location and horizontal diameter, both raised to their third power to demonstrate potential agreement with experimentally derived scaling laws. (a) Streamwise location, X_D^3 (b) Dipole diameter, D_D^3. The dashed lines have constant gradients, demonstrating that $X_D \propto t^{1/3}$ for $2000 < t < 4000$ and $D_D \propto t^{1/3}$ for $t > 2000$.

The next scaling law we consider is the rate of decay of peak vertical vorticity within the dipole, with Voropayev et al. (2008) reporting a scaling law of $\omega_z|_{\text{Max}} = \alpha_\omega t^{-1}$, where $\alpha_\omega \approx 17$ for all cases. The reciprocal relationship for the case JSD1 is plotted in figure 5.13(a). For the majority of the simulation time, up until $t \approx 6000$, the agreement with the proposed scaling law is poor, with the shallower gradient implying vorticity is decaying more slowly than expected long after figure 5.12(b) implies the dipole has become fully formed. Beyond $t \approx 6000$ the data appears to asymptote to a straight line to give agreement with equation 1.18

$$\omega_z|_{\text{Max}} = \alpha_\omega (t - t_\omega)^{-1}, \tag{5.6}$$

where t_ω is the time axis intercept for this relationship as t_D was for equation 1.16. The value of α_ω found for this case was 3.11, less than one fifth the value of 17 previously reported. Another approach to considering the vorticity decay is to consider the evolution an integral quantity such as vertical enstrophy i.e.

$$\Omega_z = \int_V \omega_z^2 \mathrm{d}V. \tag{5.7}$$

Such an integral quantity gives a more representative picture of how the vorticity evolves throughout the domain, rather than at a single grid point. If we assume that, rather than $\omega_z|_{\text{Max}} \propto t^{-1}$, the volume integral of vertical

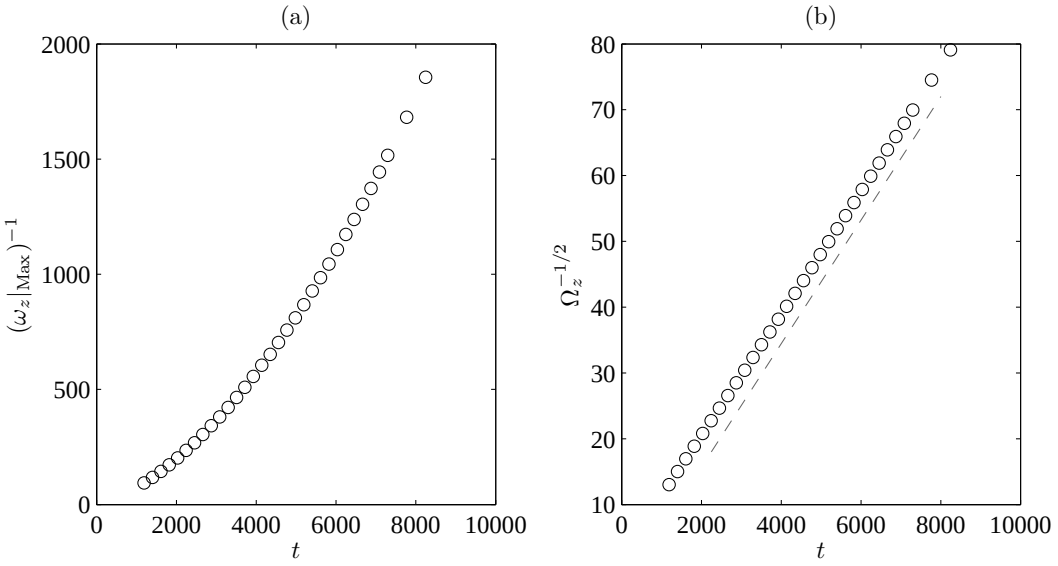

Figure 5.13: Time histories of dipole maximum vertical vorticity and total vertical enstrophy levels indicating agreement with expected scaling behaviour, with (a) $(\omega_z|_{\mathrm{Max}})^{-1}$ (b) $\Omega_z^{-1/2}$. The dashed line in (b) indicates that, for the late time dipole, $\Omega_z \propto t^{-2}$.

vorticity within either the left or right half of the dipole inversely proportional to time instead, this in turn would imply

$$\Omega_z \propto t^{-2}. \tag{5.8}$$

Such a relationship is strongly supported by figure 5.13(b).

Next, we consider the thickness of the fully formed dipole to determine whether it has an approximately constant thickness, or expands vertically with time. Examination of the lateral vorticity contours over time would suggest the dipole does indeed grow vertically with time, but this can be verified in a more quantitative fashion by considering the vertical vorticity profile through the dipole. As demonstrated by Flór et al. (1995) and Praud and Fincham (2005), a fully formed dipole has a Gaussian vorticity profile in the vertical direction at any given time, with

$$\frac{\langle\omega_z\rangle_{\mathrm{Max}}}{\omega_z|_{\mathrm{Max}}} = \exp\left(-\frac{z^2}{2(H_\omega/2)^2}\right),$$

where $\langle\omega_z\rangle_{\mathrm{Max}}$ is the maximum vertical vorticity for a given altitude, z within the dipole and H_ω is the dipole's vorticity thickness (i.e. the "width" of the Gaussian profile). From equation 1.22, we have previously deduced that according to the diffusion model,

$$\exp\left(-\frac{z^2}{2(H_\omega/2)^2}\right) = \exp\left(-\frac{z^2}{4\nu t}\right),$$

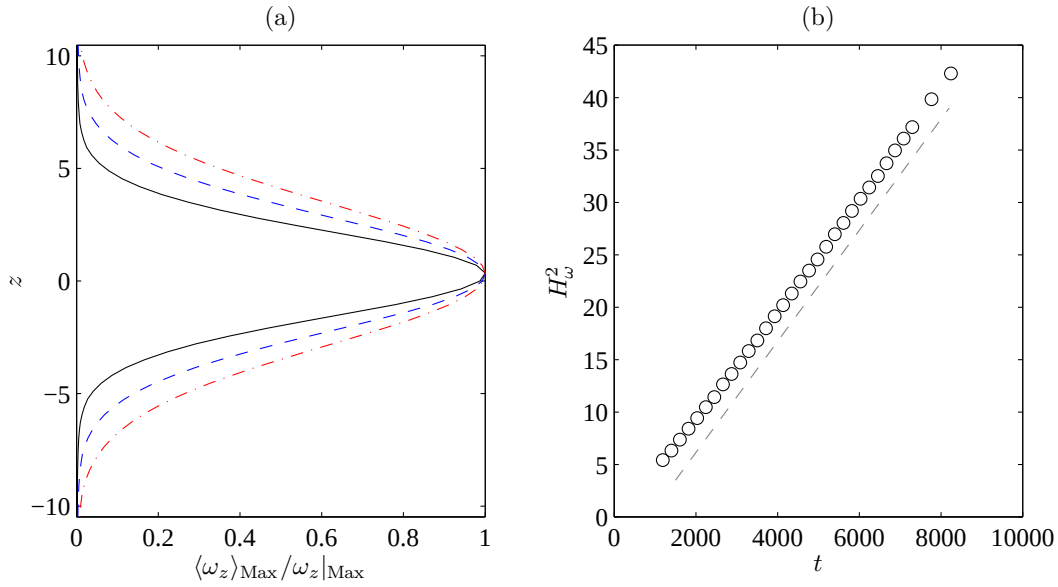

Figure 5.14: (a) Vertical profiles of normalised vertical vorticity through the dipole core at t = 3295 (—), t = 5612 (−−), t = 8244 (−·−) (b) Evolution of the square of the same dipole's vorticity thickness, H_ω, with time. The dashed line has a constant gradient, demonstrating $H_\omega \propto t^{1/2}$.

and thus, recalling that in the non-dimensional form $\nu = 1/Re$, we find the model's prediction for dipole thickness as it evolves in time according to equation 1.23 i.e.

$$H_\omega = 2\sqrt{2}\left(\frac{t}{Re}\right)^{1/2} \approx 2.828\left(\frac{t}{Re}\right)^{1/2}.$$

The multiplier, $2\sqrt{2} \approx 2.828 = \alpha_H$ is a universal constant predicted by the model. Figure 5.14(a) demonstrates the Gaussian vorticity profile through the dipole at three times after the dipole appears to be fully formed. The gradual vertical expansion of the dipole can be inferred from the increasing width of the profile with time and thus the constant thickness dipole condition reported in Voropayev et al. (1991) is not valid according to these simulations. By using a Gaussian fitting function on this profile at any given time, the time history of H_ω can be determined, with the history of H_ω^2 plotted in figure 5.14(b) to demonstrate $H_\omega^2 \propto (t - t_H)$ where t_H is the time axis offset for equation 1.23. The agreement of the simulated dipole to this particular scaling law is by far the best seen so far, with a near exact linear relationship between H_ω^2 and t. From the gradient of this line, and using Re = 1400, the value of α_H returned for this case is approximately 2.784. This is less than 2% lower than the value given by the diffusion model, suggesting further good agreement with equation 1.23, though it is prudent to examine the value of α_H from the other cases before drawing a firm conclusion.

5.2.3 Influence of Reynolds number

By analysing the results of cases JLD2 and JLD3 (with $Re = 800, 2000$ respectively) in the same way as JLD1 ($Re = 1400$), we can evaluate the effect of Reynolds number on both the early and late time development of a dipole from the impulsive momentum injection. Figure 5.15 compares the kinetic energy and buoyancy variance histories for these three cases from just before t_J until after the late time buoyant collapse. We can see from this that during the injection phase, the lateral and vertical kinetic energy levels are higher with increased Reynolds number, in part due to the lower rate of dissipation of kinetic energy from the leading vortex ring. The magnitude of the differences between cases are relatively small compared to the total energy level and do not represent any significant difference in behaviour between cases. As with JLD1, the other two cases appear to maintain quasi-axisymmetry throughout the injection phase and for a short time afterward.

Beyond $t \approx 10$, the same figure shows a more rapid drop in streamwise kinetic energy is noted for $Re = 1400, 2000$ than is seen for $Re = 800$. Recalling the earlier comparison of K_u for a neutrally and stably stratified case seen in figure 5.5, similarities can be drawn between the $Re = 800$, stably stratified case and the $Re = 1400$, neutrally stratified case. Both have K_u levels higher than the $Re = 1400$, $N = 0.2$ case for a period of 50 to 100 time units beyond $t = 10$. Examination of vorticity contours for all cases at various times reveal that for the $Re = 1400, 2000$ cases, small scale structures develop within the leading ring and trailing jet after $t \approx 10$ that are not seen for either $Re = 800$ or the neutrally stratified case. A possible explanation for this is that the stably stratified cases introduce a slight ellipticity into the leading ring, with the lateral radius larger than the vertical radius due to slight buoyant supression of vertical growth during the injection. For the higher Reynolds number cases, the combination of ring ellipticity and lower viscosity may be sufficient for development of the elliptical instability proposed by Kerswell (2002) and documented in the numerical simulations of Archer et al. (2008) for an isolated vortex ring. Such instabiltiies may be developed further through the concurrent buoyant instabilties introduced by the vertical displacement of fluid creating a locally unstable density profile within the leading ring. Whichever instability mechanism is the more dominant, the breakdown of the coherent ring and trailing jet structure into smaller vortical motions that are more susceptible to viscous dissipation is observed in all three cases.

The presence of small scale structure for $Re = 1400, 2000$ but not for $Re = 800$ is also consistent with the vertical kinetic energy levels seen in figure 5.15(c)

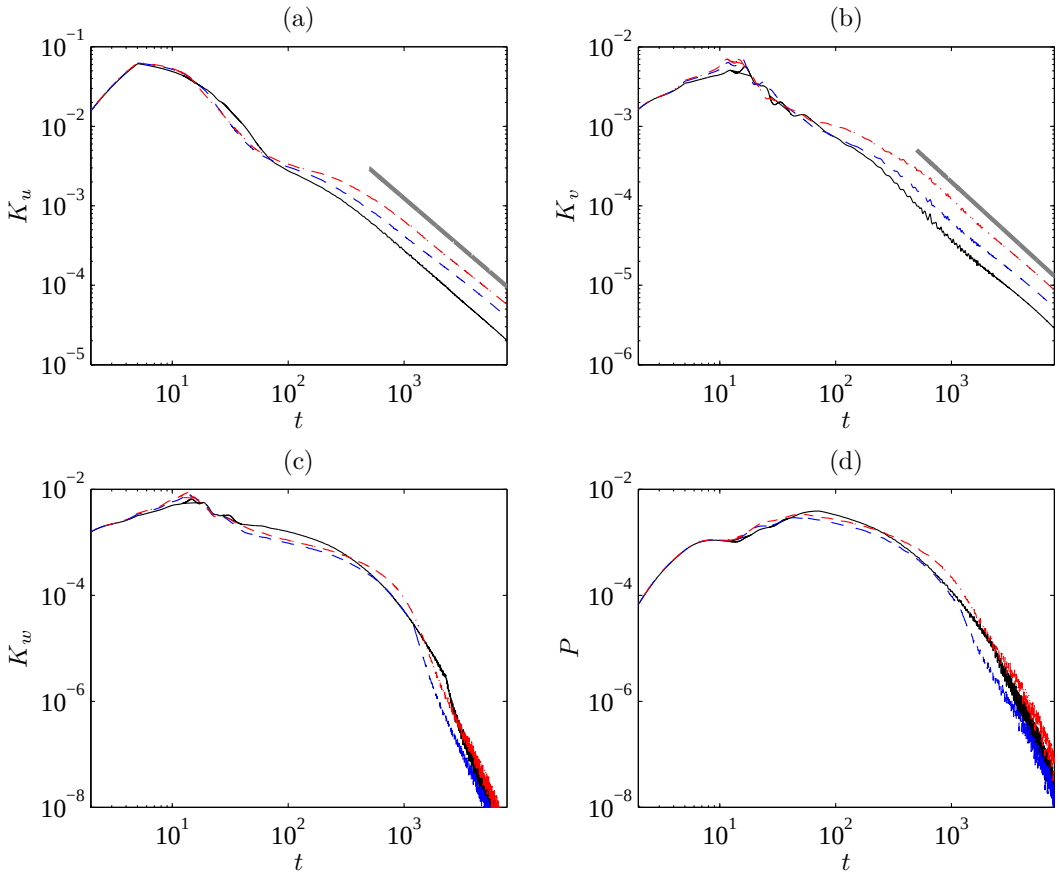

Figure 5.15: Kinetic energy and buoyancy variance histories from momentum injection phase to late time dipole phase for Re = 800 (—), Re = 1400 (−−), Re = 2000 (−·−). (a) Streamwise kinetic energy (b) Lateral kinetic energy (c) Vertical kinetic energy (d) Buoyancy variance. The thick lines in (a) and (b) indicate that at the late time $K_u \propto t^{-5/4}$ and $K_v \propto t^{-4/3}$ respectively.

between $t = 10$ and $t = 100$, which show both the higher Reynolds number cases having lower vertical kinetic energy, with the $Re = 2000$ case being marginally the more energetic. As with K_u, the smaller scale structure in these cases is more susceptible to viscous dissipation. Additionally, the increased mixing in these cases increases the local magnitude of θ and hence the rate of energy transfer from K_w to P is increased slightly, explaining the higher levels of P seen for $10 < t < 60$. The lateral kinetic energy (figure 5.15(b)) also experiences a more rapid decline at this stage for the higher Reynolds number cases, though as both have a higher level of K_v prior to $t \approx 10$, the subsequent drop in energy level brings the value of K_v in both cases back in line with that seen for $Re = 800$, rather than dropping significantly below it as seen with K_u, K_w.

Beyond $t = 100$, the merging of smaller scale motions to form the large, coherent dipole structure in each case brings the length and velocity scales for both the lower and higher Reynolds number cases back to comparable levels, such that the effects of viscosity, in the horizontal plane at least, are easier to explain, with K_u and K_v reducing according to power laws in time that seem consistent across all three cases with

$$K_u \propto t^{-5/4}, \tag{5.9}$$

$$K_v \propto t^{-4/3}, \tag{5.10}$$

as indicated in figures 5.15(a) and 5.15(b). The flow at this late stage has entered a diffusion dominated regime, with the streamwise and lateral kinetic energy levels persisting for a greater time at higher Reynolds number. The vertical kinetic energy and buoyancy variance rapidly reduce at the late time in all cases, with the start of the final, rapid decay roughly coincident for the higher Reynolds number cases at $t \approx 1000$. The $Re = 800$ case undergoes a slightly different behaviour, with an earlier starting ($t \approx 500$) but more gradual decay of these energy levels, before becoming approximately coincident with the other cases at the latest times observed.

Figure 5.16 illustrates the late time structure of the dipole from the three cases at roughly comparable times after injection (as the simulation prescribes its own time step by this point, it is difficult to extract full domain velocity fields at precisely coincident times). A clear progression in shape can be seen from the lower to higher Reynolds number cases, with $Re = 800$ giving a more "bulbous" appearance than $Re = 1400$, with $Re = 2000$ giving the most "compact" appearance of the three. As will be explored further, the dipole has entered a diffusive state by this point in time, with the lower Reynolds number cases expanding more quickly in the vertical and horizontal direction than the

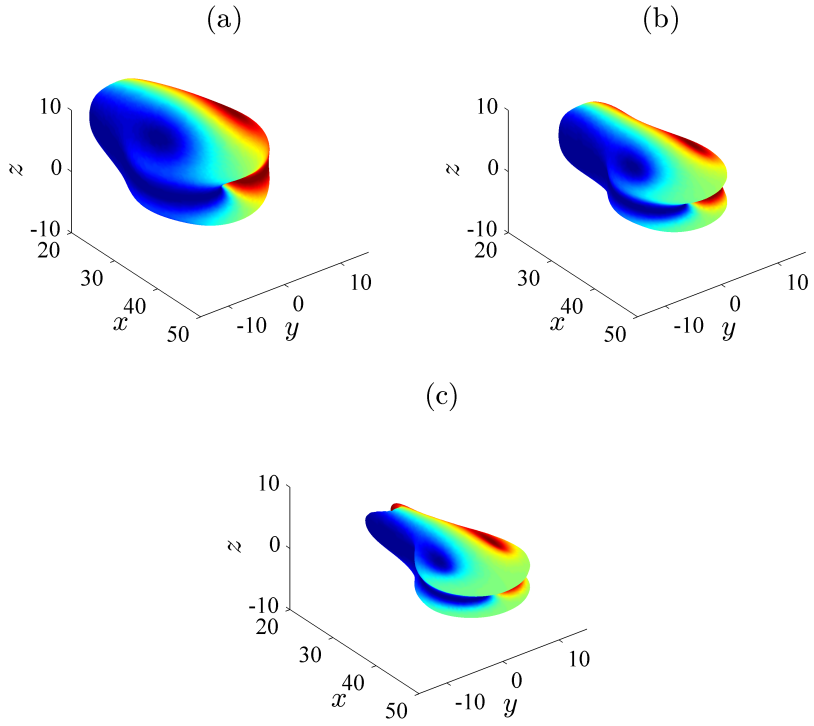

Figure 5.16: Isosurfaces of constant vorticity magnitude, $|\omega|$ for $N = 0.2$ at $t = 3410$, demonstrating the structure of the late time dipole for (a) $Re = 800, t = 5550$ (b) $Re = 1400, t = 5402$ (c) $Re = 2000, t = 5370$. Colour contouring ranges between $\pm 0.6|\omega_z|_{\text{Max}}$, with isosurface threshold set at $0.2|\omega|_{\text{Max}}$.

higher Reynolds number cases. The aspect ratio of the dipole can be defined as

$$\alpha_{HD} = \frac{H_\omega}{D_D}, \tag{5.11}$$

with the value of α_{HD} clearly larger for the lower Reynolds number cases than the higher Reynolds number cases at comparable times.

The histories of dipole streamwise centre and diameter for all three cases, calculated again using equations 3.6-3.7, are plotted in figure 5.17, along with lines indicating the required logarithmic gradient for $X_D \propto D_D \propto t^{1/3}$. While the dipole diameter indicates reasonable agreement with the expected scaling behaviour at the late time for all three cases, the dipole's streamwise centre does not, with the three cases all giving significantly different scaling with time, and all moving somewhat more slowly than predicted by $X_D \propto t^{1/3}$. Assuming that the flow seen here is representative of the dipoles seen in experimental studies, the discrepancy originates either from the method of calculating X_D or the assumption that it is proportional to $t^{1/3}$.

Firstly, with regard to calculating X_D using equation 3.6, the centre of the

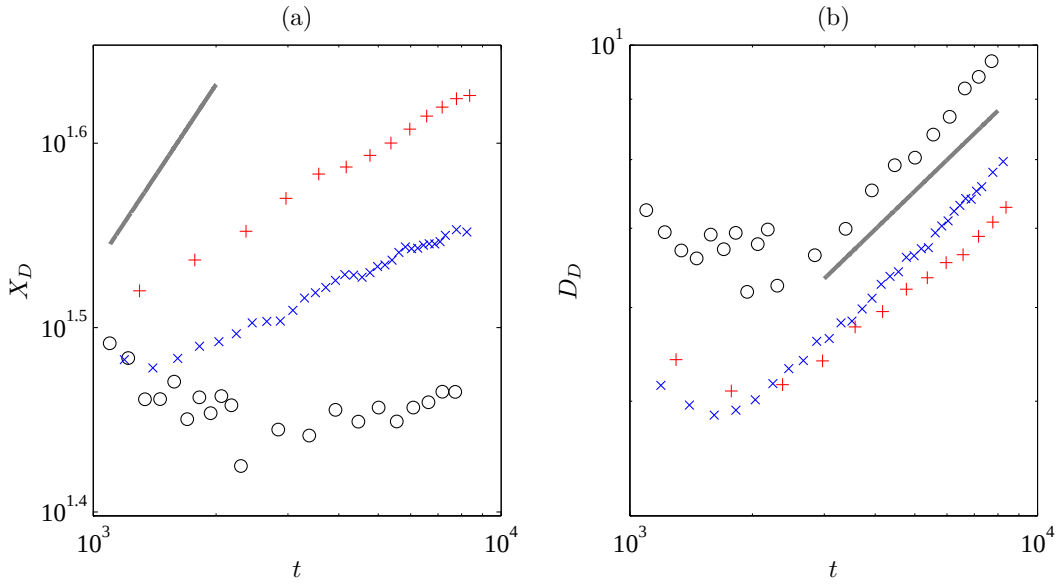

Figure 5.17: Time history of (a) dipole streamwise centre and (b) diameter, for$Re = 800$ (○), $Re = 1400$ (×), $Re = 2000$ (+). The thick lines in (a) and (b) indicate the required gradients for $X_D \propto t^{1/3}$ and $D_D \propto t^{1/3}$ respectively.

dipole will be calculated as the weighted centre of vorticity. For a circular dipole, with a vorticity distribution akin to the Lamb-Chaplygin model, this centre will lie exactly halfway between the two maximum/minimum vorticity poles. However, as seen throughout the visualisations in this chapter, the dipoles comprise both a front region, resembling a circular dipole, as well as a tail region extending behind it that becomes progressively longer with time (see figure 5.9). The vorticity contained within the tail is notably weaker than in the front region, but still significant enough to bring the calculated position of X_D behind the expected location between the poles. Additionally, while the front region propagates downstream, the tail does not (or does so at an extremely slow rate by comparison). As a consequence, this gives the impression of the dipole propagating more slowly, as a sizable proportion of its vorticity remains stationary. In order to overcome this, X_D and D_D are recalculated, but this time all points that have a vorticity magnitude lower than 50% of the maximum vorticity magnitude within the flow field are excluded from the volume integration. The practical effect of setting this threshold is illustrated in figure 5.18, which shows that this choice of threshold isolates the vorticity within the front region and excludes the tail. It leaves behind two columnar regions of contra-rotating flow, bounded top and bottom by two layers of horizontal shear between the columns and the quiescent fluid above and below it. The trend of a lower Reynolds number giving a larger vertical length scale compared to the horizontal seen in figure 5.16 are repeated for the

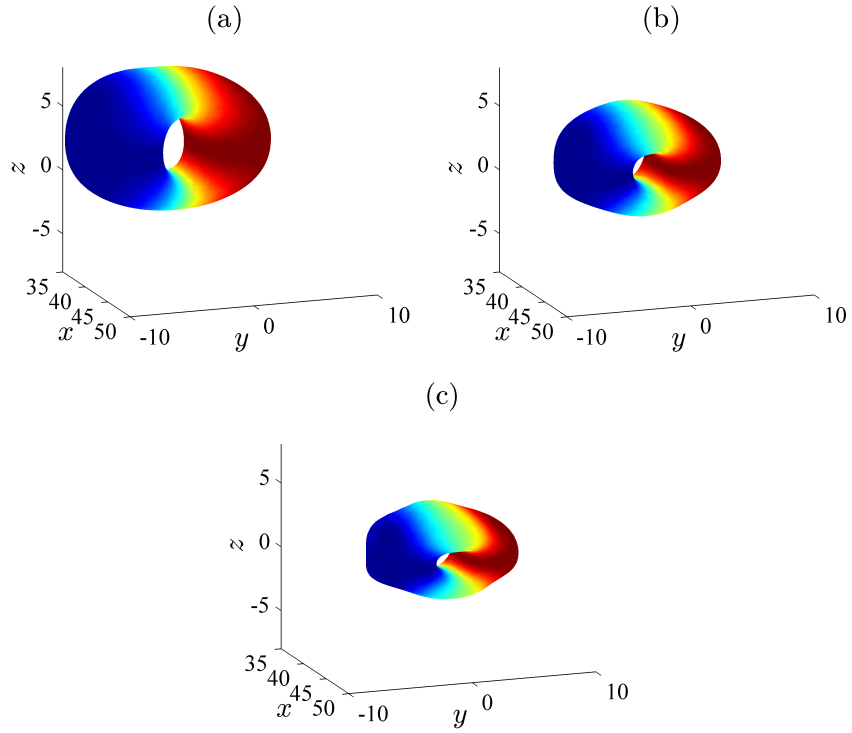

Figure 5.18: As figure 5.15 but with isosurface threshold set at $0.5|\omega|_{\text{Max}}$. Zoom level and viewing angle have been changed slightly to help demonstrate dipole core structure.

isolated dipole core.

Using this approach, much improved agreement was found with the expected scaling behaviour as indicated in figure 5.19, with the values of $\alpha_X, \alpha_D, t_X, t_D$ given in table 5.4. These values were fitted to the late time data available for each case (typically the last 5-6 markers in each plot) using a least-squares type fitting routine. The magnitude of t_X yielded by the three cases makes plotting the X_D vs. $t-t_X$ relationship for all three cases impractical on a single set of logarithmic axes, so these are distributed across figure 5.19(a)-(c), with D_D vs. $t-t_D$ given in figure 5.19(d) for all three cases.

Case	Re	α_X	t_X	α_D	t_D	Plot marker
JLD2	800	0.676	-79523	0.480	1852	○
JLD1	1400	1.194	-25146	0.365	1491	×
JLD3	2000	1.629	-12530	0.323	1511	+

Table 5.4: Constants of proportionality and time offsets for X_D and D_D time scaling plotted in figure 5.19.

A significant improvement in agreement for both scaling laws is found compared to that seen in figure 5.17. Of the two, the scaling behaviour for diameter appears to conform to equation 1.16 from a much earlier stage in all three simulations than the agreement for dipole position, which does approach the expected behaviour (equation 1.15) but appears to asymptote towards it at the late time rather than following a consistent scaling behaviour for an extended period. However, the agreement in scaling law behaviour for streamwise position is apparently much improved when the time offset for the scaling law is chosen to be t_D rather than t_X, with this improved agreement apparent in figure 5.20. This would suggest that the dipole evolution in the horizontal plane for these simulations is consistent with that observed by Voropayev et al. (2008) and related studies.

As inferred by the isosurfaces in figure 5.18, the lower Reynolds number dipole propagates more slowly and expands more quickly than a higher Reynolds number dipole. For each case, we can compare ratio of D_D to X_D to value $\alpha_{XD} = D_D/X_D = 0.23$ reported in Voropayev et al. (2008). Here we can define the ratio as

$$\alpha_{XD} = \frac{\alpha_D}{\alpha_X}, \tag{5.12}$$

which yields values of 0.710, 0.305 and 0.192 for $Re = 800, 1400, 2000$ respectively, suggesting a strong Reynolds number dependence of α_{XD} not reported in the experimental study, possibly due to the comparatively narrow range of Re_J investigated (650-1135). On closer examination of the data seen in figure 4 of Voropayev et al. (2008), it can be seen that the $D_D = 0.23X_D$ prediction, which was determined from a case with $Re_J = 850$, slightly over predicts D_D for cases with higher Re_J and under predicts D_D for cases with lower Re_J (all have roughly equivalent values of t_J and N).

Figure 5.22 gives the decay of maximum vertical vorticity within the dipole for each of the three cases to investigate whether agreement is found with the assertions of Voropayev et al. (2008), previously given as equation 1.18 i.e.

$$\omega_z|_{\text{Max}} = \alpha_\omega (t - t_\omega)^{-1},$$

where α_ω and t_ω are the scaling coefficient and time offset similar to those used for equations 1.15 and 1.16. As was the case for dipole position given in figures 5.19(a)-(c), agreement with the scaling law is found at the late time, though once again the agreement appears asymptotic as opposed to the sustained agreement seen for lateral growth in figure 5.19(d).

Next, we consider the vertical growth of the three dipoles over time. As discussed previously with equation 1.23, the diffusion model predicts that at

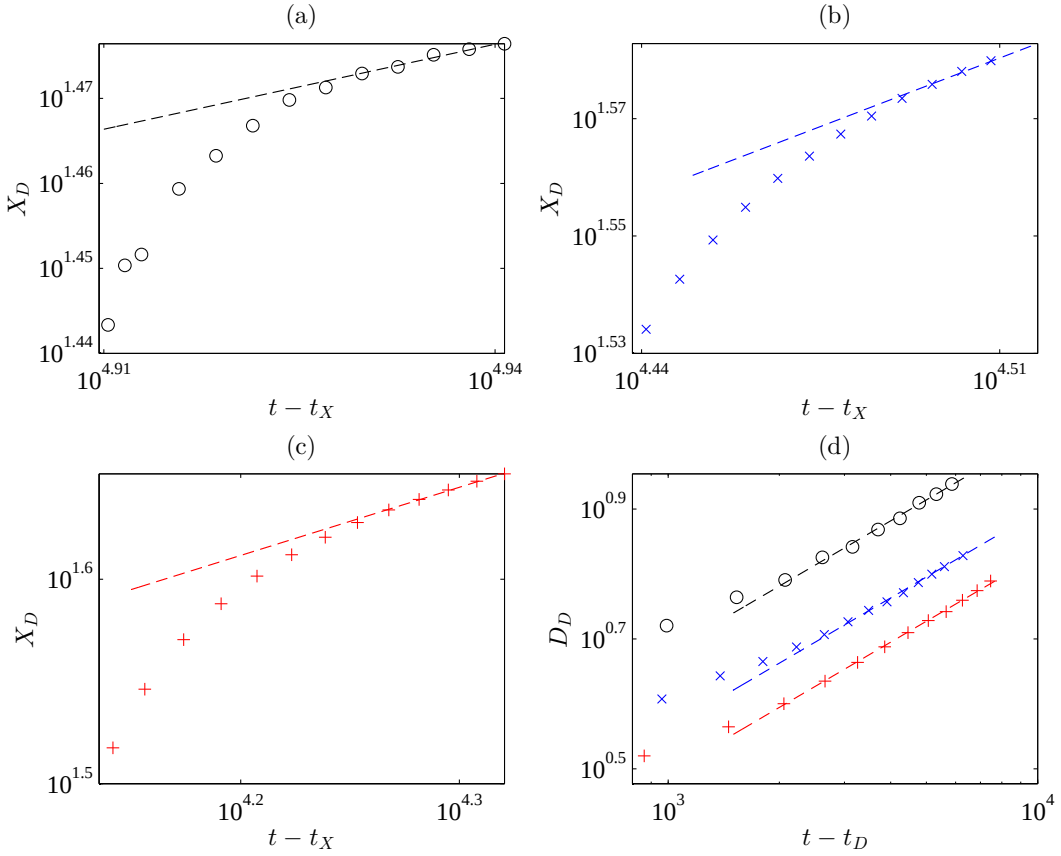

Figure 5.19: Time history of (a)-(c) dipole streamwise centre (d) dipole diameter for all three cases; Re = 800 (○), Re = 1400 (×), Re = 2000 (+). The dashed lines in each plot correspond to a best fit of the late time data corresponding to equations 1.15-1.16, with gradient and time offsets given in table 5.4.

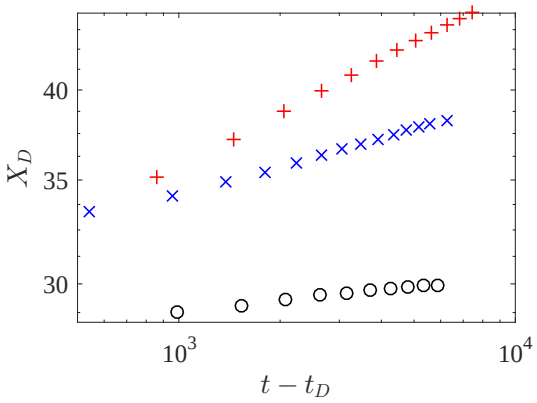

Figure 5.20: Time history of dipole streamwise centre for all three cases; Re = 800 (○), Re = 1400 (×), Re = 2000 (+). In this plot, the offset on the time axis has been set to each case's value of t_D, rather than t_x.

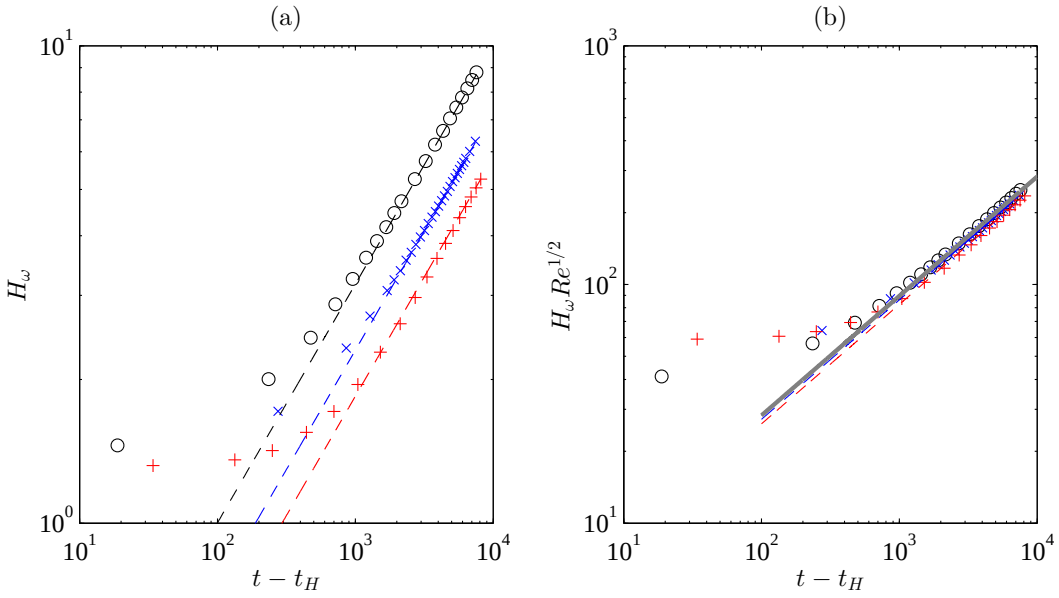

Figure 5.21: Time history of (a) dipole vertical thickness, H_ω (b) the same thickness multiplied by $Re^{1/2}$, for Re = 800 (○), Re = 1400 (×), Re = 2000 (+). The solid line in (b) indicates $H_\omega Re^{1/2} = 2\sqrt{2}(t - t_H)^{1/2}$.

the late time the dipole expands vertically such that its horizontal length scale, H_ω can be determined as $H_\omega = 2\sqrt{2}((t-t_H)/Re)^{1/2}$, a prediction supported by the results seen in figure 5.14. Figure 5.21(a) shows the relative size of the three dipoles as they evolve over time, with the three cases all giving $H_\omega \propto t^{1/2}$. As expected, the lower Reynolds number cases expand more quickly in the vertical direction due to the increased vertical diffusion of vorticity.

Figure 5.21(b) plots the same data, but now multiplied by the corresponding value of $Re^{1/2}$ for each case. According to the model, the gradient of these lines should equal $2\sqrt{2}$, with a line of $H_\omega Re^{1/2} = 2\sqrt{2}(t - t_H)^{1/2}$ plotted alongside the simulation data. Based on this plot, the diffusion model of Flór et al. (1995) appears to give an excellent prediction for the vertical growth of the vortex dipoles for different Reynolds number. The value of α_H and t_H for each case is given in table 5.5. The percentage difference between the measured α_H and the $2\sqrt{2}$ prediction is relatively small for each case, being largest for Re = 2000. This discrepancy can be reduced by evaluating the value of α_H from only the latest 2-3 data points rather than the latest 5-6, as the scaling behaviour does not precisely conform to $H_\omega \propto t^{1/2}$ until the very latest times observed. The delay in conforming to the scaling law arises due to the higher Reynolds number allowing the inertial effects within the dipole structure to persist longer before they are dominated by viscosity at the late time.

Figure 5.22 shows that, as would be expected, the lower the Reynolds num-

Case	Re	α_H	$\pm\%$ of $2\sqrt{2}$	t_H	Plot marker
JLD2	800	2.862	+1.2%	42	○
JLD1	1400	2.784	-1.6%	478	×
JLD3	2000	2.667	-5.7%	619	+

Table 5.5: Constants of proportionality and time offsets for $H_\omega Re^{1/2}$ time scaling plotted in figure 5.21(b).

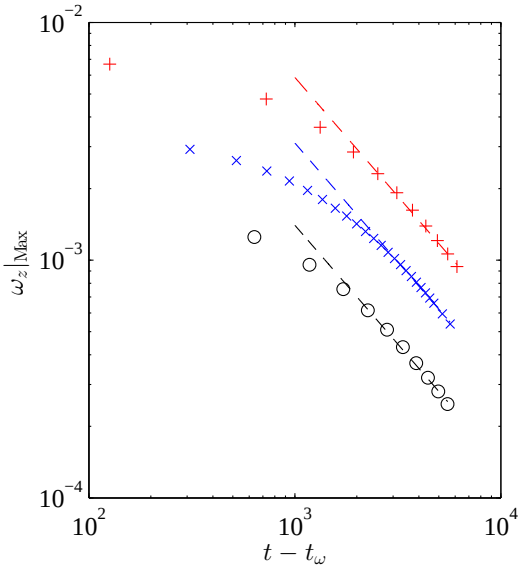

Figure 5.22: Time history of maximum vertical vorticity for Re = 800 (○), Re = 1400 (×), Re = 2000 (+). The dashed lines in each plot correspond to a best fit of the late time data corresponding to $\omega_z|_{\mathrm{Max}} = \alpha_\omega (t - t_\omega)^{-1}$.

ber, the more quickly the peak vorticity has decayed. The angular momentum within the dipole cores is more quickly spread at lower Reynolds number due to increased entrainment and dissipation of the expanding dipole, with a corresponding faster drop in the maximum vorticity.

5.2.4 Influence of stratification strength and additional impulse

With the influence of Reynolds number having been considered, the next step is to evaluate the effects of increasing stratification strength. Figure 5.23 details the time history of the kinetic energy and buoyancy variance levels in the domain for the case JLD1 (with $N = 0.2$) and the case JLD4 ($N = 1.0$). Unlike the previous comparison for different Reynolds numbers, there is a qualitative

difference in behaviour during the injection phase of the two simulations. For N = 0.2, the injection duration t_J is considerably less than the period of a single buoyant oscillation with $Nt_J/2\pi \approx 0.159$. For N = 1.0, $Nt_J/2\pi \approx 0.796$, such that well over half a buoyant cycle has passed during the injection. As a consequence, the motions induced by buoyant forces have a more pronounced effect during the injection phase for N = 1.0, with the result being a notable break in axisymmetry indicated by the values of K_v and K_w shortly before t_J. The rate of increase of K_w slows as the vertical motions within the leading ring and trailing jet are partly suppressed by buoyant forces. As the rate of kinetic energy input from the momentum injection is virtually identical between the two cases, the energy that is lost from K_w is transferred instead to both increased K_v and P. After the injection phase, the two cases give similar trends in energy histories through the collapse and internal wave generation phase, albeit with N = 1.0 the changes in behaviour occur at an accelerated rate compared to N = 0.2.

The buoyancy variance level is higher during the collapse phase for N = 1.0 as, assuming that during the vertical displacement of any given fluid particle is similar between the two cases, the stronger background density gradient means that the value of ρ' and hence θ is higher. Interestingly, the three kinetic energy components have higher values during this phase as well, though drop to levels comparable with N = 0.2 at the late time. From this we can infer a more energetic internal wave field being generated during the collapse phase, which is consistent with the elevated value of P. The late time trends of K_u and K_v were found to be very similar to those indicated in figure 5.15.

Figure 5.24 re-plots the data from figure 5.23(c)-(d) on a modified time axis, which now gives the elapsed time in terms of the number of buoyant periods that have elapsed since the end of the injection. The final collapse of the vertical kinetic energy and buoyancy variance at the late time occurs for both cases approximately 30-40 buoyant periods after injection. The differences seen in 5.23 and the similarity seen here indicate that during the injection, quasi-axisymmetric and collapse phases of the flow evolution, the changes in behaviour can be attributed to the point along the non-dimensional time scale Nt.

Isosurfaces comparing the structure of the late time dipoles at similar times for these cases are given in figure 5.25, along with a third indicating the effect of increased t_J (case JLD5). The dipole produced with N = 1.0 appears slightly more compact than N = 0.2, with a smaller diameter. A possible explanation for this is that, with the collapse phase being accelerated for higher

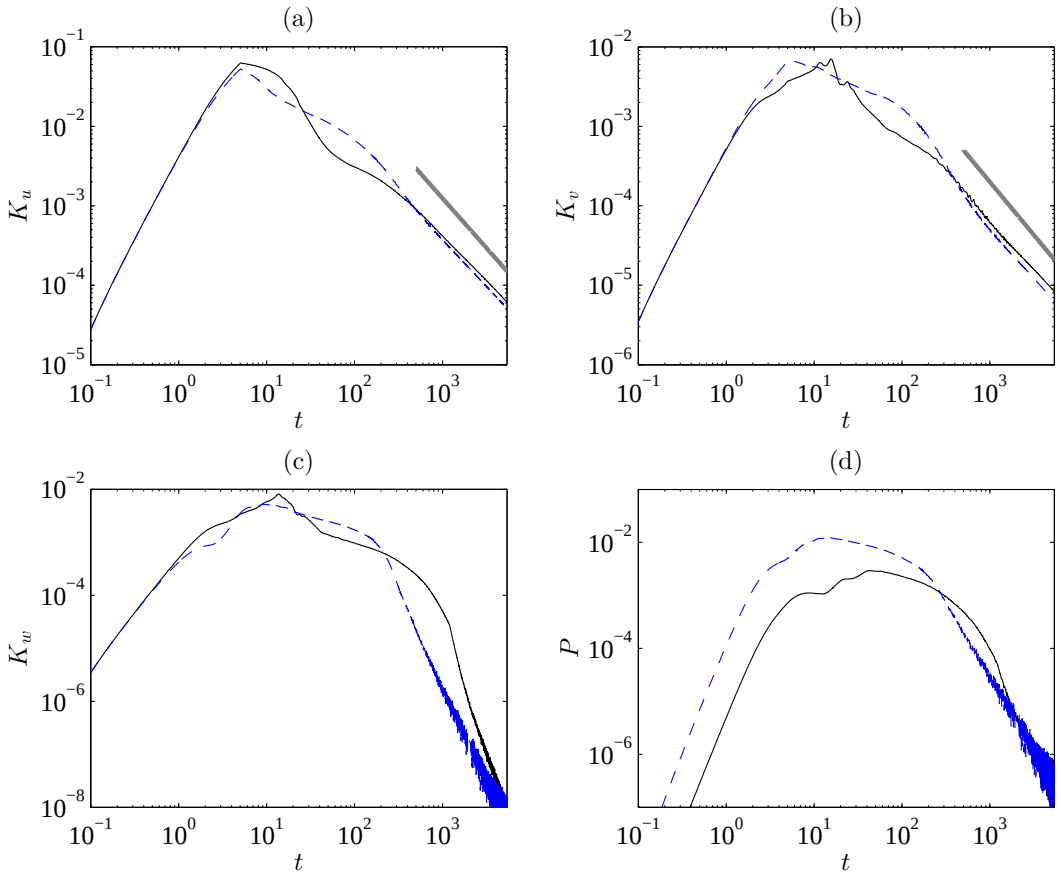

Figure 5.23: Kinetic energy and buoyancy variance histories from momentum injection phase to late time dipole phase for $N = 0.2$ (—), $N = 1.0$ (– –). (a) Streamwise kinetic energy (b) Lateral kinetic energy (c) Vertical kinetic energy (d) Buoyancy variance. The thick lines in (a) and (b) indicate that at the late time $K_u \propto t^{-5/4}$ and $K_v \propto t^{-4/3}$ respectively.

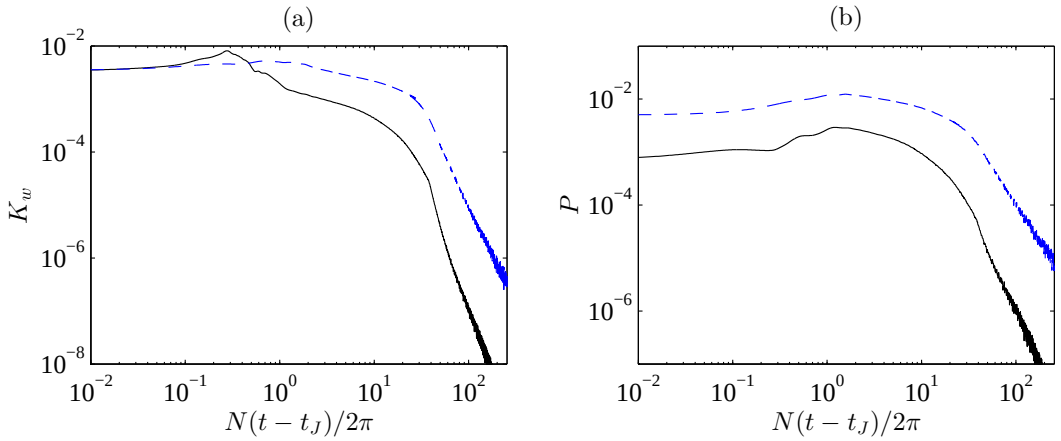

Figure 5.24: Kinetic energy and buoyancy variance histories from momentum injection phase to late time dipole phase for N = 0.2 (—), N = 1.0 (--). (a) Vertical kinetic energy (b) Buoyancy variance. The standard non-dimensional time scale, t, has been replaced by $N(t-t_J)/2\pi$, the number of buoyancy cycles that have elapsed since the end of the momentum injection for both cases.

stratification, there is less time for the collapsing ring and jet to entrain additional fluid before entering the late time dipole phase, with the momentum remaining concentrated in a smaller volume of fluid. This would also explain why the dipole in figure 5.25(b) has moved further downstream than that in (a). The additional momentum of the dipole in (c) increases the dipole propagation velocity, with the additional entrainment in the lateral direction giving a greater diameter, with the vertical length scale not appearing significantly greater than either (a) or (b), giving a lower aspect ratio and hence a "flatter" appearance.

Figure 5.26 demonstrates the agreement of the dipole's streamwise location with equation 1.15, calculated using the same 50% vorticity magnitude threshold discussed previously. As with the cases given in figure 5.19, there seems to be asymptotic agreement with the scaling law at the late time, though the time offsets are still sufficiently large and different between cases to make comparison on a single set of axes impractical. As with figure 5.20, improved scaling law agreement is apparent when using t_D instead of t_X for a time offset, with this plotted in figure 5.27. The two cases with larger t_J give a faster propagating dipole at the late time owing to the greater initial impulse they received from the momentum source. Additionally, higher stratification initially gives a more quickly propagating dipole than for the more weakly stratified cases. This appears to result from the higher stratification accelerating buoyant collapse, giving a more compact dipole in both the vertical and lateral directions,

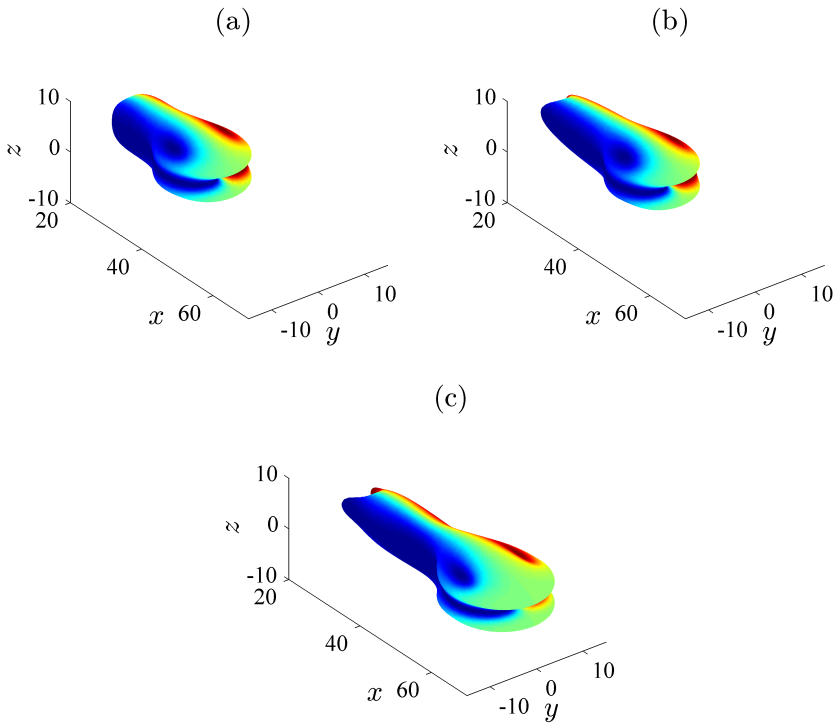

Figure 5.25: Isosurfaces of constant vorticity magnitude, $|\omega|$, demonstrating the structure of the late time dipole for (a) $t_J = 5, N = 0.2, t = 5402$ (b) $t_J = 5, N = 1.0, t = 5409$ (c) $t_J = 15, N = 0.2, t = 5750$. Colour contouring ranges between $\pm 0.6|\omega_z|_{\text{Max}}$, with isosurface threshold set at $0.2|\omega|_{\text{Max}}$.

which through conservation of momentum gives a higher dipole velocity immediately after the collapse phase than for the higher volume structure produced by a weakly stratified collapse phase.

Case	t_J	N	α_X	t_X	α_D	t_D	Plot marker
JLD1	5	0.2	1.194	-25146	0.365	1491	○
JLD4	5	1.0	1.537	-13483	0.338	893	×
JLD5	15	0.2	2.588	-5648	0.344	245	+
JLD6	15	1.0	2.827	-3182	0.360	245	□

Table 5.6: Constants of proportionality and time offsets for X_D and D_D time scaling plotted in figure 5.19.

Of further interest is the comparison of dipole diameters for the four cases given in figure 5.28. In spite of the differing impulse and stratification strength combinations, the scaling coefficient appears nearly identical for each case, all giving $\alpha_D \approx 0.35$ as detailed in table 5.6. While this may not be too surprising for different stratification strengths, as the influence of buoyancy is negligible at the late time, it would be expected that a dipole with greater forward momentum would entrain fluid and increase in diameter at a significantly higher rate, even when the time offset, t_D has been accounted for. For earlier times ($(t - t_D) < 1000$) it does appear that the rate of lateral expansion is greater for the higher impulse cases, though beyond this time the scaling behaviour between the cases becomes remarkably similar. Given that the two mechanisms for the dipole to expand are viscous entrainment (dependent on dipole momentum and viscosity) and viscous diffusion (dependent on viscosity alone), the comparable expansion rates suggests a diffusion dominated growth, as discussed further in the next section.

Figure 5.29(a) illustrates the decay of the maximum vertical vorticity within the dipole for each of the four cases. As would be expected, the peak vorticity at the early time is higher for the cases with higher impulse as greater circulation is imparted to the flow during the injection phase. Higher stratification strength also gives a higher vorticity at the early time. From visualisations of the dipoles at comparable times, such as that given in figure 5.25, it has already been observed that the initial dipole structure formed after the collapse phase is more compact for higher stratification, thus the circulation within it is more densely concentrated within the cores and the peak vorticity is higher. At the late time, the rate of decay for the cases JLD1 and JLD4 appear to

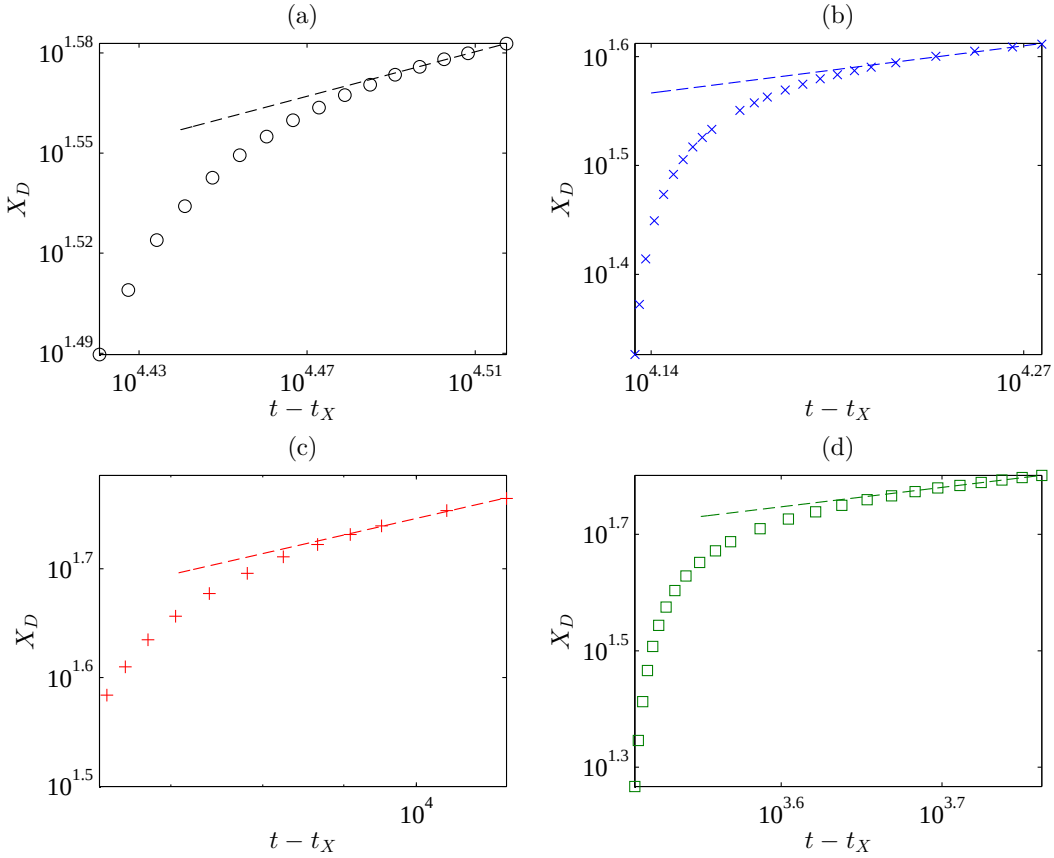

Figure 5.26: Time history of dipole streamwise location for (a) $t_J = 5, N = 0.2$ (○) (b) $t_J = 5, N = 1.0$ (×) (c) $t_J = 15, N = 0.2$ (+) (d) $t_J = 15, N = 1.0$ (□). The dashed lines in each plot correspond to a best fit of the late time data corresponding to equation 1.15, with gradient and time offsets given in table 5.6.

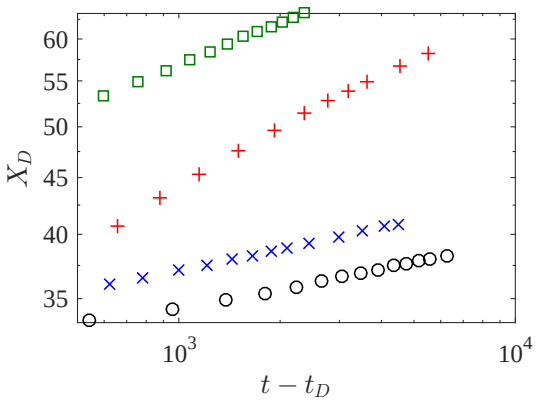

Figure 5.27: Time history of dipole streamwise location for $t_J = 5, N = 0.2$ (○), $t_J = 5, N = 1.0$ (×), $t_J = 15, N = 0.2$ (+), $t_J = 15, N = 1.0$ (□). In this plot, the offset on the time axis has been set to each case's value of t_D, rather than t_x.

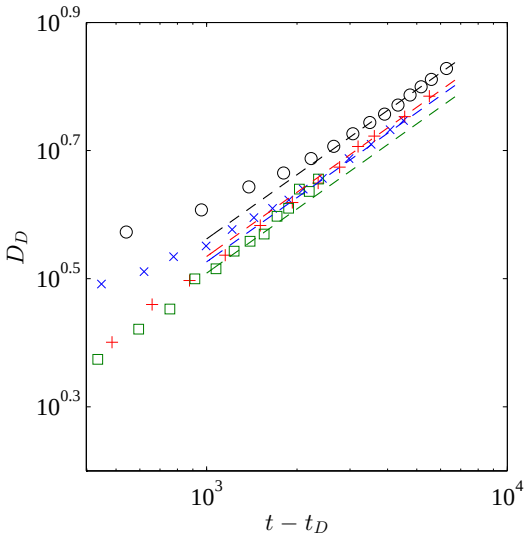

Figure 5.28: Time history of dipole diameter for $t_J = 5, N = 0.2$ (○), $t_J = 5, N = 1.0$ (×), $t_J = 15, N = 0.2$ (+), $t_J = 15, N = 1.0$ (□). The dashed lines in each plot correspond to a best fit of the late time data corresponding to equation 1.16, with gradient and time offsets given in table 5.6.

converge to a similar scaling coefficient, α_ω. The higher impulse cases also appear to be converging to a similar value, though case JLD6 had a tendency to become unstable and fail at the late time [1] , so it was not possible to run the simulation long enough to see if the final value of α_ω was truly comparable to case JLD5. Interestingly, the value of α_ω for case JLD5 (with $t_J = 15$) is found to be a little over three times greater than α_ω for cases JLD1 and JLD4 (with $t_J = 5$), implying the late time decay rate is approximately proportional to initial impulse i.e. $\alpha_\omega \propto t_J$, with it having already been demonstrated in figure 5.22 that the late time vorticity decay is also strongly dependent on Reynolds number. This single comparison is insufficient to make a definitive conclusion however, so this issue will be addressed further in subsequent chapters. What is clear, assuming that cases JLD5 and JLD6 do converge to a single value of α_ω, is that the vorticity decay, like the dipole lateral growth rate, is independent of stratification strength at the late time.

Figure 5.29(b) illustrates the dipole's vertical growth in each case, based on the Gaussian vorticity profile in the vertical direction discussed previously. It is immediately apparent that all four cases gives excellent agreement with equation 1.23 across the four cases, with each giving a very similar value of

[1] This failure appears to stem from unanticipated interaction of lingering internal waves interacting with the fringe region, and could be alleviated somewhat by limiting the timestep or decreasing the value of σ_c for the fringe, though neither change would completely eliminate the problem.

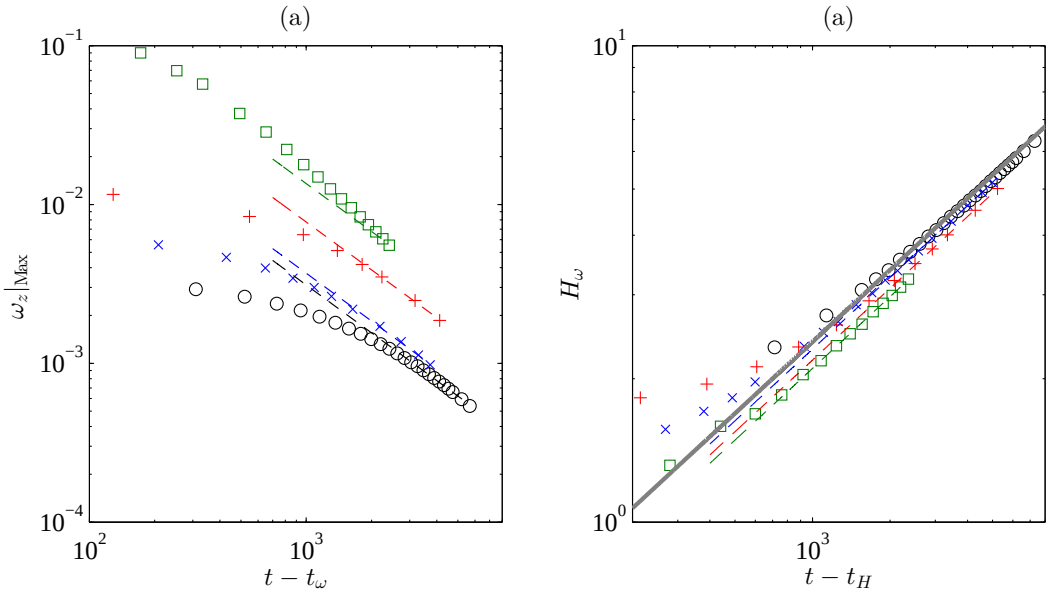

Figure 5.29: Time history of (a) maximum vertical vorticity and (b) dipole vertical thickness, for $t_J = 5, N = 0.2$ (○), $t_J = 5, N = 1.0$ (×), $t_J = 15, N = 0.2$ (+), $t_J = 15, N = 1.0$ (□). The dashed lines in each plot correspond to a best fit of the late time data corresponding to equation 1.23, with gradient and time offsets for (b) given in table 5.6. The solid line in (b) indicates $H_\omega = 2\sqrt{2}((t - t_H)/Re)^{1/2}$ with $Re = 1400$ for all four cases.

$\alpha_H \approx 2\sqrt{2}$, helping show that at the late time the vertical expansion of the dipole is governed purely by diffusion as found by Flór et al. (1995). The time taken to achieve this diffusive state, along with with the comparable rates of lateral expansion seen in figure 5.28 are considered further for all the large domain cases in the following section.

5.2.5 Late time scaling and the advection/diffusion balance

In order to further corroborate the dipole vertical growth (and Reynolds number dependence) seen for the cases considered so far, a comparison is made in this section with data from previous experimental studies. Figure 5.30 presents data from cases JLD1, JLD2 and JLD4 seen previously, along with data from Praud and Fincham (2005) and Flór et al. (1995). The data from Praud and Fincham (2005) is for a case with $Re_S \approx 12000, \hat{N} = 0.3\text{rad}s^{-1}$ and $\hat{t}_J = 4s$ and was scaled to give the same Gaussian length scale used to determine H_ω. The data from Flór et al. (1995) is for a case with $Re_J \approx 1145, \hat{N} = 1.8\text{rad}s^{-1}$ and $\hat{t}_J = 0.3s$ and does not use the vertical vorticity profile to determine thickness, instead using a profile of streamwise dipole displacement (i.e. how far each

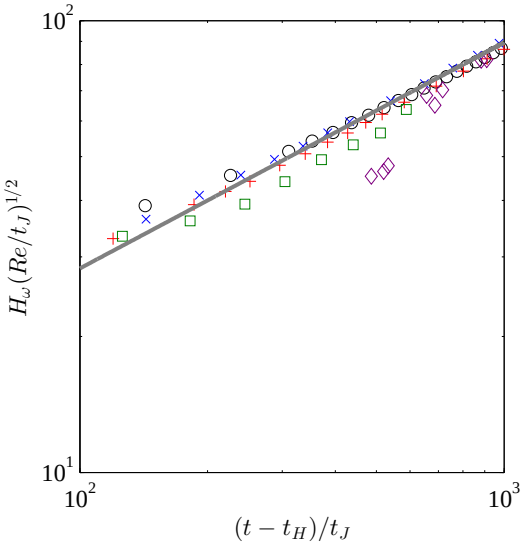

Figure 5.30: Time history of dipole vertical thickness normalised by $Re^{1/2} = \nu^{-1/2}$ and $t_J^{1/2}$, for cases JLD1 (○), JLD2 (×), JLD4 (+), along with comparable data from Praud and Fincham (2005) (□) and Flór et al. (1995) (♢). The solid line indicates $H_\omega(Re/t_J)^{1/2} = 2\sqrt{2}((t-t_H)/t_J)^{1/2}$.

vertical "layer" of the dipole has moved downstream), which is demonstrated by the authors to also follow a Gaussian profile in z from which a length scale can be determined. In the figure, the axes have been scaled using t_J as a reference timescale. The agreement of the two experimental cases to both equation 1.23 and the simulation data is encouraging, particularly at the late time.

As mentioned previously, the values of α_D for cases JLD1, JLD4, JLD5 and JLD6 are all remarkably similar given the differences in both stratification strength and total impulse. Given that all utilise $Re = 1400$, it suggests that Reynolds number is the sole important governing parameter for dipole lateral growth at the late time for these cases, with the initial conditions unimportant once the dipole has fully formed. As the flow is quasi-two dimensional by this stage, the evolution of the vertical vorticity field can be determined from the two dimensional form of the vorticity equation i.e.

$$\frac{\partial \omega_z}{\partial t} + u_i \frac{\partial \omega_z}{\partial x_i} = \nu \frac{\partial^2 \omega_z}{\partial x_i \partial x_i}. \tag{5.13}$$

At the very latest times where the dipole has expanded and diffused sufficiently, the convective term approaches zero, yielding a similar vorticity diffusion in the horizontal plane to that seen in the vertical direction such that

$$D_D \propto \left(\frac{t-t_{D2}}{Re}\right)^{1/2} = \alpha_{D2}\left(\frac{t-t_{D2}}{Re}\right)^{1/2}, \tag{5.14}$$

where t_{D2} and α_{D2} are the time offset and scaling coefficient respectively. Obviously, this scaling behaviour contradicts equation 1.16, for which reasonable

agreement had been obtained thus far. However, both types of scaling behaviour give a weak dependence of D_D on t, such that reasonable agreement may be found for both, depending on the range of t over which the correlation to the scaling law is evaluated. Figure 5.31 demonstrates the late time agreement of dipole diameter with this diffusion-based scaling behaviour for two cases conducted for this project (with different values of Re) as well as four others from literature; the same case from Praud and Fincham (2005), another case from Flór et al. (1995) with $Re_J \approx 3500, \hat{N} = 1.7\text{rad}s^{-1}$ and $\hat{t}_J = 0.6s$, DNS data from Rojanaratanangkule et al. (2012)[2] for a case with $Re = 2500$ (and the two-dimensionality of the flow achieved by free-surface confinement) and DNS data from Delbende and Rossi (2009) which used $Re = 2500$ (for a purely two-dimensional dipolar flow system).

Of the six cases considered, the two cases from this work as well as the DNS of Rojanaratanangkule et al. (2012) collapse well to a constant value of α_{D2}, which was found to be almost exactly $2\sqrt{2}$ such that $\alpha_{D2} = \alpha_H$ (with a line indicating this value added to figure 5.31). These three cases utilise equation 3.7 to determine dipole diameter, whereas Flór et al. (1995) and Praud and Fincham (2005) measure the diameter as the distance between vertical vorticity extrema at the vertical midplane (i.e. the equivalent plane to $z = 0$ in this project). Delbende and Rossi (2009) use an equivalent two-dimensional form of equation 3.7. Interestingly, the experimental cases give dipoles that expand at a much faster rate by comparison, with the data from Praud and Fincham (2005) yielding $\alpha_{D2} \approx 4\sqrt{2} \approx 2\alpha_H$. The two-dimensional case also yields a faster rate of expansion, though the simulation apparently was not run over sufficient time to achieve a well-defined scaling behaviour with time. The available data appears to be slowly tending towards $D_D(Re/t_J)^{1/2} = 2\sqrt{2}((t - t_{D2})/t_J)^{1/2}$ as with the other numerical cases, but this cannot be assured.

There are three potential reasons why the experimental data yields a faster expansion rate than the DNS data. Firstly, the differing definitions of D_D mentioned previously will only give identical answers provided the radial distribution of vertical vorticity within each dipole core is symmetric about the vorticity extrema. Though the vorticity extrema method was not favoured for this work, a check was made to see what impact the differing measurement method has on the value of D_D. Across the cases conducted for this work, calculating diameter between vorticity extrema yielded a value of D_D typically 10-15% higher than the enstrophy wighted method of equation 3.7. Though

[2]The data presented here is not included in the publication, but does originate from one of the cases covered in the work, with the data used here supplied by the author directly.

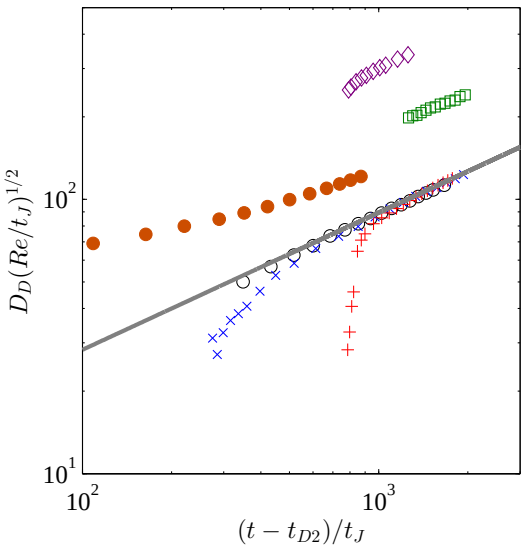

Figure 5.31: Time history of dipole diameter normalised by $Re^{1/2} = \nu^{-1/2}$ and $t_J^{1/2}$, for cases JLD1 (○), JLD3 (×), along with comparable data from Rojanaratanangkule et al. (2012) (+), Praud and Fincham (2005) (□), Flór et al. (1995) (◇) and Delbende and Rossi (2009) (•). The solid line indicates $D_D(Re/t_J)^{1/2} = 2\sqrt{2}((t - t_{D2})/t_J)^{1/2}$.

arguably a significant change, this doesn't fully explain the doubling (or more) of α_{D2} between the experimental cases compared to the DNS.

The second potential reason is that the experimental data may have been collected at times before the dipole has reached a state where the lateral growth is mostly due to diffusion, with viscous entrainment still the dominant cause of expansion. Such a transition between an entrainment dominated and diffusion dominated growth can be seen for both case JLD3 and Rojanaratanangkule et al. (2012) in figure 5.31, where D_D rises sharply at earlier times before asymptoting to the diffusive scaling later on. With the experimental data being collected over comparatively narrow time scales compared to the DNS, it is difficult to be sure whether entrainment or diffusion is dominant and thus whether it is fair to compare the relative scalings of D_D.

The third possible reason is that the vorticity distribution of the dipole structure at the late time differs substantially between the DNS and experimental cases due to use of a Gaussian forcing profile at the momentum source for both the cases in this work and the work of Rojanaratanangkule et al. (2012), as opposed to a smoothed top hat profile such as that used by Mohseni et al. (2001), which may be more representative of the forcing profile for an experimentally generated impulsive jet. The effect of these differing profiles on both the early and late time behaviour of the flow were later investigated

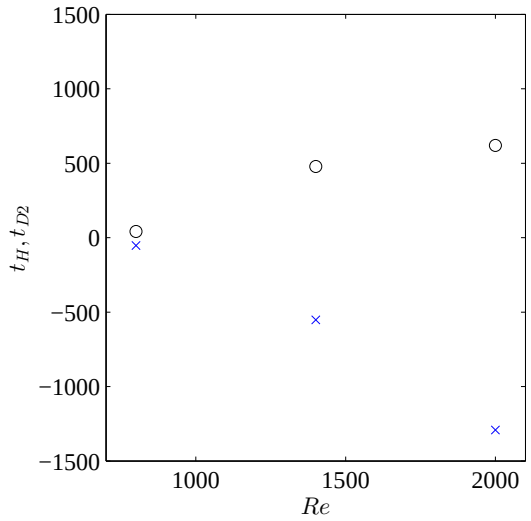

Figure 5.32: Vertical and lateral diffusion time offsets for cases JLD1-3 with t_H (○) and t_{D2} (×).

and documented in chapter 6. That research demonstrated little difference in the behaviour between cases at the late time for the different forcing profiles, the late time dipole development can be considered truly independent of initial conditions and thus the differences between the experimental and DNS scaling behaviour will almost certainly be due to the former having not reached a diffusively dominated time frame.

Regarding the dipole's aspect ratio, it had been noted previously that, from casual observations of the dipole structure for different cases, a higher value of Re yields a lower value of α_{HD}. However, as it appears that $D_D(Re/t_J)^{1/2} = 2\sqrt{2}((t-t_{D2})/t_J)^{1/2}$ at the late time, the late time aspect ratio can be calculated as a function of time by

$$\alpha_{HD} = \frac{H_\omega}{D_D} = \frac{2\sqrt{2}((t-t_H)/Re)^{1/2}}{2\sqrt{2}((t-t_{D2})/Re)^{1/2}} = \left(\frac{t-t_H}{t-t_{D2}}\right)^{1/2}. \tag{5.15}$$

The values of t_H and t_{D2} as they vary with Reynolds number for the cases JLD1-3 ($Re = 800, 1400, 2000$) are given in figure 5.32. Although these values are of course sensitive to the exact fitting used for the late time vorticity thickness and diameter data, two points are clear. Firstly, t_H is positive and t_{D2} negative such that equation 5.15 can only be valid for $t > t_H$ (and in practice, $t \gg t_H$ before it is accurate). Secondly, the percentage increase of $|t_{D2}|$ with increasing Re is much greater than the percentage increase of $|t_H|$. This in turn yields smaller values of α_{HD} with higher Reynolds number as was demonstrated in figure 5.16.

At the very late time, when $t \gg |t_H|, |t_{D2}|$, equation 5.15 implies the aspect

ratio for all dipoles, regardless of initial conditions or Reynolds number, will tend to $\alpha_{HD} = 1$. Figure 5.33 gives the time history of the dipole aspect ratio for all six large domain simulations covered so far. Similar data is presented for experimental cases in Praud and Fincham (2005), which used the dipole aspect ratio to quantify the transition in dipole behaviour from an advective phase to a diffusive one. At the early time (typically $t < 100$), H_ω is large compared to D_D as the individual vortical structures in the leading ring and trailing jet have yet to fully collapse, with the initial increase in D_D associated with the collapsing structures advecting into a dipole front and spreading laterally having yet to be realised.

After a short time, the value of H_ω drops rapidly, partly as a result of buoyant collapse and partly due to the mechanism of "viscous peel-off" considered by Godoy-Diana et al. (2004), where it was observed that the shear layers formed between the evolving structure and the quiescent fluid above and below it leads to a shedding of vertical vorticity, further reducing the ω_z based vertical length scale. At the same time, a combination of advection and entrainment leads to a marked increase in diameter, with this being the phase at which the whole structure takes on its familiar dipole appearance. The combination of decreasing thickness and increasing diameter leads to a rapid drop in α_{HD}.

Some time after this, the aspect ratio reaches its minimum value, typically between 0.6 to 0.8 for the cases seen here (with the exception of JLD2). Subsequently, the rate of vertical expansion due to diffusion exceeds the rate of lateral entrainment and the aspect ratio begins to rise again. As the lateral growth becomes more and more diffusion dominated, the increase in aspect ratio slows, with it eventually expected to reach an asymptote at $\alpha_{HD} = 1$. For the case JLD2 (with the lowest value of Re), there is a notable difference in behaviour, with the aspect ratio never dropping significantly below 1 at any time, and maintaining a steady value of 1 at the late time. This suggests that, in the lateral direction, the expansion of the dipole is dominated by diffusion even before the collapse/peel-off phase has concluded. This case in particular lends credence to the late time validity of equation 5.15.

Aside from this case, more trivial differences can be observed between cases, with higher Reynolds number (JLD3) giving a lower minimum aspect ratio than lower Reynolds number (JLD1) due to increased entrainment and a delay on the onset of diffusion dominated growth. Higher stratification strength (JLD4, JLD6) suppresses initial growth in the vertical direction giving a smaller minimum aspect ratio, but at the late time (when buoyancy has

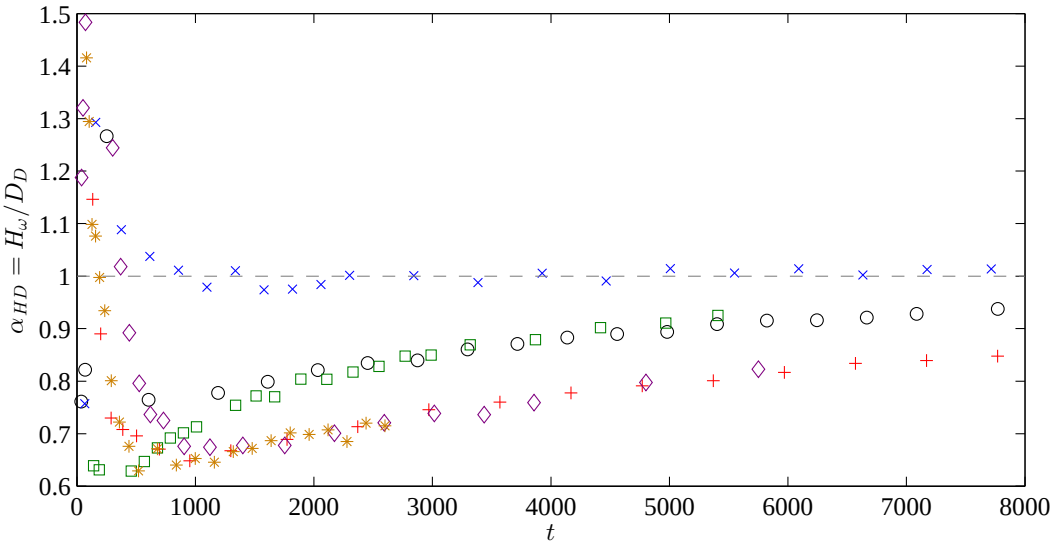

Figure 5.33: Time history of dipole aspect ratio for cases JLD1 (○), JLD2 (×), JLD3 (+), JLD4 (□), JLD5 (◇), JLD6 (*). The dashed line indicates $\alpha_{HD} = 1$.

negligible impact) the increase in aspect ratio is closely comparable with the weaker stratification equivalents (JLD1, JLD5 respectively).

To conclude this investigation of the late time behaviour, the kinetic energy levels at the late time for various cases are re-examined alongside the time history of dipole aspect ratio. Figure 5.34 presents the lateral and vertical kinetic energy histories of three cases, with the onset of late time scaling behaviours discussed previously (see equations 5.9-5.10, figure 5.15 etc.) appearing to be coincident with the transition from an advective to diffusive dipole flow. The data presented in figure 5.33 is taken at discreet time intervals making an exact value of this transition time unavailable, so an estimate based on a smooth fitting is used instead. Nonetheless, the data available is sufficiently strong to infer that the final conversion from the advective to diffusive phase is coincident with the end of significant internal wave generation for each case, with the associated sharp drop in vertical kinetic energy proving a tell tale sign of the commencement of the fully diffusive state at the late time.

5.3 Chapter summary

As detailed in this chapter, the evolution of a dipolar vortex from an initially axisymmetric momentum injection under the vertical constraint of stable stratification has been simulated through the use of the Spectral DNS code detailed in section 2.3. In accordance with all comparable experimental

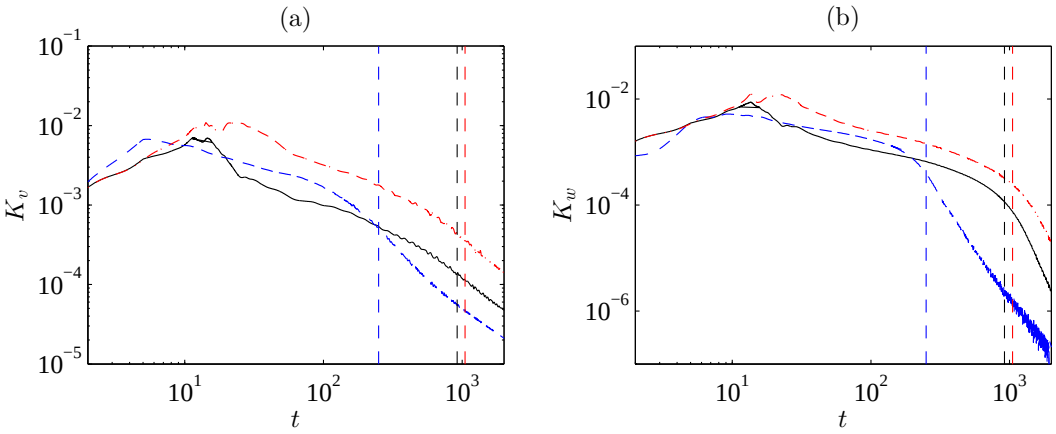

Figure 5.34: Time evolution of (a) lateral kinetic energy and (b) vertical kinetic energy for cases JLD3 (—), JLD4 (– –) and JLD5 (– · –). The dashed vertical lines indicate the approximate time where the flow transfers from the advective to the diffusive regime for each case based on the data presented in figure 5.33. The colour of each vertical line corresponds to the case it refers to.

studies, the dipole forms following the buoyant collapse of the flow as vertical motions are suppressed to leave a three dimensional structure, but consisting of quasi-horizontal velocity fields throughout its vertical extent. The stages of this evolution from momentum injection to late time vortex dipole have been quantified primarily through changes in kinetic energy and buoyancy variance levels that are not readily available via experiment, thus allowing this numerical study to present this information for the first time.

Concerning the late time dipole, excellent agreement has been found with the late time diffusive behaviour discussed in Praud and Fincham (2005) etc. with weaker agreement found with the scaling laws for vortex propagation velocity and peak vorticity proposed by Voropayev et al. (2008) and related works. In particular, the simulations documented in this chapter show the constant thickness dipole condition reported in Voropayev et al. (1991) to be invalid, with the dipole thickness increasing according to a viscous scaling law that appears universal for the range on simulation parameters considered, with these simulations providing the first directly analogous numerical results to those experimental works.

The final study documented in the following chapter investigates what effect the initial forcing condition has on the late time vortex dipole, given that the vortex dipoles seen in this chapter appear qualitatively similar to those seen in chapter 4 in spite of the completely different means of initialising the solution (initial solution with vortex ring vs. horizontal momentum injection into a quiescent domain).

Chapter 6

The influence of initial forcing conditions on the late time stratified dipole

6.1 Simulation set up and study parameters

So far, the work documented in the previous two chapters has demonstrated how axisymmetric, vortical structures undergo a collapse process due to stable stratification and how this leads to the formation of dipolar vortices that undergo a well predicted viscous scaling at the late time. However, both the vortex ring and the impulsive jet based simulations conducted previously do not necessarily provide a close representation of how an experimentally generated, impulsive jet in a stratified fluid evolves at the early time, and thus may call in to question how reliable any late time observations are (even though the results seen in section 5 showed good agreement with some of the available experimental literature). In the case of the vortex ring based simulations of chapter 4, the discrepancy arises from implementing the early time vortical structure as an initial velocity field at $t = 0$ and allowing it to evolve thereafter. Whilst this method allows for an exact definition of the initial axisymmetric structure (facilitating a "before" and "after" series of comparisons once the structure has been deformed due to the effects of stratification), it does not consider how the vortex rings formed in experimental studies (van Atta and Hopfinger, 1989; Scase and Dalziel, 2006) are affected by stratification during their initial roll up and how this impacts on their subsequent evolution. In the case of the impulsive jet simulations of chapter 5, the impulsive source uses a Gaussian forcing profile. The use of such a profile was chosen based on a number of factors including the use of such a profile in the related study

of Rojanaratanangkule et al. (2012) and numerical concerns documented in section 5.1. Whilst the use of an impulsive forcing region to generate vortical structures allows the influence of stratification to be felt throughout the roll up process and beyond, the Gaussian profile used previously is arguably unrepresentative of the equivalent forcing profiles from experimental studies and thus the simulated early time vortex ring and trailing jet structures, as well as the late time dipolar structures, may be unrepresentative of their experimental equivalents also. Differences in structure between experimentally observed starting jets and those simulated from a Gaussian source were already commented upon in section 5.2.1.

To summarise, there are enough conceptual differences between the simulations conducted so far for this project and documented experiments to question the validity of comparing the results of the two. In order to address these concerns, a further series of simulations was conducted with the aim of better representing the early time formation of the vortical structures than has been attempted so far. The key difference noted between the experimentally created starting jets and vortex rings (formed by a piston/cylinder arrangement or similar) to those generated through Gaussian forcing is a much smoother vorticity profile across the leading ring and trailing jet for the latter, with the ratio of the leading ring core radius to the overall ring radius appearing to be much higher for a Gaussian profile (though this was not assessed quantitatively in chapter 5). The numerical work of both Mohseni et al. (2001) and Rojanaratanangkule et al. (2014) details how more representative starting jets than simulated in this project so far can be generated by using a smoothed top-hat type forcing distribution, which in those cases was based around the use of an error function to create the smoothed forcing profile in the radial direction away from the streamwise axis and a Gaussian profile along the streamwise axis.

For the work detailed in this chapter, a similar smoothed top-hat profile was introduced as an alternative forcing mechanism to the Gaussian profile used in chapter 5. That profile applied an additional streamwise forcing term into the governing equations defined by

$$f_{xG} = \frac{J}{((\delta_G/2)^2\pi)^{3/2}} \exp\left(-\frac{r_3^2}{(\delta_G/2)^2}\right), \tag{6.1}$$

where δ_G is the Gaussian length scale and $r_3 = \sqrt{x^2 + y^2 + z^2}$. Instead of a combined error function and Gaussian based profile used by previous studies, a smoothed top-hat forcing profile is achieved in this work though the use of hyperbolic tangent functions in both the radial and streamwise directions with

Case	Type	Re	N	t_J	L_x, L_y, L_z	n_x, n_y, n_z
GAU1	Gaussian	2000	0.0	1	$12\pi, 4\pi, 4\pi$	640,320,320
GAU2	Gaussian	2000	0.0	5	$12\pi, 4\pi, 4\pi$	640,320,320
GAU3	Gaussian	2000	1.0	5	$12\pi, 4\pi, 4\pi$	640,320,320
HYP1	Hyperbolic	2000	0.0	1	$12\pi, 4\pi, 4\pi$	640,320,320
HYP2	Hyperbolic	2000	0.0	5	$12\pi, 4\pi, 4\pi$	640,320,320
HYP3	Hyperbolic	2000	1.0	5	$12\pi, 4\pi, 4\pi$	640,320,320
GAU4	Gaussian	2000	1.0	1	$24\pi, 8\pi, 8\pi$	1280,640,640
GAU5	Gaussian	2000	1.0	5	$24\pi, 8\pi, 8\pi$	1280,640,640
HYP4	Hyperbolic	2000	1.0	1	$24\pi, 8\pi, 8\pi$	1280,640,640
HYP5	Hyperbolic	2000	1.0	5	$24\pi, 8\pi, 8\pi$	1280,640,640

Table 6.1: Cases and flow parameters

the forcing term now given by

$$f_{xH} = \frac{J}{(\delta_H/2)^2\pi}\left(\frac{1}{2}\tanh(8(1 - r_2/(\delta_H/2))) + 1\right)\left(\frac{1}{2}\tanh(4(1 - |x|/(\delta_H/2))) + 1\right), \tag{6.2}$$

where δ_G is the radius of the forcing region from the x axis and $r_2 = \sqrt{y^2 + z^2}$.

As mentioned previously, one of the reasons a top-hat type profile was not adopted for the impulsive jet simulations conducted in chapter 5 was the difficulty of a Fourier based spectral DNS code resolving sharp changes in velocity gradients (akin to discontinuities) which could not be accurately mapped to the available number of Fourier modes. This problem could have been eased somewhat by increasing grid resolution and thus the number of modes, though at significant increases in computational cost to a level impractical for the resources of this project. However, unlike the simulations of chapter 5 the simulations described hereafter do not aim to capture a significant portion of the late time scaling behaviour and thus does not require as large a domain, allowing for increased resolution while not incurring excessive grid count. The initial grid spacing used in this chapter, given in table 6.1 is 40% smaller in each direction than that used in chapter 5.

Table 6.1 details the case parameters for this study. The Reynolds number for the Gaussian and Hyperbolic profiled sources was based on the kinematic momentum flux in both cases with both using a momentum flux of identical magnitude. For this study, all cases utilise a Reynolds number of 2000. The variation in momentum injection duration, t_J, for the Gaussian and Hyperbolic cases was intended to explore whether the duration of the momentum injection has any significant effect on the structures that are formed at the

late time. Specifically, the shorter duration cases were intended to give a formation time measured duration of less than 4, such that most (if not all) the impulse transferred to the domain is contained within a single leading vortex ring without a significant trailing jet. Conversely, the longer duration injections are intended to give an injection that extends past four formation time units and thus should form both a leading vortex ring and a trailing jet structure during the injection phase. These simulations, combined with the vortex ring initialised cases conducted both in chapter 4 should help determine both whether a vortex ring initialised case is analogous to a case where a vortex ring rolls up from a momentum injection and also what difference the presence of a trailing jet makes to the late time structure. Simulations were conducted using both neutral and stably stratified backgrounds in order to demonstrate how the early and late time flow structure differences between the Gaussian and Hyperbolic cases in particular are either reduced or exaggerated if a stably stratified background is utilised.

As in chapter 5, the grid resolution for some of the stably stratified cases was reduced at the late time to reduce computational cost once the smaller scale structures in the domain have merged to form the larger, slower dipolar vortices now expected of such flows.

6.2 Results and analysis

6.2.1 Impulsively generated structures from Gaussian and Hyperbolic sources in neutrally stratified fluid

Figure 6.1 demonstrates that the choice of a hyperbolic forcing profile generates a markedly different structure to the Gaussian profiles used in Chapter 5. For the short duration momentum injection cases (GAU1/HYP1), at a short time after the momentum injection has ceased, the Gaussian case has formed a vortex ring-like structure, but with highly eccentric cores and a significant proportion of the overall circulation in the flow field contained within a tail extending back toward the origin of the momentum injection. By contrast, the Hyperbolic momentum injection has given a more compact structure with almost all the circulation in the flow field entrained into a core that, superficially, appears to have a more circular distribution more akin to the experimentally generated vortex rings documented widely in available literature. The longer duration injection for the Gaussian case (GAU2) does appear to form a leading vortex ring and trailing jet, though the ring core is sufficiently wide to give

the vortex an overall spherical appearance. The Hyperbolic injection (HYP2) produces a more tightly formed core as before, with the emergence of smaller ring-like structures appearing in the trailing jet, somewhat more representative of the structure reported in Gharib et al. (1998) and subsequent works.

Focusing exclusively on the leading vortex ring from each of the four cases considered in Figure 6.1, the vertical vorticity distribution within the leading rings for each are given in Figure 6.2, at a time after momentum injection had ceased and the leading ring had the opportunity to advect downstream. As inferred from the vorticity contours, the core radius of the leading ring is smaller for the Hyperbolic momentum injection, with a higher peak vorticity magnitude and a pronounced inflexion in the lateral distribution of vorticity about the centre of the ring than seen for the Gaussian momentum injections. After normalising the vorticity profiles by peak vorticity magnitude and the lateral separation between the vorticity peaks of the ring, $D_{y\omega}$, it was seen that the Hyperbolic momentum injection gave a leading vortex ring with a Gaussian core distribution very similar to the rings simulated in Chapter 4, with case RSD1 taken as an example from those results. Ironically, the vortex ring formed from the Gaussian momentum injection forms a less Gaussian distribution of vorticity, with a more linear profile of vorticity between the cores, particularly for the case of longer momentum injection.

This change in structure is further reflected in both the streamwise and kinetic energy levels for the early time ring and trailing jet structure, with the Hyperbolic case giving markedly higher values of both. This would be consistent with the more compact leading ring structure given in the Hyperbolic case, which has been imparted with the same impulse at the Gaussian case but concentrates the momentum into a smaller volume, giving a higher streamwise kinetic energy. Similarly, the more compact distribution and higher peak value of vorticity for the vortex ring core as shown in figure 6.2 gives a faster core rotation and thus a higher level of kinetic energy in the lateral and vertical directions as well.

6.2.2 Impulsively generated structures from Gaussian and Hyperbolic sources in stably stratified fluid

Though there are clear structural differences between the structures produced by the Gaussian and Hyperbolic momentum sources after the initial momentum injection, the primary aim of the work in this chapter is to determine what impact this has on the late time vortex dipole in stably stratified cases, and

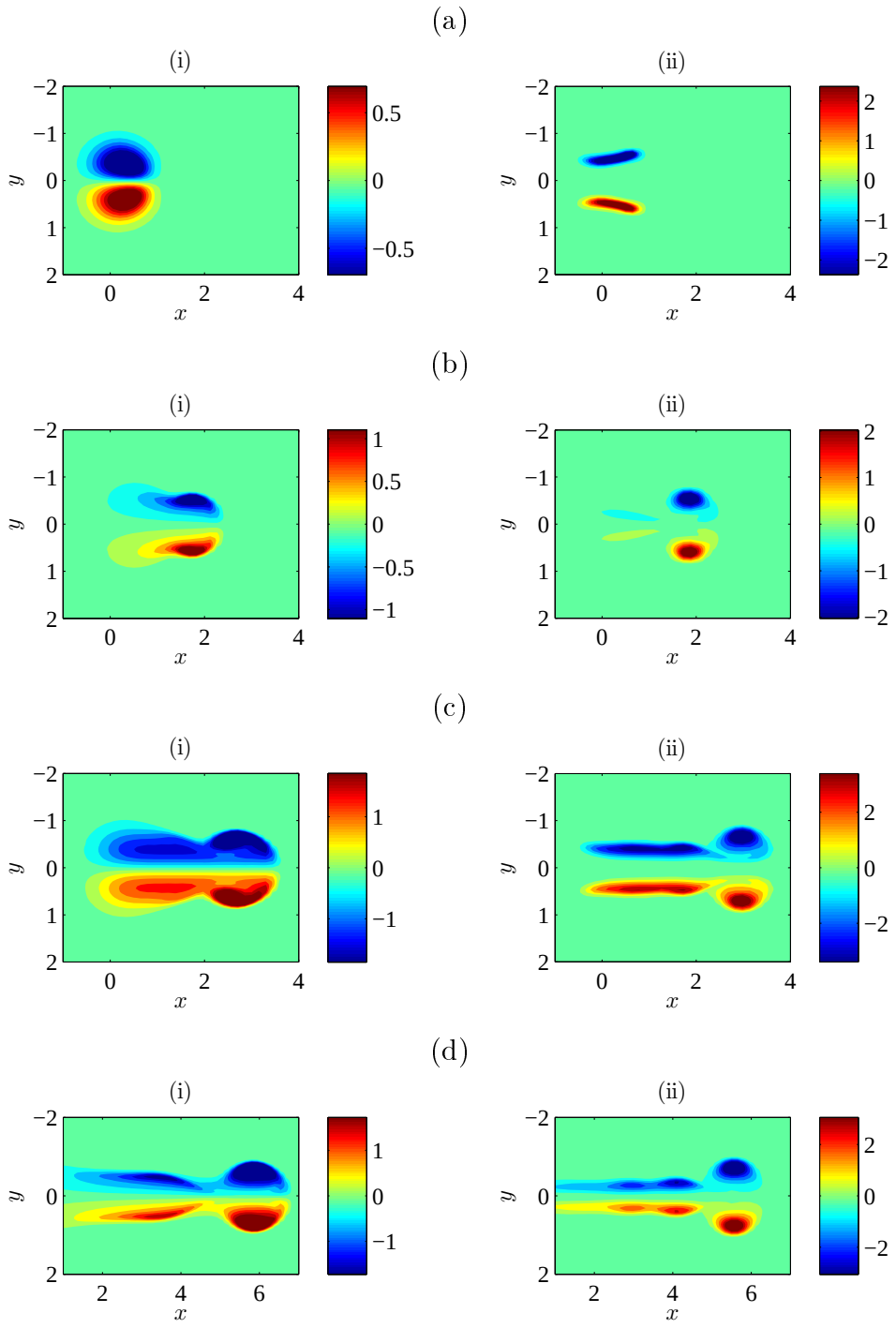

Figure 6.1: Contours of vertical vorticity, ω_z at $z = 0$ for short and long momentum injection from both Gaussian and Hyperbolic profiled momentum sources in neutrally stratified fluid. (a)(i) Case GAU1 at $t = 1$, (ii) Case HYP1 ($t_J = 1$) at $t = 1$, (b) as (a) but $t = 5$, (c)(i) Case GAU2 ($t_J = 5$) at $t = 5$, (ii) Case HYP2 ($t_J = 5$) at $t = 5$, (d) as (c) but (i) $t = 8.4$, (ii) $t = 9.2$. Colour contouring ranges between $\pm 0.6|\omega_z|_{\text{Max}}$.

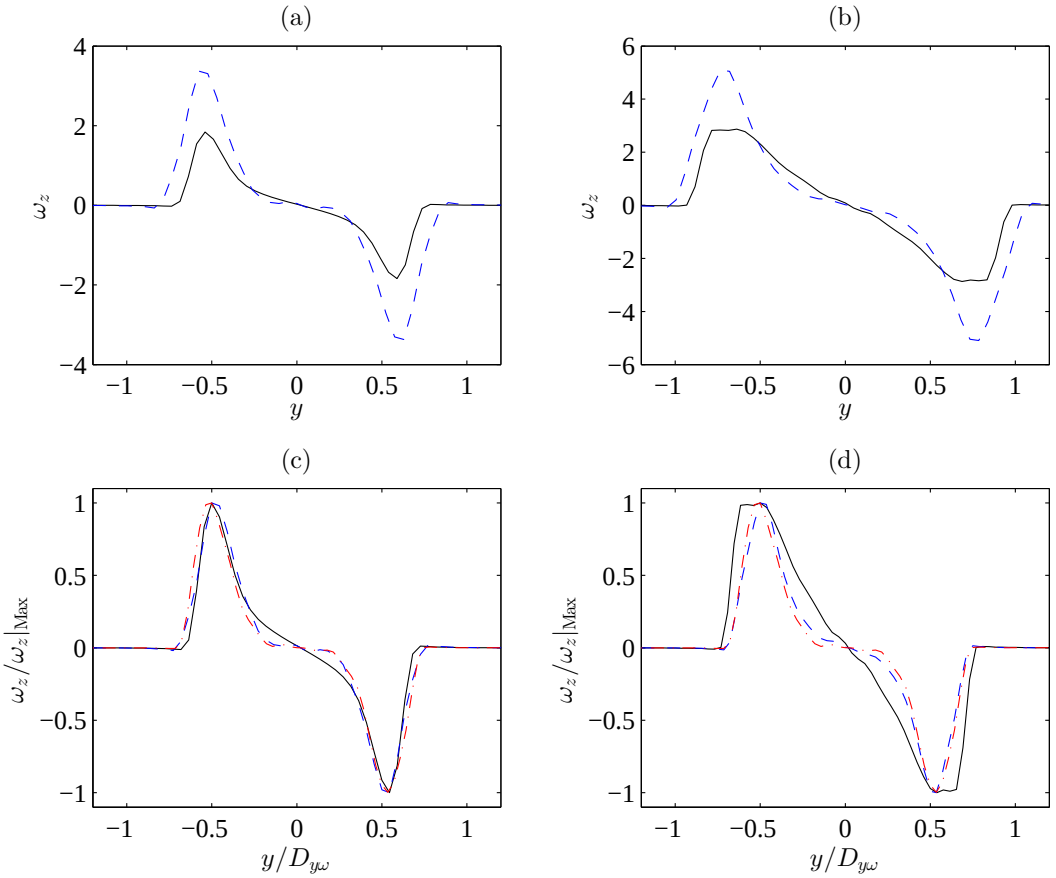

Figure 6.2: Vertical vorticity profiles across the leading vortex rings for short and long momentum injection from both Gaussian and Hyperbolic profiled momentum sources in neutrally stratified fluid, with profile taken at $z = 0$ and x coordinate equal to location of $\omega_z|_{\mathrm{Max}}$. (a) GAU1 at $t = 5$ (—), HYP1 at $t = 5$ (−−), (b) GAU2 at $t = 9.2$ (—), HYP2 at $t = 8.4$ (−−), (c) as (a) but now includes equivalent profile from RSD1 (−·−) and data rescaled by maximum vertical vorticity and lateral separation of vorticity extrema, (d) as (b) but now includes equivalent profile from RSD1 (−·−) and data rescaled by maximum vertical vorticity and lateral separation of vorticity extrema.

thus help further validate (or cast doubt upon) the results of chapter 5. Figure 6.3 gives isosurface visualisations of the initial starting jet and leading vortex ring structure for a Gaussian and Hyperbolic momentum source with $t_J = 5$ and unit buoyancy frequency. Early in the injection process the structures generated are largely representative of the neutrally stratified equivalents discussed in the previous section. At the point of the momentum injection ceasing, the axisymmetry of both cases has been lost with the Gaussian case showing the near spherical vortex ring at the leading edge expanding in the vertical direction and constricting in the lateral direction, though appearing to maintain the integrity of its core. By contrast, the Hyperbolic case shows the leading vortex ring to expand laterally and constrict vertically, while also detraining vorticity from its core into the surrounding fluid, forming loops of "halo" vorticity not unlike those seen for the isolated vortex ring cases considered in chapter 4.

In spite of the apparent structural differences between these two cases at the early time, the time history of the volume integrated kinetic energy and buoyancy variance components within the domain follow very similar trends. As observed for the neutrally stratified cases, the Hyperbolic momentum injection gives a more energetic flow due to the more compact nature of the vortical structures produced, but once injection has ceased the energy decay of both cases appears broadly equivalent as shown in figure 6.4. As would be expected from these trends, the ratio of internal to total energy is near identical for the two cases throughout as indicated in figure 6.5. All of this points to the mechanism of energy transfer between the kinetic and internal states being unaffected by the shape of the vortical structure within the domain, and more dependent on the level of momentum injected into the fluid as well as background stratification strength and viscosity. Indeed, the only previous occasion in this work where two cases with equivalent momentum, stratification strength and Reynolds number was considered was the comparison of the vortex ring case RSD2 from chapter 4 and the similar case RSD3 without radial perturbation of the initial ring, with those cases also giving near identical energy histories. The differences in vortical structure at the early time between those vortex ring cases is less extreme than observed for the Gaussian and Hyperbolic momentum sources documented in this chapter, but still demonstrates the insensitivity of the energetics of the flow to the shape of the vorticity field.

Thereafter, both the Gaussian and Hyperbolic cases undergo similar processes of vertical motion suppression, wave generation and final collapse as documented in chapter 5 before arriving at the late time viscous dipole. The

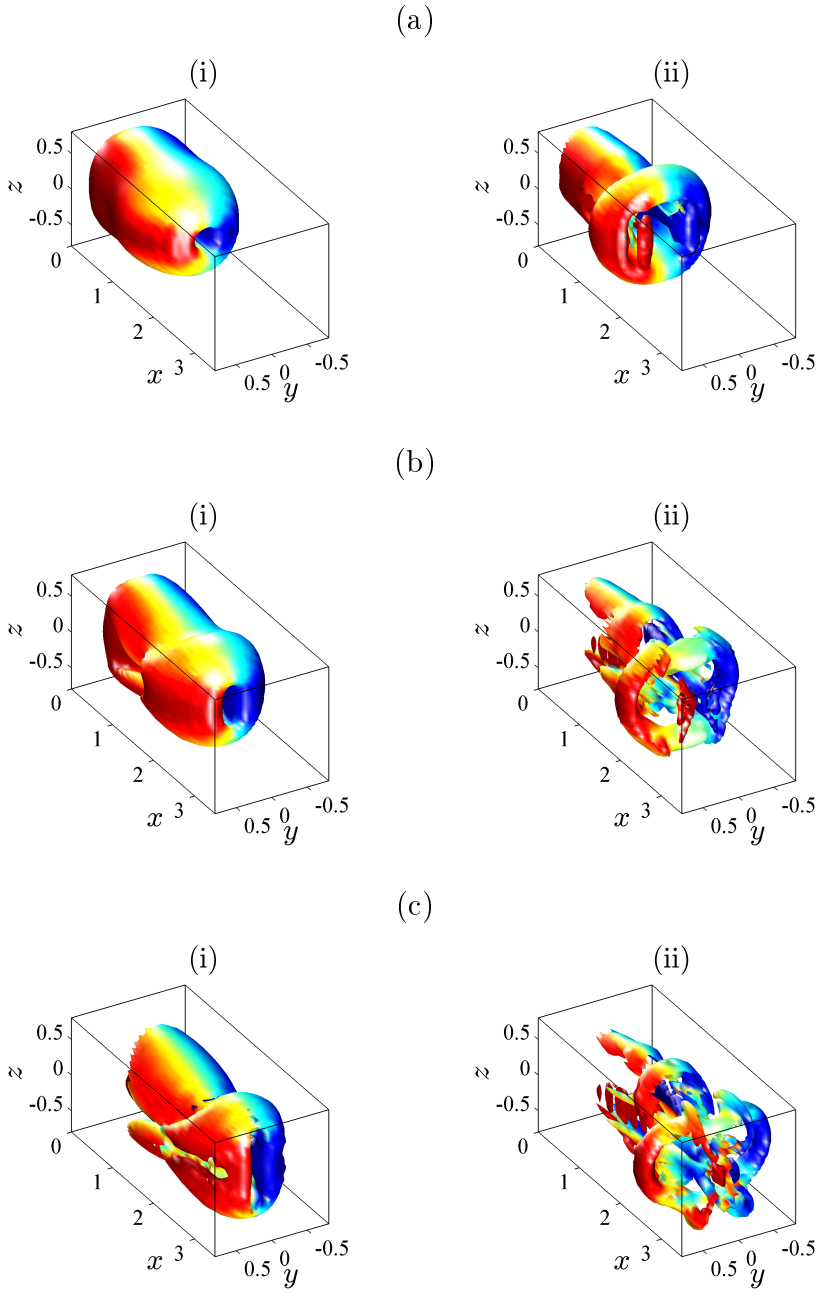

Figure 6.3: Isosurfaces of constant vorticity magnitude, $|\omega|$, for Gaussian and Hyperbolic momentum sources in stably stratified fluid (N = 1) with (a)(i) Case GAU3 at t = 3, (ii) Case HYP3 at t = 3, (b)(i) Case GAU3 at t = 4, (ii) Case HYP3 at t = 4, (c)(i) Case GAU3 at t = 5, (ii) Case HYP3 at t = 5. Colour contouring ranges between $\pm 0.6|\omega_z|_{\text{Max}}$, with isosurface threshold set at $0.25|\omega|_{\text{Max}}$.

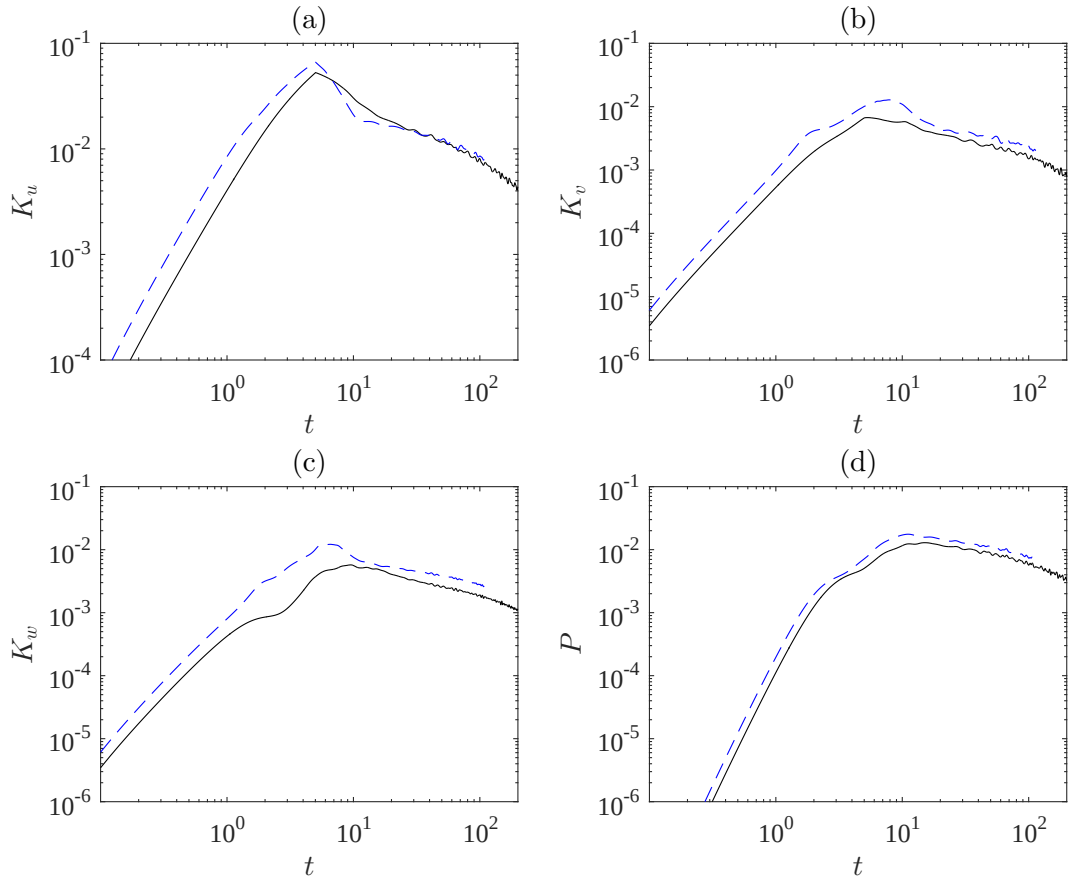

Figure 6.4: Time history of volume integrated kinetic and buoyancy variance levels for cases GAU3 (—) and HYP3 (--). Levels shown are (a) streamwise kinetic energy, K_u, (b) lateral kinetic energy, K_v (c) vertical kinetic energy and (d) buoyancy variance, P

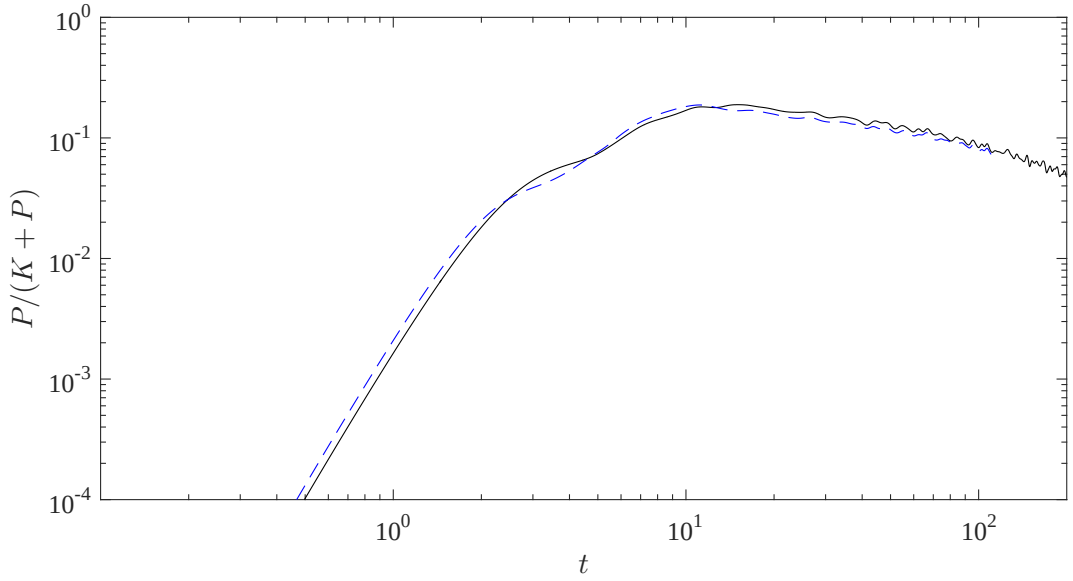

Figure 6.5: Time history of volume integrated internal to total energy ratio for cases GAU3 (—) and HYP3 (--).

isosurfaces given in figures 6.6 and 6.7 demonstrate the structure of the dipole for the Gaussian and Hyperbolic case at near identical times. Both cases give a very similar structure with the characteristic contra-rotating columns of vorticity bound by the upper and lower shear layers as seen in chapters 4 and 5. Both cases appear to have similar lateral spacing between the columns (verified further in figure 6.9), with the columns themselves having similar height (verified further in figure 6.12). The key difference in structure appears to be the shape and thickness of the shear layer, which is thinner and covers a larger area in the horizontal plane for the Hyperbolic case than the Gaussian case. This thinner shear layer might help explain why the dipole in the Hyperbolic case, while attributed the same momentum as the Gaussian case, has propagated a shorter distance over this near identical time period, with viscous drag from the thin shear layer exhibiting a larger declarative effect on the dipole than the thicker shear layer seen for the Gaussian case. Overall though, the similarity between these late time structures is much closer than the initial trailing jet and leading ring structures formed during the early stages of momentum injection.

Figure 6.8 demonstrates the vertical vorticity field at the vertical midplane at the equivalent times given in figures 6.6 and 6.7, again showing marked similarity in structure between the two dipoles. The key distinction between the two would appear to be the Gaussian case maintains a more significant tail structure in the wake of the leading dipole, with the Hyperbolic case having a far more minimal tail with a greater majority of the vertical vorticity contained within leading dipole. Arguably, the latter gives better qualitative agreement with the dipoles documented by Voropayev et al. (2008) though this is quite subjective, with the contouring levels, sampling time etc. all having an effect on how visible the tail structure is compared to the leading dipole. A more quantitative comparison of dipole structure is given in figure 6.9, with the lateral profile of vertical vorticity through the cores of the dipoles at the vertical midplane at these times. Figure 6.9(a) demonstrates that the Hyperbolic case has a slightly higher core circulation than the Gaussian case at this time, which is perhaps unsurprising given that less vorticity is contained within the tail structure, with the lateral distance between the vorticity minima and maxima again slightly higher for the hyperbolic case as documented in table 6.2. Using these distances and peak vorticity values, the lateral vorticity profiles can be normalised as demonstrated in figure 6.9(b). These normalised profiles are near identical for the two dipoles, further pointing toward the late time structure being independent of the profile of the initial momentum

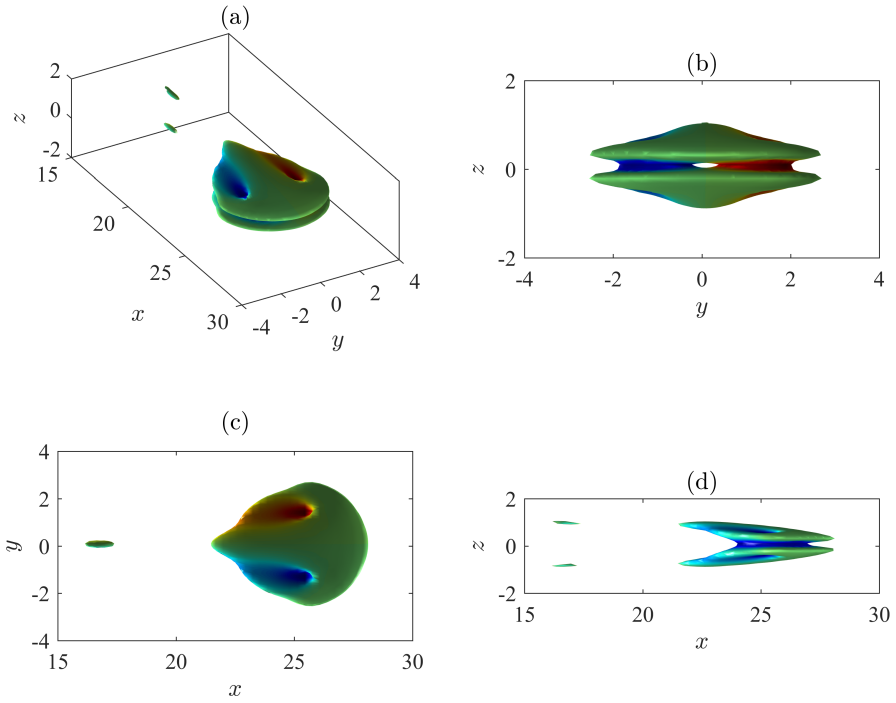

Figure 6.6: Isosurfaces of constant vorticity magnitude, $|\omega|$, for case GAU3 at t = 209 demonstrating the structure of the late time dipole (for a Gaussian profile momentum injection), with views looking from (a) positive x, negative y, positive z to negative x, positive y, negative z, (b) positive x to negative x, (c) positive z to negative z (d) negative y to positive y. Colour contouring ranges between $\pm 0.6|\omega_z|_{\text{Max}}$, with isosurface threshold set at $0.25|\omega|_{\text{Max}}$.

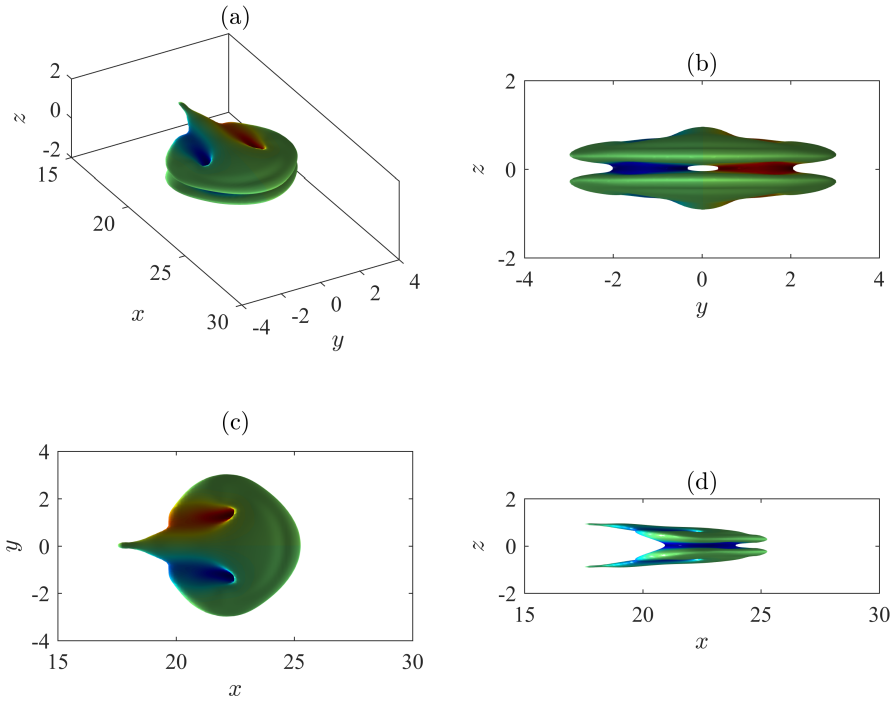

Figure 6.7: Isosurfaces of constant vorticity magnitude, $|\omega|$, for case HYP3 at $t = 211$ demonstrating the structure of the late time dipole (for a Hyperbolic profile momentum injection), with views looking from (a) positive x, negative y, positive z to negative x, positive y, negative z, (b) positive x to negative x, (c) positive z to negative z (d) negative y to positive y. Colour contouring ranges between $\pm 0.6|\omega_z|_{\text{Max}}$, with isosurface threshold set at $0.25|\omega|_{\text{Max}}$.

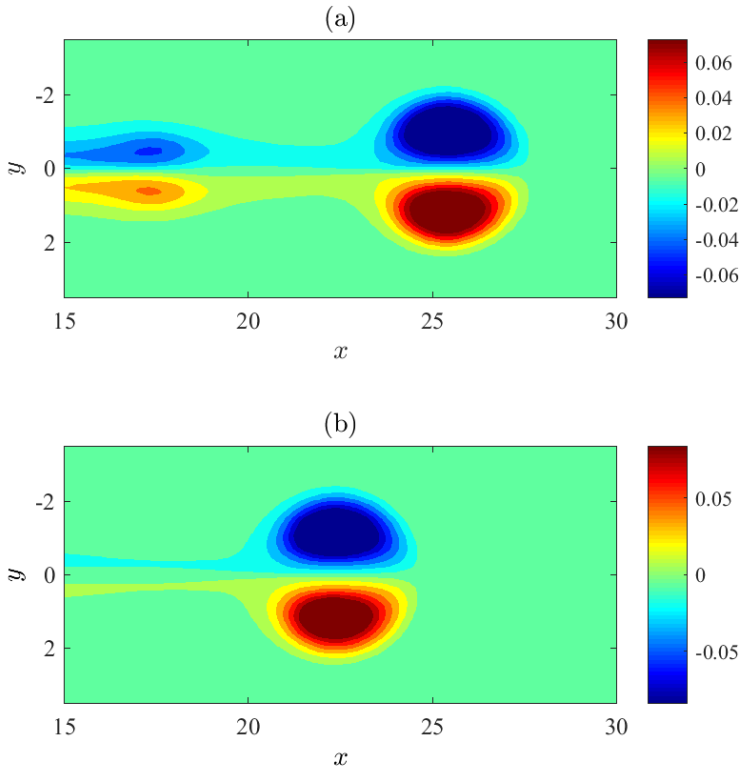

Figure 6.8: Contours of vertical vorticity, ω_z, at $z = 0$ for (a) case GAU3 at $t = 209$ and (b) case $HYP3$ at $t = 211$. Colour contouring ranges between $\pm 0.6|\omega_y|_{\text{Max}}$ and $\pm 0.6|\omega_z|_{\text{Max}}$ respectively.

Case	t	$D_{y\omega}$	$\omega_z\|_{\text{Max}}$
GAU3	209	2.094	0.121
HYP3	211	2.258	0.140
±		7.8%	15.5%

Table 6.2: Vortex dipole midplane maximum to minimum vorticity distances and maximum vorticity values for Gaussian and Hyperbolic momentum injections as used in figure 6.9(b).

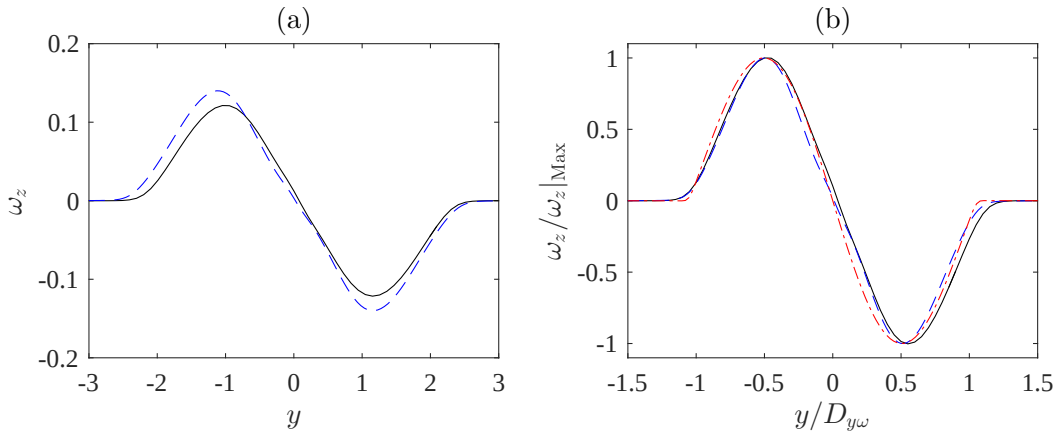

Figure 6.9: Lateral profiles of vertical vorticity, ω_z, through the late time vortex dipole, with profile taken at $z = 0$ and x coordinate equal to location of $\omega_z|_{\text{Max}}$. (a) Raw lateral vorticity profile for case GAU3 at $t = 209$ (—) and HYP3 at $t = 211$ (−−). (b) As (a) but lateral distance normalised by the distance in y between ω_z minimum and maximum for each case, and vertical vorticity normalised by $\omega_z|_{\text{Max}}$ and an additional profile added for the Lamb-Chaplygin model detailed in section 1.2.3 (−·−).

injection. In addition to this, the equivalent normalised profile for a Lamb-Chaplygin dipole model is plotted on the same axes. Both the late time dipoles appear to give excellent agreement with this model, which not only helps validate the numerical methods employed here but also lends further credence to the diffusing dipole model proposed by Praud and Fincham (2005), which simulated dipole evolution through the vertical diffusion of a Lamb-Chaplygin dipole from a vertical midplane.

Finally, the streamwise centre, diameter and vertical thickness of the late time dipoles for the Hyperbolic cases is evaluated to compare with the scaling laws defined in previous chapters, namely equations 1.15, 1.16 and 1.23 which give

Case	t_D	t_H	Plot marker
GAU4	344	190	○
HYP4	1028	313	×
HYP5	168	206	+

Table 6.3: Time offsets for dipole lateral and vertical scaling as given in figures 6.11 and 6.12).

$$X_D = \alpha_X (t - t_X)^{1/3},$$

$$D_D = \alpha_D (t - t_D)^{1/3},$$

$$H_\omega = 2\sqrt{2}\left(\frac{t - t_H}{Re}\right)^{1/2} \approx 2.828\left(\frac{t - t_H}{Re}\right)^{1/2}.$$

Good agreement for the latter two of these scaling laws was demonstrated across a range of cases for the late time dipoles in chapter 5. The values of streamwise centre and diameter are calculated here using the same methods as employed for figure 5.19, where thresholding has been used to exclude the vorticity in the tail to make for more accurate tracking of the leading dipole. As the simulations conducted for this chapter were not run for as long as those documented in chapter 5, it was not practical to calculate values of the time offset for streamwise position scaling, t_X. However, the simulations had been run long enough to obtain suitable time offsets for the diameter and vertical thickness scaling laws as documented in table 6.3. Figure 6.10 gives the time history of the late time dipole's streamwise position for cases GAU4 and HYP4 (short momentum injection, large domain) as well as HYP5 (as HYP4 but longer momentum injection). As mentioned previously, the length of these simulations was less than the simulations from chapter 5, and insufficient time appears to have been allowed for the simulation to develop to the point where the validity of the streamwise position scaling law can be properly evaluated. Nonetheless, comparing the dipole position for cases GAU4 and HYP4 does confirm the previous observation that the Gaussian profile momentum injection results in a faster propagating dipole than an equivalent Hyperbolic profile injection. Despite this, the agreement with the scaling law for dipole diameter as demonstrated in figure 6.11 was seemingly achieved for each case at the late time with dipole diameter scaling well with $D_D \propto (t - t_D)^{1/3}$. Similarly, each of the cases appears to give very similar vertical scaling behaviour at the late time, with all three appearing to collapse onto $2\sqrt{2}\left((t - t_H)/Re\right)^{1/2}$ at the

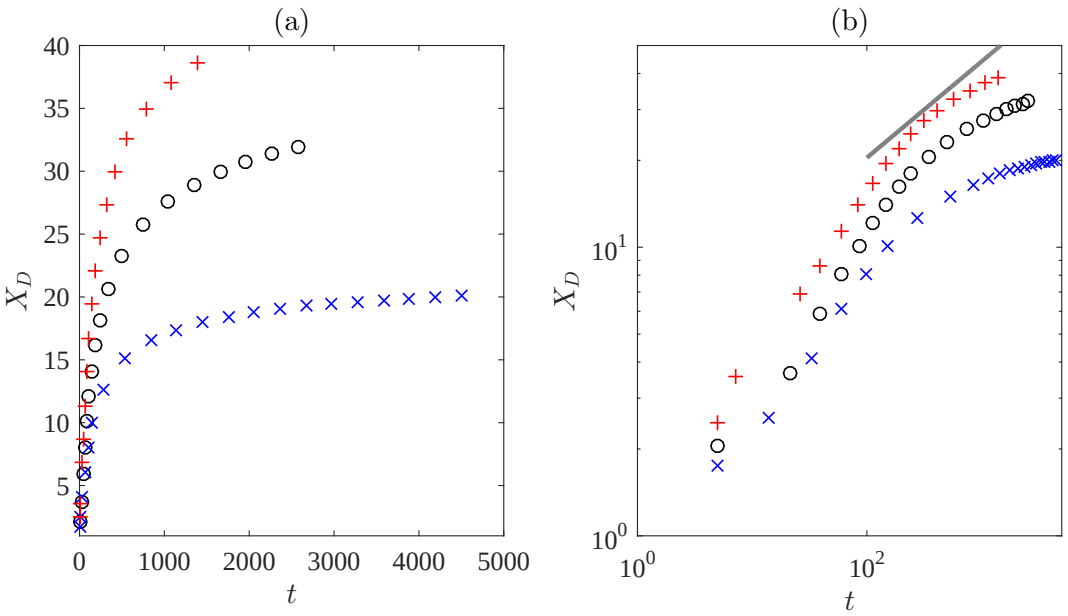

Figure 6.10: (a) Time history of dipole streamwise location, X_D, for GAU4 (○), HYP4 (×) and HYP5 (+) (b) The same data plotted on logarithmic axes with the thick line indicating $X_D \propto t^{1/3}$.

late time (figure 6.12). Thus, for all of the models and scaling laws considered here, where agreement could be found with the late time dipoles produced from a Gaussian profile momentum injection into a stably stratified fluid, similar agreement could be found for dipoles produced from an equivalent Hyperbolic profile injection.

6.3 Chapter summary

The primary purpose of this chapter has been to investigate how sensitive the late time dipole formed in a stably stratified fluid from a horizontal momentum injection is to the forcing profile of said injection. This was investigated by simulating multiple cases with equivalent viscosity and background stratification strength, but with either momentum injection provided by a source term distributed by a three-dimensional Gaussian function or a three-dimensional Hyperbolic function (scaled to give equivalent impulse to the fluid). While these cases exhibited clear structural differences at the early time in terms of the shape of the starting jet and leading vortex ring, at the late time the leading vortex dipoles were structurally similar, with the midplane vorticity profiles giving excellent agreement with the Lamb-Chaplygin model. Additionally, both profiles of momentum injection gave late time dipoles that agreed with the lateral and vertical scaling laws provided by Voropayev et al. (2008)

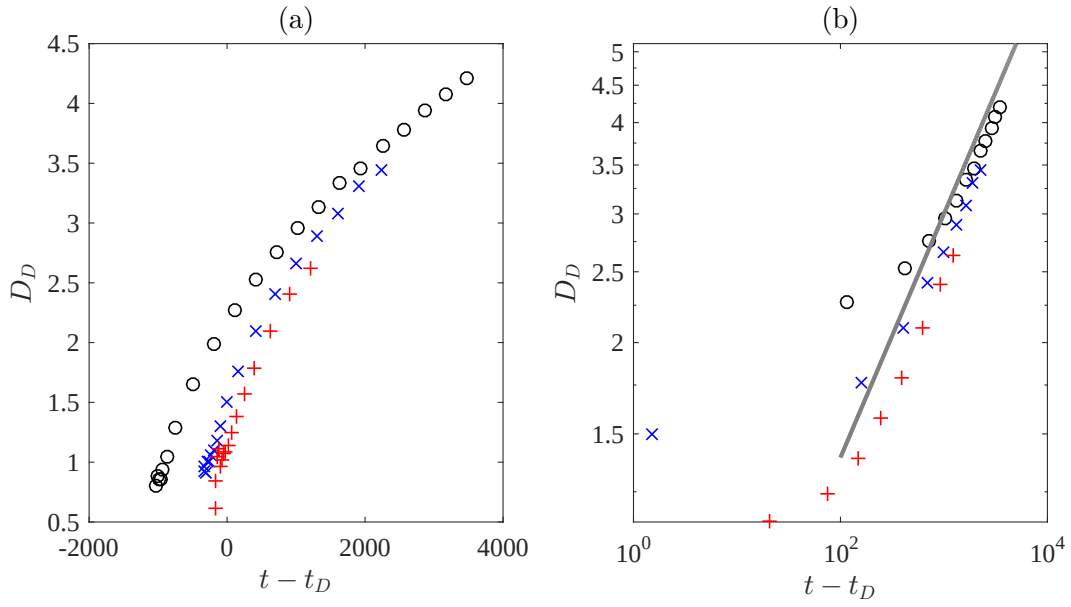

Figure 6.11: (a) Time history of dipole diameter, D_D, for GAU4 (○), HYP4 (×) and HYP5 (+) (b) The same data plotted on logarithmic axes with the thick line indicating $D_D \propto (t - t_D)^{1/3}$.

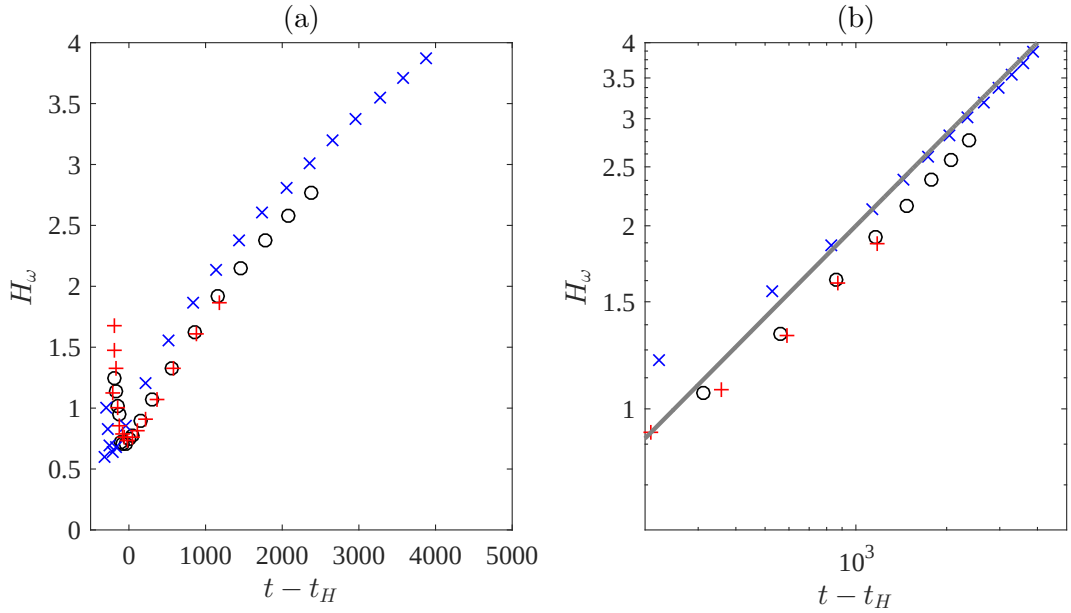

Figure 6.12: (a) Time history of dipole vertical thickness, H_ω, for GAU4 (○), HYP4 (×) and HYP5 (+) (b) The same data plotted on logarithmic axes with the thick line giving $2\sqrt{2}\left((t - t_H)/Re\right)^{1/2}$, where $Re = 2000$ for all cases.

and Praud and Fincham (2005) respectively. This is in spite of the fact that the qualitative agreement for a Gaussian momentum injection and experimental observations of starting jets in neutrally stratified fluid, or at the early time in stably stratified fluid, is apparently poor in comparison to the Hyperbolic momentum source.

Overall, the outcome of this chapter is to both lend additional credence to the results of chapter 5 in terms of describing the late time vortex dipole, and also provide further agreement between the numerical simulations of this work and experimental studies documented in literature.

Chapter 7

Conclusions and future work

7.1 Conclusions

The evolution of a dipolar vortex from an initially axisymmetric flow structure under the vertical constraint of stable stratification has been simulated through the use of the Spectral DNS code detailed in section 2.3. The two structures considered in this work are a horiztonally propogating vortex ring, as well as an axisymmetric starting jet formed from a horizontal momentum injection into an initially quiescent domain. In accordance with all comparable experimental studies, the dipole forms following the buoyant collapse of the flow as vertical motions are suppressed to leave a three dimensional structure, but consisting of quasi-horizontal velocity fields throughout its vertical extent.

The evolution of kinetic energy and buoyancy variance levels within the structure have been divided into four phases, namely (i) injection, (ii) instability development, (iii) buoyant collapse and internal wave generation, (iv) quasi-horizontal, diffusive flow. Each of these stages can be identified clearly with corresponding changes in energy levels, vorticity contours, buoyancy scalar and dipole aspect ratio (at the late time). A thorough quantification of the stages of dipole evolution through energy levels is not something discussed in any of the relevant literature reviewed in chapter 1, and as such is believed to present an original data set for future investigations to be compared against. The energy history for each of the stages is qualitatively similar between each stably stratified case, though sensitivities to the three governing parameters; Reynolds number, stratification strength and initial impulse were noted and discussed. In particular, the changes in vertical kinetic energy and buoyancy variance (which are coupled through the buoyancy flux term in the governing equations) appear to take place on a buoyancy normalised time measure, $Nt/2\pi$, at intermediate times.

Comparisons have been made with the (sometimes conflicting) scaling laws for a late time dipole proposed in literature. Most significantly, the assertion of Voropayev et al. (2008) that dipole thickness is near constant once fully formed appears to be invalid for the cases considered here. Instead, excellent agreement is found with the vertical diffusion model provided by Flór et al. (1995). Given that the experimental works used to previously verify the diffusion model all used a saline solution with approximately equal kinematic viscosity in each case (around $10^{-6}m^2s^{-1}$), there remained a question as to whether the viscous scaling model would be valid for different fluid viscosity. The range of Reynolds numbers ($Re = 1/\nu$) simulated in this work lends more credence to the model than could be achieved from experiments alone. Additionally, the other important governing parameters considered here, namely stratification strength and initial impulse, appear to have a minimal effect on the late time scaling of dipole vertical thickness, only influencing the interval between the end of the momentum injection and the time at which the diffusive behaviour becomes significant in the vertical direction. The commencement of diffusive dominated behaviour could be quantified consistently between cases as the point at which the dipole's vertical to lateral aspect ratio begins to increase after an initial rapid decrease.

Asymptotic agreement was found with the scaling behaviours for dipole streamwise position and peak vertical vorticity proposed in Voropayev et al. (2008), though both were highly sensitive to the range of data chosen to evaluate the agreement, so the validity of those experimental scaling laws (equations 1.15, 1.18) remains questionable. Much improved agreement was found with the dipole diameter scaling proposed by the same authors, though as discussed in the latter part of chapter 5, there is sufficient evidence to suggest that the dipole actually expands slightly faster as the lateral expansion becomes diffusion dominated. As such, the late time expansion of the dipole in both the lateral and vertical directions are both governed by a viscosity normalised time measure, νt. A diffusion based model for lateral expansion of the dipole is not presented in any of the literature studied for this project, though the data from this work and some (but not all) of the data from previous literature indicates that such a model may be valid. Certainly the lateral structure and expansion of the dipole is a topic warranting further investigation and could be considered further in future works. Additionally, excellent agreement was found for the vorticity profile across the late time dipole and the Lamb-Chaplygin model often used as a basis for comparison in experimental literature.

In any case, the author believes this to be first documented work that pro-

vides a set of fully resolved numerical simulations analogous to the experimental works of Voropayev et al. (1991); Praud and Fincham (2005); Voropayev et al. (2008) and others. While some previous attempts have been made to model the late time dipoles via analytical models such as those of Praud and Fincham (2005), they did not rely on fully resolving the Navier-Stokes equations as per the simulations in this work, though these models are further validated by results presented in previous chapters. In addition to verifying or contradicting the results of these experimental studies, this work offers an insight into the kinetic energy and buoyancy variance evolution from the initially axisymmetric structure to the late time dipole and a brief examination of the buoyancy scalar field, none of which is easily accessible via experiment.

7.2 Future work

Several avenues of future investigation could be taken on from the conclusions of this project. Firstly, an often cited application of research into impulsive momentum sources in a stratified fluid is the study of the wakes of submerged vehicles or marine creatures that utilise impulsive momentum injections for acceleration. An example of an experimental study that aimed to represent this was performed by Voropayev et al. (1999), using a self-propelled model submarine to generate wake structures in a testing tank of stably stratified saline fluid. A numerical study aiming to create an analogy to this would require numerical simulation of an impulsive momentum source in a moving frame of reference (or for the source itself to propagate) to mimic the effects of acceleration, as well as some way of simulating the drag imparted on the body at non-zero velocities (i.e. an accelerating force doublet).

The simulations in this work considered only the evolution of a horizontal momentum injection or horizontally propagating vortex ring. However, in the case of a momentum injection to propel a submerged body, there are likely several instances where an impulsive momentum injection would be required to have some vertical component to the propulsive vector, and so simulation could be used to determine how the structures formed from these non-horizontal momentum injections compare with the late time dipoles detailed in this thesis.

Finally, a further step in understanding vortex dipoles in a stratified fluid is achieved not just from studying the flow inside the core of the dipole at its vertical midplane, but how the flow within the dipole propagates in the vertical direction and how this may be detected at the surface of a fluid body containing such a dipole (e.g. a geophysically created dipole beneath the ocean surface

being detected from a surface signature). Again, this has been approximated experimentally though the work of Voropayev et al. (2007), though numerical literature appears to remain lacking in this area.

Appendix A

Computational resources

Two high performance computer clusters were available for the project in order to perform the necessary simulations. The University of Southampton's own cluster, Iridis 3, and the national research cluster, HECToR.

A.1 Iridis 3

Iridis 3, at the time this research was conducted, was the most powerful of two computer clusters available for research at the University of Southampton, and at the time of its introduction was the most powerful university owned supercomputer in the UK. It is available for in-house academic and postgraduate research work that requires moderate to high levels of processor count, speed and memory.

Initially the cluster was equipped with 1008 compute nodes, each with 8 2.27GHz processor cores and 22GB of memory, giving a peak system performance of over 72 Teraflops. The nodes were later upgraded to 12 processor cores each, increasing the total number of cores available to users. Software installed on Iridis 3 includes Intel supplied compilers and MPI libraries, which were used to compile and run the Fortran code scripts used in this project. The code can be ported between Iridis and HECToR with simple modifications to the compiling and batch submission procedures.

Iridis 3 has since been superseded by Iridis 4.

A.2 HECToR

HECToR (High-End Computing Terascale Resource), at the time this research was conducted, was the United Kingdom's largest and most powerful supercomputer, funded by a consortium of research councils and based at the Uni-

versity of Edinburgh. The cluster was designed for academic research such as that undertaken for this thesis, where memory and processor speed and quantity are required to levels beyond the capabilities of a single institution's cluster such as Iridis.

HECToR was based on a Cray XE6 and was equipped with 2816 compute nodes with 32 processor cores rated at 2.3GHz each, with 32GB of memory per node. The interconnect hardware provided a reported bandwidth of 5GB/s or greater, with the machine as a whole having a peak theoretical performance of 800 Teraflops. The code was compiled using a GNU copiler library as opposed to the Intel library used on Iridis.

HECToR has since been replaced by ARCHER.

A.3 Use of resources

At the time of writing this report, much of the early simulation work for the project was carried out on Iridis 3. This included all the validation simulations discussed in Chapter 3, and early test versions of simulations discussed in Chapter 5. The high clock speed and unlimited usage of Iridis 3 makes it suitable for rapid development of the code and low quality simulations, although the upper limit on cores that can be requested at one time, added to potentially lengthy queue times for sizable jobs leads to high quality production runs taking up to several days to complete after initial job submission.

HECToR's processing cores are slightly slower than Iridis, and less memory is available per core, but the total number of cores that can be requested is far higher, allowing for much larger, memory intensive jobs to be performed. The total number of core hours available to the project does have an upper limit, which makes regular lengthy test runs impractical. The validation tests for the code used in this research and some early simulations of vortex dipole flows were performed on Iridis, with the bulk of the intensive research work performed on HECToR.

References

Afanasyev, Y. (2006). Formation of vortex dipoles. *Physics of Fluids*, 18(3):037103.

Akhmetov, D. (2001). Formation and basic parameters of vortex rings. *Journal of Applied Mechanics and Technical Physics*, 42(5):794–805.

Archer, P. (2008). *A Numerical Study of Laminar to Turublent Evolution and Free-Surface Interaction of a Vortex Ring*. PhD thesis.

Archer, P., Thomas, T., and Coleman, G. (2008). Direct numerical simulation of vortex ring evolution from the laminar to the early turbulent regime. *Journal of Fluid Mechanics*, 598.

Beckers, M., Verzicco, R., and Clercx, H. (2001). Dynamics of pancake-like vortices in a stratified fluid: experiments, model and numerical simulations. *Journal of Fluid Mechanics*, 433:1–27.

Boersma, B., Brethouwer, G., and Nieuwstadt, F. (1998). A numerical investigation on the effect of the inflow conditions on the self-similar region of a round jet. *Physics of Fluids*, 10(4):899–909. Ze096 Times Cited:104 Cited References Count:23.

Coleman, G. and Sandberg, R. (2010). A primer on direct numerical simulation of turbulence – methods, procedures and guidelines. Technical report, University of Southampton.

Dabiri, J. (2009). Optimal vortex formation as a unifying principle in biological propulsion. *Annual Review of Fluid Mechanics*, 41(1):17–33.

Dabiri, J. and Gharib, M. (2004). Fluid entrainment by isolated vortex rings. *Journal of Fluid Mechanics*, 511:311–331.

Dawson, J., Worth, N., and Aydemir, E. (2010). An investigation of vortex ring formation in strongly forced jet flows by high speed particle image velocimetry.

Dazin, A., Dupont, P., and Stanislas, M. (2005). Experimental characterization of the instability of the vortex ring. part i: Linear phase. *Experiments in Fluids*, 40(3):383–399.

Dazin, A., Dupont, P., and Stanislas, M. (2006). Experimental characterization of the instability of the vortex rings. part ii: Non-linear phase. *Experiments in Fluids*, 41(3):401–413.

de Stadler, M., Sarkar, S., and Brucker, K. (2010). Effect of the prandtl number on a stratified turbulent wake. *Physics of Fluids*, 22(9):095102.

Delbende, I. and Rossi, M. (2009). The dynamics of a viscous vortex dipole. *Physics of Fluids*, 21(7):073605.

Fedorov, K. and Ginsburg, A. (1989). Mushroom-like currents (vortex dipoles): One of the most widespread forms of non-stationary coherent motions in the ocean. *Elsevier Oceanography Series*, 50:1–14.

Flór, J. and van Heijst, G. (1994). An experimental study of dipolar vortex structures in a stratified fluid. *Journal of Fluid Mechanics*, 279:101–133.

Flór, J., van Heijst, G., and Deflos, R. (1995). Decay of dipolar vortex strucutres in a stratified fluid. *Physics of Fluids*, 7(2):374–383.

Gharib, M., Rambod, E., and Shariff, K. (1998). A universal time scale for vortex ring formation. *Journal of Fluid Mechanics*, 360:121–140.

Godoy-Diana, R., Chomaz, J.-M., and Billant, P. (2004). Vertical length scale selection for pancake vortices in strongly stratified viscous fluids. *Journal of Fluid Mechanics*, 504:229–238.

Gottlieb, D. and Orszag, S. (1977). *Numerical Analysis of Spectral Methods: Theory and Applications*. Society for Industrial and Applied Mathematics, Philidelphia, Pennsylvania.

Hussaini, M. and Zang, T. (1987). Spectral methods in fluid dynamics. *Annual Review of Fluid Mechanics*, 19:339–367.

Johari, H. and Fang, H. (1997). Horizontal vortex ring motion in linearly stratified media. *Physics of Fluids*, 9(9):2605–2616.

Kerswell, R. (2002). Elliptical instability. *Annual Review of Fluid Mechanics*, 34:83–113.

Krueger, P. and Gharib, M. (2003). The significance of vortex ring formation to the impulse and thrust of a starting jet. *Physics of Fluids*, 15(5):1271.

Lighthill, J. (1978). *Waves in fluids*. Cambridge University Press, Cambridge.

Llewellyn Smith, S. and Nagem, R. (2013). Vortex pairs and dipoles. *Regular and Chaotic Dynamics*, 18(1-2):194–201.

Makarov, V. and Kizner, Z. (2011). Stability and evolution of uniform-vorticity dipoles. *Journal of Fluid Mechanics*, 672:307–325.

Marino, R., Mininni, P., and Rosenberg, D., e. a. (2013). Inverse cascades in rotating stratified turbulence: Fast growth of large scales. *EPL (Europhysics Letters)*, 102(4):44006.

Meleshko, V.v.H., G. (1994). On chaplygin's investigations of two-dimensional vortex structures in an inviscid fluid. *Journal of Fluid Mechanics*, 272:157–182.

Mohseni, K., Colonius, T., and Ran, H. (2001). Numerical experiments on vortex ring formation. *Journal of Fluid Mechanics*, 430:267–282.

Mowbray, D. and Rarity, B. (1967). A theoretical and experimental investigation of the phase configuration of internal waves of small amplitude in a density stratified liquid. *Journal of Fluid Mechanics*, 28(1):1–16.

Praud, O. and Fincham, A. (2005). The structure and dynamics of dipolar vortices in a stratified fluid. *Journal of Fluid Mechanics*, 544(-1):1.

Redford, J., Coleman, G., and Lund, T. (2015). A numerical study of a weakly stratified turbulent wake. *Journal of Fluid Mechanics*, 776:568–609.

Rind, E. (2010). *Turbulent Wakes in Turbulent Streams*. PhD thesis.

Rojanaratanangkule, W., Coleman, G., and Thomas, T. (2012). Numerical study of turbulent manoeuvring-body wakes: interaction with a non-deformable free surface. *Journal of Turbulence*, 13(17):1–22.

Rojanaratanangkule, W., Thomas, T., and Coleman, G. (2014). A numerical investigation of impulsively generated vortical structures in deep and shallow fluid layers. *Physics of Fluids*, 26(2):025108.

Rosenfeld, M.R., E. and Gharib, M. (1998). Circulation and formation number of laminar vortex rings. *Journal of Fluid Mechanics*, 376:297–318.

Ruijgrok, G. (1996). *Elements of Airplane Performance.* Delft University Press, Delft.

Ruiz, L., Whittlesey, R., and Dabiri, J. (2010). Vortex-enhanced propulsion. *Journal of Fluid Mechanics*, 668:5–32.

Saffman, P. (1970). The velocity of viscous vortex rings. *Stud. Appl. Maths*, 49:371–380.

Scase, M. and Dalziel, S. (2006). An experimental study of the bulk properties of vortex rings translating through a stratified fluid. *European Journal of Mechanics - B/Fluids*, 25(3):302–320.

Spalart, P., Moser, R., and Rogers, M. (1991). Spectral methods for the navier-stokes equations with one infinite and two periodic directions. *Journal of Computational Physics*, 96(2):297–324.

Turner, J. (1979). *Buoyancy effects in fluids.* Cambridge University Press, 1st paperback edition.

van Atta, C. and Hopfinger, E. (1989). Vortex ring instability and collapse in a stably stratified fluid. *Experiments in Fluids*, 7:197–200.

van Heijst, G. and Flór, J. (1989). Dipole formation and collisions in a stratified fluid. *Letters To Nature*, 340:212–215.

Voropayev, S., Afanasyev, Y., and Filippov, I. (1991). Horizontal jets and vortex dipoles in a stratified fluid. *Journal of Fluid Mechanics*, 227:543–566.

Voropayev, S., Fernando, H., and Morrison, R. (2008). Dipolar eddies in a decaying stratified turbulent flow. *Physics of Fluids*, 20(2):026602.

Voropayev, S., Fernando, H., and Smirnov, S.A., e. a. (2007). On surface signatures generated by submerged momentum sources. *Physics of Fluids*, 19(7):076603.

Voropayev, S., McEachern, G., and Fernando, H.J.S., e. a. (1999). Large vortex structures behind a maneuvering body in stratified fluids. *Physics of Fluids*, 11(6):1682–1684.